ISSN 1949-8470 (online)

World Journal of *Radiology*

Monthly Volume 17 Number 8 August 28, 2025

Published by Baishideng Publishing Group Inc

World Journal of Radiology

Contents Monthly Volume 17 Number 8 August 28, 2025

World Journal of Radiology

Monthly Volume 17 Number 8 August 28, 2025

Contents

ABOUT COVER

Peer Reviewer of *World Journal of Radiology*, Alessandro Posa, MD, Diagnostic and Interventional Radiologist, Emergency and Interventional Radiology Unit, Department of Diagnostic Imaging and Radiation Oncology, Fondazione Policlinico Universitario Agostino Gemelli - IRCCS, Roma 00168, Italy. alessandro.posa@gmail.com

AIMS AND SCOPE

The primary aim of *World Journal of Radiology* (*WJR*, *World J Radiol*) is to provide scholars and readers from various fields of radiology with a platform to publish high-quality basic and clinical research articles and communicate their research findings online.

WJR mainly publishes articles reporting research results and findings obtained in the field of radiology and covering a wide range of topics including state of the art information on cardiopulmonary imaging, gastrointestinal imaging, genitourinary imaging, musculoskeletal imaging, neuroradiology/head and neck imaging, nuclear medicine and molecular imaging, pediatric imaging, vascular and interventional radiology, and women's imaging.

INDEXING/ABSTRACTING

The *WJR* is now abstracted and indexed in PubMed, PubMed Central, Emerging Sources Citation Index (Web of Science), Reference Citation Analysis, China Science and Technology Journal Database, and Superstar Journals Database. The 2025 Edition of Journal Citation Reports® cites the 2024 journal impact factor (JIF) for *WJR* as 1.5; JIF without journal self cites: 1.4; 5-year JIF: 1.6; JIF Rank: 137/212 in radiology, nuclear medicine and medical imaging; JIF Quartile: Q3; and 5-year JIF Quartile: Q3.

RESPONSIBLE EDITORS FOR THIS ISSUE

NAME OF JOURNAL
World Journal of Radiology

ISSN
ISSN 1949-8470 (online)

LAUNCH DATE
January 31, 2009

FREQUENCY
Monthly

EDITORS-IN-CHIEF
Thomas J Vogl

EDITORIAL BOARD MEMBERS
https://www.wjgnet.com/1949-8470/editorialboard.htm

PUBLICATION DATE
August 28, 2025

INSTRUCTIONS TO AUTHORS
https://www.wjgnet.com/bpg/gerinfo/204

GUIDELINES FOR ETHICS DOCUMENTS
https://www.wjgnet.com/bpg/GerInfo/287

GUIDELINES FOR NON-NATIVE SPEAKERS OF ENGLISH
https://www.wjgnet.com/bpg/gerinfo/240

PUBLICATION ETHICS
https://www.wjgnet.com/bpg/GerInfo/288

PUBLICATION MISCONDUCT
https://www.wjgnet.com/bpg/gerinfo/208

ARTICLE PROCESSING CHARGE
https://www.wjgnet.com/bpg/gerinfo/242

STEPS FOR SUBMITTING MANUSCRIPTS
https://www.wjgnet.com/bpg/GerInfo/239

ONLINE SUBMISSION
https://www.f6publishing.com

World Journal of Radiology

Submit a Manuscript: https://www.f6publishing.com

World J Radiol 2025 August 28; 17(8): 111076

DOI: 10.4329/wjr.v17.i8.111076

ISSN 1949-8470 (online)

REVIEW

Stereotactic radiotherapy for brain metastases of non-small cell lung cancer: A comprehensive review

Aamir Khan, Hong-Fu Zhao, Hao Meng, Ning Wu, Lin-Lin Liu

Specialty type: Radiology, nuclear medicine and medical imaging

Provenance and peer review: Invited article; Externally peer reviewed.

Peer-review model: Single blind

Peer-review report's classification
Scientific Quality: Grade C
Novelty: Grade B
Creativity or Innovation: Grade C
Scientific Significance: Grade C

P-Reviewer: Han ZG, MD, PhD, Associate Professor, China

Received: June 23, 2025
Revised: July 16, 2025
Accepted: August 8, 2025
Published online: August 28, 2025
Processing time: 67 Days and 2 Hours

Aamir Khan, Hong-Fu Zhao, Hao Meng, Ning Wu, Lin-Lin Liu, Department of Radiation Oncology, China-Japan Union Hospital of Jilin University, Changchun 130033, Jilin Province, China

Co-corresponding authors: Ning Wu and Lin-Lin Liu.

Corresponding author: Ning Wu, MD, Professor, Department of Radiation Oncology, China-Japan Union Hospital of Jilin University, No. 126 Xiantai Street, Changchun 130033, Jilin Province, China. wuning@jlu.edu.cn

Abstract

Lung cancer, particularly non-small cell lung cancer (NSCLC), remains a leading cause of cancer-related death globally, and a significant number of patients develop brain metastasis (BM) as the disease progresses. The presence of BM, which affects up to 60% of patients with NSCLC, is correlated with an unfavorable prognosis and markedly decreased quality of life. Standard treatment options for BMs, such as whole-brain radiation therapy and surgery, have displayed limited efficacy in controlling disease progression, and they can cause significant neurocognitive side effects. Stereotactic radiotherapy (SRT), including stereotactic radiosurgery, fractionated SRT, and stereotactic body radiotherapy, represents an advanced and precise approach for treating BM that minimizes damage to surrounding healthy tissues. This review highlights recent advances in the application of SRT for treating BM of NSCLC, focusing on its underlying biological principles and mechanisms of action as well as the quality standards necessary for effective SRT implementation. The ability of SRT to deliver substantial radiation doses in a precisely targeted manner has resulted in better local tumor management, fewer side effects, and increased patient survival rates. Future research is crucial to improve SRT procedures and successfully incorporate them into multimodal therapy plans for patients with NSCLC and BM.

Key Words: Lung carcinoma; Non-small cell lung cancer; Brain metastasis; Stereotactic radiotherapy; Blood–brain barrier; Tumor microenvironment

Core Tip: Stereotactic radiotherapy (SRT) offers a precise and effective treatment option for brain metastasis (BM) in patients with non-small cell lung cancer (NSCLC), providing better local tumor control, fewer side effects, and improved survival rates compared with the effects of traditional therapies. Integrating SRT with immunotherapy has displayed promise in enhancing intracranial progression-free survival, but further research is needed to optimize treatment protocols and refine multimodal therapy strategies for patients with NSCLC and BM.

Citation: Khan A, Zhao HF, Meng H, Wu N, Liu LL. Stereotactic radiotherapy for brain metastases of non-small cell lung cancer: A comprehensive review. *World J Radiol* 2025; 17(8): 111076
URL: https://www.wjgnet.com/1949-8470/full/v17/i8/111076.htm
DOI: https://dx.doi.org/10.4329/wjr.v17.i8.111076

INTRODUCTION

Lung cancer remains a significant health issue globally, causing approximately 2 million new cases and 1.8 million fatalities each year[1]. Non-small cell lung cancer (NSCLC) is the most common form of lung cancer, accounting for 85% of all diagnosed cases[2]. Advanced NSCLC is associated with poor outcomes, as evidenced by 5-year survival rates of only 15% and 5% for especially stage III and metastatic stage IV NSCLC, respectively[3]. Throughout disease progression, as many as 60% of patients with NSCLC can experience central nervous system (CNS) involvement[4]. Brain metastasis (BM) in patients with NSCLC is correlated with reduced overall survival, progression-free survival, and quality of life; however, early detection has been demonstrated to improve patient outcomes[5]. BM occurs in nearly 50% of individuals with advanced NSCLC, significantly affecting the overall morbidity associated with the disease[6].

BM is associated with several symptoms, such as headache, seizures, and changes in vision, speech, and/or performance[7]. Prior research[8] indicated that these symptoms significantly decrease patients' quality of life. Additionally, BM associated with lung adenocarcinoma is correlated with poor prognoses, leading to an average survival of approximately 15 months. Treatment options for BM are limited, typically including surgery, radiotherapy (RT), and chemotherapy. The choice of treatment depends upon several factors, together with the patient's general health and the degree of metastasis[9,10].

Chemotherapy is an effective treatment for BM, with response rates in the brain similar to those reported in other regions of the body[11]. Targeted systemic therapies are highly effective, especially in patients with driver mutations such as EGFR and ALK–MET mutations, and they can effectively reach the CNS[11]. Although there are insufficient prospective data to determine the best timing or combination of local therapies and systemic treatments for patients with significant CNS involvement, retrospective studies suggest that initiating local interventions early could increase intracranial progression-free survival[11,12].

The management of NSCLC with BM mostly consists of surgical intervention and RT[13]. Whole-brain RT (WBRT) and stereotactic RT (SRT) are two forms of RT. SRT includes various techniques, such as fractionated SRT (FSRT), stereotactic body RT (SBRT), and stereotactic radiosurgery (SRS)[14]. Currently, most patients typically receive SRT, whereas individuals with a significant disease load receive WBRT[15]. SRT facilitates superior local control with little toxicity[16,17].

This study examined the clinical effectiveness of SRT and the underlying mechanisms in patients with lung cancer and BM. This study compared recent improvements in SRT procedures with traditional treatments to assess the effects of SRT on local control, side effects, and survival rates. This research also explored the integration of SRT with systemic medications to develop a comprehensive and successful treatment plan for patients with NSCLC.

SRT

Currently, the standard treatment for patients with limited BMs involves a combination of surgery and postoperative RT [18,19]. For individuals with an asymptomatic BM lesion, those with multiple BMs, or those ineligible for surgery because of comorbidities or challenging anatomical lesion locations, standalone RT is also considered[20]. Nevertheless, several studies reported no substantial difference in patient outcomes between RT alone and postoperative RT in terms of local disease management and overall survival[21,22]. SRT is currently recommended by the World Health Organization for the treatment of both malignant and benign tumors, in addition to neurological and vascular diseases. This treatment is especially suitable for certain difficult-to-treat or inoperable tumors, such as malignant brain tumors (*e.g.*, glioblastoma, metastatic brain tumors), spinal tumors, lung cancer, liver cancer, and pancreatic cancer[23]. For benign tumors, such as meningioma, pituitary adenoma, and acoustic neuroma, SBRT can also effectively control tumor growth and avoid surgical risks[24]. This treatment method is widely used for tumor control and symptom relief, as it targets the tumor with precise radiation beams and minimizes damage to surrounding healthy tissues. SRT has become part of regular practice in the radiation oncology field, and it is used outside of clinical trials and specialist academic institutions[25]. The three forms of SRT (SRS, FSRT and SBRT) are distinguished by their indications, fractionation, and quality standards[26]. WBRT has traditionally been the primary method used because of its ability to rapidly address both apparent and hidden lesions[27]. WBRT plays a significant role in managing numerous brain lesions, enhancing both endemic and remote CNS

tumor management. However, WBRT is associated with several adverse effects, including cognitive issues such as drowsiness and memory loss, decreased physical ability, diminished appetite, and increased fatigue[28,29]. Additionally, irradiation can cause radiation necrosis in the healthy brain parenchyma[30]. Consequently, the implementation of RT has recently transitioned to the use of less hazardous methodologies, such as SRT, which have led to increased cognitive preservation[31].

SRS

As noted by Topkan *et al*[32], SRS is an effective technique that allows a substantial dose of radiation to be precisely directed to a well-defined target in a single session. This ablative and focused strategy works similarly to surgical resection while causing less damage. SRS is the best treatment option for small BMs, and it is a good option when surgery is not possible, such as in cases in which metastases are located in deep or delicate brain areas and they cannot be removed or a patient has other health problems that preclude surgery[33-35]. Linear accelerators, CyberKnife®, and GammaKnife are the most widely utilized technologies for the radiosurgical treatment of BMs[36,37]. Schmitt *et al*[38] and Vellayappan *et al*[39] used SRS to treat BMs next to the optic nerve, brainstem, or other delicate brain structures, and they demonstrated that this approach had a better toxicity profile than other RT methods.

FSRT/MULTIFRACTION STEREOTACTIC RT

FSRT/multifraction stereotactic RT (MFSRT) is a viable approach for the management of extensive postoperative cavities after the excision of a BM[20]. This method divides radiation doses to increase the biologically effective dose (BEDs) delivered to the target lesion while simultaneously minimizing the risk of radiation necrosis in adjacent healthy brain tissue[40]. Researchers have treated patients with numerous BMs with three to five FSRT treatments[41]. FSRT/MFSRT is often used to treat lesions adjacent to vital regions, such as the brainstem[15,20]. Establishing the precise radiation doses administered by MFSRT remains difficult owing to the absence of prospective studies. Studies comparing RT approaches indicated that MFRST causes much lower rates of radiation necrosis (0%–8%) than SRS (13%–30%)[20]. Research reported that the 1-year local control rate after MFSRT alone varies between 65% and 96%[15,20]. According to Perlow *et al*[42], FSRT/MFSRT can provide therapeutic efficacy and cause few side effects when used after surgery. Additionally, FSRT/MFSRT can be used as an initial treatment before surgery.

Moreover, this method has been substantially applied clinically because it induces a lower rate of side effects and a higher rate of local control than SRS. Putz *et al*[43] reported that FSRT/MFSRT had different biological effectiveness than SRS. Although hypoxic tumor cells can persist after SRS, reoxidation-based FSRT/MFSRT achieves superior tumor control rates. Patients who undergo FSRT or MFSRT might not benefit from the SIR model because of this[44]. The development of prognostic indicators for patients with NSCLC who are receiving FSRT/MFSRT to treat brain oligometastasis is extremely important. The size of the metastatic lesion and the radiation dose are the new foci of prognostic research for FSRT/MFSRT in patients with oligometastasis[45]. Although several studies suggested different BEDs for radiation, there is no universally accepted technique for evaluating the extent of the tumor, radiation dosage, or fractionation schemes[46]. Consequently, it is essential to develop and improve prediction indices to assess the efficacy of treatment for patients with NSCLC and brain oligometastasis who are undergoing FSRT/MFSRT.

SBRT

SBRT integrates various technologies and methods, such as 3D conformal radiation, intensity-modulated RT, image guidance, motion management, and stereotactic precision. However, the hallmark of SBRT is the application of a high, ablative, or nearly ablative dose in a limited number of treatment sessions (*i.e.*, five or fewer fractions)[47]. Although the technologies and procedures used in the implementation of SBRT are intriguing, the primary purpose of this strategy is to administer a compact dosage precisely to a designated target possessing steep slopes in all directions, a technique known as geometric avoidance[48]. In contrast to traditional RT, which leverages the difference in healing between neoplastic and healthy tissues after RT to achieve a therapeutic benefit, SBRT primarily aims to target the tumor while ideally completely sparing the surrounding normal tissue[49]. Thus, this method markedly differs from traditional RT, which often affects extensive areas of healthy tissue[50].

BIOLOGICAL PRINCIPLES OF SRT

SRS was originally designed to treat a range of cranial disorders opposed to being specifically intended for the treatment of brain tumors. In the late 1960s, SRS was successfully used to treat arteriovenous malformations (AVMs), which are congenital vascular defects in which blood flows directly from arteries to veins without passing through capillaries. AVMs are characterized by poorly developed blood channels, which are highly radiosensitive. A single SRS dose of 15–25 Gy obliterates 80%–90% of small AVMs, indicating early success in the use of SRS for treating abnormal vascular

structures[50-52]. This success facilitated the use of SRS in the treatment of brain tumors and metastases[53].

MECHANISM BY WHICH SRT CONTROLS METASTASIS

The tumor microenvironment (TME) is critical at every phase of metastasis, as it shapes tumor growth, progression, and spread to distant sites[54] (Figure 1). BM is common in lung cancer, as cancer cells can infiltrate the brain parenchyma by crossing the blood-brain barrier (BBB), disrupting its defense mechanism[4,55,56]. Reactive gliosis triggers changes in astrocytes that accelerate BM growth and reduce sensitivity to chemotherapy. Additionally, various TME cells are reprogrammed to facilitate cancer spread; for example, tumor-associated macrophages, especially the M2 subtype, promote angiogenesis and immune suppression[57-59].

Tumor spread is influenced by factors such as blood flow, proximity, and the TME. Key processes include tumor cells crossing the BBB and undergoing epithelial-mesenchymal transition, enabling tumor cell detachment and invasion. Markers, such as CXCL12/CXCR4, E-cadherin, and MMP-9, and pathways, such as the EGFR/ERK and VEGF pathways, play important roles in metastasis. Noncoding RNAs, including specific microRNAs (*e.g.*, miRNA-200, miRNA-378) and lncRNAs (*e.g.*, MALAT1), contribute to metastatic adaptation in the brain by regulating the expression of tumor suppressor genes and oncogenes[60].

In NSCLC, dendritic cells (DCs) suppress T lymphocyte proliferation through regulatory T cells (Tregs), and tumor-associated neutrophils can shift to protumoral N2 phenotypes, contributing to extracellular matrix remodeling and immune evasion[61,62]. RT has complex effects on TME cells that potentially influence both treatment response and resistance. RT increases immune activation by increasing natural killer (NK) cell and $CD8^+$ T lymphocyte cytotoxicity and promoting M1 macrophage differentiation while reducing Treg infiltration[63,64]. DCs also become more active in response to RT, increasing MHC molecule expression and triggering immune responses[65].

Nonetheless, RT stimulates the secretion of TGF-β, thus facilitating tumor invasion and immune evasion. In addition, inflammatory cytokines produced by $CD8^+$ T cells and NK cells, such as tumor necrosis factor-alpha, interferon-gamma (IFN-γ), and interleukin-2, help establish a pro-apoptotic environment, potentially increasing the ability of the immune system to target cancer cells[34,66]. Tregs, which are resistant to radiation, impair $CD8^+$ T-cell activity and support cancer-associated fibroblast differentiation and antiapoptotic signaling. High-dose hypofractionated stereotactic RT (HSRT) can counteract these processes by increasing $CD8^+$ T-cell activity and reducing TGF-β secretion[67,68].

PD-L1 expression is another critical factor in the TME. Cancer cells often exploit PD-L1/PD-1 pathways to evade immune responses by inhibiting cytotoxic T lymphocytes (CTLs)[69]. In lung cancer with BM, the number of PD-L1–positive tumor-infiltrating cells is decreased, thereby reducing the efficacy of PD-L1 inhibitors compared with their efficacy in primary lung tumors[70]. RT increases PD-L1 expression in tumor cells, potentially facilitating immune evasion. However, this increase in PD-L1 expression could also increase the responsiveness of tumors to PD-L1–targeting treatments when used alongside RT[71]. High PD-L1 expression, especially in tumors with a high tumor mutational burden (TMB), generally increases the effectiveness of immunotherapies, such as nivolumab and pembrolizumab[72]. Conversely, NSCLC tumors with EGFR or ALK mutations have a lower TMB and PD-L1 expression, making them less responsive to these therapies[73].

Radiation also affects macrophage polarization, thus influencing tumor growth. Some studies revealed that low-dose radiation (10 Gy) increases the number of M1 macrophages while reducing the number of M2 macrophages and activating prosurvival pathways[74,75]. Modest radiation doses can increase IFN-γ expression, enhancing lymphocyte mobility and tumor-fighting abilities by upregulating MHC I and VCAM-1[76,77]. However, radioresistant tumors can block CTL infiltration, although RT-induced TLR upregulation and DAMP exposure increase CTL cytotoxicity[78]. During HSRT, high radiation doses increase immune-stimulating antigen production, further enhancing antitumor immunity[34].

The regulation of inflammation in the TME remains critical, as COX-2 overexpression promotes tumor growth and radioresistance. COX-2 inhibition can sensitize cancer cells to radiation, with some evidence suggesting improved survival in patients with breast or lung cancer[79,80]. However, hypoxia, which is driven by HIF-1 and VEGF, complicates the efficacy of RT. Inhibiting VEGF and related pathways using drugs such as cediranib might increase the response to RT by minimizing hypoxic cell involvement[81,82] (Figure 2). Understanding and modifying these TME interactions are crucial to counteract tumor-induced immunosuppression and optimize the efficacy of RT and systemic therapies, thereby improving both disease management and survival outcomes[83].

QUALITY REQUIREMENTS FOR SRT

SRS demands greater targeting precision, a sharply defined dose gradient, and rigorous dose verification, differing from other forms of RT[84]. Three main factors affect positioning accuracy in SRS[85].

Mechanical precision

Modern SRS systems have sub-millimeter mechanical accuracy, which is crucial for precisely targeting small areas[86].

Imaging accuracy

CT offers high-resolution, low-distortion imaging. Conversely, magnetic resonance imaging often requires thicker slices

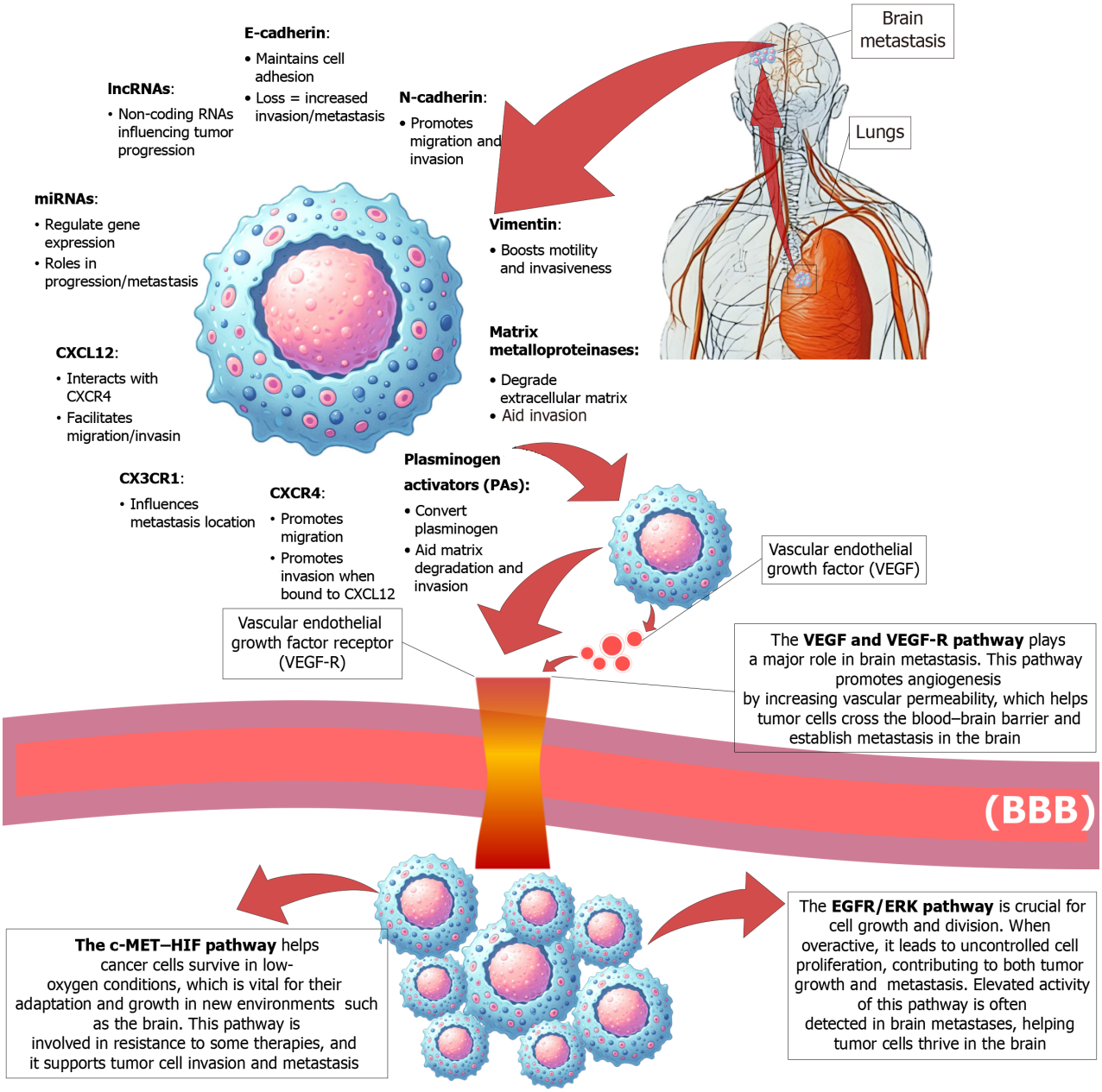

Figure 1 Molecular mechanisms driving organotropism and brain metastasis. VEGF: Vascular endothelial growth factor; BBB: Blood-brain barrier.

for better signal quality, leading to potential distortions. Although 1.5T MR systems maintain distortion within approximately 0.5 mm, 3T MR systems require careful assessment to manage distortion for SRS[87-89].

Patient movement

During intracranial SRS, a fixed stereotactic frame is used to stabilize the head, whereas frameless SRS systems face challenges from involuntary movement. Modern SRS devices are equipped with monitoring systems to limit or adjust for movements within a sub-millimeter range[90,91].

The goal of SRS is to deliver steep dose gradients to exert maximum effects on targeted lesions[32,92]. High-dose-per-fraction strategies in fractionated therapy improve machine efficiency and patient throughput. Radiosurgery devices achieve precise dose distributions through different techniques. The GammaKnife converges approximately 200 beams at a focal point. Novalis uses a gantry that moves along multiple arcs, and CyberKnife delivers photons from various directions to create nonisocentric dose patterns[93,94].

Given the intense, localized doses that are administered in SRS, dose verification is essential to minimize the risk of tissue damage[95]. Elative dose distributions are accurately measured, and radiochromic films are often used for absolute dose quantification. In GammaKnife planning systems, the 1 mm/3% criterion typically yields gamma index values exceeding 97%, highlighting its precision. Accurate absorbed dose measurements, particularly with smaller fields, are critical for SRS applications[96-98].

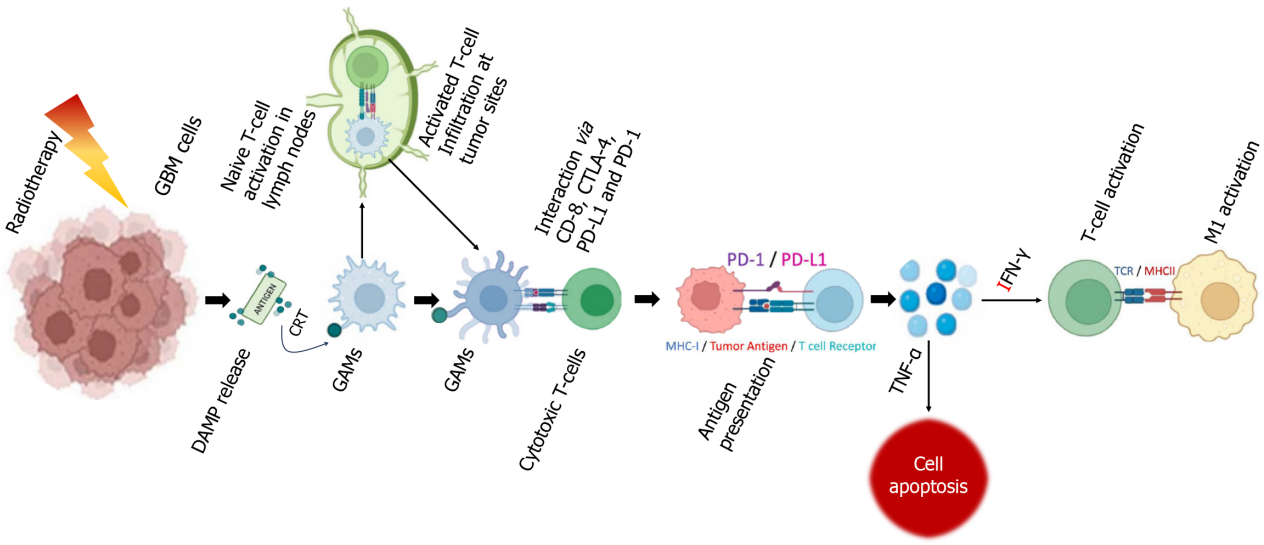

Figure 2 Biological activity of stereotactic radiotherapy in the treatment of brain metastasis.

EFFECTIVENESS OF SRT

The outcomes of SRT for BM treatment have been frequently reported across various populations. The key factors that influence prognosis include age, the number of metastases, the presence of extracranial metastases, and the Karnofsky Performance Status. According to the diagnosis-specific Graded Prognostic Assessment, patients with BM generally have a poor prognosis, with a median survival of 3–15 months[99,100]. Table 1 presents findings from various studies that assessed the effectiveness of SRT compared with that of WBRT.

LIMITATIONS AND FUTURE DIRECTIONS

For larger BMs (greater than 2 cm in diameter), SRS is being used more frequently alongside conservative approaches[18]. Patients typically exhibit prominent neurological symptoms and potentially experience vasogenic edema or mass effects, which frequently necessitate immediate surgical intervention. After achieving gross total resection, postoperative SRS at a median dose of 15 Gy has been associated with increased local control and overall survival in patients with tumors averaging 8.7–9.6 mL in volume[101-103]. However, SRS is associated with some risks, including potential neurological issues because of extensive resection and symptomatic radionecrosis, particularly with a large target volume margin (> 1.0 mm)[104]. A study on NSCLC revealed that a gross tumor volume greater than 15 mL is a primary predictor of local recurrence[103]. Additionally, the rates of radionecrosis increase substantially when more than 10 mL of healthy brain tissue receives 12 Gy, with rates reported between 15% and 55%[17]. To reduce this risk, FSRS, such as that with V12 volumes exceeding 8.5 mL and doses of 30 Gy over five fractions or 27 Gy over three fractions, is advised, especially for treating metastases near critical brain areas[103].

Radiation necrosis remains a notable risk of SRS, particularly in cases involving large treatment volumes[105]. This condition can appear 1 to 2 years post-treatment, and it is often indicated by radiographic changes or symptoms such as headaches, drowsiness, seizures, and death in severe cases[106]. Recent studies investigated the combination of SRS with immunotherapies and targeted therapies, focusing on the potential synergistic benefits of pairing SRS with immune checkpoint inhibitors[107-109].

CONCLUSION

SRT represents a significant advancement in treating BMs in patients with NSCLC. This technique increases precision and minimizes collateral damage to surrounding brain tissue, thereby improving local control and extending patient survival. To maximize the benefits of SRT, further clinical studies are needed to refine the timing, radiation dosage, and fractionation protocols. Future research efforts should focus on improving predictive metrics and identifying biomarkers to develop tailored, personalized treatment for patients with lung cancer BMs. Additionally, exploring emerging technologies, such as advanced imaging techniques or novel RT methods, holds great potential for improving the effectiveness of SRT. Areas that require further clinical validation include the combination of SRT with other treatment modalities or the optimization of fractionation schedules, as such advancements could significantly enhance patient outcomes. By outlining these potential research directions, this paper can serve as a guide for future work in the field, encouraging further exploration and development to optimize efficacy and expand treatment indications.

Table 1 The use of stereotactic radiotherapy to treat brain metastasis of lung cancer and its effectiveness compared with whole-brain radiotherapy

Ref.	Objective	Dosage	Key findings	Effectiveness	Toxicity	Concluding remarks
Luo *et al*[97]	Local and cerebral control in NSCLC patients treated with CyberKnife™ SRT	27 Gy in three fractions (69%), 18–25 Gy in one fraction (18%), 30 Gy in five fractions (9%)	Local control rate = 78.7%, cerebral control rate = 43%, median overall survival = 10.1 months	Effective for local control, minimal toxicity	Acute toxicity = 17%, severe toxicity = 2%	Suitable for patients with few BMs, close follow-up is needed
Fessart *et al* [99]	Survival predictors in patients with lung cancer and BM	Single 20-Gy fraction for SRT, 7–10 Gy/fraction for HFSRT	Disease control rate = 84%, median overall survival = 6.1 months	Effective with better control than WBRT	Grade III–IV toxicity = 4%	Well-tolerated, patient selection is key
Guo *et al* [100]	Palliative RT for BM and quality of life	WBRT = 30 Gy for 10 fractions, SRS = 20 Gy single fraction	Response rate = 50%–75%, neurological improvement rate = 75%	Improves quality of life, better than WBRT alone	Short term: Neurological symptoms; long term: Memory loss	Treatment should be individualized according to patients' conditions
Gunnarsson *et al*[101]	Effectiveness of SRT in patients with lung cancer and BM	BED 10 SRT ≥ 50 Gy	Median overall survival = 19 months	Effective with controlled extracranial disease	No marked toxicity difference	SRT is effective, particularly with stable extracranial disease
Hashmi *et al* [102]	Cognitive deterioration in SRS *vs* SRS + WBRT patients	SRS = 20–24 Gy, SRS + WBRT = 18–20 Gy (SRS) + 30 Gy (WBRT)	Cognitive deterioration: 63.5% (SRS) *vs* 91.7% (SRS + WBRT), median survival = 10.4 months (SRS), 7.4 months (SRS + WBRT)	SRS alone results in less cognitive decline	Cognitive deterioration	SRS preferred for minimizing cognitive decline without impacting survival

NSCLC: Non-small cell lung cancer; BM: Brain metastasis; SRT: Stereotactic radiotherapy; SRS: Stereotactic radiosurgery; WBRT: Whole-brain radiotherapy; HFSRT: Hypofractionated stereotactic radiotherapy; BED: Biologically effective dose.

ACKNOWLEDGEMENTS

Sincere gratitude is extended to Professor Guan Wei for her invaluable assistance and insightful guidance throughout the process of writing this paper.

FOOTNOTES

Author contributions: Khan A was responsible for extensive literature reading and manuscript writing; Zhao HF and Meng H provided technical guidance throughout the preparation of the review; Liu LL and Wu N as co-corresponding authors, proposed the research concept and provided overall supervision and strategic direction for the work.

Supported by the National Key Research and Development Program of China, No. 2022YFE0110200; Project of Science and Technology Department of Jilin Province, No. 20240501002GH and No. YDZJ202102CXJD020; Jilin University Norman Bethune Medical Department "Medicine+X" Project, No. 2022JBGS04; Project of Development and Reform Commission of Jilin Province, No. 2021C023; Department of Human Resources and Social Security Project of Jilin Province; and 20th Batch of Innovation and Entrepreneurship Talent Funding Project of Jilin Province.

Conflict-of-interest statement: The authors declare no conflict of interests for this article.

Country of origin: China

ORCID number: Ning Wu 0000-0002-6938-3834; Lin-Lin Liu 0000-0001-5093-7940.

S-Editor: Liu H
L-Editor: A
P-Editor: Lei YY

REFERENCES

1 **Sharma R**. Mapping of global, regional and national incidence, mortality and mortality-to-incidence ratio of lung cancer in 2020 and 2050. *Int J Clin Oncol* 2022; **27**: 665-675 [*RCA*] [PMID: 35020103 DOI: 10.1007/s10147-021-02108-2] [FullText] [Full Text(PDF)]

2 **Rodak O**, Peris-Díaz MD, Olbromski M, Podhorska-Okołów M, Dzięgiel P. Current Landscape of Non-Small Cell Lung Cancer: Epidemiology, Histological Classification, Targeted Therapies, and Immunotherapy. *Cancers (Basel)* 2021; **13**: 4705 [*RCA*] [PMID: 34572931 DOI: 10.3390/cancers13184705] [FullText] [Full Text(PDF)]

3 **Chaft JE**, Rimner A, Weder W, Azzoli CG, Kris MG, Cascone T. Evolution of systemic therapy for stages I-III non-metastatic non-small-cell lung cancer. *Nat Rev Clin Oncol* 2021; **18**: 547-557 [*RCA*] [PMID: 33911215 DOI: 10.1038/s41571-021-00501-4] [FullText]

4 **Tsui DCC**, Camidge DR, Rusthoven CG. Managing Central Nervous System Spread of Lung Cancer: The State of the Art. *J Clin Oncol* 2022; **40**: 642-660 [*RCA*] [PMID: 34985937 DOI: 10.1200/JCO.21.01715] [FullText]

5 **Buriolla S**, Pelizzari G, Corvaja C, Alberti M, Targato G, Bortolot M, Torresan S, Cortiula F, Fasola G, Follador A. Immunotherapy in NSCLC Patients with Brain Metastases. *Int J Mol Sci* 2022; **23**: 7068 [*RCA*] [PMID: 35806080 DOI: 10.3390/ijms23137068] [FullText] [Full Text(PDF)]

6 **Zhang Q**, Abdo R, Iosef C, Kaneko T, Cecchini M, Han VK, Li SS. The spatial transcriptomic landscape of non-small cell lung cancer brain metastasis. *Nat Commun* 2022; **13**: 5983 [*RCA*] [PMID: 36216799 DOI: 10.1038/s41467-022-33365-y] [FullText] [Full Text(PDF)]

7 **Mukherjee S**, Ali S, Hashmi S, Jahan S. History, Origin and Types of Neurological Disorders. Applications of Stem Cells and derived Exosomes in Neurodegenerative. Springer, Singapore, 2023 [DOI: 10.1007/978-981-99-3848-3_1] [FullText]

8 **Souza VGP**, Forder A, Telkar N, Stewart GL, Carvalho RF, Mur LAJ, Lam WL, Reis PP. Identifying New Contributors to Brain Metastasis in Lung Adenocarcinoma: A Transcriptomic Meta-Analysis. *Cancers (Basel)* 2023; **15**: 4526 [*RCA*] [PMID: 37760494 DOI: 10.3390/cancers15184526] [FullText]

9 **Achrol AS**, Rennert RC, Anders C, Soffietti R, Ahluwalia MS, Nayak L, Peters S, Arvold ND, Harsh GR, Steeg PS, Chang SD. Brain metastases. *Nat Rev Dis Primers* 2019; **5**: 5 [*RCA*] [PMID: 30655533 DOI: 10.1038/s41572-018-0055-y] [FullText]

10 **Souza VGP**, de Araújo RP, Santesso MR, Seneda AL, Minutentag IW, Felix TF, Hamamoto Filho PT, Pewarchuk ME, Brockley LJ, Marchi FA, Lam WL, Drigo SA, Reis PP. Advances in the Molecular Landscape of Lung Cancer Brain Metastasis. *Cancers (Basel)* 2023; **15**: 722 [*RCA*] [PMID: 36765679 DOI: 10.3390/cancers15030722] [FullText] [Full Text(PDF)]

11 **Page S**, Milner-Watts C, Perna M, Janzic U, Vidal N, Kaudeer N, Ahmed M, McDonald F, Locke I, Minchom A, Bhosle J, Welsh L, O'Brien M. Systemic treatment of brain metastases in non-small cell lung cancer. *Eur J Cancer* 2020; **132**: 187-198 [*RCA*] [PMID: 32380429 DOI: 10.1016/j.ejca.2020.03.006] [FullText]

12 **Nigen B**, Goronflot T, Herbreteau G, Mathiot L, Sagan C, Raimbourg J, Bennouna J, Thillays F, Pons-Tostivint E. Impact of first-line immunotherapy on survival and intracranial outcomes in a cohort of non-small cell lung cancer patients with brain metastases at diagnosis. *Lung Cancer* 2023; **184**: 107321 [*RCA*] [PMID: 37586178 DOI: 10.1016/j.lungcan.2023.107321] [FullText]

13 **Wrona A**, Dziadziuszko R, Jassem J. Management of brain metastases in non-small cell lung cancer in the era of tyrosine kinase inhibitors. *Cancer Treat Rev* 2018; **71**: 59-67 [*RCA*] [PMID: 30366200 DOI: 10.1016/j.ctrv.2018.10.011] [FullText]

14 **Su Z**, Zhou L, Xue J, Lu Y. Integration of stereotactic radiosurgery or whole brain radiation therapy with immunotherapy for treatment of brain metastases. *Chin J Cancer Res* 2020; **32**: 448-466 [*RCA*] [PMID: 32963458 DOI: 10.21147/j.issn.1000-9604.2020.04.03] [FullText] [Full Text (PDF)]

15 **Thomsen BJ**, Soliman H. The modern management of untreated large (>2 cm) brain metastases: a narrative review. *Chin Clin Oncol* 2022; **11**: 16 [*RCA*] [PMID: 35534794 DOI: 10.21037/cco-21-136] [FullText]

16 **Guénolé M**, Lucia F, Bourbonne V, Dissaux G, Reygagne E, Goasduff G, Pradier O, Schick U. Impact of concomitant systemic treatments on toxicity and intracerebral response after stereotactic radiotherapy for brain metastases. *BMC Cancer* 2020; **20**: 991 [*RCA*] [PMID: 33050910 DOI: 10.1186/s12885-020-07491-z] [FullText] [Full Text(PDF)]

17 **Loo M**, Clavier JB, Attal Khalifa J, Moyal E, Khalifa J. Dose-Response Effect and Dose-Toxicity in Stereotactic Radiotherapy for Brain Metastases: A Review. *Cancers (Basel)* 2021; **13**: 6086 [*RCA*] [PMID: 34885193 DOI: 10.3390/cancers13236086] [FullText] [Full Text(PDF)]

18 **Diehl CD**, Giordano FA, Grosu AL, Ille S, Kahl KH, Onken J, Rieken S, Sarria GR, Shiban E, Wagner A, Beck J, Brehmer S, Ganslandt O, Hamed M, Meyer B, Münter M, Raabe A, Rohde V, Schaller K, Schilling D, Schneider M, Sperk E, Thomé C, Vajkoczy P, Vatter H, Combs SE. Opportunities and Alternatives of Modern Radiation Oncology and Surgery for the Management of Resectable Brain Metastases. *Cancers (Basel)* 2023; **15**: 3670 [*RCA*] [PMID: 37509330 DOI: 10.3390/cancers15143670] [FullText]

19 **Moravan MJ**, Fecci PE, Anders CK, Clarke JM, Salama AKS, Adamson JD, Floyd SR, Torok JA, Salama JK, Sampson JH, Sperduto PW, Kirkpatrick JP. Current multidisciplinary management of brain metastases. *Cancer* 2020; **126**: 1390-1406 [*RCA*] [PMID: 31971613 DOI: 10.1002/cncr.32714] [FullText]

20 **Zoghbi M**, Moussa MJ, Dagher J, Haroun E, Qdaisat A, Singer ED, Karam YE, Yeung SJ, Chaftari P. Brain Metastasis in the Emergency Department: Epidemiology, Presentation, Investigations, and Management. *Cancers (Basel)* 2024; **16**: 2583 [*RCA*] [PMID: 39061222 DOI: 10.3390/cancers16142583] [FullText]

21 **Møller DS**, Lutz CM, Khalil AA, Alber M, Holt MI, Kandi M, Schmidt HH, Tvilum M, Appelt A, Knap MM, Hoffmann L. Survival benefits for non-small cell lung cancer patients treated with adaptive radiotherapy. *Radiother Oncol* 2022; **168**: 234-240 [*RCA*] [PMID: 35121030 DOI: 10.1016/j.radonc.2022.01.039] [FullText]

22 **Savoca G**, Calvaruso M, Minafra L, Bravatà V, Cammarata FP, Iacoviello G, Abbate B, Evangelista G, Spada M, Forte GI, Russo G. Local Disease-Free Survival Rate (LSR) Application to Personalize Radiation Therapy Treatments in Breast Cancer Models. *J Pers Med* 2020; **10**: 177 [*RCA*] [PMID: 33080870 DOI: 10.3390/jpm10040177] [FullText] [Full Text(PDF)]

23 **Xing Y**, Yasinjan F, Cui J, Peng Y, He M, Liu W, Hong X. Advancements and current trends in tumor treating fields: a scientometric analysis. *Int J Surg* 2024; **110**: 2978-2991 [*RCA*] [PMID: 38349201 DOI: 10.1097/JS9.0000000000001151] [FullText] [Full Text(PDF)]

24 **Martin F**, Magnier F, Berger L, Miroir J, Chautard E, Verrelle P, Lapeyre M, Biau J. Fractionated stereotactic radiotherapy of benign skull-base tumors: a dosimetric comparison of volumetric modulated arc therapy with Rapidarc® versus non-coplanar dynamic arcs. *Radiat Oncol* 2016; **11**: 58 [*RCA*] [PMID: 27090091 DOI: 10.1186/s13014-016-0632-8] [FullText] [Full Text(PDF)]

25 **Vlaskou Badra E**, Baumgartl M, Fabiano S, Jongen A, Guckenberger M. Stereotactic radiotherapy for early stage non-small cell lung cancer: current standards and ongoing research. *Transl Lung Cancer Res* 2021; **10**: 1930-1949 [*RCA*] [PMID: 34012804 DOI: 10.21037/tlcr-20-860] [FullText] [Full Text(PDF)]

26 **Mangoni M**, Borghesi S, Aristei C, Becherini C. Radiobiology of stereotactic radiotherapy. *Rep Pract Oncol Radiother* 2022; **27**: 57-62 [*RCA*] [PMID: 35402022 DOI: 10.5603/RPOR.a2022.0005] [FullText] [Full Text(PDF)]

27 **Amin S**, Baine M, Lin C. Immunotherapy plus stereotactic body radiation therapy or whole-brain radiation therapy in brain metastases. *Immunotherapy* 2023; **15**: 163-174 [*RCA*] [PMID: 36748364 DOI: 10.2217/imt-2022-0051] [FullText]

28 **Munshi A**, Sarkar B, Pandey V, Sonkar DR. Radiotherapy Induced Central Nervous System Toxicity. Complications of Cancer Therapy: Best Practices in Prevention and Management. Springer, Singapore, 2024 [DOI: 10.1007/978-981-99-0984-1_17] [FullText]

29 **Scampoli C**, Cammelli S, Galietta E, Siepe G, Buwenge M, Macchia G, Deodato F, Cilla S, Strigari L, Chiesa S, Morganti AG. Memantine in the Prevention of Radiation-Induced Brain Damage: A Narrative Review. *Cancers (Basel)* 2022; **14**: 2736 [*RCA*] [PMID: 35681716 DOI: 10.3390/cancers14112736] [FullText] [Full Text(PDF)]

30 **Yang X**, Ren H, Fu J. Treatment of Radiation-Induced Brain Necrosis. *Oxid Med Cell Longev* 2021; **2021**: 4793517 [*RCA*] [PMID: 34976300 DOI: 10.1155/2021/4793517] [FullText] [Full Text(PDF)]

31 **van Grinsven EE**, Nagtegaal SHJ, Verhoeff JJC, van Zandvoort MJE. The Impact of Stereotactic or Whole Brain Radiotherapy on Neurocognitive Functioning in Adult Patients with Brain Metastases: A Systematic Review and Meta-Analysis. *Oncol Res Treat* 2021; **44**: 622-636 [*RCA*] [PMID: 34482312 DOI: 10.1159/000518848] [FullText]

32 **Topkan E**, Kucuk A, Senyurek S, Sezen D, Durankus NK, Akdemir EY, Saglam Y, Bolukbasi Y, Pehlivan B, Selek U. Radiosurgery Techniques for Brain Metastases. *J Cancer Tumor Int* 2020; **10**: 1-14 [DOI: 10.9734/jcti/2020/v10i230122] [FullText]

33 **Halima A**, Suh JH, Lo SS, Angelov L, Murphy ES, Chao ST. Repeat Stereotactic Radiosurgery for Brain Metastasis. Intracranial Stereotactic Radiosurgery Boca Raton: CRC Press, 2021

34 **Levis M**, Gastino A, De Giorgi G, Mantovani C, Bironzo P, Mangherini L, Ricci AA, Ricardi U, Cassoni P, Bertero L. Modern Stereotactic Radiotherapy for Brain Metastases from Lung Cancer: Current Trends and Future Perspectives Based on Integrated Translational Approaches. *Cancers (Basel)* 2023; **15**: 4622 [*RCA*] [PMID: 37760591 DOI: 10.3390/cancers15184622] [FullText]

35 **McCutcheon IE**. Stereotactic Radiosurgery to Prevent Local Recurrence of Brain Metastasis After Surgery: Neoadjuvant Versus Adjuvant. *Acta Neurochir Suppl* 2021; **128**: 85-100 [*RCA*] [PMID: 34191064 DOI: 10.1007/978-3-030-69217-9_9] [FullText]

36 **Chambrelant I**, Jarnet D, Bou-Gharios J, Le Fèvre C, Kuntz L, Antoni D, Jenny C, Noël G. Stereotactic Radiation Therapy of Single Brain Metastases: A Literature Review of Dosimetric Studies. *Cancers (Basel)* 2023; **15**: 3937 [*RCA*] [PMID: 37568753 DOI: 10.3390/cancers15153937] [FullText]

37 **Soldá F**, Tancu C, Kitchen N, Fersht N. Neurosurgical applications of radiotherapy. *Surgery (Oxford)* 2024; **42**: 590-598 [DOI: 10.1016/j.mpsur.2024.05.012] [FullText]

38 **Schmitt D**, Blanck O, Gauer T, Fix MK, Brunner TB, Fleckenstein J, Loutfi-Krauss B, Manser P, Werner R, Wilhelm ML, Baus WW, Moustakis C. Technological quality requirements for stereotactic radiotherapy: Expert review group consensus from the DGMP Working Group for Physics and Technology in Stereotactic Radiotherapy. *Strahlenther Onkol* 2020; **196**: 421-443 [*RCA*] [PMID: 32211939 DOI: 10.1007/s00066-020-01583-2] [FullText] [Full Text(PDF)]

39 **Vellayappan BA**, Lim MC, Yong C, Teo K, Malone S, Lo S. Target Delineation for Radiosurgery (Including Postoperative Cavity Radiosurgery) in Brain Metastases. Radiotherapy in Managing Brain Metastases. Springer, Cham, 2020 [DOI: 10.1007/978-3-030-43740-4_11] [FullText]

40 **McKelvey KJ**, Hudson AL, Donaghy H, Stoner SP, Wheeler HR, Diakos CI, Howell VM. Differential effects of radiation fractionation regimens on glioblastoma. *Radiat Oncol* 2022; **17**: 17 [*RCA*] [PMID: 35073960 DOI: 10.1186/s13014-022-01990-y] [FullText] [Full Text (PDF)]

41 **Piras A**, Boldrini L, Menna S, Sanfratello A, D'Aviero A, Cusumano D, Di Cristina L, Messina M, Spada M, Angileri T, Daidone A. Five-Fraction Stereotactic Radiotherapy for Brain Metastases: A Single-Institution Experience on Different Dose Schedules. *Oncol Res Treat* 2022; **45**: 408-414 [*RCA*] [PMID: 35172322 DOI: 10.1159/000522645] [FullText]

42 **Perlow HK**, Ho C, Matsui JK, Prasad RN, Klamer BG, Wang J, Damante M, Upadhyay R, Thomas E, Blakaj DM, Beyer S, Lonser R, Hardesty D, Raval RR, Prabhu R, Elder JB, Palmer JD. Comparing pre-operative versus post-operative single and multi-fraction stereotactic radiotherapy for patients with resectable brain metastases. *Clin Transl Radiat Oncol* 2023; **38**: 117-122 [*RCA*] [PMID: 36420099 DOI: 10.1016/j.ctro.2022.11.004] [FullText] [Full Text(PDF)]

43 **Putz F**, Weissmann T, Oft D, Schmidt MA, Roesch J, Siavooshhaghighi H, Filimonova I, Schmitter C, Mengling V, Bert C, Frey B, Lettmaier S, Distel LV, Semrau S, Fietkau R. FSRT vs. SRS in Brain Metastases-Differences in Local Control and Radiation Necrosis-A Volumetric Study. *Front Oncol* 2020; **10**: 559193 [*RCA*] [PMID: 33102223 DOI: 10.3389/fonc.2020.559193] [FullText] [Full Text(PDF)]

44 **Chen T**, Tang M, Zhou Y, Wang Z, Li S, Wang H, Lu Y, Wang J, Shen W. Pretreatment lymphocyte-to-monocyte ratio as a prognostic factor and influence on dose-effect in fractionated stereotactic radiotherapy for oligometastatic brain metastases in non-small cell lung cancer patients. *Front Oncol* 2023; **13**: 1216852 [*RCA*] [PMID: 37456254 DOI: 10.3389/fonc.2023.1216852] [FullText] [Full Text(PDF)]

45 **Klement RJ**, Sweeney RA. Metabolic factors associated with the prognosis of oligometastatic patients treated with stereotactic body radiotherapy. *Cancer Metastasis Rev* 2023; **42**: 927-940 [*RCA*] [PMID: 37261610 DOI: 10.1007/s10555-023-10110-5] [FullText]

46 **Moreno AC**, Fellman B, Hobbs BP, Liao Z, Gomez DR, Chen A, Hahn SM, Chang JY, Lin SH. Biologically Effective Dose in Stereotactic Body Radiotherapy and Survival for Patients With Early-Stage NSCLC. *J Thorac Oncol* 2020; **15**: 101-109 [*RCA*] [PMID: 31479748 DOI: 10.1016/j.jtho.2019.08.2505] [FullText]

47 **Cellini F**, Arcelli A, Simoni N, Caravatta L, Buwenge M, Calabrese A, Brunetti O, Genovesi D, Mazzarotto R, Deodato F, Mattiucci GC, Silvestris N, Valentini V, Morganti AG. Basics and Frontiers on Pancreatic Cancer for Radiation Oncology: Target Delineation, SBRT, SIB technique, MRgRT, Particle Therapy, Immunotherapy and Clinical Guidelines. *Cancers (Basel)* 2020; **12**: 1729 [*RCA*] [PMID: 32610592 DOI: 10.3390/cancers12071729] [FullText] [Full Text(PDF)]

48 **Conde-Moreno AJ**, Zucca Aparicio D, Pérez-Calatayud MJ, López-Campos F, Celada Álvarez F, Rubio Rodríguez C, Fernández-Letón P, Gómez-Caamaño A, Contreras Martínez J. Recommended procedures and responsibilities for radiosurgery (SRS) and extracranial stereotactic body radiotherapy (SBRT): report of the SEOR in collaboration with the SEFM. *Clin Transl Oncol* 2021; **23**: 1281-1291 [*RCA*] [PMID: 33565008 DOI: 10.1007/s12094-020-02540-2] [FullText]

49 **Schill NC**, Smith HW. The Role of Radiation in the Treatment of Hepatocellular Carcinoma. In: Tsoulfas G, editor. Liver Cancer-Multidisciplinary Approach. United Kingdom: IntechOpen Limited, 2024 [DOI: 10.5772/intechopen.1005029] [FullText]

50 **Song CW**, Glatstein E, Marks LB, Emami B, Grimm J, Sperduto PW, Kim MS, Hui S, Dusenbery KE, Cho LC. Biological Principles of Stereotactic Body Radiation Therapy (SBRT) and Stereotactic Radiation Surgery (SRS): Indirect Cell Death. *Int J Radiat Oncol Biol Phys*

2021; **110**: 21-34 [*RCA*] [PMID: 30836165 DOI: 10.1016/j.ijrobp.2019.02.047] [FullText]

51 **Daou BJ**, Palmateer G, Thompson BG, Maher CO, Hayman JA, Lam KL, Wahl DR, Kim M, Pandey AS. Stereotactic Radiosurgery for Brain Arteriovenous Malformations: Evaluation of Obliteration and Review of Associated Predictors. *J Stroke Cerebrovasc Dis* 2020; **29**: 104863 [*RCA*] [PMID: 32689634 DOI: 10.1016/j.jstrokecerebrovasdis.2020.104863] [FullText]

52 **Shaaban A**, Tos SM, Mantziaris G, Kotecha R, Fariselli L, Gorgulho A, Levivier M, Ma L, Paddick I, Pollock BE, Regis J, Suh JH, Yomo S, Sahgal A, Sheehan JP. Repeat Single-Session Stereotactic Radiosurgery for Cerebral Arteriovenous Malformations: A Systematic Review, Meta-Analysis, and International Stereotactic Radiosurgery Society Practice Guidelines. *Neurosurgery* 2025; **96**: 29-40 [*RCA*] [PMID: 38912814 DOI: 10.1227/neu.0000000000003049] [FullText]

53 **Fatima N**, Meola A, Ding VY, Pollom E, Soltys SG, Chuang CF, Shahsavari N, Hancock SL, Gibbs IC, Adler JR, Chang SD. The Stanford stereotactic radiosurgery experience on 7000 patients over 2 decades (1999-2018): looking far beyond the scalpel. *J Neurosurg* 2021; **135**: 1725-1741 [*RCA*] [PMID: 33799297 DOI: 10.3171/2020.9.JNS201484] [FullText]

54 **Neophytou CM**, Panagi M, Stylianopoulos T, Papageorgis P. The Role of Tumor Microenvironment in Cancer Metastasis: Molecular Mechanisms and Therapeutic Opportunities. *Cancers (Basel)* 2021; **13**: 2053 [*RCA*] [PMID: 33922795 DOI: 10.3390/cancers13092053] [Full Text] [Full Text(PDF)]

55 **McDonald B**, Barth K, Schmidt MHH. The origin of brain malignancies at the blood-brain barrier. *Cell Mol Life Sci* 2023; **80**: 282 [*RCA*] [PMID: 37688612 DOI: 10.1007/s00018-023-04934-1] [FullText] [Full Text(PDF)]

56 **Mortezaee K**. Organ tropism in solid tumor metastasis: an updated review. *Future Oncol* 2021; **17**: 1943-1961 [*RCA*] [PMID: 33728946 DOI: 10.2217/fon-2020-1103] [FullText]

57 **Ge Z**, Ding S. The Crosstalk Between Tumor-Associated Macrophages (TAMs) and Tumor Cells and the Corresponding Targeted Therapy. *Front Oncol* 2020; **10**: 590941 [*RCA*] [PMID: 33224886 DOI: 10.3389/fonc.2020.590941] [FullText] [Full Text(PDF)]

58 **Jablonska PA**, Galán N, Barranco J, Leon S, Robledano R, Echeveste JI, Calvo A, Aristu J, Serrano D. Presence of Activated (Phosphorylated) STAT3 in Radiation Necrosis Following Stereotactic Radiosurgery for Brain Metastases. *Int J Mol Sci* 2023; **24**: 14219 [*RCA*] [PMID: 37762522 DOI: 10.3390/ijms241814219] [FullText]

59 **Tan Y**, Wang M, Zhang Y, Ge S, Zhong F, Xia G, Sun C. Tumor-Associated Macrophages: A Potential Target for Cancer Therapy. *Front Oncol* 2021; **11**: 693517 [*RCA*] [PMID: 34178692 DOI: 10.3389/fonc.2021.693517] [FullText] [Full Text(PDF)]

60 **Sereno M**, Hernandez de Córdoba I, Gutiérrez-Gutiérrez G, Casado E. Brain metastases and lung cancer: molecular biology, natural history, prediction of response and efficacy of immunotherapy. *Front Immunol* 2023; **14**: 1297988 [*RCA*] [PMID: 38283359 DOI: 10.3389/fimmu.2023.1297988] [FullText] [Full Text(PDF)]

61 **Wu L**, Zhang XH. Tumor-Associated Neutrophils and Macrophages-Heterogenous but Not Chaotic. *Front Immunol* 2020; **11**: 553967 [*RCA*] [PMID: 33343560 DOI: 10.3389/fimmu.2020.553967] [FullText] [Full Text(PDF)]

62 **Yan M**, Zheng M, Niu R, Yang X, Tian S, Fan L, Li Y, Zhang S. Roles of tumor-associated neutrophils in tumor metastasis and its clinical applications. *Front Cell Dev Biol* 2022; **10**: 938289 [*RCA*] [PMID: 36060811 DOI: 10.3389/fcell.2022.938289] [FullText] [Full Text(PDF)]

63 **Gómez V**, Mustapha R, Ng K, Ng T. Radiation therapy and the innate immune response: Clinical implications for immunotherapy approaches. *Br J Clin Pharmacol* 2020; **86**: 1726-1735 [*RCA*] [PMID: 32388875 DOI: 10.1111/bcp.14351] [FullText] [Full Text(PDF)]

64 **Wang Y**. Advances in Hypofractionated Irradiation-Induced Immunosuppression of Tumor Microenvironment. *Front Immunol* 2020; **11**: 612072 [*RCA*] [PMID: 33569059 DOI: 10.3389/fimmu.2020.612072] [FullText] [Full Text(PDF)]

65 **Punnanitinont A**, Kannisto ED, Matsuzaki J, Odunsi K, Yendamuri S, Singh AK, Patnaik SK. Sublethal Radiation Affects Antigen Processing and Presentation Genes to Enhance Immunogenicity of Cancer Cells. *Int J Mol Sci* 2020; **21**: 2573 [*RCA*] [PMID: 32272797 DOI: 10.3390/ijms21072573] [FullText] [Full Text(PDF)]

66 **Sprooten J**, De Wijngaert P, Vanmeerbeerk I, Martin S, Vangheluwe P, Schlenner S, Krysko DV, Parys JB, Bultynck G, Vandenabeele P, Garg AD. Necroptosis in Immuno-Oncology and Cancer Immunotherapy. *Cells* 2020; **9**: 1823 [*RCA*] [PMID: 32752206 DOI: 10.3390/cells9081823] [FullText] [Full Text(PDF)]

67 **Cinier J**, Hubert M, Besson L, Di Roio A, Rodriguez C, Lombardi V, Caux C, Ménétrier-Caux C. Recruitment and Expansion of Tregs Cells in the Tumor Environment-How to Target Them? *Cancers (Basel)* 2021; **13**: 1850 [*RCA*] [PMID: 33924428 DOI: 10.3390/cancers13081850] [FullText] [Full Text(PDF)]

68 **Patel RR**, Verma V, Barsoumian HB, Ning MS, Chun SG, Tang C, Chang JY, Lee PP, Gandhi S, Balter P, Dunn JD, Chen D, Puebla-Osorio N, Cortez MA, Welsh JW. Use of Multi-Site Radiation Therapy for Systemic Disease Control. *Int J Radiat Oncol Biol Phys* 2021; **109**: 352-364 [*RCA*] [PMID: 32798606 DOI: 10.1016/j.ijrobp.2020.08.025] [FullText]

69 **Cui JW**, Li Y, Yang Y, Yang HK, Dong JM, Xiao ZH, He X, Guo JH, Wang RQ, Dai B, Zhou ZL. Tumor immunotherapy resistance: Revealing the mechanism of PD-1 / PD-L1-mediated tumor immune escape. *Biomed Pharmacother* 2024; **171**: 116203 [*RCA*] [PMID: 38280330 DOI: 10.1016/j.biopha.2024.116203] [FullText]

70 **Ma SC**, Tang XR, Long LL, Bai X, Zhou JG, Duan ZJ, Wang J, Fu QJ, Zhu HB, Guo XJ, Zhang YP, Guo ZQ, Wu DH, Dong ZY. Integrative evaluation of primary and metastatic lesion spectrum to guide anti-PD-L1 therapy of non-small cell lung cancer: results from two randomized studies. *Oncoimmunology* 2021; **10**: 1909296 [*RCA*] [PMID: 33996262 DOI: 10.1080/2162402X.2021.1909296] [FullText] [Full Text(PDF)]

71 **Wang Y**, Zhang T, Huang Y, Li W, Zhao J, Yang Y, Li C, Wang L, Bi N. Real-World Safety and Efficacy of Consolidation Durvalumab After Chemoradiation Therapy for Stage III Non-small Cell Lung Cancer: A Systematic Review and Meta-analysis. *Int J Radiat Oncol Biol Phys* 2022; **112**: 1154-1164 [*RCA*] [PMID: 34963558 DOI: 10.1016/j.ijrobp.2021.12.150] [FullText]

72 **Ricciuti B**, Wang X, Alessi JV, Rizvi H, Mahadevan NR, Li YY, Polio A, Lindsay J, Umeton R, Sinha R, Vokes NI, Recondo G, Lamberti G, Lawrence M, Vaz VR, Leonardi GC, Plodkowski AJ, Gupta H, Cherniack AD, Tolstorukov MY, Sharma B, Felt KD, Gainor JF, Ravi A, Getz G, Schalper KA, Henick B, Forde P, Anagnostou V, Jänne PA, Van Allen EM, Nishino M, Sholl LM, Christiani DC, Lin X, Rodig SJ, Hellmann MD, Awad MM. Association of High Tumor Mutation Burden in Non-Small Cell Lung Cancers With Increased Immune Infiltration and Improved Clinical Outcomes of PD-L1 Blockade Across PD-L1 Expression Levels. *JAMA Oncol* 2022; **8**: 1160-1168 [*RCA*] [PMID: 35708671 DOI: 10.1001/jamaoncol.2022.1981] [FullText] [Full Text(PDF)]

73 **Tafe LJ**. Non-Small Cell Lung Cancer as a Precision Oncology Paradigm: Emerging Targets and Tumor Mutational Burden (TMB). *Adv Anat Pathol* 2020; **27**: 3-10 [*RCA*] [PMID: 31567128 DOI: 10.1097/PAP.0000000000000244] [FullText]

74 **Becherini C**, Lancia A, Detti B, Lucidi S, Scartoni D, Ingrosso G, Carnevale MG, Roghi M, Bertini N, Orsatti C, Mangoni M, Francolini G, Marani S, Giacomelli I, Loi M, Pergolizzi S, Bonzano E, Aristei C, Livi L. Modulation of tumor-associated macrophage activity with radiation therapy: a systematic review. *Strahlenther Onkol* 2023; **199**: 1173-1190 [*RCA*] [PMID: 37347290 DOI: 10.1007/s00066-023-02097-3] [Full

Text] [Full Text(PDF)]
75 **Zhang Y**, Feng Z, Liu J, Li H, Su Q, Zhang J, Huang P, Wang W, Liu J. Polarization of tumor-associated macrophages by TLR7/8 conjugated radiosensitive peptide hydrogel for overcoming tumor radioresistance. *Bioact Mater* 2022; **16**: 359-371 [*RCA*] [PMID: 35386314 DOI: 10.1016/j.bioactmat.2021.12.033] [FullText] [Full Text(PDF)]
76 **Donlon NE**, Power R, Hayes C, Reynolds JV, Lysaght J. Radiotherapy, immunotherapy, and the tumour microenvironment: Turning an immunosuppressive milieu into a therapeutic opportunity. *Cancer Lett* 2021; **502**: 84-96 [*RCA*] [PMID: 33450360 DOI: 10.1016/j.canlet.2020.12.045] [FullText]
77 **Jorgovanovic D**, Song M, Wang L, Zhang Y. Roles of IFN-γ in tumor progression and regression: a review. *Biomark Res* 2020; **8**: 49 [*RCA*] [PMID: 33005420 DOI: 10.1186/s40364-020-00228-x] [FullText] [Full Text(PDF)]
78 **Ashrafizadeh M**, Farhood B, Eleojo Musa A, Taeb S, Najafi M. Damage-associated molecular patterns in tumor radiotherapy. *Int Immunopharmacol* 2020; **86**: 106761 [*RCA*] [PMID: 32629409 DOI: 10.1016/j.intimp.2020.106761] [FullText]
79 **Li S**, Jiang M, Wang L, Yu S. Combined chemotherapy with cyclooxygenase-2 (COX-2) inhibitors in treating human cancers: Recent advancement. *Biomed Pharmacother* 2020; **129**: 110389 [*RCA*] [PMID: 32540642 DOI: 10.1016/j.biopha.2020.110389] [FullText]
80 **Wang D**, Cabalag CS, Clemons NJ, DuBois RN. Cyclooxygenases and Prostaglandins in Tumor Immunology and Microenvironment of Gastrointestinal Cancer. *Gastroenterology* 2021; **161**: 1813-1829 [*RCA*] [PMID: 34606846 DOI: 10.1053/j.gastro.2021.09.059] [FullText]
81 **Kabakov AE**, Yakimova AO. Hypoxia-Induced Cancer Cell Responses Driving Radioresistance of Hypoxic Tumors: Approaches to Targeting and Radiosensitizing. *Cancers (Basel)* 2021; **13**: 1102 [*RCA*] [PMID: 33806538 DOI: 10.3390/cancers13051102] [FullText] [Full Text(PDF)]
82 **Qi S**, Deng S, Lian Z, Yu K. Novel Drugs with High Efficacy against Tumor Angiogenesis. *Int J Mol Sci* 2022; **23**: 6934 [*RCA*] [PMID: 35805939 DOI: 10.3390/ijms23136934] [FullText] [Full Text(PDF)]
83 **Bilotta MT**, Antignani A, Fitzgerald DJ. Managing the TME to improve the efficacy of cancer therapy. *Front Immunol* 2022; **13**: 954992 [*RCA*] [PMID: 36341428 DOI: 10.3389/fimmu.2022.954992] [FullText] [Full Text(PDF)]
84 **Chung H**, Lee D. Stereotactic Radiosurgery. *Prog Med Phys* 2020; **31**: 63-70 [DOI: 10.14316/pmp.2020.31.3.63] [FullText]
85 **Tanaka M**. Basic Knowledge and Overview of Brain AVMs. *J Neuroendovasc Ther* 2025; **19**: 2024-0037 [*RCA*] [PMID: 40018280 DOI: 10.5797/jnet.ra.2024-0037] [FullText] [Full Text(PDF)]
86 **Freislederer P**, Kügele M, Öllers M, Swinnen A, Sauer TO, Bert C, Giantsoudi D, Corradini S, Batista V. Recent advanced in Surface Guided Radiation Therapy. *Radiat Oncol* 2020; **15**: 187 [*RCA*] [PMID: 32736570 DOI: 10.1186/s13014-020-01629-w] [FullText] [Full Text(PDF)]
87 **Taghizadeh S**, Labuda C, Yang CC, Morris B, Kanakamedala MR, Vijayakumar S, Rey-Dios R, Duggar WN, Florez E, Fatemi A. Optimizing MRI sequences and images for MRI-based stereotactic radiosurgery treatment planning. *Rep Pract Oncol Radiother* 2019; **24**: 12-19 [*RCA*] [PMID: 30337843 DOI: 10.1016/j.rpor.2018.09.010] [FullText]
88 **Grishchuk D**, Dimitriadis A, Sahgal A, De Salles A, Fariselli L, Kotecha R, Levivier M, Ma L, Pollock BE, Regis J, Sheehan J, Suh J, Yomo S, Paddick I. ISRS Technical Guidelines for Stereotactic Radiosurgery: Treatment of Small Brain Metastases (≤1 cm in Diameter). *Pract Radiat Oncol* 2023; **13**: 183-194 [*RCA*] [PMID: 36435388 DOI: 10.1016/j.prro.2022.10.013] [FullText]
89 **Nayak KS**, Lim Y, Campbell-Washburn AE, Steeden J. Real-Time Magnetic Resonance Imaging. *J Magn Reson Imaging* 2022; **55**: 81-99 [*RCA*] [PMID: 33295674 DOI: 10.1002/jmri.27411] [FullText]
90 **Solberg TD**, Balter JM, Benedict SH, Fraass BA, Kavanagh B, Miyamoto C, Pawlicki T, Potters L, Yamada Y. Quality and safety considerations in stereotactic radiosurgery and stereotactic body radiation therapy: Executive summary. *Pract Radiat Oncol* 2012; **2**: 2-9 [*RCA*] [PMID: 25740120 DOI: 10.1016/j.prro.2011.06.014] [FullText] [Full Text(PDF)]
91 **Taillez A**, Bimbai AM, Lacornerie T, Le Deley MC, Lartigau EF, Pasquier D. Studies of Intra-Fraction Prostate Motion During Stereotactic Irradiation in First Irradiation and Re-Irradiation. *Front Oncol* 2021; **11**: 690422 [*RCA*] [PMID: 34336678 DOI: 10.3389/fonc.2021.690422] [FullText] [Full Text(PDF)]
92 **Mendel JT**, Jaster AW, Yu FF, Morris LC 3rd, Lynch PT, Shah BR, Agarwal A, Timmerman RD, Nedzi LA, Raj KM. Fundamentals of Radiation Oncology for Neurologic Imaging. *Radiographics* 2020; **40**: 827-858 [*RCA*] [PMID: 32216705 DOI: 10.1148/rg.2020190138] [Full Text]
93 **Griffin RJ**, Ahmed MM, Amendola B, Belyakov O, Bentzen SM, Butterworth KT, Chang S, Coleman CN, Djonov V, Formenti SC, Glatstein E, Guha C, Kalnicki S, Le QT, Loo BW Jr, Mahadevan A, Massaccesi M, Maxim PG, Mohiuddin M, Mohiuddin M, Mayr NA, Obcemea C, Petersson K, Regine W, Roach M, Romanelli P, Simone CB 2nd, Snider JW, Spitz DR, Vikram B, Vozenin MC, Abdel-Wahab M, Welsh J, Wu X, Limoli CL. Understanding High-Dose, Ultra-High Dose Rate, and Spatially Fractionated Radiation Therapy. *Int J Radiat Oncol Biol Phys* 2020; **107**: 766-778 [*RCA*] [PMID: 32298811 DOI: 10.1016/j.ijrobp.2020.03.028] [FullText]
94 **Kilby W**, Naylor M, Dooley JR, Maurer CR, Sayeh S. A Technical Overview of the CyberKnife System. Handbook of Robotic and Image-Guided Surgery. *Elsevier* 2020; 15-38 [DOI: 10.1016/b978-0-12-814245-5.00002-5] [FullText]
95 **Padelli F**, Aquino D, Fariselli L, De Martin E. IBA myQA SRS Detector for CyberKnife Robotic Radiosurgery Quality Assurance. *Appl Sci* 2022; **12**: 7791 [*RCA*] [DOI: 10.3390/app12157791] [FullText]
96 **Casolaro P**. Radiochromic Films for the Two-Dimensional Dose Distribution Assessment. *Appl Sci* 2021; **11**: 2132 [*RCA*] [DOI: 10.3390/app11052132] [FullText]
97 **Luo D**, Han EY, Wen Z, Mackin DS, Krafft SP, Li J, Wang X, Briere TM. Use of uniform shots for robust planning of mask-based treatment in Gamma Knife Icon. *Phys Med* 2020; **73**: 135-157 [*RCA*] [PMID: 32361402 DOI: 10.1016/j.ejmp.2020.04.013] [FullText]
98 **Muñoz L**, Kron T, Petasecca M, Bucci J, Jackson M, Metcalfe P, Rosenfeld AB, Biasi G. Consistency of small-field dosimetry, on and off axis, in beam-matched linacs used for stereotactic radiosurgery. *J Appl Clin Med Phys* 2021; **22**: 185-193 [*RCA*] [PMID: 33440049 DOI: 10.1002/acm2.13160] [FullText] [Full Text(PDF)]
99 **Fessart E**, Mouttet Audouard R, Le Tinier F, Coche-Dequeant B, Lacornerie T, Tresch E, Scherpereel A, Lartigau E, Mirabel X, Pasquier D. Stereotactic irradiation of non-small cell lung cancer brain metastases: evaluation of local and cerebral control in a large series. *Sci Rep* 2020; **10**: 11201 [*RCA*] [PMID: 32641798 DOI: 10.1038/s41598-020-68209-6] [FullText] [Full Text(PDF)]
100 **Guo D**, Liu J, Li Y, Chen Q, Zhao Y, Guo X, Zhu S, Ji S. A Novel Score Combining Magnetic Resonance Spectroscopy Parameters and Systemic Immune-Inflammation Index Improves Prognosis Prediction in Non-Small Cell Lung Cancer Patients With Brain Metastases After Stereotactic Radiotherapy. *Front Oncol* 2022; **12**: 762230 [*RCA*] [PMID: 35756607 DOI: 10.3389/fonc.2022.762230] [FullText] [Full Text (PDF)]
101 **Gunnarsson K**, Hallqvist A. Stereotactic radiotherapy for brain metastases in patients with lung cancer; outcome and toxicity in clinical practice. *Rep Pract Oncol Radiother* 2022; **27**: 410-418 [*RCA*] [PMID: 36186692 DOI: 10.5603/RPOR.a2022.0056] [FullText] [Full Text

(PDF)]

102 **Hashmi MF**, Agarwal MS, Maani EV, Arora RD, Cascella M. Palliative Radiation Therapy for Brain Metastases. 2023 Jun 4. In: StatPearls [Internet]. Treasure Island (FL): StatPearls Publishing, 2025 [PMID: 33085339] [FullText]

103 **Nardone V**, Romeo C, D'Ippolito E, Pastina P, D'Apolito M, Pirtoli L, Caraglia M, Mutti L, Bianco G, Falzea AC, Giannicola R, Giordano A, Tagliaferri P, Vinciguerra C, Desideri I, Loi M, Reginelli A, Cappabianca S, Tassone P, Correale P. The role of brain radiotherapy for EGFR- and ALK-positive non-small-cell lung cancer with brain metastases: a review. *Radiol Med* 2023; **128**: 316-329 [*RCA*] [PMID: 36786970 DOI: 10.1007/s11547-023-01602-z] [FullText] [Full Text(PDF)]

104 **Shiue K**, Sahgal A, Lo SS. Precision Radiation for Brain Metastases With a Focus on Hypofractionated Stereotactic Radiosurgery. *Semin Radiat Oncol* 2023; **33**: 114-128 [*RCA*] [PMID: 36990629 DOI: 10.1016/j.semradonc.2023.01.004] [FullText]

105 **Minniti G**, Niyazi M, Andratschke N, Guckenberger M, Palmer JD, Shih HA, Lo SS, Soltys S, Russo I, Brown PD, Belka C. Current status and recent advances in resection cavity irradiation of brain metastases. *Radiat Oncol* 2021; **16**: 73 [*RCA*] [PMID: 33858474 DOI: 10.1186/s13014-021-01802-9] [FullText] [Full Text(PDF)]

106 **Wang K**, Tepper JE. Radiation therapy-associated toxicity: Etiology, management, and prevention. *CA Cancer J Clin* 2021; **71**: 437-454 [*RCA*] [PMID: 34255347 DOI: 10.3322/caac.21689] [FullText]

107 **Desagneaux A**, Charles J, Kastler A, Dols A-, Leccia M, Elhalawani H, Aizer A, Flandin I, Verry C. Safety and outcomes of combined immune checkpoint inhibitor and radiation therapy for patients with melanoma brain metastases. 2022 Preprint [DOI: 10.21203/rs.3.rs-1680749/v1] [FullText]

108 **Hendriks LEL**, Henon C, Auclin E, Mezquita L, Ferrara R, Audigier-Valette C, Mazieres J, Lefebvre C, Rabeau A, Le Moulec S, Cousin S, Duchemann B, le Pechoux C, Botticella A, Ammari S, Gazzah A, Caramella C, Adam J, Lechapt E, Planchard D, De Ruysscher D, Dingemans AM, Besse B. Outcome of Patients with Non-Small Cell Lung Cancer and Brain Metastases Treated with Checkpoint Inhibitors. *J Thorac Oncol* 2019; **14**: 1244-1254 [*RCA*] [PMID: 30780002 DOI: 10.1016/j.jtho.2019.02.009] [FullText]

109 **Kotecha R**, Kim JM, Miller JA, Juloori A, Chao ST, Murphy ES, Peereboom DM, Mohammadi AM, Barnett GH, Vogelbaum MA, Angelov L, Suh JH, Ahluwalia MS. The impact of sequencing PD-1/PD-L1 inhibitors and stereotactic radiosurgery for patients with brain metastasis. *Neuro Oncol* 2019; **21**: 1060-1068 [*RCA*] [PMID: 30796838 DOI: 10.1093/neuonc/noz046] [FullText]

World Journal of Radiology

Submit a Manuscript: https://www.f6publishing.com

World J Radiol 2025 August 28; 17(8): 107463

DOI: 10.4329/wjr.v17.i8.107463

ISSN 1949-8470 (online)

MINIREVIEWS

Radiological insights into diverticulitis: Clinical manifestations, complications, and differential diagnosis

Mehmet Simsar, Yesim Y Yuruk, Olgun Sahin, Hilal Sahin

Specialty type: Radiology, nuclear medicine and medical imaging

Provenance and peer review: Invited article; Externally peer reviewed.

Peer-review model: Single blind

Peer-review report's classification

Scientific Quality: Grade B, Grade C, Grade C, Grade D

Novelty: Grade B, Grade C, Grade C, Grade D

Creativity or Innovation: Grade B, Grade C, Grade D, Grade D

Scientific Significance: Grade B, Grade C, Grade D, Grade D

P-Reviewer: Qiu WS, MD, PhD, Associate Chief Physician, Associate Research Scientist, Professor, China; Tasci B, PhD, Associate Professor, Türkiye

Received: March 24, 2025

Revised: June 10, 2025

Accepted: August 6, 2025

Published online: August 28, 2025

Processing time: 157 Days and 12.3 Hours

Mehmet Simsar, Olgun Sahin, Hilal Sahin, Department of Radiology, University of Health Sciences, Izmir City Hospital, Izmir 35540, Türkiye

Yesim Y Yuruk, Department of Radiology, University of Health Sciences, Izmir Tepecik Training and Research Hospital, Izmir 35020, Türkiye

Corresponding author: Hilal Sahin, MD, Associate Professor, Department of Radiology, University of Health Sciences, Izmir City Hospital, Şevket ince mahallesi, 2148/11. Sokak No: 1/11, Izmir 35540, Türkiye. hilal.sahin1@sbu.edu.tr

Abstract

Diverticulitis is an infection of the diverticular sacs protruding from the intestinal wall. It typically presents as elevated inflammatory markers and left lower quadrant abdominal pain. Although clinical symptoms and biomarkers are essential for diagnosis, imaging methods, particularly computed tomography (CT), are critical due to the inability to perform endoscopic procedures in the acute phase because of the risk of perforation. Various classification systems that include imaging findings have been developed. The most recent and widely accepted system is the Sartelli classification, which is endorsed by the World Society of Emergency Surgery. This classification describes stages of diverticulitis ranging from edematous bowel wall thickening and phlegmon in the adjacent mesentery to microperforation, localized or distant abscess formation, and generalized peritonitis with free fluid and air. Imaging findings are also pivotal in diagnosing and managing complications such as abscesses, pylephlebitis, fistulas, and gastrointestinal bleeding. Moreover, imaging can differentiate diverticulitis from infectious colitis, epiploic appendagitis, ischemic colitis, colorectal carcinoma, and inflammatory bowel disease. This review focuses on the radiological findings of diverticulitis. We specifically discuss CT imaging and emphasize its clinical manifestations, significant complications, and differential diagnosis.

Key Words: Diverticulitis; Computed tomography; Sartelli classification; Complicated diverticulitis; Abscess; Peritonitis; Imaging in diverticulitis

Core Tip: Abdominal pain is one of the most common complaints leading to emergency department visits. A significant proportion of patients presenting with elevated inflammatory markers are diagnosed with diverticular disease, including diverticulitis and its complications. A standardized classification system and computed tomography imaging are crucial for ensuring accurate diagnosis and appropriate treatment. This review provides a comprehensive overview of the imaging findings, classification, and complications of diverticulitis.

Citation: Simsar M, Yuruk YY, Sahin O, Sahin H. Radiological insights into diverticulitis: Clinical manifestations, complications, and differential diagnosis. *World J Radiol* 2025; 17(8): 107463
URL: https://www.wjgnet.com/1949-8470/full/v17/i8/107463.htm
DOI: https://dx.doi.org/10.4329/wjr.v17.i8.107463

INTRODUCTION

Intestinal diverticula are pouches involving the mucosa, submucosa, and muscular layers of the intestinal wall. Pseudodiverticula are associated with advanced age and formed by the protrusion of the mucosa and submucosa through the circular muscle layer of the colon[1]. The term diverticulosis refers to asymptomatic pseudodiverticula, while diverticulitis denotes diverticula accompanied by inflammation. Diverticulitis may present as a complicated (*e.g.*, associated with abscess, fistula, stricture, perforation, or peritonitis) or uncomplicated form. Collectively, these conditions are encompassed under the broader classification of diverticular disease[2].

The annual incidence of colonic diverticulitis in the United States is 209 cases per 100000 individuals[3]. Although the pathophysiology of diverticular disease has not been clearly defined, factors such as fiber deficiency and microbiota are thought to play a role in the onset of the disease. The fiber content in the diet influences the size and consistency of stool. Without enough fiber intraluminal pressure can increase causing the herniation of the colonic mucosa through weak areas in the muscular layer. Other factors, such as altered neuromuscular activity and genetics, also contribute to the development of diverticular disease[4]. The retraction and entrapment of submucosal blood vessels within the diverticula combined with fecal obstruction of the diverticular orifice promote bacterial overgrowth and prolonged exposure within the lumen. These events initiate ischemic processes that heighten the risk of inflammation, thereby leading to the onset of diverticulitis[5].

The clinical recognition of acute colonic diverticulitis (ACD) can be challenging because left lower quadrant pain, leukocytosis, and fever are common symptoms. Radiology is crucial in differentiating diverticulitis from other diseases with similar findings and guiding treatment decisions, including conservative management, percutaneous drainage, and surgical intervention[6].

LITERATURE REVIEW

A structured literature review was conducted using the PubMed, Scopus, and Web of Science databases between January and June 2025. The following MeSH terms and keywords were used: "Diverticulitis", "complicated diverticulitis", "Hinchey classification", "Sartelli classification", "Segmental colitis associated with diverticulosis", "colorectal cancer", "deep learning", and "computed tomography". Studies published in English over the past decade were included to reflect contemporary clinical practice and technological advancements. All computed tomography (CT) images used in this review were retrospectively retrieved in anonymized form from the institutional Picture Archiving and Communication System with approval from the local institutional review board. No identifiable patient information was included.

RADIOLOGICAL TECHNIQUES AND PROTOCOL OPTIMIZATION

Diverticular disease is investigated through radiological imaging and endoscopic procedures. Although endoscopy can provide valuable diagnostic information, its use is limited in cases of acute diverticulitis due to the risk of perforation and bleeding[7]. At this point the role of radiology becomes crucial. Historically, barium enema studies were conducted. Currently, ultrasound (US) and CT are preferred due to their ability to detect intraluminal and extracolonic pathologies such as abscess formation[8].

US is typically the first-line imaging modality. It is a practical modality in situations where radiation exposure should be avoided, such as during pregnancy and in patients who are lean. However, its diagnostic accuracy is dependent on the experience of the operator, and its effectiveness is reduced when evaluating deep abdominal regions in patients with obesity[7,9].

According to various meta-analyses, research studies, and systematic reviews, there are no statistically significant differences in the sensitivity and specificity of US and CT. However, CT demonstrates clear superiority in identifying complicated cases and detecting alternative or coexisting pathologies unrelated to diverticulitis. These advantages

contribute to the ability of CT to provide comprehensive prognostic information[8,10,11].

Contrast-enhanced CT imaging in the portal venous phase is recommended. This approach is beneficial for assessing complicated diverticulitis because CT grading after the initial episode is crucial for predicting prognosis. Contrast-enhanced CT is superior to non-contrast studies in evaluating complicated cases. Additionally, the portal venous phase efficiently detects complications such as pylephlebitis. If there is clinical suspicion of diverticular bleeding, arterial-phase CT angiography is advised as it can localize the source of bleeding and reveal any structural causes. This information helps guide catheter-based angiographic procedures. Oral contrast is generally not recommended due to limited diagnostic benefits and the difficulty of administration. However, rectal contrast may be considered in suspected fistula cases[7,12,13].

Advantages of magnetic resonance imaging (MRI) are the lack of ionizing radiation, superior soft tissue contrast, and suitability for repeated imaging when necessary. MRI also offers significant advantages in special patient populations such as pregnant individuals. In cases where US findings are inconclusive, particularly during pregnancy, there has been a growing shift toward using non-contrast MRI as a second-line imaging modality[14]. However, MRI also has notable limitations, including longer acquisition times, higher costs, and reduced availability in emergency settings when compared with CT. While MRI has shown comparable sensitivity and specificity to CT in diagnosing ACD, further studies are needed to establish its broader clinical utility[15].

In the existing literature the radiological features of diverticular disease have predominantly been described for CT due to its rapid accessibility and widespread availability. Furthermore, most staging classifications are based on CT imaging. This review primarily focused on the CT findings associated with diverticular disease.

ACUTE DIVERTICULITIS

In 1978, Hinchey *et al*[16] classified patients with acute diverticulitis into four stages based on intraoperative findings as follows: Stage 1 represented pericolic phlegmon; stage 2 described intraabdominal abscess; stage 3 involved purulent peritonitis; and stage 4 was characterized by fecal peritonitis resulting from a large perforation. With advancements in CT technology and its increasing utilization over time, Kaiser *et al*[17] integrated imaging findings into Hinchey's intraoperative classification and created the Modified Hinchey Classification in 2005. This modification introduced stage 0 and subdivided stage 1 into 1A and 1B. Stage 0 was defined as colonic wall thickening in patients with clinical symptoms. Stage 1A was defined as colonic wall thickening accompanied by pericolic phlegmon, and stage 1B was defined as colonic wall thickening with an associated pericolic or mesocolic abscess.

The American Association for the Surgery of Trauma (AAST) developed the AAST grading system for ACD. This classification provided more accurate guidance for surgical decision-making than the Hinchey classification. It yielded similar predictive outcomes for complications and procedural interventions. The AAST grading system evaluated patients clinically, radiologically, operatively, and pathologically to categorize disease severity from stage 1, representing mild disease, to stage 5, indicating severe disease[18,19].

In 2015 the World Society of Emergency Surgery introduced the Sartelli classification, which is based on radiological findings. According to this classification, patients are divided into two main groups: Complicated and uncomplicated. Complicated cases are further categorized into four stages, with stages 1 and 2 subdivided into subgroups A and B[20]. The detailed staging criteria of the classification systems are presented in a comparative table (Table 1).

The staging systems for diverticulitis have specific advantages and limitations. Although the Hinchey classification holds historical significance, it relies on intraoperative findings and lacks sufficient detail for imaging-based staging. The Modified Hinchey system adapts these principles to include radiological use yet remains relatively simplistic. The AAST classification combines clinical, radiological, and surgical factors to create a comprehensive classification system; however, its complexity may limit its routine use. The World Society of Emergency Surgery endorses the Sartelli classification and provides a thorough CT-based approach for clinical staging. It is simpler than the AAST classification and is easily applicable in routine emergency settings. This review presented the approach to acute diverticulitis primarily through the framework of the Sartelli classification.

Acute uncomplicated diverticulitis (stage 0)

The thickening of the colonic wall with diverticula is defined as an increase in the density of the pericolic fat[20]. A hallmark feature of ACD is the moderate focal thickening of the colonic wall accompanied by disproportionately pronounced fat stranding. Additional indicative signs of the inflammatory process include mesenteric vessel engorgement, commonly referred to as the centipede sign, and fluid accumulation at the root of the sigmoid mesentery, known as the comma sign (Figure 1)[21-23].

The thickness of the colonic wall is determined by measuring the maximum distance perpendicular to the central axis from the serosal to the mucosal surface, excluding extramural components such as abscesses and the lumen of the filled bowel segment. In cases where the lumen cannot be identified, the total serosa-to-serosa distance is measured and divided by two. The wall thickness is considered normal for a distended segment up to 3 mm and in a collapsed segment up to 8 mm (Figure 2)[22,24,25].

Acute complicated diverticulitis

Diverticular inflammation in complicated cases is often associated with microperforation/perforation and abscess formation. The Sartelli classification emphasizes imaging findings more than the Hinchey classification. It categorizes complicated diverticulitis in stages 3 and 4 based on the presence of extraluminal gas and fluid either adjacent to or

Table 1 Classifications in use for staging of acute diverticulitis

Stage	Hinchey classification[16]	Modified Hinchey classification by Kaiser *et al*[17]	AAST grade[18]	WSES classification by Sartelli *et al*[20]
0	N/A	Mild clinical diverticulitis	N/A	Uncomplicated diverticulitis
1	Pericolic abscess or phlegmon	1A: Confined pericolic inflammation-phlegmon	Colonic inflammation	1A: Pericolic air bubbles or little pericolic fluid without abscess
		1B: Pericolic-mesocolic abscess		1B: Abscess ≤ 4 cm
2	Pelvic, distant intrabdominal, or retroperitoneal abscess	Pelvic, distant intraabdominal, or retroperitoneal abscess	Colon microperforation or pericolic phlegmon without abscess	2A: Abscess > 4 cm
				2B: Distant air (> 5 cm from inflamed bowel segment)
3	Generalized purulent peritonitis	Generalized purulent peritonitis	Localized pericolic abscess	Diffuse fluid without distant free air (no hole in colon)
4	Generalized fecal peritonitis	Generalized fecal peritonitis	Distant and/or multiple abscesses	Diffuse fluid with distant free air (persistent hole in the colon
5	N/A	N/A	Free colonic perforation with generalized peritonitis	N/A

AAST: American Association for the Surgery of Trauma; WSES: The World Society of Emergency Surgery; N/A: Not applicable.

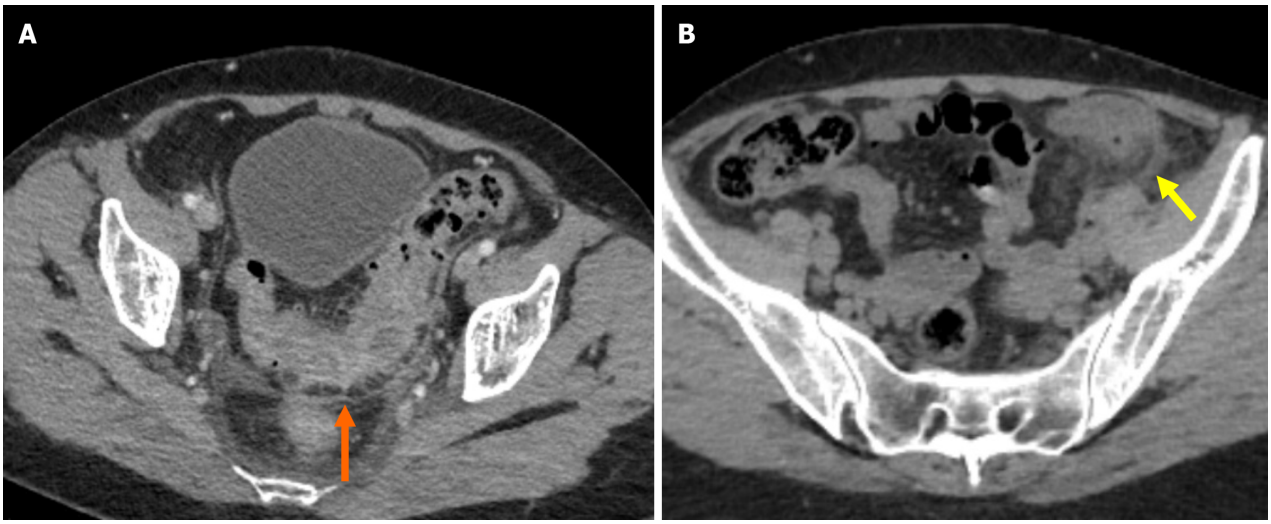

Figure 1 Acute uncomplicated diverticulitis. A: Axial contrast-enhanced computed tomography (CT) image showed engorgement of the mesenteric vessels, a finding known as the centipede sign (orange arrow); B: Axial non-contrast CT image showed thickening and fluid collection of the left latero-conal fascia, a finding known as the comma sign (yellow arrow).

distant from the inflamed bowel loop. In contrast the Hinchey classification differentiates these stages based on purulent or fecal peritonitis. Sartelli *et al*[26] subdivided staging according to abscess size, using 4 cm as the threshold to distinguish between stages 1B and 2A. These criteria aid clinicians in determining the appropriate treatment approach and the most suitable intervention[16,20,26].

Stage 1A: Diverticular inflammation with microperforation without abscess formation and/or peritoneal involvement is the defining characteristic of stage 1A. On CT imaging it appears as pericolic air pockets or a small amount of pericolic fluid. In patients without evidence of distant air on CT, broad-spectrum antibiotic therapy is considered sufficient for management (Figure 3A).

Stage 1B: Stage 1B is defined as the presence of an abscess with a diameter of less than 4 cm. Treatment options include antibiotic therapy or percutaneous drainage (Figure 3B).

Stage 2A: Stage 2A is defined as the presence of an abscess with a diameter of more than 4 cm. Treatment options include antibiotic therapy or percutaneous drainage (Figure 4A).

Stage 2B: Stage 2B is characterized by the presence of distant air located more than 5 cm from the affected colonic loop

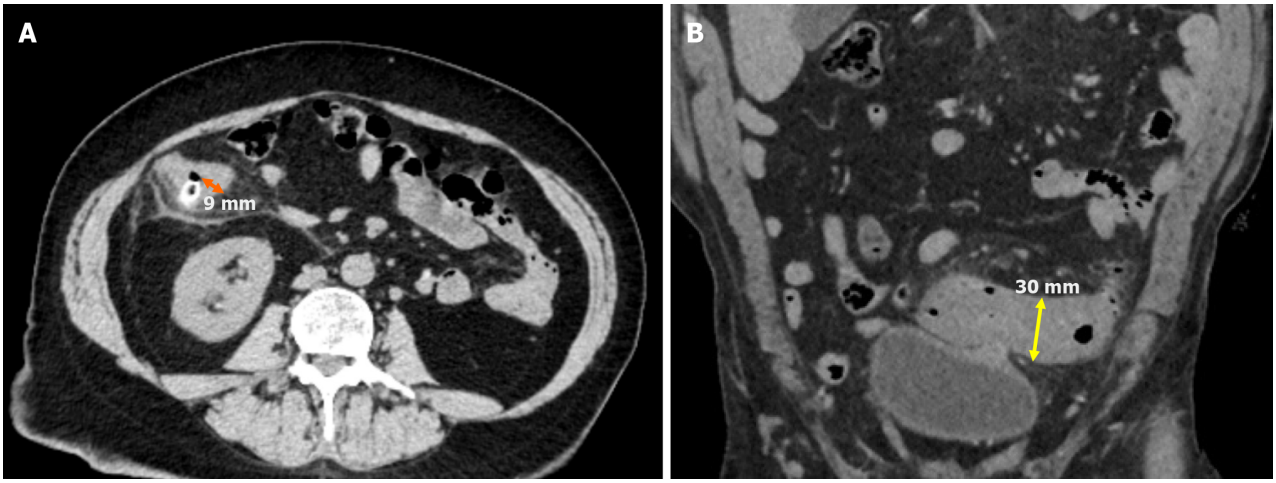

Figure 2 Measurement of colonic wall thickness. A: Axial non-contrast computed tomography (CT) image demonstrated right colonic diverticulitis with a distinguishable lumen. The maximum colonic wall thickness was 9 mm (orange line); B: Coronal non-contrast CT image showed sigmoid colonic diverticulitis. Since the lumen was not visualized, the serosa-to-serosa distance was measured at 30 mm (yellow double-sided arrow). Half of this distance was the estimated luminal wall thickness, calculated as 15 mm.

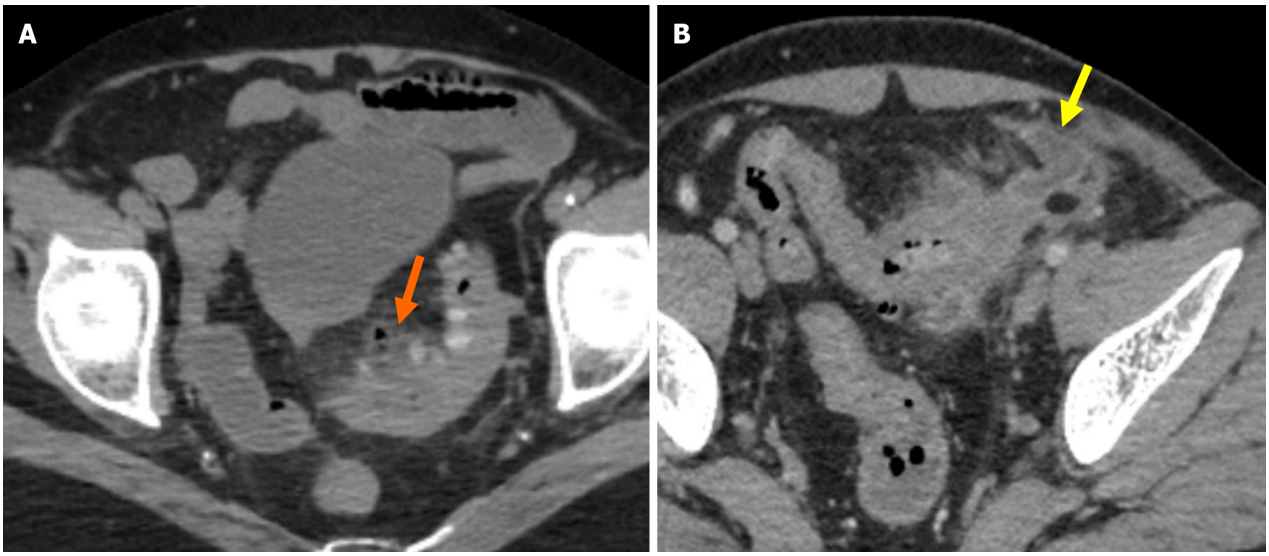

Figure 3 Sartelli stage 1A and stage 1B diverticulitis. A: On contrast-enhanced axial computed tomography (CT) imaging, colonic wall thickening, fat stranding, and pericolic air bubbles were observed in the sigmoid colon, consistent with Sartelli stage 1A diverticulitis (orange arrow); B: Contrast-enhanced axial CT imaging revealed findings consistent with Sartelli stage 1B diverticulitis, including colonic wall thickening, pericolic fat stranding, and a fluid collection measuring approximately 2.5 cm on the anterior aspect of the sigmoid colon, indicative of an abscess (yellow arrow).

without widespread peritoneal fluid. Although surgical intervention is generally preferred, conservative management may be considered in selected cases (Figure 4B).

Stage 3: Stage 3 is defined as the presence of widespread fluid in at least two distant abdominal quadrants without free air. Treatment typically involves peritoneal lavage and colonic resection (Figure 5).

Stage 4: Stage 4 is characterized by the presence of widespread fluid and distant free air secondary to diverticular perforation. Hartmann's resection is the preferred treatment approach (Figure 6).

Diverticulitis complications

Small perforations frequently occur during diverticulitis and are commonly managed with antibiotics and supportive care. However, uncontrolled perforations may lead to severe complications such as abscess formation, pylephlebitis, bowel obstruction, hemorrhage, and fistula, which all necessitate aggressive interventions. Recognizing and appropriately treating these complications is essential to minimizing morbidity and mortality[27].

Perforation: Severe inflammation of the diverticulum can lead to bacterial overgrowth, impaired perfusion, hypoxia,

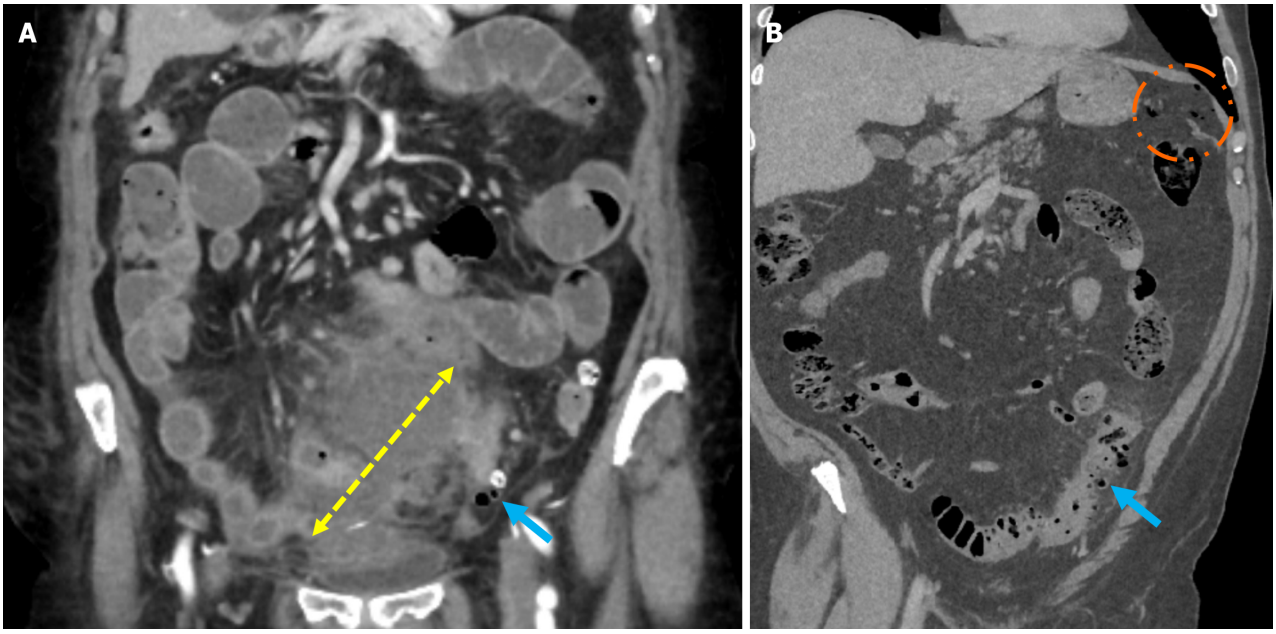

Figure 4 Sartelli stage 2A and stage 2B diverticulitis. A: Contrast-enhanced coronal reformatted computed tomography (CT) images demonstrated diverticulitis in the sigmoid colon (blue arrow) and an adjacent abscess formation measuring approximately 7 cm long (yellow double-sided arrow), consistent with Sartelli stage 2A diverticulitis; B: Contrast-enhanced coronal CT images revealed long-segment diffuse colonic wall thickening, pericolic fat stranding, and diverticulitis in the sigmoid colon (blue arrow) along with the presence of intraperitoneal free millimetric air (orange circle), consistent with Sartelli stage 2B diverticulitis.

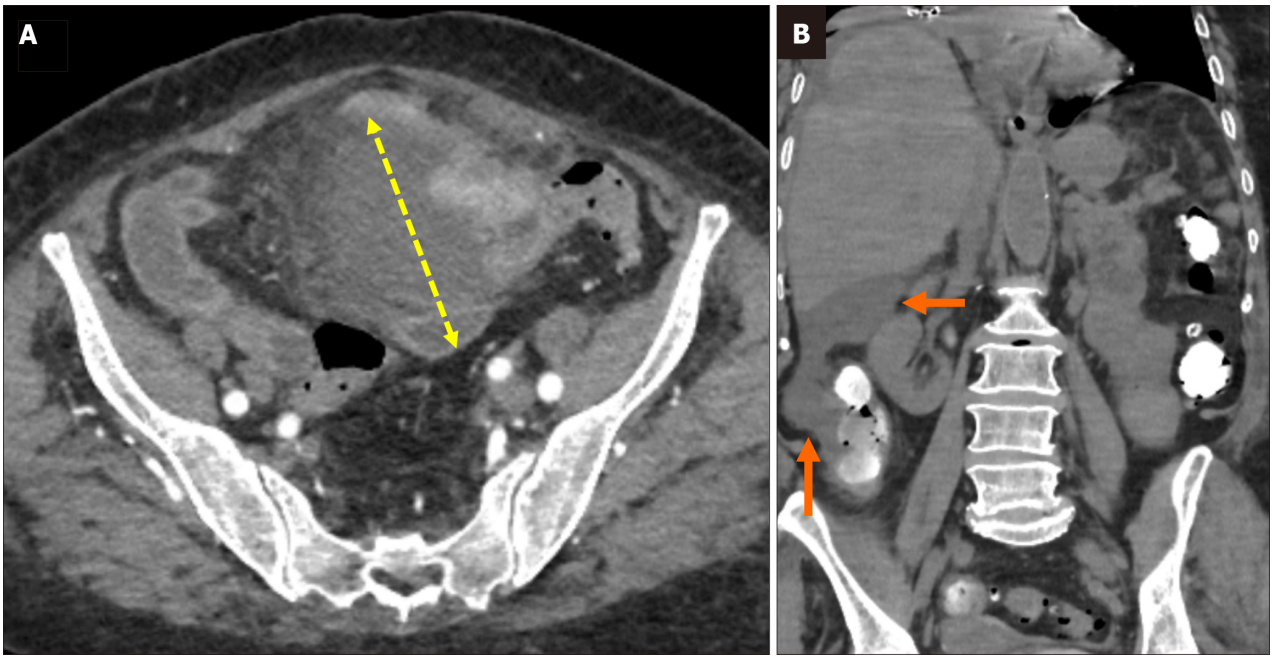

Figure 5 Sartelli stage 3 diverticulitis. A: Axial contrast-enhanced computed tomography (CT) demonstrated findings of sigmoid colon diverticulitis with an associated abscess formation long (yellow double-sided arrow) in the midline abdomen; B: Coronal oral contrast-enhanced CT image showed free intraperitoneal fluid extending into the right paracolic and perihepatic spaces (orange arrows), with no evidence of free air in the same patient.

necrosis, and loss of intestinal wall integrity, ultimately resulting in perforation[5]. Perforations typically occur in sigmoid colonic diverticulitis. They are characterized by localized free air adjacent to the inflamed colon, which remains self-contained. Clinical findings depend on the perforation site in cases where diverticular perforation is not self-limiting. Perforations on the peritoneal surface result in intraperitoneal free air, whereas those occurring on the mesenteric surface may allow free air to track retroperitoneally, potentially extending to the perirenal space, mediastinum, or even the scrotal sac[4,6,27-29]. Perforation can be directly identified on CT as bowel wall integrity disruption, extraluminal gas, and leakage of contrast material. Indirect signs include segmental wall thickening, inflammatory fat stranding, and the presence of an abscess (Figure 7)[6].

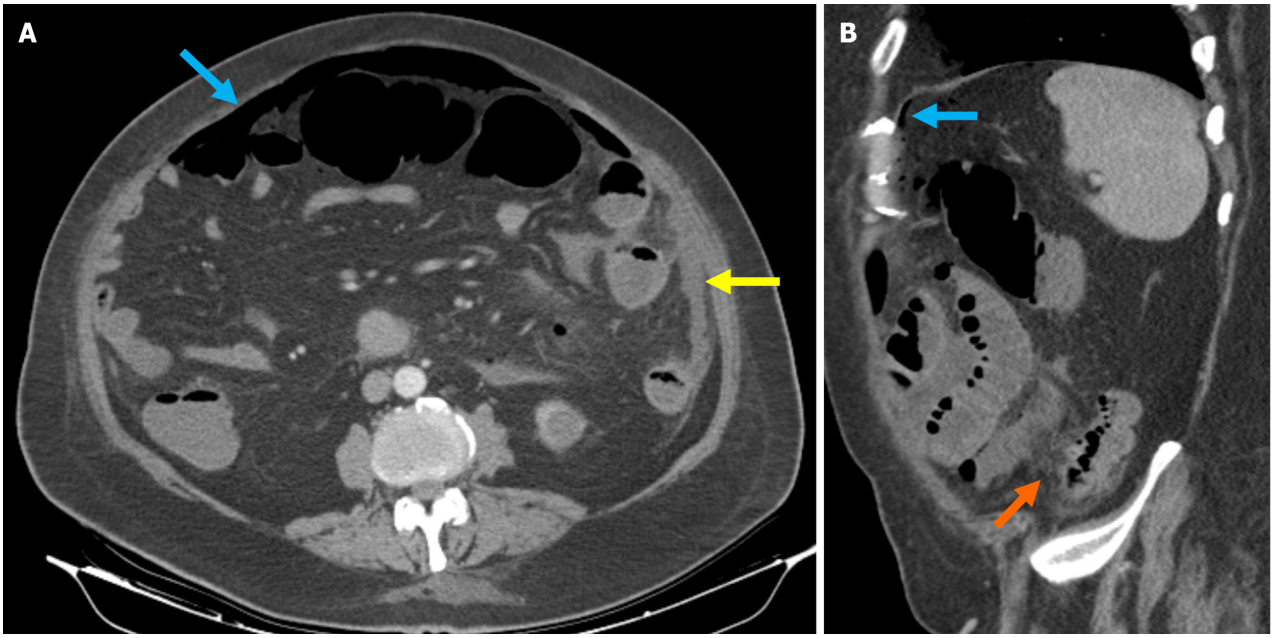

Figure 6 Sartelli stage 4 diverticulitis. A: Axial reformatted contrast-enhanced computed tomography (CT) image including widespread intraabdominal free air (blue arrow) and free fluid (yellow arrow), more prominently around the left colon; B: Sagittal reformatted contrast-enhanced CT image also included widespread intraabdominal free air (blue arrow). Pericolic fat stranding and inflammatory changes in the pericolic fat (orange arrow) were also observed, indicative of diverticulitis. Surgical intervention confirmed perforated diverticulitis originating from the left colon.

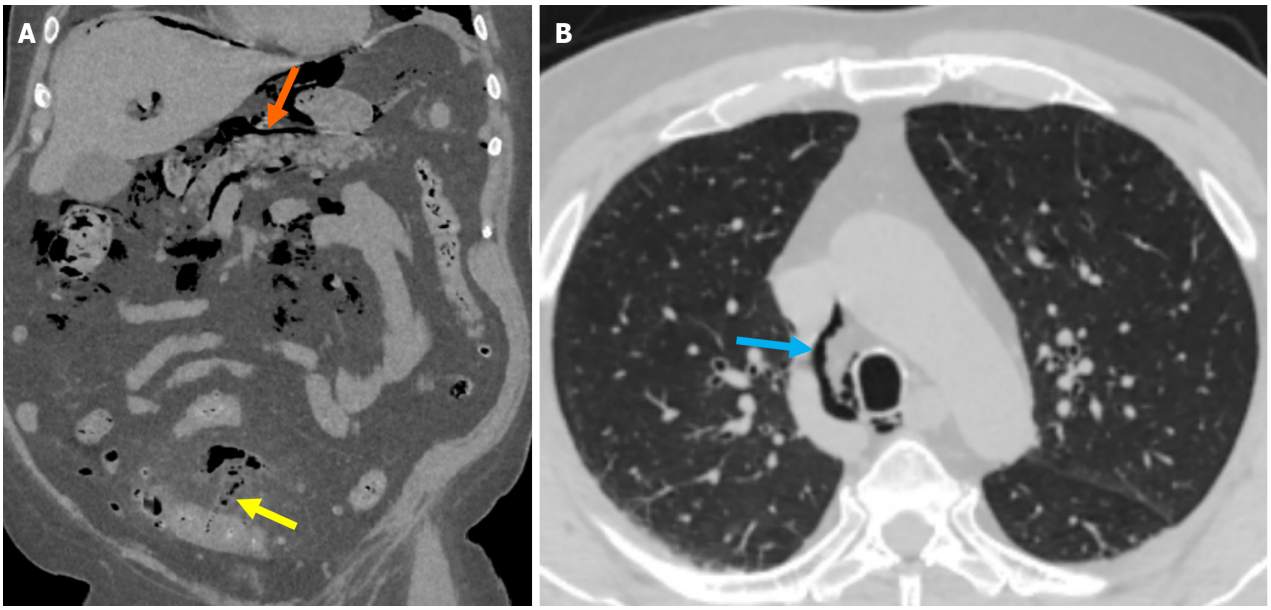

Figure 7 Free air extending to the mediastinum due to sigmoid colon diverticulitis perforation. A: Non-contrast coronal reformatted computed tomography (CT) image at the abdominal level demonstrated the presence of air in the mesentery of the sigmoid colon (yellow arrow), consistent with perforation. The air was seen surrounding the portal structures in the hepatic hilum and extending retroperitoneally (orange arrow); B: Lung window axial CT image at the thoracic level showed that the air column extended to the mediastinum (blue arrow).

Abscess: Abscess formation can occur intramurally, pericolic, or at a distant location and typically develops as a progression from phlegmon. Abscesses should be assessed based on their maximum diameter relative to the location of the inflamed colonic segment and the potential for fistula formation into adjacent organs[4]. Abscesses are classified by the Sartelli or Hinchey classifications and are managed through antibiotic therapy, percutaneous drainage, or surgical intervention depending on their severity and clinical presentation[26].

Abscesses secondary to diverticulitis can develop in distant organs such as the liver, lungs, spine, and brain. Microorganisms may translocate through mucosal defects, enter the portal system, and spread hematogenously to the liver and other organs. The formation of abscesses in distant organs significantly increases the morbidity and mortality associated with the disease[30,31].

A tubo-ovarian abscess should be considered in the differential diagnosis and as a possible consequence of diverticulitis in cases of lower quadrant pain. In patients with low-risk factors for pelvic inflammatory disease (PID) (*e.g.*, postmenopausal females, those not engaging in sexual activity), the presence of PID should raise suspicion for complications related to diverticulitis. Due to their close anatomical proximity, sigmoid colon diverticula may facilitate transperitoneal spread leading to the development of tubo-ovarian abscess. Additionally, underlying neoplastic processes such as ovarian and colorectal cancer should be included in the differential diagnosis of this patient group (Figure 8)[32,33].

Fistula: Two mechanisms are thought to play a role in fistula formation. The first involves direct erosion and adhesion of the ruptured diverticulum to the adjacent tissue due to the inflammatory process. The second mechanism occurs when a diverticular abscess erodes the surrounding tissue and forms a fistula[34].

The most common fistula occurs between the sigmoid colon and the bladder. This occurrence presents as recurrent urinary tract infections, fecaluria, and pneumaturia. On CT imaging the loss of fat plane separation between the colonic loop and the bladder and the thickening of the adjacent colonic and bladder walls is observed. Additionally, the presence of air within the bladder and the passage of contrast material from a rectal or urinary foley catheter through the fistula are diagnostic findings[35,36]. Another common cause of vesicointestinal fistula is Crohn's disease (CD). However, CD-related fistulas typically occur between the terminal ileum and the bladder and primarily affect the right side of the bladder. Fistulas secondary to diverticulitis most commonly involve the left posterior aspect of the bladder[27].

Depending on the location of diverticulitis, fistulous tracts will less commonly develop toward adjacent bowel loops, the uterus, gallbladder, vagina, or the skin[37]. Myometrial abscess formation and free air within the endometrial cavity are commonly observed in colo-uterine fistulas[38]. Fluid-sensitive sequences can depict the fistulous tract as a fluid-filled channel on MRI and CT, aiding in the diagnosis (Figure 9).

Pylephlebitis: Pylephlebitis is ascending septic thrombophlebitis. It is not specific to diverticulitis, occurring in other intraabdominal infections. Pylephlebitis is a rare condition, with an incidence ranging from 0.37 to 2.7 cases per 100000 person-years. It typically presents as nonspecific symptoms such as abdominal pain, leading to delayed diagnosis. The condition may progress to septic shock and carries a mortality rate of 8.7%-32.0%[39]. The primary treatment for pylephlebitis is broad-spectrum antibiotics and anticoagulation therapy although the source of infection may require surgical management[40].

The affected mesenteric vessels are associated with the venous structures responsible for draining the colonic segment involved in diverticulitis. For example, the sigmoid colon is the most commonly affected site in diverticulitis, and phlebitis initially manifests in the local venous structures draining the sigmoid colon, followed by thrombus formation in the inferior mesenteric vein and portal vein. In more advanced cases, pulmonary septic thromboembolism secondary to diverticulitis has also been reported[13,41,42].

Early hepatic abnormalities are characterized by non-opacified intrahepatic branches of the portal vein and central or peripheral regions of low attenuation, resulting from reduced intrahepatic blood flow. Hepatic abscess formation may occur if appropriate treatment is not administered. Then a more complex therapeutic approach is necessary (Figure 10)[13].

Bleeding: Diverticular bleeding is the leading cause of lower gastrointestinal hemorrhage[43]. Although endoscopy facilitates the diagnosis and treatment of diverticular bleeding, studies have shown that the combination of colonoscopy following contrast-enhanced CT improves the detection rate of the bleeding source[44].

Diverticular bleeding typically results from hemorrhage of an ectatic vessel within a chronic diverticular focus. Since early intervention is crucial for effective management, a colonoscopy within the first 12-24 hours is recommended. In cases of massive bleeding, the utility of a colonoscopy may be limited due to the need for bowel preparation and procedural constraints. Therefore, CT angiography is often preferred because it does not require prior preparation and is not restricted by the bleeding volume. The presence of intraluminal contrast extravasation following intravenous contrast administration suggests active bleeding. Oral contrast administration is not recommended in patients suspected of bleeding as it may obscure extravasation. On non-contrast imaging, hyperdense intraluminal content may indicate hemorrhage, while dynamic studies demonstrating contrast extravasation in the portal venous phase further support the presence of active bleeding[4,45,46].

CHRONIC DIVERTICULITIS

Patients with chronic diverticulitis experience abdominal pain and obstructive symptoms lasting for at least 2 months without fever or leukocytosis. Pathological findings demonstrate that fibrosis is linked to acute or chronic inflammatory changes[47]. Recurrent acute diverticular episodes lead to chronic muscular hypertrophy, wall thickening, and fibrosis of the colon, ultimately resulting in luminal narrowing. This condition may mimic or obscure malignancy, and differentiation is made through CT imaging and endoscopic evaluation[4].

The most significant findings supporting diverticulitis on CT imaging include pericolic inflammation and segmental involvement exceeding 10 cm. Findings indicative of colon cancer include the presence of pericolic lymph nodes and a luminal mass[48,49]. The absence of diverticula in the affected segment and the presence of the shoulder phenomenon (wall thickening that forms a mass with an abrupt, perpendicular transition to the adjacent colonic mucosa) are additional distinguishing features of colon cancer. The luminal narrowing is also frequently associated with this finding[4,48,49]. In some patients, follow-up imaging and colonoscopy evaluation can provide a more accurate diagnosis (Figure 11)[4].

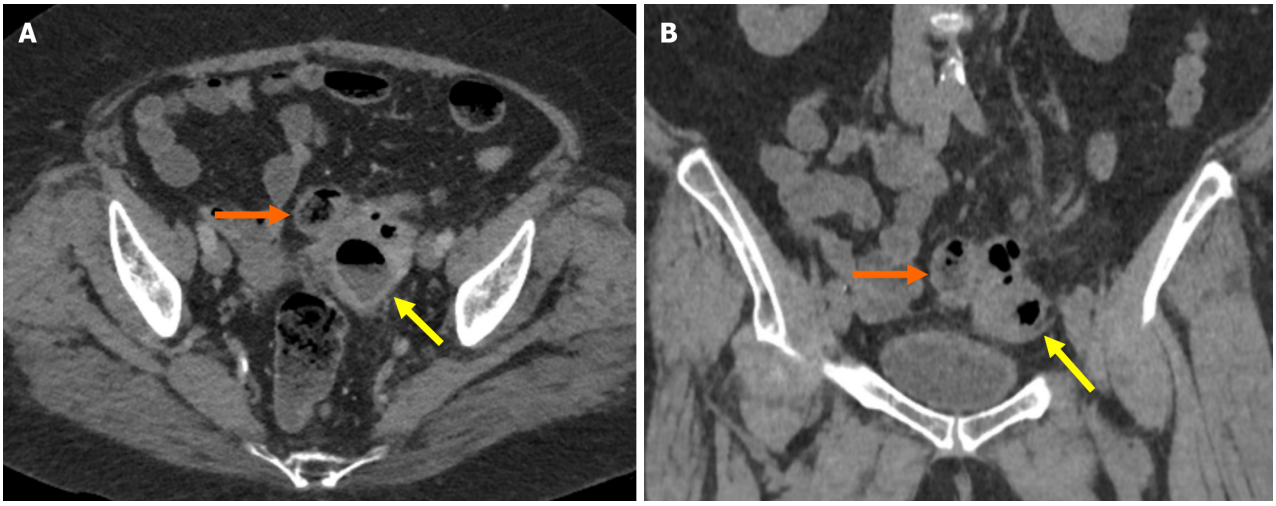

Figure 8 Tubo-ovarian abscess secondary to sigmoid colon diverticulitis. A: Contrast-enhanced axial; B: Non-contrast coronal computed tomography images. Demonstrated a left tubo-ovarian abscess (yellow arrows) in a postmenopausal female patient with a history of diverticular disease. The abscess, which was later determined secondary to diverticulitis, was observed with a loss of fat planes between the sigmoid colon (orange arrows) and the abscess area.

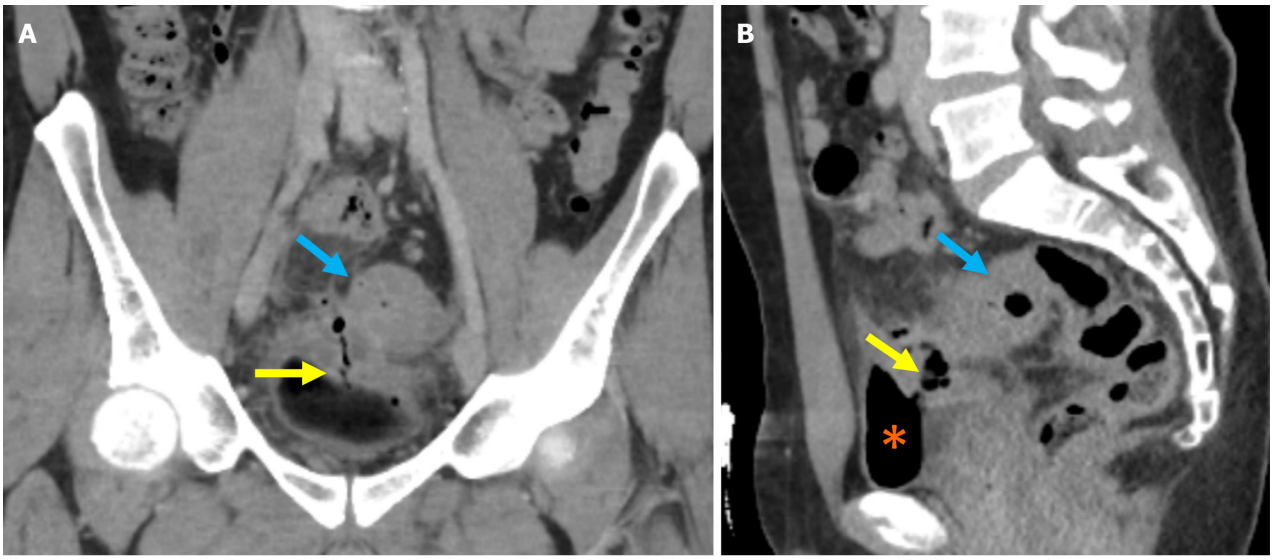

Figure 9 Colo-vesical fistula secondary to sigmoid colon diverticulitis. A young male patient with fecaluria and pneumaturia. A: Coronal contrast-enhanced computed tomography image demonstrated findings consistent with sigmoid diverticulitis. Loss of fat planes between the sigmoid colon (blue arrows), an air-filled tract extending from the sigmoid colon to the bladder lumen, indicative of a colo-vesical fistula (yellow arrows), and the adjacent bladder segment with bladder wall thickening in the affected area was visualized; B: The presence of intraluminal air within the bladder was noted (orange asterisks).

SEGMENTAL COLITIS ASSOCIATED WITH DIVERTICULOSIS

Segmental colitis associated with diverticulosis (SCAD) is characterized by active chronic luminal mucosal inflammation involving the colonic segment affected by diverticulitis. It is most frequently localized in the sigmoid colon, and the disease often presents with rectal bleeding. Differentiation from other conditions, such as CD, ulcerative colitis, and infectious colitis, can be challenging[50].

In elderly patients with a history of diverticulitis attacks and isolated inflammation localized to the sigmoid colon, SCAD should be considered. Diagnosis of SCAD requires a combination of endoscopic findings and clinical history. The preservation of the proximal colon and rectum and the typical older age of affected patients distinguishes SCAD from ulcerative colitis. However, SCAD shares similar CT findings with CD. In CD the gastrointestinal tract (most notably the terminal ileum) is affected in a segmental pattern. The length of segmental inflammation is greater in SCAD cases than in CD and diverticulitis. While diverticulitis typically presents with inflammation centered around the diverticular areas, SCAD is characterized by mucosal inflammation within the interdiverticular regions. Systemic symptoms such as fever and diarrhea are more frequently observed in infectious colitis[51,52].

In a study conducted by Urquhart *et al*[53], CT features associated with SCAD were described as concentric colonic wall thickening not centered around the diverticula, prominent mesenteric vascularity, and mild pericolic inflammation.

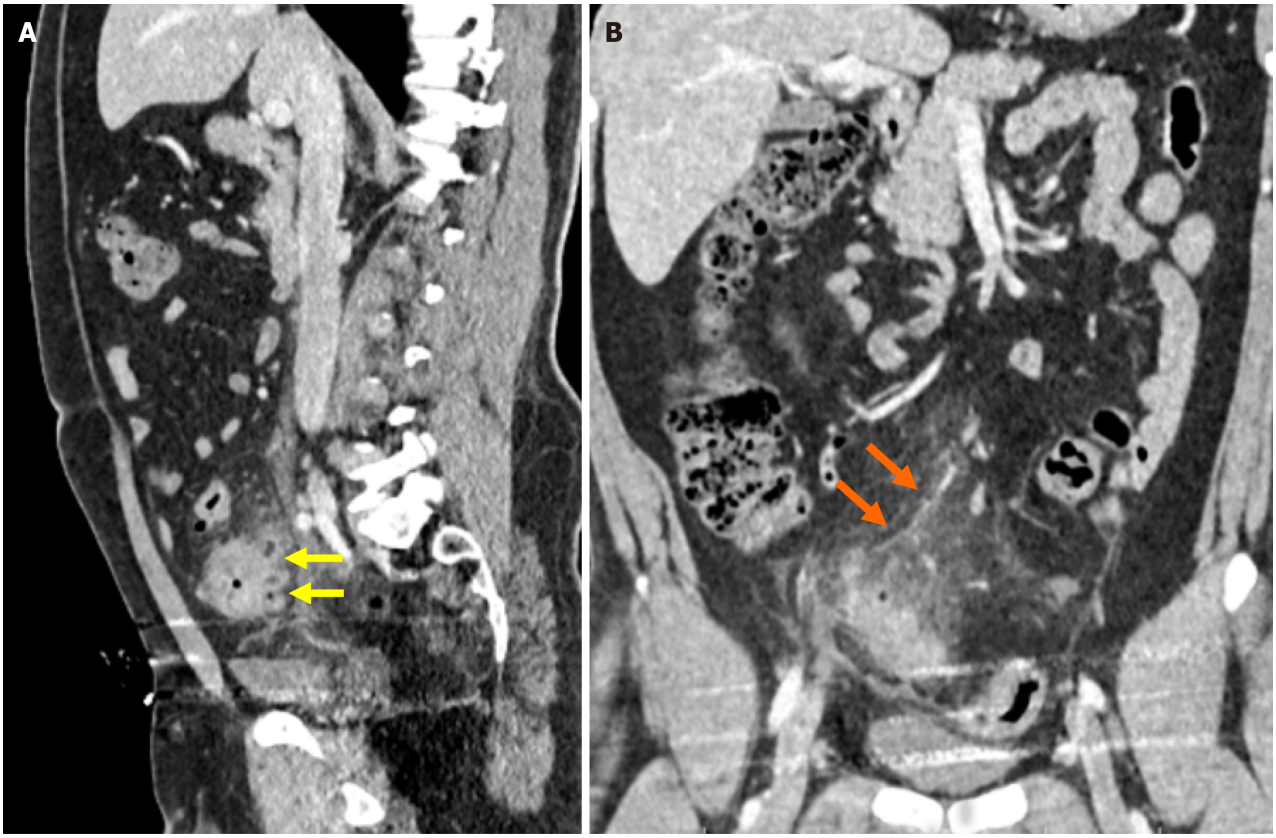

Figure 10 Pylephlebitis secondary to sigmoid colon diverticulitis. A: Contrast-enhanced sagittal reformatted computed tomography (CT) image demonstrated segmental wall thickening of the sigmoid colon, fat stranding in the surrounding mesenteric fat, and the presence of multiple diverticula, consistent with diverticulitis (yellow arrow); B: Contrast-enhanced coronal reformatted CT image showed a dilated venous structure with a lack of contrast enhancement in continuity with the inferior mesenteric vein, suggestive of thrombophlebitis (orange arrow).

The length of the affected segment in the sigmoid colon was greater in SCAD compared with CD and diverticulitis. Moreover, findings such as inflamed diverticula and pericolic fat stranding were less commonly observed in SCAD than in diverticulitis.

FUTURE DIRECTIONS FOR ARTIFICIAL INTELLIGENCE INTEGRATION

The growing presence of artificial intelligence (AI) in radiology is evident across all stages of the imaging process. AI enables faster and clearer image generation, helping clinicians make more confident diagnoses and informed treatment plans[54]. AI also enables precise analysis of numerous quantitative imaging features that are imperceptible to human senses through techniques such as radiomics and deep learning. By assessing and quantifying body composition, AI can provide valuable insights into disease severity and progression[54,55].

In a 2022 study conducted within a healthcare-focused AI competition, CT datasets were developed to evaluate six abdominal emergencies including diverticulitis. Diverticulitis was identified as the most challenging to detect due to the imaging similarities with other conditions, the scarcity of representative cases, and the lack of prominent distinguishing features. Despite typical CT signs such as bowel wall thickening and pericolic fat stranding, it often mimics pathologies like appendicitis or colitis, complicating its diagnosis[56].

AI has become increasingly prevalent in radiology, and current research on its application to diverticulitis has mainly concentrated on its role in differentiating diverticulitis from colorectal cancer. In a study conducted by Ziegelmayer *et al* [57], a cohort of 585 patients with a history of surgery for either colorectal cancer or acute diverticulitis was evaluated using a three-dimensional convolutional neural network. On the test set the model achieved a sensitivity of 83.3% and a specificity of 86.6%. Radiologist-only readings yielded a sensitivity of 77.6% and a specificity of 81.6%. When AI-supported radiologists were involved, sensitivity increased to 85.6% and specificity to 91.3%. Furthermore, the false-negative rate decreased from 22.0% to 14.3%.

The improvement in diagnostic accuracy for imaging interpretation in patients with colorectal cancer or acute diverticulitis is clinically significant. It is important because both conditions may require emergency surgery in the event of perforation; however, the surgical approaches differ substantially. Colorectal cancer typically necessitates oncological resection of the affected bowel segment along with the regional lymphatic basin, whereas limited resection of the diseased bowel segment is often sufficient in cases of acute diverticulitis[58].

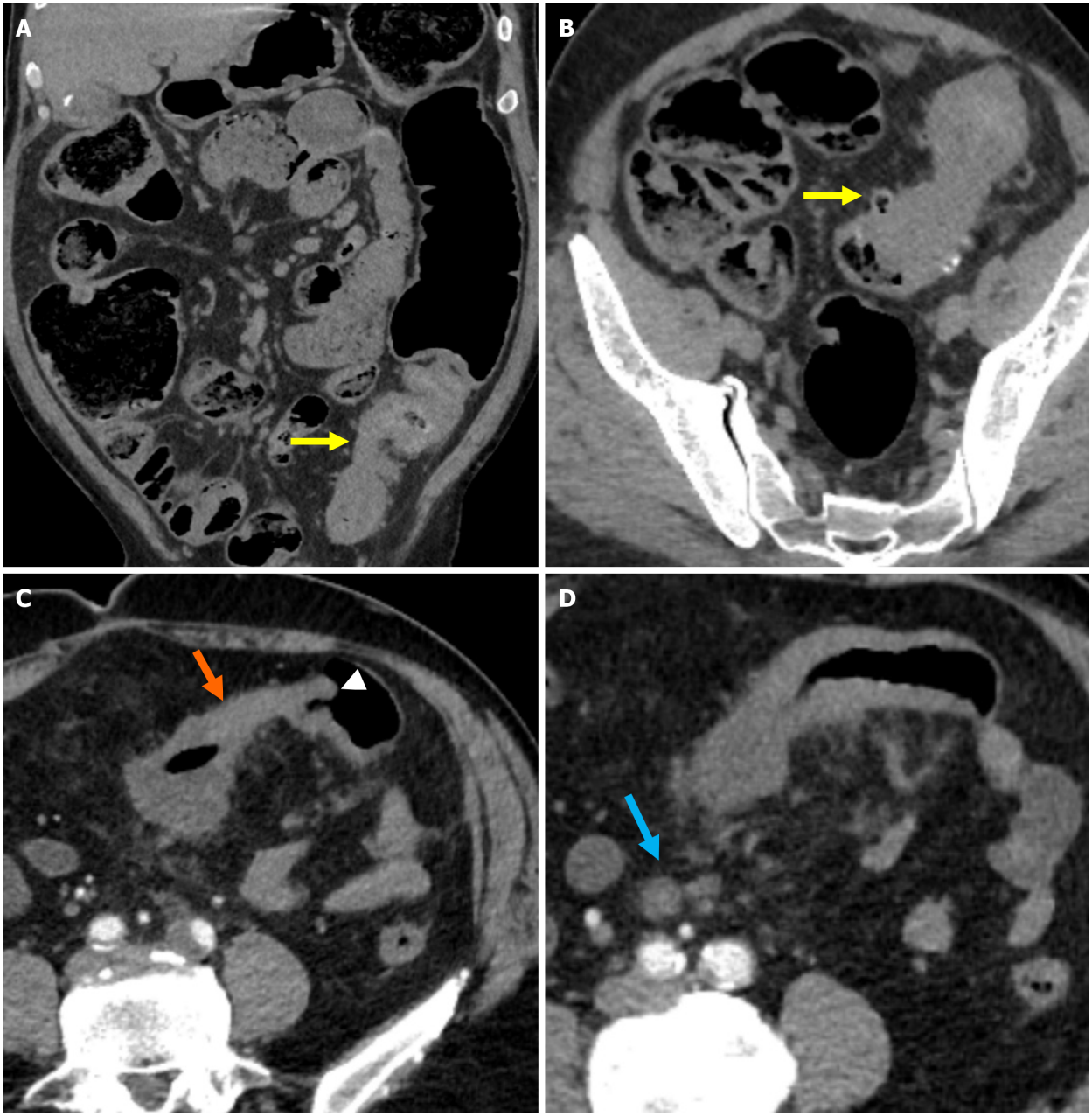

Figure 11 Distinguishing features of chronic sigmoid diverticulitis and colorectal cancer. A and B: Non-contrast-enhanced coronal reformatted computed tomography (CT) image and non-contrast-enhanced axial CT image showed long-segment, diffuse wall thickening in the sigmoid colon, luminal narrowing due to fibrosis, and diverticula (yellow arrows). Recurrent obstruction with proximal bowel loop dilatation was evident. The absence of pathological lymphadenopathy in the mesocolon served as a key diagnostic clue; C: Marked wall thickening of the affected bowel segment (orange arrow) with the shoulder phenomenon (white arrowhead) without visible diverticula; D: Rounded, metastatic lymph nodes (blue arrow) in the mesentery of the affected sigmoid segment accompanied by fat stranding consistent with pericolic fat infiltration.

LIMITATIONS

Limitations of this narrative review should be acknowledged. One limitation was the inclusion of only English-language papers. The recent emergence of certain conditions as distinct entities and the limited availability of prospective studies on these topics also posed challenges during the preparation of this manuscript. Because SCAD was described only recently, there are limited dedicated imaging features and related studies, which may affect the generalizability of the findings. Few prospective studies have concentrated on the use of AI in diverticular disease. Further studies are warranted to confirm the role of new tools, such as AI, across various clinical situations.

CONCLUSION

Diverticular disease is a prevalent gastrointestinal disorder, and its incidence continues to increase due to evolving

dietary habits and lifestyle changes in modern populations. The presenting symptoms leading to hospital admission depend on whether the disease is complicated or uncomplicated. The advantages of utilizing US for assessing diverticular disease are the ease of use, no risks associated with ionizing radiation, cost-effectiveness, and diagnostic accuracy comparable with CT. However, US is less effective than CT in identifying complicated diverticular disease and differentiating from other mimicking pathologies, which limits its use in these clinical scenarios. CT is crucial in diagnosing, identifying complications, and guiding disease staging using the Sartelli classification.

The stage of the disease can be determined to allow clinicians to predict the clinical course and select from a broad spectrum of treatment options ranging from conservative management to percutaneous drainage or surgical intervention. In addition to providing valuable information about diverticulitis, CT imaging is critical for differentiating alternative diagnoses and identifying concurrent pathologies during diagnosis and follow-up. In SCAD cases imaging alone is insufficient, and diagnosis requires integrating clinical findings and endoscopic features.

As in numerous medical domains, AI is increasingly important in the radiological evaluation of diverticulitis, with recent promising efforts focusing on its effectiveness in differentiating it from colorectal cancer. For radiologists, understanding the current staging systems and recognizing the imaging findings associated with common complications are essential to facilitate effective communication with surgeons and gastroenterologists and to ensure accurate diagnosis and appropriate management planning for patients.

FOOTNOTES

Author contributions: Simsar M and Sahin H conceptualized and designed the study; Simsar M, Yuruk YY, and Sahin O conducted the literature review, carried out the analysis, drafted the original manuscript, and made critical revisions; Sahin H supervised the review, advised the review design, and critically revised the manuscript. All authors prepared the draft and approved the submitted version.

Conflict-of-interest statement: The authors declare no conflicts of interest.

Country of origin: Türkiye

ORCID number: Mehmet Simsar 0009-0001-1438-694X; Yesim Yekta Yuruk 0009-0002-6478-4636; Olgun Sahin 0000-0003-0366-9220; Hilal Sahin 0000-0001-8726-8998.

S-Editor: Qu XL
L-Editor: A
P-Editor: Lei YY

REFERENCES

1 **Feuerstein JD**, Falchuk KR. Diverticulosis and Diverticulitis. *Mayo Clin Proc* 2016; **91**: 1094-1104 [*RCA*] [PMID: 27156370 DOI: 10.1016/j.mayocp.2016.03.012] [FullText]
2 **Young-Fadok TM**. Diverticulitis. *N Engl J Med* 2018; **379**: 1635-1642 [*RCA*] [PMID: 30354951 DOI: 10.1056/NEJMcp1800468] [FullText]
3 **Bharucha AE**, Parthasarathy G, Ditah I, Fletcher JG, Ewelukwa O, Pendlimari R, Yawn BP, Melton LJ, Schleck C, Zinsmeister AR. Temporal Trends in the Incidence and Natural History of Diverticulitis: A Population-Based Study. *Am J Gastroenterol* 2015; **110**: 1589-1596 [*RCA*] [PMID: 26416187 DOI: 10.1038/ajg.2015.302] [FullText]
4 **Sugi MD**, Sun DC, Menias CO, Prabhu V, Choi HH. Acute diverticulitis: Key features for guiding clinical management. *Eur J Radiol* 2020; **128**: 109026 [*RCA*] [PMID: 32422553 DOI: 10.1016/j.ejrad.2020.109026] [FullText]
5 **Wedel T**, Barrenschee M, Lange C, Cossais F, Böttner M. Morphologic Basis for Developing Diverticular Disease, Diverticulitis, and Diverticular Bleeding. *Viszeralmedizin* 2015; **31**: 76-82 [*RCA*] [PMID: 26989376 DOI: 10.1159/000381431] [FullText] [Full Text(PDF)]
6 **Sessa B**, Galluzzo M, Ianniello S, Pinto A, Trinci M, Miele V. Acute Perforated Diverticulitis: Assessment With Multidetector Computed Tomography. *Semin Ultrasound CT MR* 2016; **37**: 37-48 [*RCA*] [PMID: 26827737 DOI: 10.1053/j.sult.2015.10.003] [FullText]
7 **Flor N**, Maconi G, Cornalba G, Pickhardt PJ. The Current Role of Radiologic and Endoscopic Imaging in the Diagnosis and Follow-Up of Colonic Diverticular Disease. *AJR Am J Roentgenol* 2016; **207**: 15-24 [*RCA*] [PMID: 27082846 DOI: 10.2214/AJR.16.16138] [FullText]
8 **Liljegren G**, Chabok A, Wickbom M, Smedh K, Nilsson K. Acute colonic diverticulitis: a systematic review of diagnostic accuracy. *Colorectal Dis* 2007; **9**: 480-488 [*RCA*] [PMID: 17573739 DOI: 10.1111/j.1463-1318.2007.01238.x] [FullText]
9 **Kandagatla PG**, Stefanou AJ. Current Status of the Radiologic Assessment of Diverticular Disease. *Clin Colon Rectal Surg* 2018; **31**: 217-220 [*RCA*] [PMID: 29942210 DOI: 10.1055/s-0037-1607466] [FullText]
10 **Laméris W**, van Randen A, Bipat S, Bossuyt PM, Boermeester MA, Stoker J. Graded compression ultrasonography and computed tomography in acute colonic diverticulitis: meta-analysis of test accuracy. *Eur Radiol* 2008; **18**: 2498-2511 [*RCA*] [PMID: 18523784 DOI: 10.1007/s00330-008-1018-6] [FullText]
11 **Ripollés T**, Sebastián-Tomás JC, Martínez-Pérez MJ, Manrique A, Gómez-Abril SA, Torres-Sanchez T. Ultrasound can differentiate complicated and noncomplicated acute colonic diverticulitis: a prospective comparative study with computed tomography. *Abdom Radiol (NY)*

2021; **46**: 3826-3834 [*RCA*] [PMID: 33765176 DOI: 10.1007/s00261-021-03060-5] [FullText]

12 **Tiralongo F**, Di Pietro S, Milazzo D, Galioto S, Castiglione DG, Ini' C, Foti PV, Mosconi C, Giurazza F, Venturini M, Zanghi' GN, Palmucci S, Basile A. Acute Colonic Diverticulitis: CT Findings, Classifications, and a Proposal of a Structured Reporting Template. *Diagnostics (Basel)* 2023; **13**: 3628 [*RCA*] [PMID: 38132212 DOI: 10.3390/diagnostics13243628] [FullText] [Full Text(PDF)]

13 **Balthazar EJ**, Gollapudi P. Septic thrombophlebitis of the mesenteric and portal veins: CT imaging. *J Comput Assist Tomogr* 2000; **24**: 755-760 [*RCA*] [PMID: 11045699 DOI: 10.1097/00004728-200009000-00017] [FullText]

14 **Kechagias KS**, Katsikas-Triantafyllidis K, Geropoulos G, Giannos P, Zafeiri M, Tariq-Mian I, Paraskevaidi M, Mitra A, Kyrgiou M. Diverticulitis during pregnancy: A review of the reported cases. *Front Med (Lausanne)* 2022; **9**: 942666 [*RCA*] [PMID: 36438049 DOI: 10.3389/fmed.2022.942666] [FullText]

15 **Jerjen F**, Zaidi T, Chan S, Sharma A, Mudliar R, Soomro K, Jimenez Y, Reed W. Magnetic Resonance Imaging for the diagnosis and management of acute colonic diverticulitis: a review of current and future use. *J Med Radiat Sci* 2021; **68**: 310-319 [*RCA*] [PMID: 33607699 DOI: 10.1002/jmrs.458] [FullText] [Full Text(PDF)]

16 **Hinchey EJ**, Schaal PG, Richards GK. Treatment of perforated diverticular disease of the colon. *Adv Surg* 1978; **12**: 85-109 [*RCA*] [PMID: 735943] [FullText]

17 **Kaiser AM**, Jiang JK, Lake JP, Ault G, Artinyan A, Gonzalez-Ruiz C, Essani R, Beart RW Jr. The management of complicated diverticulitis and the role of computed tomography. *Am J Gastroenterol* 2005; **100**: 910-917 [*RCA*] [PMID: 15784040 DOI: 10.1111/j.1572-0241.2005.41154.x] [FullText]

18 **Choi J**, Bessoff K, Bromley-Dulfano R, Li Z, Gupta A, Taylor K, Wadhwa H, Seltzer R, Spain DA, Knowlton LM. Prospectively Assigned AAST Grade versus Modified Hinchey Class and Acute Diverticulitis Outcomes. *J Surg Res* 2021; **259**: 555-561 [*RCA*] [PMID: 33248670 DOI: 10.1016/j.jss.2020.10.016] [FullText]

19 **Shafi S**, Aboutanos M, Brown CV, Ciesla D, Cohen MJ, Crandall ML, Inaba K, Miller PR, Mowery NT; American Association for the Surgery of Trauma Committee on Patient Assessment and Outcomes. Measuring anatomic severity of disease in emergency general surgery. *J Trauma Acute Care Surg* 2014; **76**: 884-887 [*RCA*] [PMID: 24553565 DOI: 10.1097/TA.0b013e3182aafdba] [FullText]

20 **Sartelli M**, Moore FA, Ansaloni L, Di Saverio S, Coccolini F, Griffiths EA, Coimbra R, Agresta F, Sakakushev B, Ordoñez CA, Abu-Zidan FM, Karamarkovic A, Augustin G, Costa Navarro D, Ulrych J, Demetrashvili Z, Melo RB, Marwah S, Zachariah SK, Wani I, Shelat VG, Kim JI, McFarlane M, Pintar T, Rems M, Bala M, Ben-Ishay O, Gomes CA, Faro MP, Pereira GA Jr, Catani M, Baiocchi G, Bini R, Anania G, Negoi I, Kecbaja Z, Omari AH, Cui Y, Kenig J, Sato N, Vereczkei A, Skrovina M, Das K, Bellanova G, Di Carlo I, Segovia Lohse HA, Kong V, Kok KY, Massalou D, Smirnov D, Gachabayov M, Gkiokas G, Marinis A, Spyropoulos C, Nikolopoulos I, Bouliaris K, Tepp J, Lohsiriwat V, Çolak E, Isik A, Rios-Cruz D, Soto R, Abbas A, Tranà C, Caproli E, Soldatenkova D, Corcione F, Piazza D, Catena F. A proposal for a CT driven classification of left colon acute diverticulitis. *World J Emerg Surg* 2015; **10**: 3 [*RCA*] [PMID: 25972914 DOI: 10.1186/1749-7922-10-3] [FullText] [Full Text(PDF)]

21 **Minordi LM**, Larosa L, Berte G, Pecere S, Manfredi R. CT of the acute colonic diverticulitis: a pictorial essay. *Diagn Interv Radiol* 2020; **26**: 546-551 [*RCA*] [PMID: 33180020 DOI: 10.5152/dir.2020.19645] [FullText]

22 **Fernandes T**, Oliveira MI, Castro R, Araújo B, Viamonte B, Cunha R. Bowel wall thickening at CT: simplifying the diagnosis. *Insights Imaging* 2014; **5**: 195-208 [*RCA*] [PMID: 24407923 DOI: 10.1007/s13244-013-0308-y] [FullText] [Full Text(PDF)]

23 **Pereira JM**, Sirlin CB, Pinto PS, Jeffrey RB, Stella DL, Casola G. Disproportionate fat stranding: a helpful CT sign in patients with acute abdominal pain. *Radiographics* 2004; **24**: 703-715 [*RCA*] [PMID: 15143223 DOI: 10.1148/rg.243035084] [FullText]

24 **Dickerson EC**, Chong ST, Ellis JH, Watcharotone K, Nan B, Davenport MS, Al-Hawary M, Mazza MB, Rizk R, Morris AM, Cohan RH. Recurrence of Colonic Diverticulitis: Identifying Predictive CT Findings-Retrospective Cohort Study. *Radiology* 2017; **285**: 850-858 [*RCA*] [PMID: 28837412 DOI: 10.1148/radiol.2017161374] [FullText]

25 **Wiesner W**, Mortelé KJ, Ji H, Ros PR. Normal colonic wall thickness at CT and its relation to colonic distension. *J Comput Assist Tomogr* 2002; **26**: 102-106 [*RCA*] [PMID: 11801911 DOI: 10.1097/00004728-200201000-00015] [FullText]

26 **Sartelli M**, Weber DG, Kluger Y, Ansaloni L, Coccolini F, Abu-Zidan F, Augustin G, Ben-Ishay O, Biffl WL, Bouliaris K, Catena R, Ceresoli M, Chiara O, Chiarugi M, Coimbra R, Cortese F, Cui Y, Damaskos D, De' Angelis GL, Delibegovic S, Demetrashvili Z, De Simone B, Di Marzo F, Di Saverio S, Duane TM, Faro MP, Fraga GP, Gkiokas G, Gomes CA, Hardcastle TC, Hecker A, Karamarkovic A, Kashuk J, Khokha V, Kirkpatrick AW, Kok KYY, Inaba K, Isik A, Labricciosa FM, Latifi R, Leppäniemi A, Litvin A, Mazuski JE, Maier RV, Marwah S, McFarlane M, Moore EE, Moore FA, Negoi I, Pagani L, Rasa K, Rubio-Perez I, Sakakushev B, Sato N, Sganga G, Siquini W, Tarasconi A, Tolonen M, Ulrych J, Zachariah SK, Catena F. 2020 update of the WSES guidelines for the management of acute colonic diverticulitis in the emergency setting. *World J Emerg Surg* 2020; **15**: 32 [*RCA*] [PMID: 32381121 DOI: 10.1186/s13017-020-00313-4] [FullText] [Full Text (PDF)]

27 **Onur MR**, Akpinar E, Karaosmanoglu AD, Isayev C, Karcaaltincaba M. Diverticulitis: a comprehensive review with usual and unusual complications. *Insights Imaging* 2017; **8**: 19-27 [*RCA*] [PMID: 27878550 DOI: 10.1007/s13244-016-0532-3] [FullText] [Full Text(PDF)]

28 **Kim SH**, Shin SS, Jeong YY, Heo SH, Kim JW, Kang HK. Gastrointestinal tract perforation: MDCT findings according to the perforation sites. *Korean J Radiol* 2009; **10**: 63-70 [*RCA*] [PMID: 19182505 DOI: 10.3348/kjr.2009.10.1.63] [FullText] [Full Text(PDF)]

29 **Fosi S**, Giuricin V, Girardi V, Di Caprera E, Costanzo E, Di Trapano R, Simonetti G. Subcutaneous emphysema, pneumomediastinum, pneumoretroperitoneum, and pneumoscrotum: unusual complications of acute perforated diverticulitis. *Case Rep Radiol* 2014; **2014**: 431563 [*RCA*] [PMID: 25136471 DOI: 10.1155/2014/431563] [FullText] [Full Text(PDF)]

30 **Linsen PVM**, Schrier VJMM. Decoding pylephlebitis: Tracing the path of infected thrombosis and liver abscesses. *Radiol Case Rep* 2023; **18**: 3820-3823 [*RCA*] [PMID: 37663570 DOI: 10.1016/j.radcr.2023.08.054] [FullText]

31 **Navarrete D**, Patil S, Dandachi D. Acute Streptococcus constellatus Pyogenic Liver Abscess Due to an Atypical Presentation of Sigmoid Diverticulitis Complicated by Pericolonic Abscess. *Cureus* 2020; **12**: e10940 [*RCA*] [PMID: 33200054 DOI: 10.7759/cureus.10940] [FullText] [Full Text(PDF)]

32 **Metz Y**, Nagler J. Diverticulitis presenting as a tubo-ovarian abscess with subsequent colon perforation. *World J Gastrointest Surg* 2011; **3**: 70-72 [*RCA*] [PMID: 21666809 DOI: 10.4240/wjgs.v3.i5.70] [FullText] [Full Text(PDF)]

33 **Protopapas AG**, Diakomanolis ES, Milingos SD, Rodolakis AJ, Markaki SN, Vlachos GD, Papadopoulos DE, Michalas SP. Tubo-ovarian abscesses in postmenopausal women: gynecological malignancy until proven otherwise? *Eur J Obstet Gynecol Reprod Biol* 2004; **114**: 203-209 [*RCA*] [PMID: 15140516 DOI: 10.1016/j.ejogrb.2003.10.032] [FullText]

34 **Small WP**, Smith AN. Fistula and conditions associated with diverticular disease of the colon. *Clin Gastroenterol* 1975; **4**: 171-199 [*RCA*]

[PMID: 1167350] [FullText]
35 **Najjar SF**, Jamal MK, Savas JF, Miller TA. The spectrum of colovesical fistula and diagnostic paradigm. *Am J Surg* 2004; **188**: 617-621 [*RCA*] [PMID: 15546583 DOI: 10.1016/j.amjsurg.2004.08.016] [FullText]
36 **Coakley KM**, Davis BR, Kasten KR. Complicated Diverticular Disease. *Clin Colon Rectal Surg* 2021; **34**: 96-103 [*RCA*] [PMID: 33642949 DOI: 10.1055/s-0040-1716701] [FullText]
37 **Woods RJ**, Lavery IC, Fazio VW, Jagelman DG, Weakley FL. Internal fistulas in diverticular disease. *Dis Colon Rectum* 1988; **31**: 591-596 [*RCA*] [PMID: 3402284 DOI: 10.1007/BF02556792] [FullText]
38 **Choi PW**. Colouterine fistula caused by diverticulitis of the sigmoid colon. *J Korean Soc Coloproctol* 2012; **28**: 321-324 [*RCA*] [PMID: 23346512 DOI: 10.3393/jksc.2012.28.6.321] [FullText] [Full Text(PDF)]
39 **Maejima T**, Hashimoto E, Hirose K, Miyazaki K, Suzuki M, Maeno T. Pylephlebitis Secondary to Diverticulitis Diagnosed by Abdominal Ultrasound and Computed Tomography. *Cureus* 2024; **16**: e73358 [*RCA*] [PMID: 39659306 DOI: 10.7759/cureus.73358] [FullText]
40 **Gajendran M**, Muniraj T, Yassin M. Diverticulitis complicated by pylephlebitis: a case report. *J Med Case Rep* 2011; **5**: 514 [*RCA*] [PMID: 21985694 DOI: 10.1186/1752-1947-5-514] [FullText] [Full Text(PDF)]
41 **Jevtic D**, Gavrancic T, Pantic I, Nordin T, Nordstrom CW, Antic M, Pantic N, Kaljevic M, Joksimovic B, Jovanovic M, Petcu E, Jecmenica M, Milovanovic T, Sprecher L, Dumic I. Suppurative Thrombosis of the Portal Vein (Pylephlebits): A Systematic Review of Literature. *J Clin Med* 2022; **11**: 4992 [*RCA*] [PMID: 36078922 DOI: 10.3390/jcm11174992] [FullText] [Full Text(PDF)]
42 **Wali L**, Shah A, Sleiman S, Hogsand T, Humphries S. Acute pylephlebitis secondary to perforated sigmoid diverticulitis: A case report. *Radiol Case Rep* 2021; **16**: 1504-1507 [*RCA*] [PMID: 33981372 DOI: 10.1016/j.radcr.2021.03.042] [FullText] [Full Text(PDF)]
43 **Nagata N**, Niikura R, Ishii N, Kaise M, Omata F, Tominaga N, Kitagawa T, Ikeya T, Kobayashi K, Furumoto Y, Narasaka T, Iwata E, Sugimoto M, Itoi T, Uemura N, Kawai T. Cumulative evidence for reducing recurrence of colonic diverticular bleeding using endoscopic clipping versus band ligation: Systematic review and meta-analysis. *J Gastroenterol Hepatol* 2021; **36**: 1738-1743 [*RCA*] [PMID: 33295071 DOI: 10.1111/jgh.15370] [FullText]
44 **Nagata N**, Niikura R, Aoki T, Moriyasu S, Sakurai T, Shimbo T, Shinozaki M, Sekine K, Okubo H, Watanabe K, Yokoi C, Yanase M, Akiyama J, Uemura N. Role of urgent contrast-enhanced multidetector computed tomography for acute lower gastrointestinal bleeding in patients undergoing early colonoscopy. *J Gastroenterol* 2015; **50**: 1162-1172 [*RCA*] [PMID: 25812518 DOI: 10.1007/s00535-015-1069-9] [FullText]
45 **Nagata N**, Ishii N, Manabe N, Tomizawa K, Urita Y, Funabiki T, Fujimori S, Kaise M. Guidelines for Colonic Diverticular Bleeding and Colonic Diverticulitis: Japan Gastroenterological Association. *Digestion* 2019; **99** Suppl 1: 1-26 [*RCA*] [PMID: 30625484 DOI: 10.1159/000495282] [FullText]
46 **Schreyer AG**, Layer G; German Society of Digestive and Metabolic Diseases (DGVS) as well as the German Society of General and Visceral Surgery (DGAV) in collaboration with the German Radiology Society (DRG). S2k Guidlines for Diverticular Disease and Diverticulitis: Diagnosis, Classification, and Therapy for the Radiologist. *Rofo* 2015; **187**: 676-684 [*RCA*] [PMID: 26019048 DOI: 10.1055/s-0034-1399526] [FullText]
47 **Sheiman L**, Levine MS, Levin AA, Hogan J, Rubesin SE, Furth EE, Laufer I. Chronic diverticulitis: clinical, radiographic, and pathologic findings. *AJR Am J Roentgenol* 2008; **191**: 522-528 [*RCA*] [PMID: 18647926 DOI: 10.2214/AJR.07.3597] [FullText]
48 **Chintapalli KN**, Chopra S, Ghiatas AA, Esola CC, Fields SF, Dodd GD 3rd. Diverticulitis versus colon cancer: differentiation with helical CT findings. *Radiology* 1999; **210**: 429-435 [*RCA*] [PMID: 10207426 DOI: 10.1148/radiology.210.2.r99fe48429] [FullText]
49 **Lips LM**, Cremers PT, Pickhardt PJ, Cremers SE, Janssen-Heijnen ML, de Witte MT, Simons PC. Sigmoid cancer versus chronic diverticular disease: differentiating features at CT colonography. *Radiology* 2015; **275**: 127-135 [*RCA*] [PMID: 25426771 DOI: 10.1148/radiol.14132829] [FullText]
50 **Schembri J**, Bonello J, Christodoulou DK, Katsanos KH, Ellul P. Segmental colitis associated with diverticulosis: is it the coexistence of colonic diverticulosis and inflammatory bowel disease? *Ann Gastroenterol* 2017; **30**: 257-261 [*RCA*] [PMID: 28469355 DOI: 10.20524/aog.2017.0126] [FullText] [Full Text(PDF)]
51 **Cassieri C**, Brandimarte G, Elisei W, Lecca GP, Goni E, Penna A, Picchio M, Tursi A. How to Differentiate Segmental Colitis Associated With Diverticulosis and Inflammatory Bowel Diseases. *J Clin Gastroenterol* 2016; **50** Suppl 1: S36-S38 [*RCA*] [PMID: 27622359 DOI: 10.1097/MCG.0000000000000630] [FullText]
52 **Freeman HJ**. Segmental Colitis Associated with Diverticulosis (SCAD). *Curr Gastroenterol Rep* 2023; **25**: 130-133 [*RCA*] [PMID: 37129830 DOI: 10.1007/s11894-023-00871-y] [FullText] [Full Text(PDF)]
53 **Urquhart SA**, Ewy MW, Flicek KT, Fidler JL, Sheedy SP, Harmsen WS, Chedid VG, Coelho-Prabhu N. Clinical and Radiographic Characteristics in Segmental Colitis Associated With Diverticulosis, Diverticulitis, and Crohn's Disease. *Gastro Hep Adv* 2024; **3**: 901-909 [*RCA*] [PMID: 39286621 DOI: 10.1016/j.gastha.2024.06.002] [FullText] [Full Text(PDF)]
54 **Loper MR**, Makary MS. Evolving and Novel Applications of Artificial Intelligence in Abdominal Imaging. *Tomography* 2024; **10**: 1814-1831 [*RCA*] [PMID: 39590942 DOI: 10.3390/tomography10110133] [FullText] [Full Text(PDF)]
55 **Rogers W**, Thulasi Seetha S, Refaee TAG, Lieverse RIY, Granzier RWY, Ibrahim A, Keek SA, Sanduleanu S, Primakov SP, Beuque MPL, Marcus D, van der Wiel AMA, Zerka F, Oberije CJG, van Timmeren JE, Woodruff HC, Lambin P. Radiomics: from qualitative to quantitative imaging. *Br J Radiol* 2020; **93**: 20190948 [*RCA*] [PMID: 32101448 DOI: 10.1259/bjr.20190948] [FullText]
56 **Koç U**, Sezer EA, Özkaya YA, Yarbay Y, Beşler MS, Taydaş O, Yalçın A, Evrimler Ş, Kızıloğlu HA, Kesimal U, Atasoy D, Oruç M, Ertuğrul M, Karakaş E, Karademir F, Sebik NB, Topuz Y, Aktan ME, Sezer Ö, Aydın Ş, Varlı S, Akdoğan E, Ülgü MM, Birinci Ş. Elevating healthcare through artificial intelligence: analyzing the abdominal emergencies data set (TR_ABDOMEN_RAD_EMERGENCY) at TEKNOFEST-2022. *Eur Radiol* 2024; **34**: 3588-3597 [*RCA*] [PMID: 37947834 DOI: 10.1007/s00330-023-10391-y] [FullText]
57 **Ziegelmayer S**, Reischl S, Havrda H, Gawlitza J, Graf M, Lenhart N, Nehls N, Lemke T, Wilhelm D, Lohöfer F, Burian E, Neumann PA, Makowski M, Braren R. Development and Validation of a Deep Learning Algorithm to Differentiate Colon Carcinoma From Acute Diverticulitis in Computed Tomography Images. *JAMA Netw Open* 2023; **6**: e2253370 [*RCA*] [PMID: 36705919 DOI: 10.1001/jamanetworkopen.2022.53370] [FullText]
58 **Maguire LH**, Alavi K, Sudan R, Wise PE, Kaiser AM, Bordeianou L. Surgical Considerations in the Treatment of Small Bowel Crohn's Disease. *J Gastrointest Surg* 2017; **21**: 398-411 [*RCA*] [PMID: 27966058 DOI: 10.1007/s11605-016-3330-9] [FullText]

World Journal of Radiology

Submit a Manuscript: https://www.f6publishing.com

World J Radiol 2025 August 28; 17(8): 109447

DOI: 10.4329/wjr.v17.i8.109447

ISSN 1949-8470 (online)

MINIREVIEWS

Role of imaging in chronic otitis media and its complications

Kemal Bugra Memis, Sonay Aydin

Specialty type: Radiology, nuclear medicine and medical imaging

Provenance and peer review: Invited article; Externally peer reviewed.

Peer-review model: Single blind

Peer-review report's classification

Scientific Quality: Grade A, Grade A

Novelty: Grade B, Grade B

Creativity or Innovation: Grade B, Grade B

Scientific Significance: Grade A, Grade B

P-Reviewer: Slimi H, PhD, Associate Professor, Tunisia

Received: May 12, 2025

Revised: June 4, 2025

Accepted: July 31, 2025

Published online: August 28, 2025

Processing time: 109 Days and 11 Hours

Kemal Bugra Memis, Sonay Aydin, Department of Radiology, Faculty of Medicine, Erzincan Binali Yildirim University, Erzincan 24000, Basbaglar, Türkiye

Corresponding author: Kemal Bugra Memis, MD, Department of Radiology, Faculty of Medicine, Erzincan Binali Yıldırım University, No. 1429 Street, Erzincan 24000, Basbaglar, Türkiye. kemalbugramemis@gmail.com

Abstract

Chronic otitis media (COM) is a long-standing inflammatory condition affecting the middle ear and mastoid cavity, often resulting in progressive structural damage and functional deficits. Radiological imaging is fundamental in diagnosing the disease, assessing its severity, and identifying possible complications. The literature indicates that the prevalence rates of extracranial and intracranial complications range from 0.69% to 5%, while the mortality rate for intracranial complications is 26%. While magnetic resonance imaging is particularly useful in distinguishing soft tissue abnormalities and detecting intracranial extensions like meningitis, brain abscess, and sigmoid sinus thrombosis, high-resolution computed tomography remains the preferred modality for evaluating bony erosion, cholesteatoma, and mastoid involvement. Key complications such as ossicular chain destruction, facial nerve damage, and labyrinthine fistulae can be precisely identified using advanced imaging modalities, allowing for timely and effective surgical intervention. This minireview underscores the essential role of radiology in both diagnosing and managing COM, highlighting critical imaging findings that facilitate early detection and inform treatment decisions. A collaborative approach among radiologists, otolaryngologists, and infectious disease specialists is crucial for improving clinical outcomes in affected patients.

Key Words: Otomastoiditis; Intracranial complications; Temporal bone; Computed tomography; Magnetic resonance imaging; Diffusion-weight imaging

Core Tip: Chronic otitis media is a long-term inflammatory disease affecting the middle ear, which, if not properly managed, can result in both extracranial and intracranial complications. Magnetic resonance imaging is particularly valuable in assessing soft tissue involvement and distinguishing cholesteatomas from other inflammatory conditions, especially through the use of diffusion-weighted imaging (DWI). Recently, sensitivity of DWI in the diagnosis of cholestatoma was shown to be 88% and specificity of 96%. Meanwhile, high-resolution computed tomography remains the primary imaging modality for evaluating bony erosion, ossicular chain damage, and mastoid pathology, providing essential details for diagnosis and treatment planning.

Citation: Memis KB, Aydin S. Role of imaging in chronic otitis media and its complications. *World J Radiol* 2025; 17(8): 109447
URL: https://www.wjgnet.com/1949-8470/full/v17/i8/109447.htm
DOI: https://dx.doi.org/10.4329/wjr.v17.i8.109447

INTRODUCTION

Chronic otitis media (COM) is a long-standing inflammatory condition of the middle ear and mastoid cavity, often arising from untreated acute otitis media. It is typically characterized by a perforated tympanic membrane, persistent ear discharge, and gradual hearing loss. If left untreated, COM may lead to severe complications, both extracranially and intracranially. Early diagnosis and timely intervention are crucial to preventing these outcomes[1]. COM and its complications are still an important cause of mortality and morbidity. The latest research reveals that the prevalence of extracranial and intracranial complications varies between 0.69% and 5%. The mortality rate in patients with complications is 16.1% and in patients with intracranial complications is 26.3%[2,3]. The morbidity rate in patients who developed complications was 11.8%[3]. COM persists as a significant worldwide health problem, being the primary cause of preventable hearing impairment in developing nations. Global epidemiological studies indicate that around 300 million individuals are afflicted by COM, with over 85% of cases arising in low-income nations[4].

Extracranial complications of COM include mastoid abscess, Bezold abscess, facial nerve palsy, and labyrinthitis. Intracranial complications include brain abscess, meningitis, lateral sinus thrombophlebitis and extradural abscess[2,3]. While brain abscess is the most common intracranial complication, mastoid abscess is the most common extracranial complication[5]. Incidence of most seen intracranial and extracranial complications of COM depicted in Table 1.

Radiological imaging is indispensable in the comprehensive assessment of COM. The use of high-resolution computed tomography (HRCT) for examining the temporal bone remains the preferred method for evaluating bony changes in patients with COM[5,6]. HRCT is particularly effective in detecting bony erosions, cholesteatomas, scutum defects, and mastoid involvement, all of which play a significant role in surgical planning. Several studies emphasize the diagnostic value of HRCT in identifying cholesteatomas and assessing the extent of bony damage, which is critical for determining appropriate surgical interventions[6,7]. On the other hand, magnetic resonance imaging (MRI) is essential for evaluating soft tissue abnormalities and detecting complications extending to the intracranial space, such as brain abscesses and meningitis. Among its various techniques, diffusion-weighted imaging (DWI) stands out for its ability to differentiate cholesteatomas from other inflammatory or post-surgical changes. MRI also offers superior resolution for assessing facial nerve involvement and labyrinthine conditions, which are critical factors in treatment decisions. The combination of DWI and MRI with conventional computed tomography has been shown to significantly enhance diagnostic accuracy in cases of COM and its complications[8]. The pathophysiology of COM involves chronic bacterial infection, biofilm formation, and dysfunction of the Eustachian tube, all contributing to progressive tissue destruction. Complications, including ossicular chain erosion, labyrinthine fistulae, and facial nerve damage, can be precisely identified through HRCT and MRI. Early detection of these complications is essential for prompt intervention, ultimately improving patient outcomes [9].

ROLE OF HRCT IN DIAGNOSING COM AND ITS COMPLICATIONS

If left untreated, COM can lead to severe complications, including both extracranial and intracranial sequelae. Early diagnosis and intervention are crucial to prevent these adverse outcomes[6]. HRCT of the temporal bone is considered the gold standard for evaluating bony structures in patients with COM. It effectively detects ossicular chain erosion, cholesteatoma, scutum defects, and mastoid involvement, providing vital information for surgical planning. HRCT is particularly useful in identifying cholesteatoma and other bony abnormalities associated with COM[7]. Additionally, HRCT aids in assessing the extent of disease involvement, which is essential for determining the appropriate surgical approach. By providing detailed imaging of the temporal bone, HRCT enables clinicians to plan surgeries more effectively, potentially improving patient outcomes[10]. HRCT is instrumental in identifying complications such as mastoiditis, labyrinthitis, and facial nerve involvement. It can detect complications like facial nerve erosion and labyrinthine fistulae, which are critical for surgical planning[11]. While HRCT provides detailed bony imaging, it has limitations in assessing soft tissue involvement and intracranial complications. Therefore, combining HRCT with other imaging modalities, such as MRI, can offer a more comprehensive evaluation[12]. The HRCT protocol, thin sections (usually 0.625 to 1.25 mm) should be taken and the generation of images should be performed using a sharp algorithm

Table 1 Incidence of intracranial and extracranial complications of chronic otitis media

Complication	Type	Incidence (%)[1]
Brain abscess	Intracranial	18-42
Meningitis	Intracranial	21-72
Lateral sinus thrombosis	Intracranial	2-26
Extradural abscess	Intracranial	7-16
Mastoid abscess	Extracranial	40-68
Facial nerve paralysis	Extracranial	13-58
Labyrinthitis	Extracranial	7-34
Bezold abscess	Extracranial	5-10

[1]Data were obtained from Lin *et al*[2], Ahmad *et al*[3], and Penido Nde *et al*[5].

(*e.g.* bone algorithm). HRCT plays a pivotal role in the diagnosis and management of COM, offering detailed insights into bony structures and facilitating informed surgical decisions. Its ability to detect complications and assess the extent of disease involvement makes it an indispensable tool in the clinical evaluation of COM[10-12].

ROLE OF MRI IN DIAGNOSING COM AND ITS COMPLICATIONS

MRI has become a pivotal tool in evaluating soft tissue involvement in COM and detecting intracranial complications that may arise due to the disease. Unlike HRCT, which focuses on bony structures, MRI is particularly effective in assessing soft tissue changes, such as cholesteatoma and inflammation[8,12]. MRI, especially with the use of DWI, plays a crucial role in distinguishing between benign and malignant forms of cholesteatoma, which is critical for appropriate management[13]. The high sensitivity of DWI allows for the detection of cholesteatoma with great accuracy, even in cases where it might not be apparent on HRCT scans[12,13]. Additionally, MRI is indispensable for detecting intracranial complications, including brain abscesses, meningitis, and sigmoid sinus thrombosis, which can arise due to the spread of infection from the middle ear[14]. For patients with COM, MRI also assists in evaluating facial nerve involvement, labyrinthine fistulae, and ossicular chain erosion[15]. MRI can provide a comprehensive overview of both soft tissue and bony structures, allowing clinicians to assess the extent of disease and plan surgical interventions accordingly. This multidimensional capability of MRI helps in both preoperative planning and in monitoring post-treatment outcomes[12]. The signal-to-noise ratio of images obtained using multi-channel phased array coils is significantly improved. MRI offers significant advantages in diagnosing and managing COM and its complications. Its ability to assess soft tissue structures, detect cholesteatomas, and identify intracranial and extracranial complications makes it an essential modality in the comprehensive management of this condition[12-15].

ROLE OF COMBINED IMAGING APPROACH IN DIAGNOSING COM AND ITS COMPLICATIONS

In routine practice, the majority of centers employ a multimodal imaging strategy for diagnosing complications of COM. HRCT excels in evaluating the condition of the ossicular chain, mastoid ventilation, and bone degradation, whereas diffusion-weighted MRI sequences are particularly adept at distinguishing soft tissue lesions like cholesteatoma. A combined imaging technique integrates the advantages of both modalities to enhance diagnostic precision. As a result, the rationale for surgical planning is established with greater confidence. Unnecessary operations are prevented. The combined method yields significant success, particularly in identifying recurrent or persistent cholesteatomas. The integration of HRCT and MRI for the early detection and appropriate therapy of COM and its consequences is a crucial diagnostic approach in modern otological practice[12,16].

Figure 1 shows otomastoiditis and cholesteatoma in the right mastoid cells and middle ear cavity on contrast-enhanced temporal MRI of a 27-year-old male. Additionally, Figure 2 shows intracranial abscess, meningitis and subcutaneous abscess detected in the MRI examination of the same patient. Figure 3 shows findings consistent with labyrinthitis on T2W temporal MRI in a 38-year-old male patient diagnosed with COM. Figure 4 shows MRI of a 43-year-old female patient with COM showing findings of lateral sinus thrombosis extending to the sigmoid sinus.

CONCLUSION

COM and its complications pose significant challenges in both diagnosis and management, necessitating precise imaging

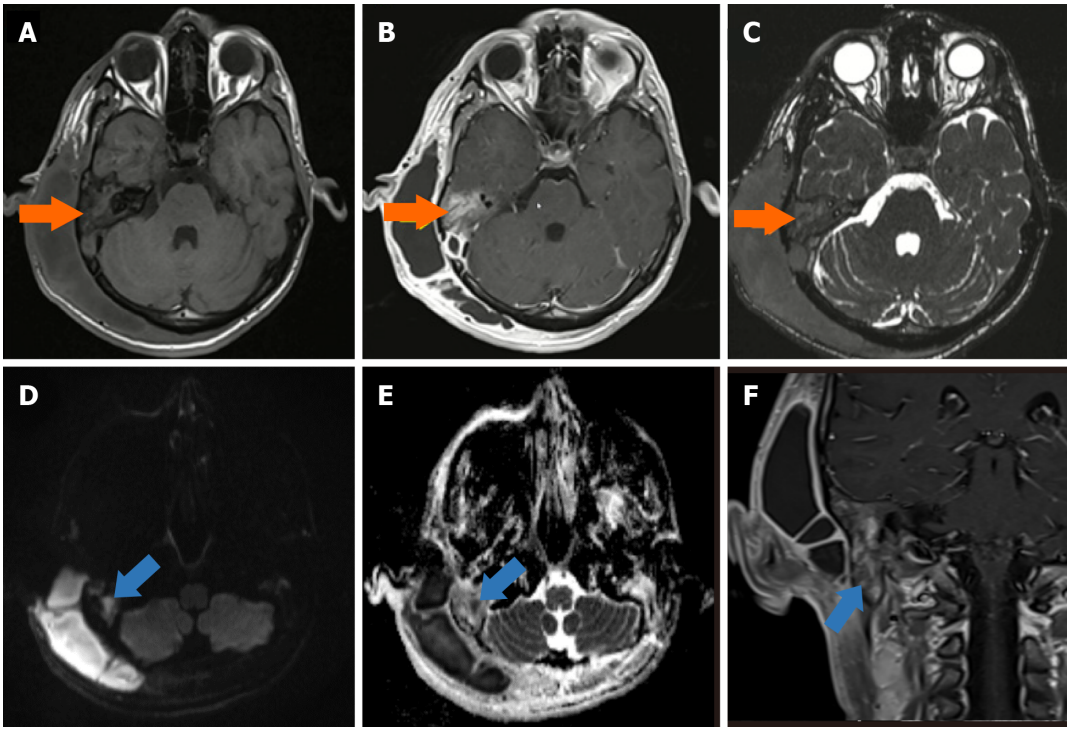

Figure 1 Otomastoiditis and accompanying cholesteatoma. A: The axial pre-contrast T1W; B: Post-contrast T1W; C: 3D-constructive interference in a steady state MR images show hyper-enhanced inflammatory alterations in the mastoid cells and middle ear on the right side (orange arrows); D: The axial diffusion-weighted; E: Apparent diffusion coefficient map; F: Coronal post-contrast T1W magnetic resonance images show the presence of cholesteatoma in the right inferior mastoid cells, which was not enhanced, but had significant diffusion restriction (blue arrows).

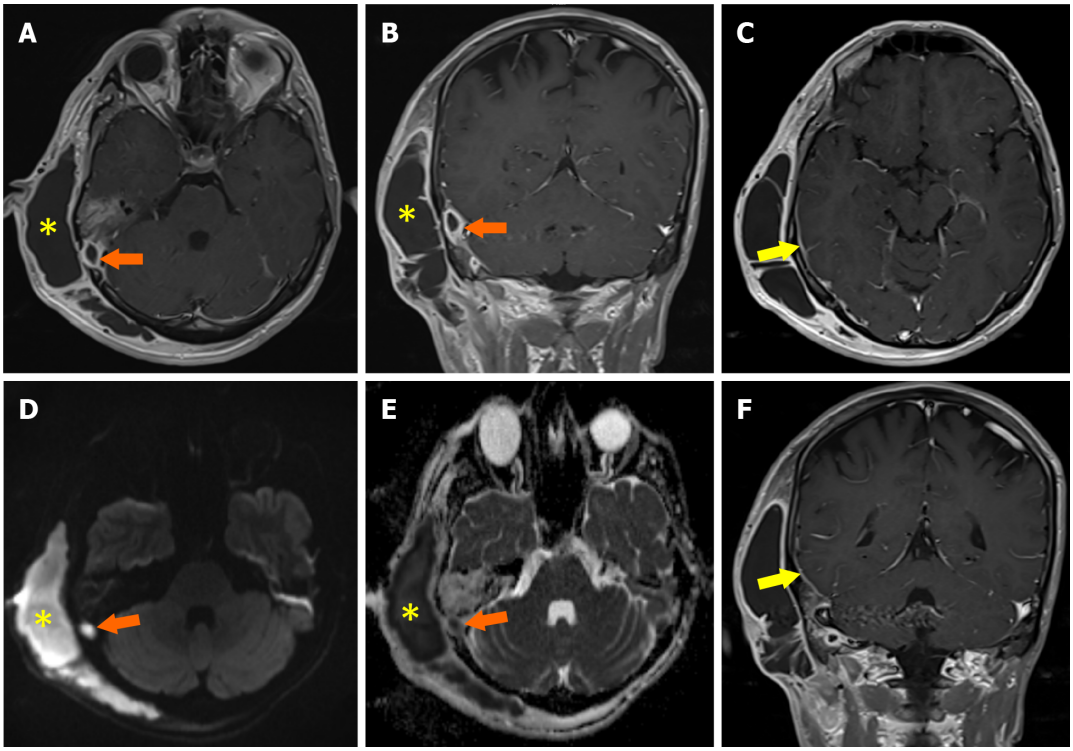

Figure 2 Meningitis with subcutaneous and intracranial abscess. A: The axial post-contrast T1W; B: Coronal post-contrast T1W; C: Axial post-contrast T1W; D: Axial diffusion-weighted; E: Apparent diffusion coefficient map; F: Coronal post-contrast T1W magnetic resonance images show abscesses in the subcutaneous adipose tissue (yellow asterisks) and intracranial (orange arrows) area with a thick and hyperenhanced wall and centrally restricted diffusion. The axial post-contrast T1W and coronal post-contrast T1W magnetic resonance images show meningeal enhancement compatible with meningitis in the right parietotemporal area (yellow arrows).

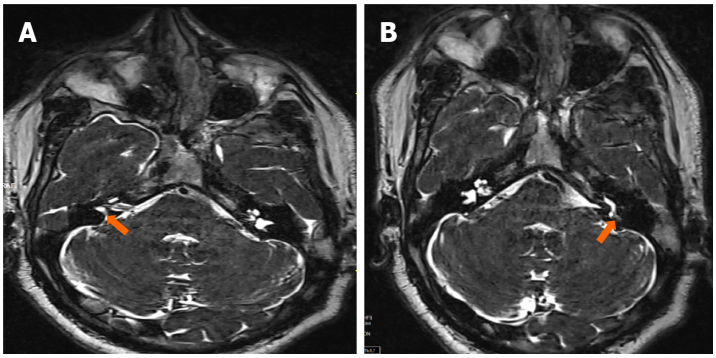

Figure 3 Labyrinthitis. A: The axial 3D-constructive interference in a steady state (CISS) magnetic resonance image showing focal signal loss in the vestibule (orange arrow) on right side; B: The axial 3D-CISS magnetic resonance image showing focal signal loss in the horizontal semicircular canal (orange arrow) on left side.

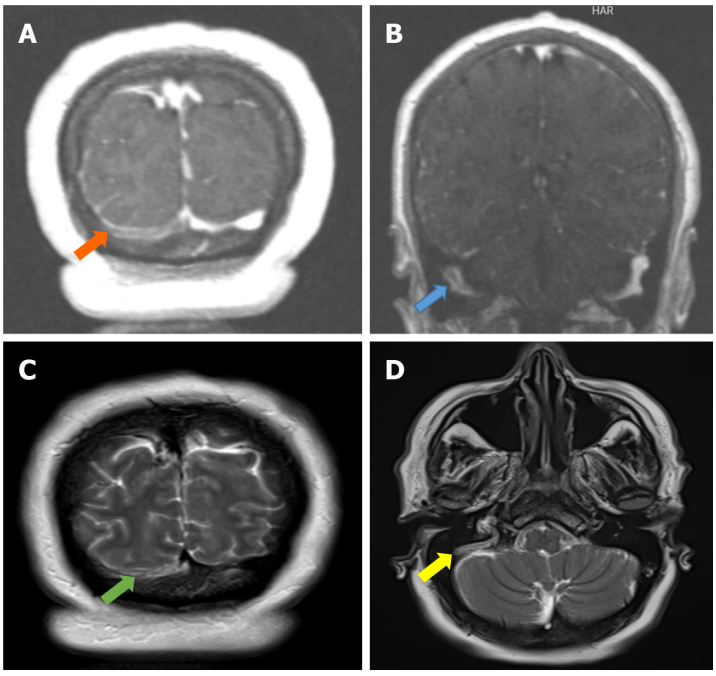

Figure 4 Lateral sinus thrombosis. A: The coronal post-contrast T1W cerebral magnetic resonance venography image shows loss of signal along the right transverse sinus (orange arrow); B: The coronal post-contrast T1W cerebral magnetic resonance venography image shows loss of signal along the right sigmoid sinus (blue arrow); C: The coronal T2W magnetic resonance image shows hyperintensity due to flow void loss in the right transverse sinus (green arrow); D: Axial T2W magnetic resonance image shows hyperintensity due to flow void loss in the right sigmoid sinus (yellow arrow).

techniques to ensure timely intervention. HRCT remains the preferred modality for evaluating bony erosion, mastoid involvement, and ossicular chain destruction, providing essential details for surgical planning. Meanwhile, MRI plays a crucial role in differentiating soft tissue abnormalities, particularly in distinguishing cholesteatomas from other inflammatory lesions, as well as identifying extracranial and intracranial complications. Early detection of these complications is vital in preventing severe morbidities, including hearing loss, facial nerve paralysis, and life-threatening infections such as meningitis and brain abscess. The integration of advanced imaging techniques, such as improved DWI sequences (*e.g.*, RESOLVE DWI), holds promise for further increasing diagnostic accuracy, reducing the need for unnecessary surgical interventions, and improving patient outcomes. As research continues to refine imaging protocols and enhance the sensitivity and specificity of radiological tools, the role of HRCT and MRI in the evaluation of COM is expected to become even more precise and indispensable. Future studies should focus on optimizing imaging methodologies to facilitate earlier diagnosis, better disease characterization, and more effective treatment planning, ultimately minimizing complications and improving the quality of life for affected individuals.

Finally, we recommend routine HRCT in all suspected unsafe CSOM cases and reserved MRI for suspected intracranial spread.

FOOTNOTES

Author contributions: Memis KB performed data acquisition and the majority of the writing, prepared the figures and tables; Aydin S provided the input in writing the paper, designed the outline and coordinated the writing of the paper.

Conflict-of-interest statement: The authors declare no conflict of interest.

Country of origin: Türkiye

ORCID number: Kemal Bugra Memis 0009-0007-6746-3906; Sonay Aydin 0000-0002-3812-6333.

S-Editor: Qu XL
L-Editor: A
P-Editor: Zhao S

REFERENCES

1 **Osma U**, Cureoglu S, Hosoglu S. The complications of chronic otitis media: report of 93 cases. *J Laryngol Otol* 2000; **114**: 97-100 [*RCA*] [PMID: 10748823 DOI: 10.1258/0022215001905012] [FullText]
2 **Lin YS**, Lin LC, Lee FP, Lee KJ. The prevalence of chronic otitis media and its complication rates in teenagers and adult patients. *Otolaryngol Head Neck Surg* 2009; **140**: 165-170 [*RCA*] [PMID: 19201282 DOI: 10.1016/j.otohns.2008.10.020] [FullText]
3 **Ahmad Z**, Zubair MY, Chandra K, Khalique N. A Study of Complications, Sinonasal Predispositions and Microbiological Profile of Chronic Otitis Media. *Indian J Otolaryngol Head Neck Surg* 2023; **75**: 403-408 [*RCA*] [PMID: 37206706 DOI: 10.1007/s12070-023-03512-y] [Full Text]
4 **Onifade A**, Katolo HW, Mookerjee S, Bhutta MF. Epidemiology of Chronic Suppurative Otitis Media: Systematic Review To Estimate Global Prevalence. *J Epidemiol Glob Health* 2025; **15**: 55 [*RCA*] [PMID: 40178730 DOI: 10.1007/s44197-025-00396-9] [FullText] [Full Text(PDF)]
5 **Penido Nde O**, Chandrasekhar SS, Borin A, Maranhão AS, Gurgel Testa JR. Complications of otitis media - a potentially lethal problem still present. *Braz J Otorhinolaryngol* 2016; **82**: 253-262 [*RCA*] [PMID: 26420564 DOI: 10.1016/j.bjorl.2015.04.007] [FullText] [Full Text(PDF)]
6 **Aljehani M**, Alhussini R. The Correlation Between Preoperative Findings of High-Resolution Computed Tomography (HRCT) and Intraoperative Findings of Chronic Otitis Media (COM). *Clin Med Insights Ear Nose Throat* 2019; **12**: 1179550619870471 [*RCA*] [PMID: 31452605 DOI: 10.1177/1179550619870471] [FullText] [Full Text(PDF)]
7 **Singh R**, Rai R, Singh P, Sethi S, Ahluwalia APS, Choudhary G. High-resolution computed tomography (HRCT) in pediatric and adult patients with unsafe chronic suppurative otitis media (CSOM) and its surgical correlation. *J Family Med Prim Care* 2020; **9**: 4067-4073 [*RCA*] [PMID: 33110811 DOI: 10.4103/jfmpc.jfmpc_455_20] [FullText] [Full Text(PDF)]
8 **Yorgancılar E**, Yildirim M, Gun R, Bakir S, Tekin R, Gocmez C, Meric F, Topcu I. Complications of chronic suppurative otitis media: a retrospective review. *Eur Arch Otorhinolaryngol* 2013; **270**: 69-76 [*RCA*] [PMID: 22249835 DOI: 10.1007/s00405-012-1924-8] [FullText]
9 **Khairkar M**, Deshmukh P, Maity H, Deotale V. Chronic Suppurative Otitis Media: A Comprehensive Review of Epidemiology, Pathogenesis, Microbiology, and Complications. *Cureus* 2023; **15**: e43729 [*RCA*] [PMID: 37727177 DOI: 10.7759/cureus.43729] [FullText]
10 **Mustafa A**, Heta A, Kastrati B, Dreshaj Sh. Complications of chronic otitis media with cholesteatoma during a 10-year period in Kosovo. *Eur Arch Otorhinolaryngol* 2008; **265**: 1477-1482 [*RCA*] [PMID: 18478242 DOI: 10.1007/s00405-008-0707-8] [FullText]
11 **Sun J**, Sun J. Intracranial complications of chronic otitis media. *Eur Arch Otorhinolaryngol* 2014; **271**: 2923-2926 [*RCA*] [PMID: 24162767 DOI: 10.1007/s00405-013-2778-4] [FullText]
12 **Popescu C**, Văruț RM, Puticiu M, Belghiru VI, Banicioiu M, Rotaru LT, Popescu M, Cosmin AC, Popescu AIS. Comprehensive Management of Cholesteatoma in Otitis Media: Diagnostic Challenges, Imaging Advances, and Surgical Outcome. *J Clin Med* 2024; **13**: 6791 [*RCA*] [PMID: 39597935 DOI: 10.3390/jcm13226791] [FullText] [Full Text(PDF)]
13 **Pant B**, Sharma N, Bahal N, Sammal M. Role of Non-Echo-Planar Diffusion Weighted MRI Imaging (DWI MRI) in Unsafe Chronic Otitis Media (CSOM): A Clinical Study at a Tertiary Care Center in Uttarakhand. *Indian J Otolaryngol Head Neck Surg* 2024; **76**: 5305-5311 [*RCA*] [PMID: 39559126 DOI: 10.1007/s12070-024-04967-3] [FullText]
14 **Tsilis NS**, Vlastarakos PV, Chalkiadakis VF, Kotzampasakis DS, Nikolopoulos TP. Chronic otitis media in children: an evidence-based guide for diagnosis and management. *Clin Pediatr (Phila)* 2013; **52**: 795-802 [*RCA*] [PMID: 23539681 DOI: 10.1177/0009922813482041] [Full Text]
15 **Hutz MJ**, Moore DM, Hotaling AJ. Neurological Complications of Acute and Chronic Otitis Media. *Curr Neurol Neurosci Rep* 2018; **18**: 11 [*RCA*] [PMID: 29445883 DOI: 10.1007/s11910-018-0817-7] [FullText]
16 **Burakgazi G**, Bayaroğullari H, Öztürk F, Arli C, Motor VK, Yanmaz R, Atci N. Radiological Imaging of Rare Intracranial Complications Secondary to Otitis Media and Mastoiditis. *J Craniofac Surg* 2017; **28**: 620-624 [*RCA*] [PMID: 28468135 DOI: 10.1097/SCS.0000000000003391] [FullText]

World Journal of Radiology

Submit a Manuscript: https://www.f6publishing.com

World J Radiol 2025 August 28; 17(8): 111065

DOI: 10.4329/wjr.v17.i8.111065

ISSN 1949-8470 (online)

ORIGINAL ARTICLE

Retrospective Cohort Study

Prognostic value of arterial spin-labeling perfusion in anoxic brain injury: A retrospective cohort study

Bryce D Beutler, Daniel Antwi-Amoabeng, Dane Weinert, Ishan Shah, Mark B Ulanja, Alastair E Moody, Xiaomeng Lei, Alexander Lerner, Mark S Shiroishi, Reza Assadsangabi

Specialty type: Radiology, nuclear medicine and medical imaging

Provenance and peer review: Invited article; Externally peer reviewed.

Peer-review model: Single blind

Peer-review report's classification

Scientific Quality: Grade C, Grade C

Novelty: Grade C, Grade C

Creativity or Innovation: Grade C, Grade D

Scientific Significance: Grade C, Grade C

P-Reviewer: Ren S, MD, PhD, Assistant Professor, Chief Physician, Postdoctoral Fellow, China; Yuksel S, MD, Full Professor, Türkiye

Received: June 24, 2025

Revised: July 4, 2025

Accepted: August 5, 2025

Published online: August 28, 2025

Processing time: 66 Days and 16.4 Hours

Bryce D Beutler, Dane Weinert, Alexander Lerner, Reza Assadsangabi, Department of Radiology, University of Southern California, Keck School of Medicine, Los Angeles, CA 90033, United States

Daniel Antwi-Amoabeng, Department of Internal Medicine, Christus Ochsner St. Patrick Hospital, Lake Charles, LA 70601, United States

Ishan Shah, Department of Neurosurgery, University of Southern California, Keck School of Medicine, Los Angeles, CA 90033, United States

Mark B Ulanja, Taussig Cancer Center, Cleveland Clinic, Cleveland, OH 44195, United States

Alastair E Moody, Department of Anesthesiology, University of Utah, Salt Lake, UT 84132, United States

Xiaomeng Lei, Department of Radiology, Keck School of Medicine of University of Southern California, Los Angeles, CA 90033, United States

Mark S Shiroishi, Department of Radiology, Los Angeles General Medical Center, Los Angeles, CA 90033, United States

Corresponding author: Bryce D Beutler, Academic Fellow, Department of Radiology, University of Southern California, Keck School of Medicine, 1500 San Pablo Street, Los Angeles, CA 90033, United States. brycebeutler@hotmail.com

Abstract

BACKGROUND

Anoxic brain injury is a potentially lethal condition characterized by cerebral hypoperfusion and irreversible neuronal injury. Arterial spin-labeling (ASL) perfusion and diffusion-weighted imaging (DWI) magnetic resonance imaging (MRI) have been proposed as tools to detect cerebral ischemic changes and may aid in the assessment of anoxic injury.

AIM

To explore the relationship between regional ASL perfusion patterns and clinical outcomes following cardiac arrest.

METHODS
We performed a retrospective review to identify patients with clinical suspicion of anoxic brain injury who underwent MRI within 15 days of cardiac arrest. Receiver operator characteristic (ROC) analysis and univariate logistic regression were used to evaluate associations between ASL perfusion scores, DWI signal intensity, and the following clinical features: (1) Myoclonus status epilepticus (MSE) within 24 hours; (2) Absent extensor or motor reflexes (EMR) at day 3 post-arrest; and (3) Absent brainstem reflexes (BSR) within 15 days.

RESULTS
Twenty-eight patients met inclusion criteria. Increased ASL signal in the left occipital lobe was significantly associated with MSE (P = 0.038), while a trend was observed between right frontal ASL signal and EMR (P = 0.078). ROC analysis showed that ASL scores ≥ 7 were associated with higher odds of absent BSR (OR 2.14, P = 0.53), though this did not reach statistical significance. DWI signal intensity did not show significant associations with clinical outcomes. The overall discriminatory performance of ASL for predicting outcomes was limited (AUC ≈ 0.52).

CONCLUSION
This exploratory study suggests that regional ASL hyperperfusion, particularly in the left occipital and right frontal lobes, may be associated with adverse clinical signs following cardiac arrest. However, most findings did not reach statistical significance, and the study was underpowered to detect small-to-moderate effects. These preliminary results should be interpreted with caution and considered hypothesis-generating. Larger, prospective studies are warranted to clarify the prognostic value of ASL perfusion imaging in anoxic brain injury.

Key Words: Arterial spin-labeling; Anoxic brain injury; Arterial spin-labeling perfusion; Diffusion weighted imaging; Diffusion-weighted imaging

Core Tip: Anoxic brain injury is a devastating clinical entity characterized by severe cerebral hypoperfusion with resultant neuronal cell death. Arterial spin-labeling (ASL) perfusion and diffusion-weighted imaging magnetic resonance imaging has recently been used to detect global and focal cerebral ischemic changes that may play a role in the assessment of anoxic brain injury. In this retrospective cohort study, we found that elevated ASL signal involving the left occipital lobe and right frontal lobe is predictive of poor outcomes, suggesting that ASL signal may have important prognostic implications in the setting of anoxic brain injury.

Citation: Beutler BD, Antwi-Amoabeng D, Weinert D, Shah I, Ulanja MB, Moody AE, Lei X, Lerner A, Shiroishi MS, Assadsangabi R. Prognostic value of arterial spin-labeling perfusion in anoxic brain injury: A retrospective cohort study. *World J Radiol* 2025; 17(8): 111065
URL: https://www.wjgnet.com/1949-8470/full/v17/i8/111065.htm
DOI: https://dx.doi.org/10.4329/wjr.v17.i8.111065

INTRODUCTION

Anoxic brain injury is a dynamic process characterized by cell swelling and oncotic cell death, which manifests as diffusion restriction on magnetic resonance imaging (MRI), and a later period of reperfusion injury and disruption of the blood-brain barrier, which may present as superphysiologic cerebral blood flow on arterial spin-labeling (ASL) perfusion sequences. The current prognostic tools and clinical prediction models rely primarily on correlation of patient history, neurological examination, and electroencephalography. However, as of this writing, imaging plays a limited role in predicting outcomes and likelihood of functional recovery.

There is emerging evidence that diffusion-weighted imaging (DWI) and ASL sequences can depict underlying pathophysiological processes that have important prognostic implications in the setting of anoxic brain injury. A retrospective study by Pollock *et al*[1] established that the presence of increased signal on both DWI and ASL sequences was predictive of unfavorable patient outcomes. In addition, although the sample size was relatively small, some patients who were found to have superphysiologic hyperperfusion on ASL sequences without corresponding diffusion restriction demonstrated relatively favorable outcomes with at least partial neurological recovery[1]. A subsequent study by Li *et al* [2] showed a positive relationship between ASL and DWI signal intensity. Authors hypothesized that anoxia manifests with regional diffusion restriction, likely related to cell swelling, and corresponding regional hyperperfusion, reflecting disruption of the blood-brain barrier and loss of autoregulation.

We aimed to evaluate the relationship between the pattern of diffusion restriction, cerebral hyperperfusion, and patient outcomes in the setting of anoxic brain injury. The identification of imaging findings predictive of patient outcomes could

help improve the accuracy and reliability of prognostication and ultimately inform management.

MATERIALS AND METHODS

Study design and population

We conducted a retrospective review of the electronic health record at our institution to identify participants with clinical suspicion of anoxic brain injury who underwent at least one MRI study within 15 days of cardiac arrest and subsequent return of spontaneous circulation (ROSC). The study period spanned from September 1, 2020 to July 1, 2022.

The study was approved by the Institutional Review Board of the University of Southern California, Keck School of Medicine.

Imaging protocols

All MRI studies were performed using a 1.5T General Electric scanner. The imaging protocols included ASL and DWI sequences. The ASL imaging parameters were as follows: Flip angle (FA) of 155 degrees, repetition time of 4885 ms, and echo time of 10.47 ms. For DWI, the parameters included a FA of 90 degrees and a b-value of 1000 s/mm^2.

Measurement techniques

ASL perfusion and DWI signal intensity was measured in twelve brain regions (bilateral frontal, parietal, temporal, and occipital lobes; thalami; and basal ganglia) by two independent observers. The observers used a region of interest (ROI) approach, selecting approximately 30 mm^2 areas for analysis (Figure 1). The mean and maximum signal intensity within each ROI was recorded and normalized using the signal intensity within the ipsilateral cerebellar hemisphere as an internal reference value.

Clinical data collection

Relevant clinical data were recorded for each patient, including the time from ROSC to the MRI, discharge disposition (*e.g.*, discharged home, transferred to a rehabilitation facility, or deceased), and changes in Glasgow Coma Scale (GCS) score from ROSC to disposition.

In addition, we assessed the presence of three established clinical parameters associated with unfavorable outcomes in anoxic brain injury.

Absent brainstem reflexes: Evaluated at any point within the 15 days following cardiac arrest.

Myoclonus status epilepticus: Assessed within the first day of cardiac arrest.

Absent pupil or corneal reflexes or absent extensor or motor reflexes: Assessed on day 3 post-arrest.

Statistical analysis

The mean and maximum ASL perfusion and DWI signal intensity was quantitatively assessed at 12 different brain regions using a 30 mm^2 ROI. A normalized scale was then constructed using the signal intensity within the ipsilateral cerebellar hemisphere as an internal reference value. Scores ranged from 0-12 based on the signal intensity within the selected brain region relative to the cerebellar hemisphere; a score of 0 represented ASL perfusion or DWI signal intensity equal to or lower than that of the ipsilateral cerebellar hemisphere while a score of 12 indicated ASL perfusion or DWI signal intensity markedly greater than that of the cerebellar hemisphere. Receiver operator characteristics (ROC) analysis was employed to evaluate the performance of ASL perfusion scores in predicting clinical outcomes. The optimal cutoff point was determined based on sensitivity and specificity analyses.

Univariate logistic regression was performed to assess the odds of the selected clinical parameters for scores above the optimal cutoff point. Confidence intervals (CI) and *P* values were calculated to provide statistical significance of the findings. Inter-rater reliability for ASL perfusion and DWI measurements was assessed using the intraclass correlation coefficient (ICC). Due to the small sample size and limited outcome events, multivariable modeling was not performed to adjust for potential confounders such as time from arrest to MRI or patient comorbidities. Univariate logistic regression was used to explore associations, with the recognition that confounding effects may influence results.

ROC curve analysis was used to evaluate the discriminative ability of ASL perfusion scores and DWI signal intensity for predicting unfavorable clinical outcomes, including absent brainstem reflexes (BSR) and myoclonus status epilepticus (MSE). Optimal cutoff values were determined by maximizing Youden's index.

Univariate logistic regression was employed to estimate odds ratios for clinical outcomes above or below the ASL cutoff scores. Given the small sample size and limited number of outcome events, multivariable models were not constructed to avoid model overfitting. As such, no adjustment for potential confounders [*e.g.*, age, time to MRI, targeted temperature management (TTM)] was performed. This approach was intended to preserve statistical stability and should be interpreted as exploratory.

All analyses were performed using complete-case data; no imputation methods were applied. Clinical and imaging variables were recorded prospectively and reviewed retrospectively to minimize missingness, and data were complete for all primary variables used in ROC and regression analyses.

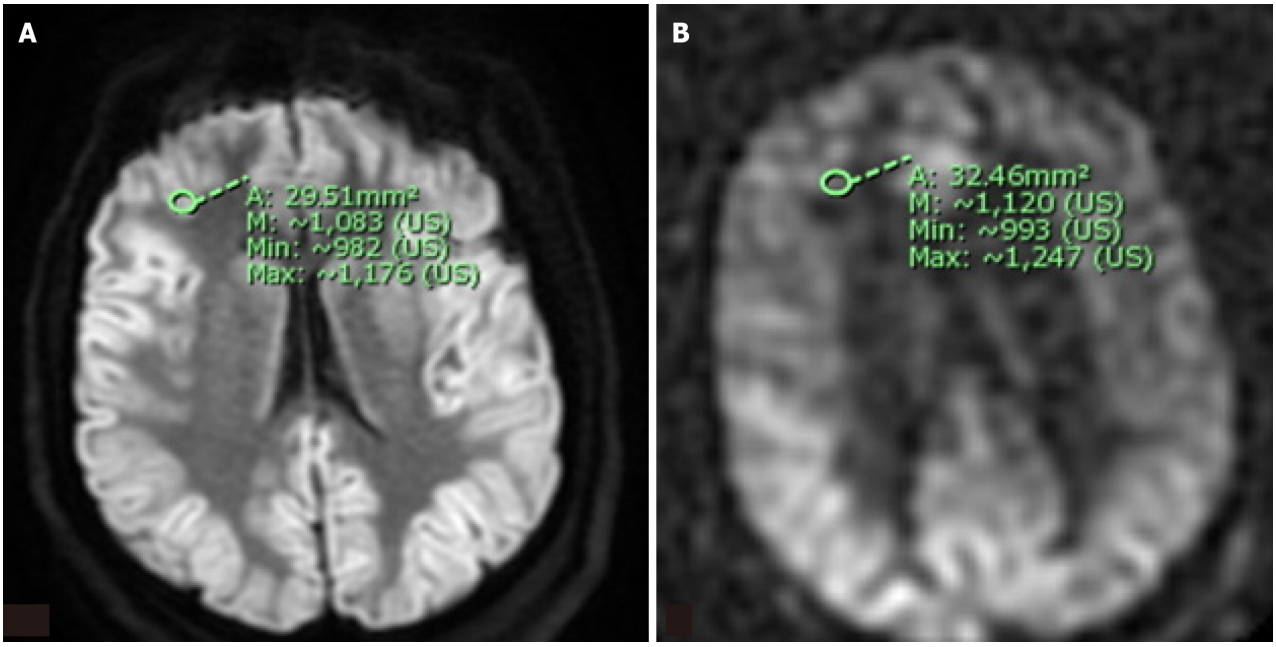

Figure 1 Representative diffusion weighted imaging and arterial spin-labeling sequences illustrating region of interest selection for semiquantiative analysis of signal intensity. A region of interest (ROI) measuring approximately 30 mm² areas was selected for each of twelve brain regions (bilateral frontal, parietal, temporal, and occipital lobes; thalami; and basal ganglia). The raw mean and maximum signal intensity within each ROI was recorded and normalized on a 0-12 point scale using the signal intensity within the ipsilateral cerebellar hemisphere as an internal reference value. A: A representative example of an ROI within the right frontal lobe on a diffusion weighted imaging sequence; B: A representative example of an ROI within the right frontal lobe on the corresponding arterial spin-labeling sequence.

RESULTS

A total of 28 patients (19 males, 9 females; mean age 58, range 26-84) were included in the analysis. The time between ROSC and MRI acquisition ranged from 3 to 16 days (mean time to acquisition: 6.2 days; median time to acquisition: 5 days). Electroencephalographic (EEG) findings included generalized burst suppression, triphasic waves, focal epilepitform discharges, generalized polyspike and slow wave epileptiform discharges, and most commonly, nonspecific diffuse slowing.

ROC analysis

The ROC analysis showed that ASL scores ≥ 7 were associated with a non-significant increase in the odds of absent BSR (OR 2.14, $P = 0.53$), with high specificity (100%) and negative predictive value (85.7%). However, this association did not reach statistical significance and should be interpreted as exploratory. In addition, ASL scores ≥ 7 showed a non-significant trend toward increased odds of MSE (OR 1.19, $P = 0.82$), with a sensitivity of 100% and a positive predictive value of 57.1%. This trend did not achieve statistical significance and is considered hypothesis-generating. The area under the ROC curve was 0.52 for ASL perfusion in predicting absent BSR and 0.52 for predicting MSE-values indicating no meaningful discriminatory power. These results suggest that the ASL score cutoff of ≥ 7 Lacks prognostic utility in this sample (Table 1).

Reliability metrics

The ICC for raw ASL was 0.63, indicating moderate reliability between observers, while normalized ASL showed poor reliability (ICC 0.21). For DWI, the ICC was 0.86 for raw data and 0.74 for normalized data, reflecting high inter-observer agreement.

The low inter-rater reliability for normalized ASL signal intensity is likely attributable to the variability introduced by the normalization strategy. We selected the ipsilateral cerebellar hemisphere as an internal reference region in an effort to control for patient-level and scanner-level differences in perfusion signal intensity, a method previously described in cerebral perfusion imaging literature. However, this reference region may itself be affected in global hypoperfusion states, such as post-anoxic injury, introducing inconsistency across measurements. Additionally, while ROI placement was guided by consistent anatomical landmarks and involved approximately 30 mm² areas, subtle differences in manual placement can disproportionately impact normalized values-especially in cortical regions with low perfusion or heterogeneous signal.

Correlation between ASL and DWI

The Pearson correlation between ASL and DWI revealed a moderate positive relationship in the frontal lobe (0.53-0.68, $P < 0.05$) and a low positive correlation in the temporal, parietal, and occipital lobes (0.36-0.49, $P < 0.05$). Normalized data

Table 1 Statistically significant associations between arterial spin-labeling signal intensity, arterial spin-labeling-diffusion-weighted imaging correlation, and patient outcomes

Variable/region	Finding	*P* value
Right occipital lobe	↑ ASL in late subacute scans	< 0.05
Left parietal lobe	↑ ASL in those with absent BSR	< 0.05
Occipital/temporal lobes	↓ ASL in those with absent EMR	< 0.05
ASL-DWI correlation (frontal, occipital, *etc.*)	Positive correlation	< 0.05

ASL: Arterial spin-labeling; BSR: Absent brainstem reflexes; DWI: Diffusion-weighted imaging; EMR: Absent extensor or motor reflexes.

showed a low-moderate positive correlation in the frontal and occipital lobes (0.39-0.56, $P < 0.05$) (Figure 2).

Clinical variables and ASL signal intensity

ASL signal intensity analysis related to clinical variables revealed higher signal intensity in the right occipital lobe for late subacute scans compared to early subacute scans ($P < 0.05$). There were no significant differences in ASL signal intensity between patients with and without changes in GCS ($n = 10$ *vs* 18), between those transferred and those who died in the hospital ($n = 9$ *vs* 19), or between those with and without MSE within the first day of arrest ($n = 16$ *vs* 12). However, patients with absent BSRs at any point within the 15 days following survived cardiac arrest (no *vs* yes, $n = 24$ *vs* 4) had higher mean intensity in the left parietal lobe ($P < 0.05$).

Patients with absent pupil or corneal reflexes or absent extensor or motor reflexes (EMR) at day 3 post-arrest (no *vs* yes, $n = 9$ *vs* 18) had lower intensity in occipital lobes and mean intensity in temporal lobes ($P < 0.05$).

The mean ASL perfusion signal intensity in the left frontal lobe showed good performance for predicting MSE (AUC = 0.7552). In addition, the mean ASL perfusion signal intensity in the right frontal lobe demonstrated good performance for predicting absent BSR (AUC = 0.7251) (Figure 3A and B). The relationship between ASL perfusion signal intensity and outcomes is summarized in Table 1.

The mean DWI signal intensity averaged across all 12 brain regions showed better performance for predicting absent BSR as compared to ASL perfusion signal intensity (Figure 3C). A detailed visual summary of the study population, methodology, and statistically significant findings is shown in Figure 4.

Power analysis

A post hoc power analysis was conducted to evaluate the statistical power of the study given the sample size of 28 patients. For the ROC analysis evaluating the predictive performance of ASL perfusion in the left frontal lobe for MSE (AUC = 0.76), the estimated power was approximately 70%-75% at a significance level of 0.05. In contrast, the analysis predicting absent BSRs using right frontal ASL perfusion (AUC = 0.73) had lower power (approximately 45%-55%) due to the small number of patients with this outcome ($n = 4$). These findings suggest moderate power to detect associations in some comparisons, but limited power in others, particularly those with low event rates.

Clinical heterogeneity and subgroup analyses

Although the criteria for MSE, EMR, and BSR were defined using established prognostic standards, we acknowledge that clinical heterogeneity across patients may influence outcome interpretation. Factors such as targeted TTM, sedative use, and EEG patterns can affect the timing and reliability of these prognostic signs.

To explore these effects, subgroup analyses were performed. Among the 28 patients, 14 (50%) received TTM following cardiac arrest. Within this subgroup, no statistically significant differences in ASL perfusion scores were observed compared to non-TTM patients, though the small sample size limits interpretability. Similarly, EEG patterns were available in 24 patients. Of these, 8 exhibited generalized burst suppression, 5 had epileptiform discharges (polyspike or focal), and 11 showed diffuse slowing. ASL perfusion scores were descriptively higher in patients with epileptiform activity, but these differences did not reach statistical significance. These findings highlight the complexity of prognosticating anoxic brain injury and underscore the need to account for clinical modifiers such as TTM and EEG background. The lack of significant differences may reflect limited power rather than true absence of effect. Larger, prospective studies with stratified enrollment are warranted to better evaluate the interaction between perfusion imaging and these clinical variables.

DISCUSSION

Anoxic brain injury, defined as irreversible neuronal damage secondary to prolonged hypoxia or anoxia, is a leading cause of death and disability in the United States and worldwide, affecting hundreds of thousands of individuals annually. The prognosis is dire. Survivors face poor functional outcomes while family members often confront profound economic hardship associated with prolonged inpatient rehabilitation and round-the-clock care[3,4].

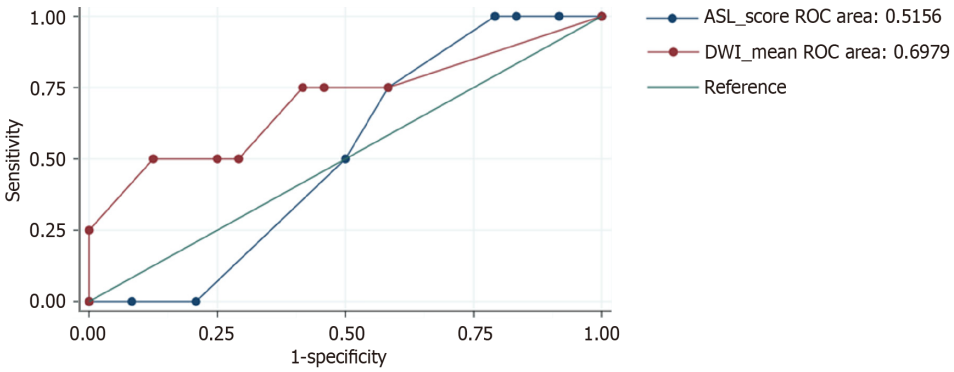

Figure 2 Relationship between arterial spin-labeling and diffusion-weighted imaging signal intensity. There was a moderate positive relationship in the frontal lobe (0.53-0.68, $P < 0.05$) and a low positive correlation in the temporal, parietal, and occipital lobes (0.36-0.49, $P < 0.05$). Normalized data showed a low-moderate positive correlation in the frontal and occipital lobes. ROC: Receiver operator characteristic.

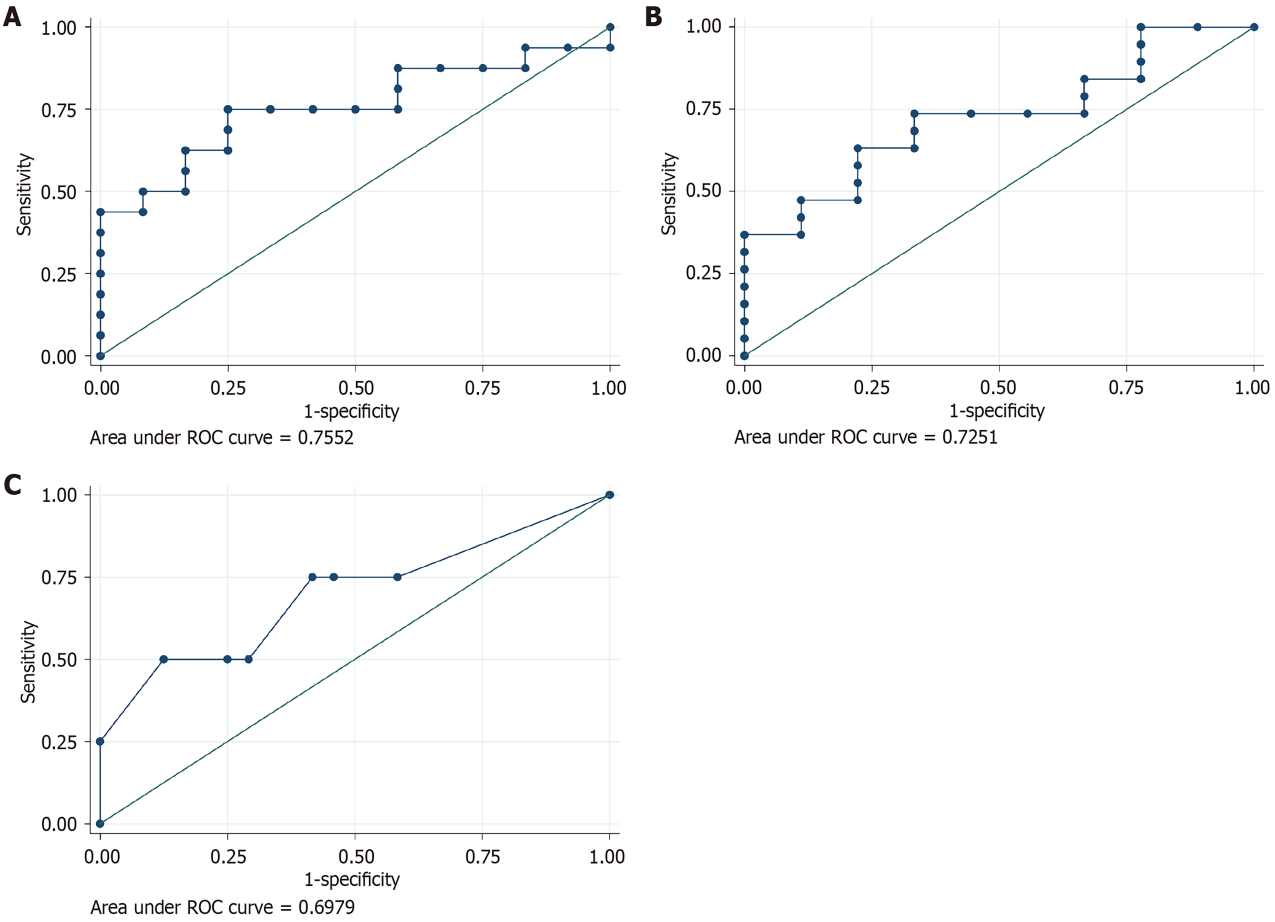

Figure 3 Relationship between arterial spin-labeling and diffusion weighted imaging signal intensity and patient outcomes. A: Relationship between arterial spin-labeling (ASL) signal intensity within the left frontal lobe and likelihood of within one day of anoxic brain injury; B: Relationship between ASL signal intensity within the right frontal lobe and likelihood of absent brainstem reflexes (BSR) during the course of hospitalization; C: Relationship between diffusion weighted imaging signal intensity and likelihood of absent BSR during the course of hospitalization.

Cardiac arrest represents the most common underlying cause of anoxic brain injury, accounting for the vast majority of cases[5]. However, any pathophysiologic process that results in diminished cerebral blood flow-including drug overdose, stroke, toxic exposure, asphyxiation, and trauma-can lead to anoxic brain injury[6]. A diagnosis is established based on correlation of clinical history, neurologic examination, electroencephalography, and laboratory studies[7].

The prognosis of patients with anoxic brain injury varies based on age, the severity of insult, and the duration of hypoxia or anoxia, among other factors. However, as of this writing, there are no validated criteria that can reliably predict patient outcomes. Clinical manifestations of anoxic brain injury that are highly suggestive of poor outcomes include loss of BSRs, status myoclonus, and a GCS motor score of two or lower[8,9]. Somatosensory evoked potentials may also have prognostic value; limited data suggest that an absent electrical response within the bilateral median nerves

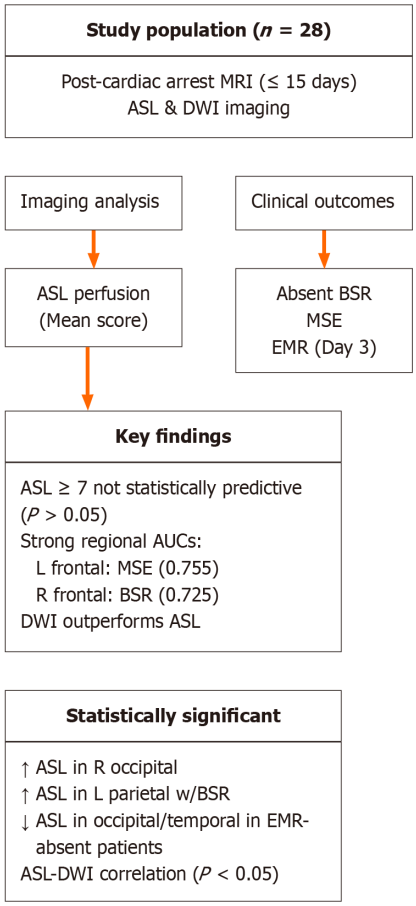

Figure 4 Visual summary of the study population, methodology, and key exploratory findings. A total of 28 patients were included in the analysis. Clinical outcomes of interest included absent brainstem reflexes (BSR), myoclonus status epilepticus (MSE), and absent extensor or motor reflexes. While certain regional arterial spin-labeling (ASL) perfusion patterns-such as left frontal ASL signal with MSE and right frontal ASL signal with BSR-showed relatively higher area under the curve values, these associations did not reach statistical significance and should be interpreted cautiously. Diffusion-weighted imaging demonstrated relatively better predictive performance compared to ASL in this limited cohort. BSR: Brainstem reflexes; MSE: Myoclonus status epilepticus; EMR: Absent extensor or motor reflexes; ASL: Arterial spin-labeling; AUC: Area under the curve; DWI: Diffusion-weighted imaging; MRI: Magnetic resonance imaging.

is highly specific for poor neurological outcomes[10]. High serum neuron-specific enolase and S-100B values may portend a poor prognosis, but the data are inconsistent, and specific cutoff values remain to be established[8,11].

There are two distinct mechanisms by which anoxia causes reversible or irreversible brain injury in the setting of cardiac arrest or any other medical event that reduces cerebral perfusion. In the first phase of anoxic brain injury, interruption of cellular aerobic metabolism results in adenosine triphosphate depletion and failure of the transmembrane sodium-potassium pump, which in turn leads to an overwhelming influx of sodium and water and consequent cell swelling. The increased cell volume reduces the extracellular space by an order of magnitude, preventing the free diffusion of water molecules; increased signal on diffusion weighted MRI sequences represents the imaging manifestation of the oncotic cell death pathway[12]. In the central nervous system, astrocytic swelling is significantly more pronounced relative to neuronal swelling, and thus the presence of diffusion restriction within the brain does not necessarily indicate irreversible neuronal loss[13]. The second phase of anoxic brain injury is characterized by the activation of homeostatic physiologic mechanisms, often aided by cardiopulmonary resuscitation, resulting in postischemic hyperperfusion. Increased blood flow within the cerebrovascular bed produces a neuroinflammatory cascade, mediated by microglia and circulating leukocytes, and activation of proteases and phospholipases that cause further neuronal damage[14,15].

Neuroimaging, including computed tomography (CT), MRI, and positron emission tomography, plays a central role in the assessment of patients with suspected anoxic brain injury. A CT scan is typically acquired shortly after presentation to exclude intracranial hemorrhage, mass effect, large territory infarct, of any other potential precipitating cause of anoxia or hypoxia. However, CT scan is of limited value for assessing patient prognosis. Other neuroimaging modalities, such as MRI, are significantly more sensitive and specific to evaluate the extent of anoxic brain injury.

DWI and fluid-attenuated inversion recovery (FLAIR) MRI sequences have emerged as powerful predictive tools for individuals who have suffered anoxic brain injury. In a 2010 prospective study by Choi *et al*[16], authors found that a pattern of diffusion restriction involving the cortex and deep gray nuclei was associated with poor outcomes, whereas the absence of diffusion abnormalities within these regions indicated a high probability of at least partial neurological recovery. Quantitative analysis of diffusion abnormalities using apparent diffusion coefficient (ADC) sequences has also be used to predict patient outcomes. In a prospective study by Wijman *et al*[17], investigators assessed the value of ADC signal intensity to predict survival and functional outcomes using the validated Glasgow Outcome Scale (GOS). Patients

were divided into three groups: Death at six months; GOS score of 3 at six months, indicating severe disability; or a GOS score of 4 or 5 at six months, indicating some degree of neurological recovery with only mild to moderate disability. Authors concluded that the volume of brain parenchyma with an ADC value below 650 × 10^{-6} mm^2/sec correlated with the risk of death; patients with a high percentage of brain tissue below the ADC threshold were significantly less likely to survive than those with values above the ADC threshold. Authors also found that survivors with ADC values greater than 450 × 10^{-6} mm^2/sec were significantly more likely than those with lower ADC values to experience a favorable functional outcome[17]. Notably, the Wijman group acquired imaging between two and five days after the initial event that precipitated anoxic brain injury, as previous studies have shown that DWI and ADC values evolve during the first 48 hours of anoxia and may not depict the full extent of injury[18,19].

A qualitative scoring system developed by Hirsch *et al*[20] that incorporates DWI and FLAIR signal characteristics was recently shown to predict outcomes in patients with anoxic brain injury. In a 2015 study that included 68 patients who presented after cardiac arrest, investigators assessed the prognostic value of a scoring system based on lesion location and degree of DWI and FLAIR signal abnormality. A high total score based on the qualitative signal intensity within the cortex was up to 63% sensitive and 100% specific for prediction of unfavorable outcomes. The sensitivity increased to 84% when correlated with known predictors of poor outcomes, including absent motor reflexes and somatosensory evoked potentials. Authors concluded that integration of the imaging-based scoring system with established clinical parameters could help reliably predict patient outcomes in the setting of anoxic brain injury.

It has recently been hypothesized that postischemic hyperperfusion can be detected and quantified using ASL perfusion sequences. In a 2008 retrospective study by Pollock *et al*[1], authors showed that pulsed ASL perfusion sequences reliably demonstrated global cerebral hyperperfusion in the setting of anoxic brain injury. Diffusion restriction was present in most patients and was often diffuse, involving the cortices, basal ganglia, or watershed territories. Notably, of the four patients who survived in the Pollock study, two were found to have global hyperperfusion on pulsed ASL perfusion sequences without evidence of concomitant diffusion restriction, suggesting that there may be some prognostic significance to the pattern of superphysiologic cerebral perfusion relative to diffusion restriction on imaging. In a subsequent study by Li *et al*[2], authors described a homogeneously positive relationship between ASL and DWI signal intensity in patients with anoxic brain injury, with discrete regional ASL perfusion abnormalities corresponding to areas of diffusion restriction. Authors proposed that coexistent regional hyperperfusion and diffusion restriction may reflect disruption of the blood-brain barrier and aberrant autoregulation in areas of high demand.

The results of our analysis are consistent with those described by Pollock *et al*[1] and suggest that DWI and ASL perfusion MRI sequences may play a role in predicting patient outcomes in anoxic brain injury. Although our study was underpowered to establish statistical significance, there were several observations that may be clinically meaningful and warrant further examination. First, there was a direct correlation between mean DWI signal intensity and the likelihood of absent BSR following the anoxic event, suggesting that global elevation in DWI signal intensity may predict poor outcomes. Second, patients who presented with MSE within 24 hours of anoxic brain injury were found to have elevated ASL perfusion signal intensity within the left frontal lobe, which indicates that ASL perfusion sequences may be assessed alongside physical examination and electroencephalography to confirm suspected MSE. Third, there was a direct correlation between ASL perfusion signal intensity within the right frontal lobe and the likelihood of absent BSR on day three post-anoxic brain injury; these findings suggest that a frontal lobe ASL perfusion signal abnormality may be related to outcomes, although a larger sample size would again be required to establish statistical significance.

One of the novel contributions of this study is the observation that increased ASL perfusion signal intensity in the frontal lobes-particularly the left frontal lobe-was associated with the presence of MSE following cardiac arrest. While prior work has described global hypoperfusion or posterior-predominant changes in anoxic brain injury, few studies have investigated focal hyperperfusion patterns and their clinical significance. Our findings suggest that frontal ASL hyperintensity may reflect selective regional vulnerability or excitotoxic cortical hyperactivity related to seizure activity, which may not be evident on conventional structural imaging. Although the ROC performance was moderate (AUC = 0.76), this association warrants further investigation, especially in the context of perfusion-based prognostication strategies. These results, if validated, could help identify a subset of patients with poor neurologic prognosis and support earlier risk stratification.

We propose that qualitative or semiquantitative assessment of ASL signal intensity may have prognostic significance if there is concurrent diffusion restriction, with higher ASL signal intensity relative to an internal control indicating a higher likelihood of an unfavorable outcome or death. While clinical examination and EEG remain central to prognostication following cardiac arrest, these modalities can be limited by sedation, metabolic derangements, or technical variability. ASL perfusion imaging offers a noninvasive, quantitative method to assess regional cerebral blood flow, which may provide supplementary information-particularly in patients with unclear or suppressed neurological findings. In our cohort, increased frontal lobe ASL signal was associated with MSE, a clinical marker of poor prognosis, suggesting that ASL may help identify cortical hyperexcitability or early neurovascular uncoupling. Although these findings are preliminary, the integration of ASL into a multimodal prognostic algorithm could enhance confidence in early decision-making, especially when clinical signs are ambiguous or discordant. However, in the absence of diffusion restriction, ASL signal intensity may be of limited value for prognostication. Indeed, ASL signal characteristics should be interpreted with caution and correlated with the clinical history and other imaging findings. Global or regional ASL hyperintense signal can be seen in hepatic encephalopathy, posterior reversible encephalopathy syndrome, and migraines, among other etiologies, and the presence of superphysiologic cerebral blood flow does not necessarily indicate anoxic injury[21-24].

There are several limitations of our study. The sample size was small and few patients experienced functional or neurological recovery. A larger sample size would allow for a more precise ASL signal value threshold to predict unfavorable outcomes. Although an ASL score ≥ 7 was associated with higher odds of absent BSR and MSE, the ROC analysis demonstrated poor discriminatory performance for these outcomes (AUCs of 0.52 and 0.52, respectively), and the

results were not statistically significant. These findings suggest that the ASL cutoff score in this cohort lacked sufficient sensitivity or specificity for reliable clinical use. Given the small sample size and low event rates, the apparent trends may reflect statistical noise rather than a true association. Accordingly, these results should be interpreted with caution and considered hypothesis-generating rather than confirmatory. Larger studies are needed to validate any potential perfusion-based thresholds in post-anoxic injury prognostication. In addition, other causes of elevated ASL signal intensity, such as luxury reperfusion related to hypoperfusion-related infarct, could not be definitively excluded. Image quality was acceptable but somewhat degraded by motion artifact in some patients and it is possible that ASL perfusion signal intensity within the predefined structures was over- or underestimated in some cases. All imaging in this study was conducted on a 1.5T General Electric MRI scanner, which may limit the generalizability of our findings to studies performed at 3.0T or on scanners from other manufacturers. While 3.0T systems typically offer higher signal-to-noise ratios and improved spatial resolution, they may also introduce increased susceptibility effects and variability in ASL quantification parameters. These technical differences can affect both perfusion signal intensity and normalization metrics. As such, validation of our results across different field strengths and platforms will be important to confirm the clinical applicability of ASL-based prognostication in broader settings.

One additional limitation of this study was the low inter-rater reliability for normalized ASL signal intensity. This may be due in part to variability introduced by the normalization process, which used the ipsilateral cerebellar hemisphere as the internal reference region. While cerebellar normalization is a commonly used method to account for inter-individual and scanner-related signal differences in ASL studies[25], it can be problematic in post-arrest patients where diffuse hypoperfusion or cerebellar involvement may compromise its stability as a reference. Additionally, manual ROI placement-although anatomically guided-may have introduced variability, especially in regions with low or heterogeneous perfusion. Small discrepancies in ROI positioning could disproportionately affect normalized values due to signal scaling. In future studies, adopting a consistent and structurally preserved reference region, such as the pons or occipital cortex, may help reduce variability and improve reproducibility[26]. Automated or atlas-based segmentation may also offer a more objective approach to ROI definition. These methodological refinements may strengthen the reliability of normalized ASL measures and should be considered in subsequent validation studies.

CONCLUSION

Our analysis provides important insight into the value of ASL perfusion and DWI sequences for the prediction of patient outcomes in anoxic brain injury. In addition, our findings provide a framework for future analyses and suggest that careful examination of ASL perfusion signal intensity within the frontal lobes may have prognostic significance. Given the limited sample size and the exploratory nature of this study, the observed trends should be interpreted with caution. Most associations between ASL or DWI signal intensity and clinical outcomes did not reach statistical significance, and the analyses were underpowered to detect modest effects. While some regional ASL patterns-such as frontal hyperperfusion associated with MSE-appear promising, these findings require confirmation in larger studies. Our results should be considered hypothesis-generating and may help guide the design of future prospective trials investigating perfusion imaging as a prognostic tool in post-anoxic brain injury.

FOOTNOTES

Author contributions: Beutler BD writing original draft; data curation; Antwi-Amoabeng D and Ulanja MB formal analysis and data curation; Weinert D conceptualization and data curation; Shah I formal analysis, writing review and editing; Moody AE writing review and editing and validation; Lei X formal analysis and validation; Lerner A conceptualization; Shiroishi MS writing review and editing; Assadsangabi R conceptualization; supervision.

Institutional review board statement: This study was approved by the Institutional Review Board of the University of Southern California, Keck School of Medicine, with a waiver of informed consent granted due to its retrospective design and use of de-identified patient data.

Informed consent statement: This study was approved by the Institutional Review Board of the University of Southern California, Keck School of Medicine, with a waiver of informed consent granted due to its retrospective design and use of de-identified patient data.

Conflict-of-interest statement: The authors declare no actual or potential conflicts of interest.

Data sharing statement: The data that support the findings of this study are available from the corresponding author upon reasonable request.

STROBE statement: The authors have read the STROBE Statement-checklist of items, and the manuscript was prepared and revised according to the STROBE Statement-checklist of items.

Country of origin: United States

ORCID number: Bryce D Beutler 0000-0002-5071-1826; Daniel Antwi-Amoabeng 0000-0001-8594-004X; Mark B Ulanja 0000-0001-5966-3966; Alastair E Moody 0000-0002-5232-7705; Xiaomeng Lei 0000-0001-8899-5177.

S-Editor: Qu XL
L-Editor: A
P-Editor: Lei YY

REFERENCES

1 **Pollock JM**, Whitlow CT, Deibler AR, Tan H, Burdette JH, Kraft RA, Maldjian JA. Anoxic injury-associated cerebral hyperperfusion identified with arterial spin-labeled MR imaging. *AJNR Am J Neuroradiol* 2008; **29**: 1302-1307 [*RCA*] [PMID: 18451089 DOI: 10.3174/ajnr.A1095] [FullText]
2 **Li N**, Wingfield MA, Nickerson JP, Pettersson DR, Pollock JM. Anoxic Brain Injury Detection with the Normalized Diffusion to ASL Perfusion Ratio: Implications for Blood-Brain Barrier Injury and Permeability. *AJNR Am J Neuroradiol* 2020; **41**: 598-606 [*RCA*] [PMID: 32165356 DOI: 10.3174/ajnr.A6461] [FullText]
3 **Nichol G**, Stiell IG, Hebert P, Wells GA, Vandemheen K, Laupacis A. What is the quality of life for survivors of cardiac arrest? A prospective study. *Acad Emerg Med* 1999; **6**: 95-102 [*RCA*] [PMID: 10051899 DOI: 10.1111/j.1553-2712.1999.tb01044.x] [FullText]
4 **Burke DT**, Shah MK, Dorvlo AS, Al-Adawi S. Rehabilitation outcomes of cardiac and non-cardiac anoxic brain injury: a single institution experience. *Brain Inj* 2005; **19**: 675-680 [*RCA*] [PMID: 16195180 DOI: 10.1080/02699050400024953] [FullText]
5 **Laver S**, Farrow C, Turner D, Nolan J. Mode of death after admission to an intensive care unit following cardiac arrest. *Intensive Care Med* 2004; **30**: 2126-2128 [*RCA*] [PMID: 15365608 DOI: 10.1007/s00134-004-2425-z] [FullText]
6 **Messina Z**, Hays Shapshak A, Mills R. Anoxic Encephalopathy. 2023 Jan 28. In: StatPearls [Internet]. Treasure Island (FL): StatPearls Publishing; 2025 Jan- [PMID: 30969655] [FullText]
7 **Ramiro JI**, Kumar A. Updates on management of anoxic brain injury after cardiac arrest. *Mo Med* 2015; **112**: 136-141 [*RCA*] [PMID: 25958659] [FullText]
8 **Horn J**, Cronberg T, Taccone FS. Prognostication after cardiac arrest. *Curr Opin Crit Care* 2014; **20**: 280-286 [*RCA*] [PMID: 24717695 DOI: 10.1097/MCC.0000000000000085] [FullText]
9 **Wijdicks EF**, Hijdra A, Young GB, Bassetti CL, Wiebe S; Quality Standards Subcommittee of the American Academy of Neurology. Practice parameter: prediction of outcome in comatose survivors after cardiopulmonary resuscitation (an evidence-based review) [RETIRED]: report of the Quality Standards Subcommittee of the American Academy of Neurology. *Neurology* 2006; **67**: 203-210 [*RCA*] [PMID: 16864809 DOI: 10.1212/01.wnl.0000227183.21314.cd] [FullText]
10 **Cronberg T**, Brizzi M, Liedholm LJ, Rosén I, Rubertsson S, Rylander C, Friberg H. Neurological prognostication after cardiac arrest--recommendations from the Swedish Resuscitation Council. *Resuscitation* 2013; **84**: 867-872 [*RCA*] [PMID: 23370163 DOI: 10.1016/j.resuscitation.2013.01.019] [FullText]
11 **Sandroni C**, Cavallaro F, Callaway CW, D'Arrigo S, Sanna T, Kuiper MA, Biancone M, Della Marca G, Farcomeni A, Nolan JP. Predictors of poor neurological outcome in adult comatose survivors of cardiac arrest: a systematic review and meta-analysis. Part 2: Patients treated with therapeutic hypothermia. *Resuscitation* 2013; **84**: 1324-1338 [*RCA*] [PMID: 23831242 DOI: 10.1016/j.resuscitation.2013.06.020] [FullText]
12 **Liang D**, Bhatta S, Gerzanich V, Simard JM. Cytotoxic edema: mechanisms of pathological cell swelling. *Neurosurg Focus* 2007; **22**: E2 [*RCA*] [PMID: 17613233 DOI: 10.3171/foc.2007.22.5.3] [FullText] [Full Text(PDF)]
13 **Lafrenaye AD**, Simard JM. Bursting at the Seams: Molecular Mechanisms Mediating Astrocyte Swelling. *Int J Mol Sci* 2019; **20**: 330 [*RCA*] [PMID: 30650535 DOI: 10.3390/ijms20020330] [FullText] [Full Text(PDF)]
14 **Bhalala US**, Koehler RC, Kannan S. Neuroinflammation and neuroimmune dysregulation after acute hypoxic-ischemic injury of developing brain. *Front Pediatr* 2014; **2**: 144 [*RCA*] [PMID: 25642419 DOI: 10.3389/fped.2014.00144] [FullText] [Full Text(PDF)]
15 **Sandroni C**, Cronberg T, Sekhon M. Brain injury after cardiac arrest: pathophysiology, treatment, and prognosis. *Intensive Care Med* 2021; **47**: 1393-1414 [*RCA*] [PMID: 34705079 DOI: 10.1007/s00134-021-06548-2] [FullText] [Full Text(PDF)]
16 **Choi SP**, Park KN, Park HK, Kim JY, Youn CS, Ahn KJ, Yim HW. Diffusion-weighted magnetic resonance imaging for predicting the clinical outcome of comatose survivors after cardiac arrest: a cohort study. *Crit Care* 2010; **14**: R17 [*RCA*] [PMID: 20152021 DOI: 10.1186/cc8874] [FullText] [Full Text(PDF)]
17 **Wijman CA**, Mlynash M, Caulfield AF, Hsia AW, Eyngorn I, Bammer R, Fischbein N, Albers GW, Moseley M. Prognostic value of brain diffusion-weighted imaging after cardiac arrest. *Ann Neurol* 2009; **65**: 394-402 [*RCA*] [PMID: 19399889 DOI: 10.1002/ana.21632] [FullText] [Full Text(PDF)]
18 **Hald JK**, Brunberg JA, Dublin AB, Wootton-Gorges SL. Delayed diffusion-weighted MR abnormality in a patient with an extensive acute cerebral hypoxic injury. *Acta Radiol* 2003; **44**: 343-346 [*RCA*] [PMID: 12752010 DOI: 10.1080/j.1600-0455.2003.00050.x] [FullText]
19 **Greer DM**. MRI in anoxic brain injury. *Neurocrit Care* 2004; **1**: 213-215 [*RCA*] [PMID: 16174918 DOI: 10.1385/NCC:1:2:213] [FullText]
20 **Hirsch KG**, Mlynash M, Jansen S, Persoon S, Eyngorn I, Krasnokutsky MV, Wijman CA, Fischbein NJ. Prognostic value of a qualitative brain MRI scoring system after cardiac arrest. *J Neuroimaging* 2015; **25**: 430-437 [*RCA*] [PMID: 25040353 DOI: 10.1111/jon.12143] [Full Text]
21 **Li Y**, Liu H, Yang J, Tian X, Yang H, Geng Z. Combining arterial-spin labeling with functional magnetic resonance imaging measurement for characterizing patients with minimal hepatic encephalopathy. *Hepatol Res* 2017; **47**: 862-871 [*RCA*] [PMID: 27717156 DOI: 10.1111/hepr.12827] [FullText]
22 **Weinstein JD**, Hamam O, Urrutia VC, Lu H, Luna LP, Tekes-Brady A, Bahouth M, Yedavalli V. Added Value of Arterial Spin Labeling in

Detecting Posterior Reversible Encephalopathy Syndrome as a Stroke Mimic on Baseline Neuroimaging: A Single Center Experience. *Front Neurol* 2022; **13**: 831218 [*RCA*] [PMID: 35309569 DOI: 10.3389/fneur.2022.831218] [FullText] [Full Text(PDF)]

23 **Pollock JM**, Deibler AR, Burdette JH, Kraft RA, Tan H, Evans AB, Maldjian JA. Migraine associated cerebral hyperperfusion with arterial spin-labeled MR imaging. *AJNR Am J Neuroradiol* 2008; **29**: 1494-1497 [*RCA*] [PMID: 18499796 DOI: 10.3174/ajnr.A1115] [FullText]

24 **Zhang XD**, Zhang LJ, Wu SY, Lu GM. Multimodality magnetic resonance imaging in hepatic encephalopathy: an update. *World J Gastroenterol* 2014; **20**: 11262-11272 [*RCA*] [PMID: 25170210 DOI: 10.3748/wjg.v20.i32.11262] [FullText] [Full Text(PDF)]

25 **Alsop DC**, Detre JA, Golay X, Günther M, Hendrikse J, Hernandez-Garcia L, Lu H, MacIntosh BJ, Parkes LM, Smits M, van Osch MJ, Wang DJ, Wong EC, Zaharchuk G. Recommended implementation of arterial spin-labeled perfusion MRI for clinical applications: A consensus of the ISMRM perfusion study group and the European consortium for ASL in dementia. *Magn Reson Med* 2015; **73**: 102-116 [*RCA*] [PMID: 24715426 DOI: 10.1002/mrm.25197] [FullText]

26 **Mutsaerts HJ**, Steketee RM, Heijtel DF, Kuijer JP, van Osch MJ, Majoie CB, Smits M, Nederveen AJ. Inter-vendor reproducibility of pseudo-continuous arterial spin labeling at 3 Tesla. *PLoS One* 2014; **9**: e104108 [*RCA*] [PMID: 25090654 DOI: 10.1371/journal.pone.0104108] [Full Text] [Full Text(PDF)]

World Journal of Radiology

Submit a Manuscript: https://www.f6publishing.com

World J Radiol 2025 August 28; 17(8): 109373

DOI: 10.4329/wjr.v17.i8.109373

ISSN 1949-8470 (online)

ORIGINAL ARTICLE

Retrospective Study

Developing and validating a computed tomography radiomics strategy to predict lymph node metastasis in pancreatic cancer

Shuai Ren, Bin Qin, Marcus J Daniels, Liang Zeng, Ying Tian, Zhong-Qiu Wang

Specialty type: Radiology, nuclear medicine and medical imaging

Provenance and peer review: Invited article; Externally peer reviewed.

Peer-review model: Single blind

Peer-review report's classification

Scientific Quality: Grade C

Novelty: Grade C

Creativity or Innovation: Grade C

Scientific Significance: Grade C

P-Reviewer: Li SF

Received: May 12, 2025

Revised: May 21, 2025

Accepted: July 22, 2025

Published online: August 28, 2025

Processing time: 110 Days and 23.5 Hours

Shuai Ren, Bin Qin, Liang Zeng, Ying Tian, Zhong-Qiu Wang, Department of Radiology, Jiangsu Province Hospital of Chinese Medicine, Affiliated Hospital of Nanjing University of Chinese Medicine, Nanjing 210029, Jiangsu Province, China

Marcus J Daniels, Department of Radiology, NYU Langone Health, New York, NY 10016, United States

Corresponding author: Zhong-Qiu Wang, MD, Deputy Director, Head, Professor, Department of Radiology, Jiangsu Province Hospital of Chinese Medicine, Affiliated Hospital of Nanjing University of Chinese Medicine, No. 155 Hanzhong Road, Nanjing 210029, Jiangsu Province, China. zhongqiuwang@njucm.edu.cn

Abstract

BACKGROUND

Lymph node metastasis (LNM) is a key prognostic factor in pancreatic cancer (PC). Accurate preoperative prediction of LNM remains challenging. Radiomics offers a noninvasive method to extract quantitative imaging features that may aid in predicting LNM.

AIM

To investigate the potential value of a computed tomography (CT)-based radiomics model in prediction of LNM in PC.

METHODS

A retrospective analysis was performed on 168 pathologically confirmed PC patients who underwent contrast-enhanced-CT. Among them, 107 cases had no LNM, while 61 cases had confirmed LNM. These patients were randomly divided into a training cohort (n = 135) and a validation cohort (n = 33). A total of 792 radiomics features were extracted, comprising 396 features from the arterial phase and another 396 from the portal venous phase. The Minimum Redundancy Maximum Relevance and Least Absolute Shrinkage and Selection Operator methods were used for feature selection and Radiomics model construction. The receiver operating characteristic curve was employed to assess the diagnostic potential of the model, and DeLong test was used to compare the area under the curve (AUC) values of the model.

RESULTS

Six radiomics features from the arterial phase and nine from the portal venous

phase were selected. The Radscore model demonstrated strong predictive performance for LNM in both the training and test cohorts, with AUC values ranging from 0.86 to 0.94, sensitivity between 66.7% and 91.7%, specificity from 71.4% to 100.0%, accuracy between 78.8% and 91.1%, PPV ranging from 64.7% to 100.0%, and negative predictive value between 84.0% and 93.8%. No significant differences in AUC values were observed between the arterial and portal venous phases in either the training or test set.

CONCLUSION
The preoperative CT-based radiomics model exhibited robust predictive capability for identifying LNM in PC.

Key Words: Computed tomography; Radiomics; Lymph node metastasis; Pancreatic cancer; Model construction

Core Tip: A preoperative computed tomography-based radiomics model demonstrates high accuracy in predicting lymph node metastasis (LNM) in pancreatic cancer, providing a non-invasive tool to guide personalized treatment. Unlike traditional imaging, radiomics detects microstructural patterns invisible to the human eye, enhancing LNM detection irrespective of phase (arterial *vs* portal). Clinically, this model could refine preoperative staging, identify candidates for curative surgery, or prioritize neoadjuvant chemotherapy for high-risk patients, optimizing outcomes. Prospective validation is needed for broader adoption.

Citation: Ren S, Qin B, Daniels MJ, Zeng L, Tian Y, Wang ZQ. Developing and validating a computed tomography radiomics strategy to predict lymph node metastasis in pancreatic cancer. *World J Radiol* 2025; 17(8): 109373
URL: https://www.wjgnet.com/1949-8470/full/v17/i8/109373.htm
DOI: https://dx.doi.org/10.4329/wjr.v17.i8.109373

INTRODUCTION

Pancreatic cancer (PC) stands as a formidable challenge in the landscape of oncology, renowned for its aggressive nature, late diagnosis, and dismal prognosis[1,2]. Among the various factors influencing the course of the disease, lymph node metastasis (LNM) plays a pivotal role in determining treatment strategies, prognosis, and patient outcomes[3]. LNM occurs when cancer cells from the primary tumor migrate to nearby lymph nodes *via* the lymphatic system. In PC, lymph node involvement is frequent and has a significant impact on both disease staging and prognosis. The presence of LNM is indicative of disease progression and often signifies a more advanced stage of PC. The staging of PC, as defined by the Tumor, Node, Metastasis classification system, heavily relies on the presence or absence of LNM. Patients with lymph node involvement are typically categorized as having advanced-stage disease (*e.g.*, stage III or IV), indicating a poorer prognosis compared to those with localized disease. The extent of LNM, such as the number and size of involved nodes, further influences prognostication. Previous studies have shown that patients with no LNM report 5-year survival rates of up to 40%, whereas those with LNM have a survival rate of less than 10%[4,5].

Detection of LNM profoundly influences treatment decisions in patients with PC. Patients with localized disease and no lymph node involvement may be candidates for curative-intent surgical resection, which offers the best chance of long-term survival[6]. However, the presence of LNM may necessitate neoadjuvant chemotherapy (NAC) or radiation therapy to downstage the disease, or palliative interventions to alleviate symptoms and improve quality of life[7,8].

LNM serves as a predictive marker for disease recurrence in patients with PC. Even after surgical resection of the primary tumor, the presence of metastatic spread to regional lymph nodes increases the risk of locoregional recurrence and distant metastasis. Close surveillance and NAC may be recommended for patients with LNM to monitor recurrence and improve survival outcomes. Previous reports have indicated that PC patients with potentially resectable cancers who underwent NAC followed by curative surgery exhibited improved survival and longer time to recurrence[6-8]. This is particularly notable for those with LNM, underscoring the importance of a pre-treatment diagnosis of LNM as a critical determinant for developing a more personalized treatment strategy in PC patients[9].

Computed tomography (CT) imaging emerges as a primary tool for assessing LNM, offering detailed anatomical visualization and the ability to identify suspicious lymph nodes based on size, morphology, and enhancement characteristics[10]. Advancements in CT technology and imaging protocols have further enhanced its diagnostic accuracy and clinical utility in LNM detection. Multidetector CT scanners, contrast-enhanced (CE) imaging techniques, and functional imaging parameters enable improved visualization and characterization of lymphatic spread, facilitating more precise staging and treatment planning. Additionally, the integration of artificial intelligence and machine learning algorithms holds great promise for enhancing the sensitivity and specificity of CT-based lymph node detection algorithms.

In recent years, the field of radiomics has emerged as a promising approach for extracting quantitative data from medical images to aid in diagnosis, prognosis, and treatment planning[11,12]. Radiomics enables the analysis of tumor characteristics at a much finer level than what is visible to the human eye, allowing for the identification of subtle patterns, textures, and biomarkers that may be indicative of tumor behavior, response to treatment, or overall patient

outcomes[13]. The integration of radiomics into clinical practice has the potential to revolutionize cancer care by providing non-invasive, quantitative insights into tumor biology and behavior, leading to more informed decision-making and improved patient outcomes[14]. In this paper, we investigated the potential value of a preoperative CT-based radiomics model in predicting LNM in PC.

MATERIALS AND METHODS

Patients

This study was approved by the institutional review board and patient informed consent was waived due to its retrospective nature. All eligible patients were consecutively recruited from the author's hospital between January 2019 and January 2022 and informed consent was waived due to its retrospective nature. Inclusion criteria were as follows: (1) Histopathologically confirmed diagnosis of PC; (2) Preoperative imaging indicated resectable disease, excluding those with American Joint Committee on Cancer stage T4[15]; (3) Had ≥ 15 Lymph nodes harvested during surgery to ensure adequate pathological evaluation[16]; and (4) Underwent CE-CT within 30 days prior to surgery. Exclusion criteria were as follows: (1) Absence of CE-CT within 30 days prior to surgery; (2) Incomplete clinical data, histopathological results, or undefined tumor staging; (3) Poor CT image quality unsuitable for tumor segmentation; and (4) Received NAC or radiotherapy before CT imaging. Finally, a total of 168 patients with PC were enrolled in this study, as illustrated in Figure 1. The cases were divided into training and test cohorts (n = 135 and n = 33, respectively) using an 8:2 stratified random sampling method.

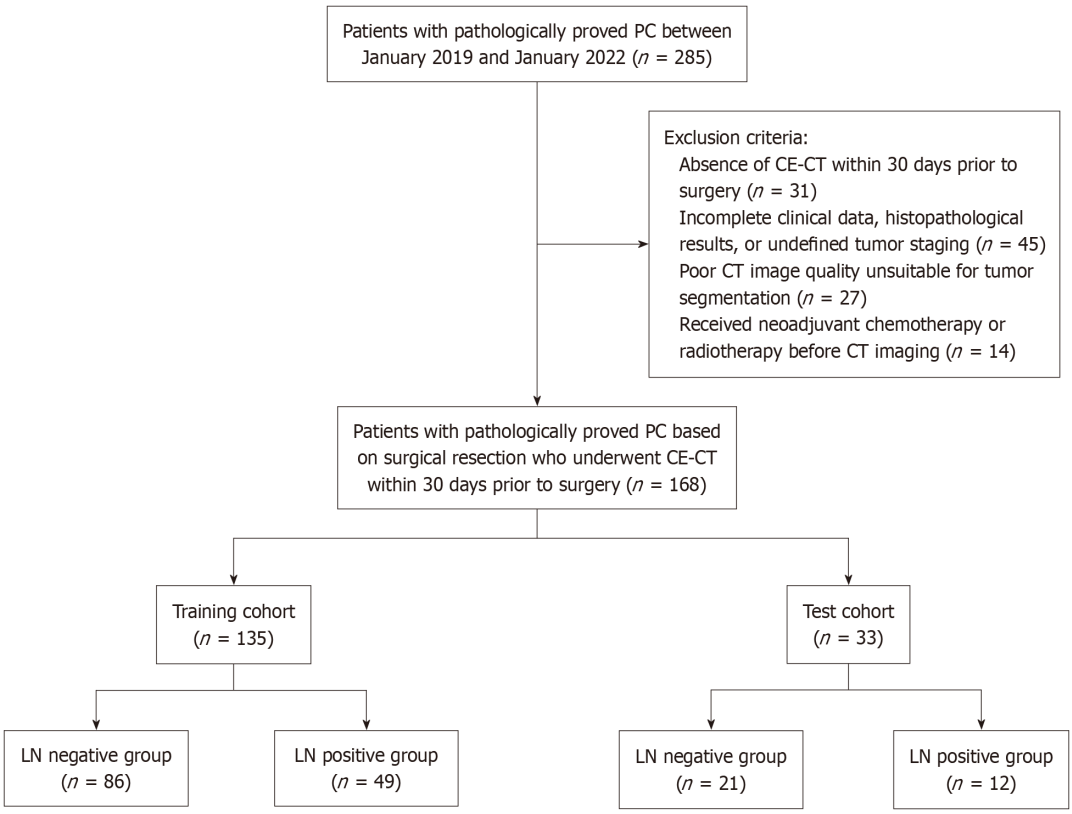

Figure 1 Flowchart of patient selection for the study. PC: Pancreatic cancer; CE-CT: Contrast-enhanced computed tomography; LN: Lymph node.

CT examination

All patients underwent a triple-phase CT scan, which included the precontrast, late arterial, and portal venous phases. The CT scanning was conducted using one of the following scanners: (1) GE Optima 670 (GE Healthcare, Tokyo, Japan); (2) GE LightSpeed VCT 64 (GE HealthCare, Milwaukee, Wisconsin, United States); and (3) Philips Brilliance 64 (Philips Healthcare, DA Best, the Netherlands). The scan parameters included a tube voltage of 120 Kvp, tube current ranging from 200 to 400 mAs, helical pitch between 0.984 and 1.375, and a reconstruction slice thickness of 1.0 mm with an interval of 1.0 mm. An administration of 100-120 mL of nonionic contrast media (Omnipaque 350, Bayer Pharmaceuticals) was performed at a rate of 3.0-4.0 mL/second following the precontrast CT scan. The late arterial and portal venous phases were acquired at 35 seconds and 70 seconds, respectively.

Tumor segmentation

Three-dimensional regions of interest (ROIs) were manually delineated on thin-slice CT images during the late arterial and portal venous phases using ITK-SNAP software (version 3.6.0; http://www.itksnap.org/pmwiki/pmwiki.php). Radiologist 1, who has 9 years of abdominal imaging experience and 6 years of tumor segmentation experience involving 221 patients with confirmed pancreatic diseases[11,17], performed the initial ROI delineations along the tumor margins. To assess reproducibility, the intraclass correlation coefficient (ICC) was calculated for intra-observer agreement. Thirty patients were randomly selected, and their ROIs were redelineated by radiologist 1 and by a second radiologist, who has 5 years of abdominal imaging experience and 2 years of tumor segmentation experience, after a 4-week interval. Both radiologists were blinded to the LNM status to reduce bias. An ICC value of 0.75 or higher was considered indicative of good agreement and retained for further analysis.

Feature extraction and selection

All radiomics features were normalized using z-score normalization prior to feature extraction and selection, which helps reduce variability due to differences in scanner parameters and acquisition protocols. The ICC was used to assess the repeatability of each radiomics feature, both intra- and inter-observer. In our study, only the features with ICC values greater than 0.75 were included. To reduce dimensionality and remove redundant or irrelevant features, we employed a two-stage selection approach, first applying minimum redundancy maximum relevance (MRMR), followed by least absolute shrinkage and selection operator (LASSO). Initially, MRMR was performed to eliminate redundant and irrelevant features, resulting in the retention of 30 features. Subsequently, LASSO was conducted to select the optimized subset of features to construct the final model.

Construction and validation of the model

The Radscore was calculated by applying linear weighting to the selected features identified by the LASSO algorithm. The diagnostic efficacy of the model for predicting LNM was assessed using receiver operating characteristic (ROC) curve analysis. The area under the ROC curve (AUC) with 95%CI, along with specificity, sensitivity, accuracy, negative predictive value (NPV), and positive predictive value (PPV), were utilized to evaluate the diagnostic performance of the radiomics models. Additionally, decision curve analysis was employed to assess the radiomics model by calculating the net benefit at different threshold probabilities.

Statistical analysis

Statistical analysis was conducted using SPSS v.24 (IBM Corp., Chicago, IL, United States) and R software v.3.6.1. Non-normally distributed data were compared between groups using the Mann-Whitney *U* test, while normally distributed continuous data were analyzed using Student's *t*-test after confirming normality. Normal data were presented as mean ± SD, and categorical data were reported as counts and percentages. The χ^2 test was applied to compare categorical variables between groups. Inter-observer reproducibility of radiomics features was assessed using the ICC, with coefficients greater than 0.75 indicating good reproducibility. The diagnostic performance of the radiomics model was evaluated using ROC curve analysis. The DeLong test was employed to compare the AUC values of the Radscore model in predicting LNM in PC. A significance level of $P < 0.05$ was considered statistically significant.

RESULTS

Patient and tumor characteristics

A total of 168 PC patients were ultimately enrolled in this study. The characteristics of PC patients with and without LNM are summarized in Table 1. No significant differences were observed between the two groups in terms of age, gender, clinical symptoms, or tumor markers.

Feature extraction and selection

The Analysis Kit software (version V3.0.0.R, GE Healthcare) was utilized to extract a total of 792 radiomics features from each patient's ROIs, with 396 features obtained from the late arterial phase and another 396 from the portal venous phase. These radiomics features, extracted from each phase of CT imaging, encompassed various categories, including 42 histogram features, 9 morphological features, 144 grey level co-occurrence matrix features, 11 grey level size zone matrix features, 180 grey level run-length matrix features, and 10 Haralick features. The MRMR and LASSO algorithms were employed to identify the most informative subset of features from the original set. As a result, 6 features from the late arterial phase and 9 features from the portal venous phase were selected for subsequent analysis, as shown in Figure 2A and B. Following the determination of the number of features using MRMR and LASSO methods, we selected the most predictive subset of features and evaluated the corresponding coefficients, as depicted in Figure 2C and D.

Development and validation of CT-based radiomics model

The Radscore was calculated by summing the selected features weighted by their coefficients. For the late arterial phase: Radscore = 0.653 * original_shape_Flatness + 0.132 * original_shape_Sphericity + -0.256 * original_firstorder_10Percentile + -0.411 * original_firstorder_Median + 0.164 * original_glszm_LargeAreaHighGrayLevelEmphasis + 1.217 * original_ngtdm_Coarseness + -0.2. For the portal venous phase: Radscore = 1.18 * original_shape_Flatness + -0.227 * original_shape_Maximum^{2}DDiameterRow + -0.11 * original_shape_MinorAxisLength + 0.079 * original_shape_Sphericity

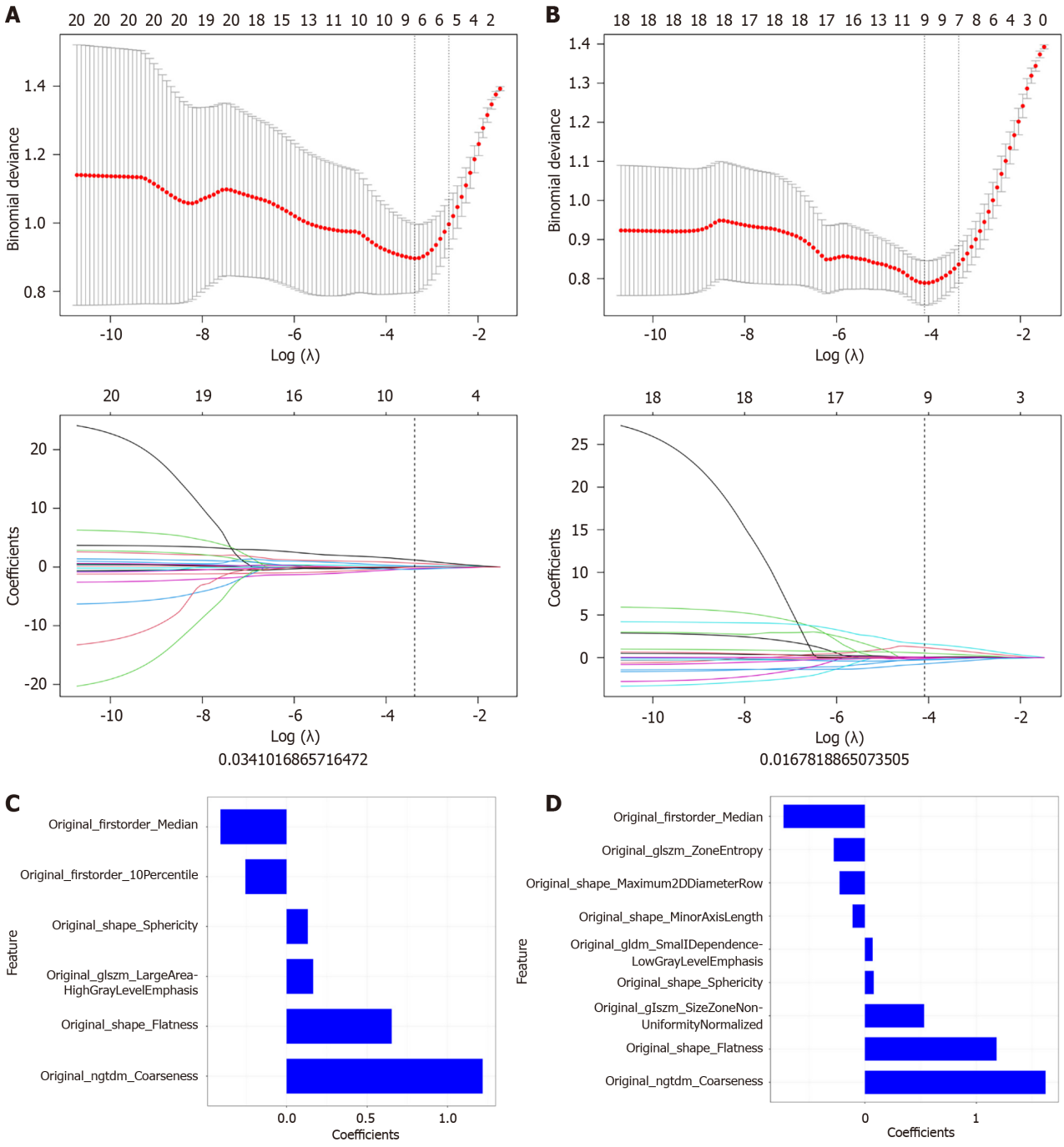

Figure 2 Radiomics feature selection and coefficient visualization using LASSO regression. A and B: The optimal regularization parameter (λ) for the LASSO regression model was selected *via* 10-fold cross-validation in the training (A) and test (B) cohorts. The plots display binomial deviance against log(λ), with the vertical dashed line indicating the optimal log(λ) of -4. This resulted in 6 non-zero features for the training cohort and 9 for the test cohort; C and D: The corresponding coefficients of the selected radiomics features are shown for the training (C) and test (D) cohorts. The Y-axis lists the selected features, and the X-axis shows their respective coefficients.

+ -0.73 * original_firstorder_Median + 0.068 * original_gldm_SmallDependenceLowGrayLevelEmphasis + 0.53 * original_glszm_SizeZoneNonUniformityNormalized + -0.279 * original_glszm_ZoneEntropy + 1.62 * original_ngtdm_Coarseness + -0.358. Subsequently, we compared the Radscores between PC with and without LNM, in both the training and test cohorts, with separate analyses conducted for the late arterial and portal venous phases, as depicted in Figure 3A and B.

We then conducted ROC analysis to assess the performance of the model, as presented in Table 2 and illustrated in Figure 3C and D. In the training set, the Radscore model achieved an AUC of 0.92 (0.87-0.97), demonstrating 89.8% sensitivity, 84.9% specificity, 77.2% PPV, 93.6% NPV, and 86.7% accuracy in the arterial phase. Similarly, in the portal venous phase, the Radscore model attained an AUC of 0.94 (0.90-0.98), with 85.7% sensitivity, 94.2% specificity, 89.4% PPV, 92.0% NPV, and 91.1% accuracy in the training set. In the test set, the Radscore model exhibited an AUC of 0.86 (0.73-1.00), with 91.7% sensitivity, 71.4% specificity, 64.7% PPV, 93.8% NPV, and 78.8% accuracy in the arterial phase.

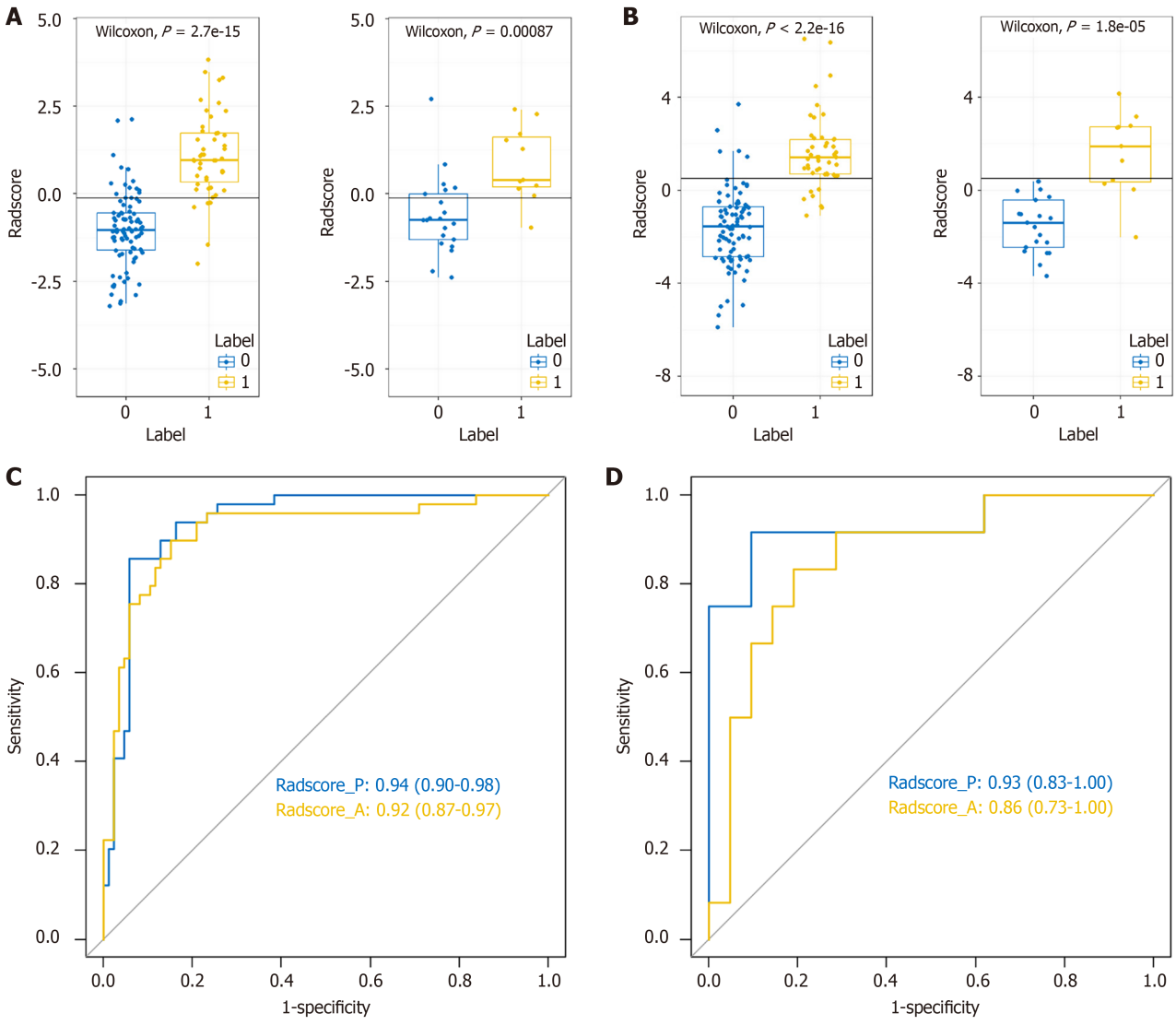

Figure 3 Diagnostic performance of the Radscore model. A and B: Distribution of Radscore values for predicting LNM in the training (A) and test (B) cohorts. Blue dots represent patients without LNM, and yellow dots represent those with LNM; C and D: Receiver operating characteristic curves of the Radscore model for the training (C) and test (D) cohorts. Radscore_A refers to the model derived from arterial phase computed tomography images, while Radscore_P refers to the model derived from portal venous phase images. The area under the curve was used to evaluate model performance.

Similarly, in the portal venous phase, the Radscore model demonstrated an AUC of 0.93 (0.83-1.00), with 66.7% sensitivity, 100.0% specificity, 100.0% PPV, 84.0% NPV, and 87.9% accuracy. The DeLong test was utilized to compare the AUC values of the Radscore model in predicting LNM. No significant difference was observed in AUC values between the late arterial and portal venous phases in the training set (P = 0.51) or in the test set (P = 0.41). The calibration curves for the training and test cohorts are depicted in Figure 4A and B, respectively. Subsequently, we utilized decision curve analysis to evaluate the clinical utility of the model in both cohorts, as demonstrated in Figure 4C and D.

DISCUSSION

PC is considered one of the deadliest forms of cancer, primarily due to its tendency to be diagnosed at an advanced stage when treatment options are limited. PC patients with positive LNM experience a poorer prognosis regardless of whether they undergo surgical resection. The presence of LNM serves as a significant prognostic indicator in PC patients, influencing treatment decisions. For PC patients with positive lymph node involvement, considering NAC or immunotherapy prior to surgical resection is advisable[18,19]. Therefore, accurately assessing lymph node status prior to surgical resection is essential in clinical practice. Early detection is particularly critical for tumors measuring ≤ 2 cm, as determining lymph node involvement enables appropriate staging and identification of patients with stage I PC (T1N0M0)[20]. Presently, assessing LNM through imaging examinations lacks both sensitivity and specificity, posing challenges in preoperatively identifying LNM. Consequently, there arises a necessity to develop a predictive model that is both sensitive and efficient for preoperative assessment of LNM in PC patients.

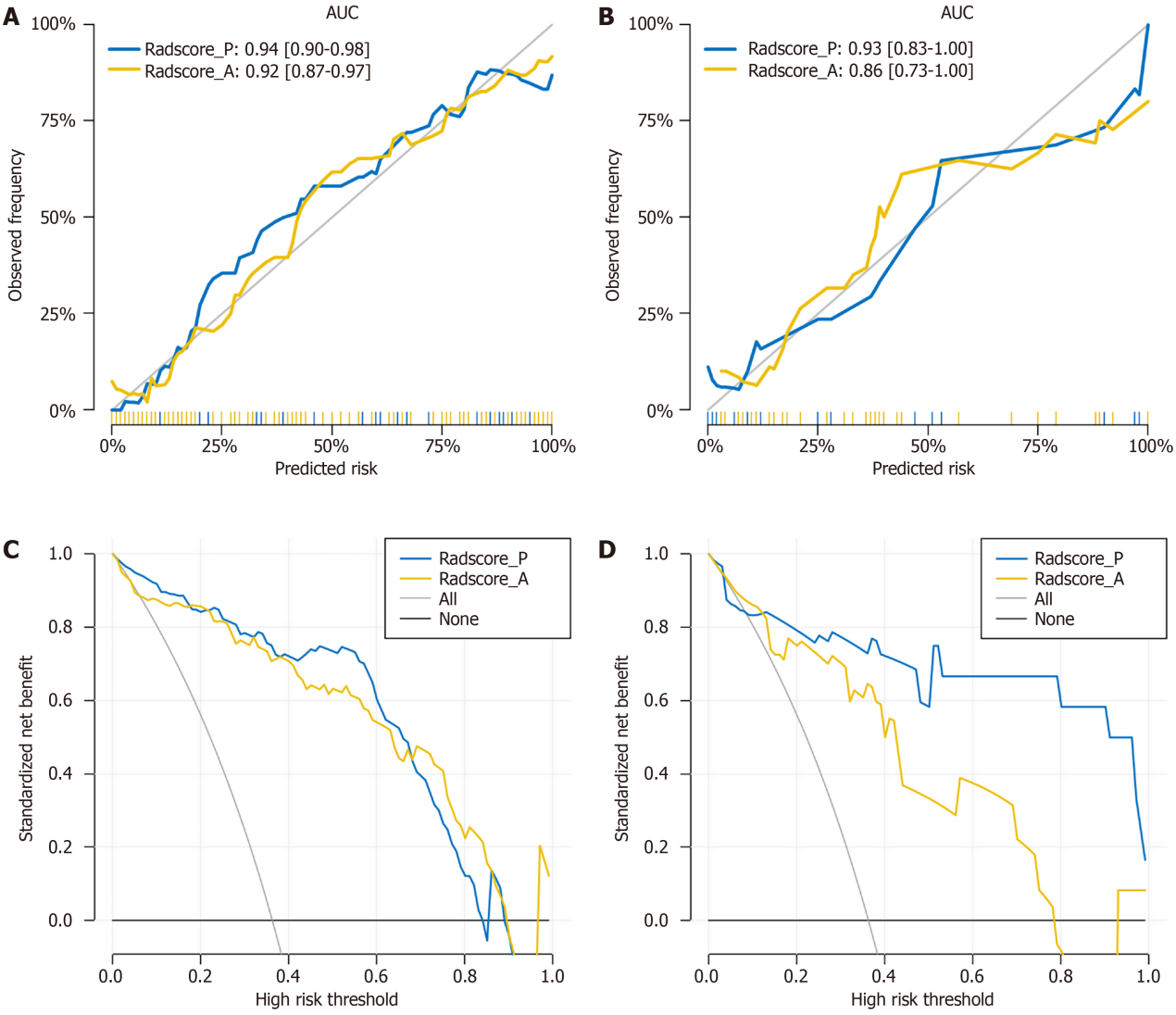

Figure 4 Calibration and decision curve analysis of the Radscore model. A and B: Calibration curves for the Radscore model in the training (A) and test (B) cohorts. The gray diagonal line represents perfect prediction. The blue and yellow dotted lines show the calibration performance of Radscore_P (portal venous phase) and Radscore_A (arterial phase), respectively; C and D: Decision curve analysis for the Radscore model in the training (C) and test (D) cohorts. The X-axis indicates the threshold probability, and the Y-axis shows the net clinical benefit. The gray and black lines represent treat-all and treat-none strategies, respectively. The radiomics models, particularly Radscore_P, provided higher net benefit than Radscore_A across most threshold ranges in the test cohort (D). AUC: Area under the curve.

CT is advised as the primary imaging method for assessing LNM in PC[20]. Nevertheless, a meta-analysis revealed that utilizing CT to evaluate extraregional LNM in pancreatic and periampullary cancer resulted in a pooled sensitivity of 25% and a PPV of 28%[21]. Radiomics entails rapidly advancing research focused on extracting quantitative metrics, referred to as radiomic features, from medical images. These features characterize tissue and lesion properties such as heterogeneity and shape and possess the potential, either individually or when combined with demographic, histologic, genomic, or proteomic data, to contribute to clinical decision-making[22]. Due to the significant role of preoperative lymph node status, several investigations have constructed predictive models for LNM by integrating radiomics models with clinical characteristics. These predictive models have been applied across different diseases, including gastric cancer, biliary tract cancer, endometrial cancer, and colorectal cancer[23–26]. In this study, we explored the potential value of preoperative CT-based radiomics model in predicting LNM in PC.

In our study, we utilized the MRMR method to eliminate redundant and irrelevant features, resulting in the retention of 30 features. Following this, we employed the LASSO method to identify the most predictive subset of features and determined their coefficients to calculate the Radscore. Six radiomics features were selected from the late arterial phase, and 9 features were chosen from the portal venous phase for model construction. Our Radscore model exhibited excellent predictive prowess for LNM across both training and test cohorts during the late arterial and portal venous phases, boasting impressive metrics: An AUC ranging from 0.86 (0.73-1.00) to 0.94 (0.90-0.98), sensitivity between 66.7% and 91.7%, specificity from 71.4% to 100.0%, accuracy spanning 78.8% to 91.1%, PPV ranging from 64.7% to 100.0%, and NPV between 84.0% and 93.8%. The Delong test showed that there was no significant difference in AUC values between the late arterial and portal venous phases in the training set (P = 0.51) or in the test set (P = 0.41). Lu *et al*[27] recently devised a multimodal model that integrates multiphase CE-CT imaging and clinical characteristics, including experts' experience,

Table 1 Demographic characteristics of pancreatic cancer patients with or without lymph node metastasis, *n* (%)/mean ± SD/median (25th-75th percentiles)

Variables	PC with LNM (*n* = 61)	PC without LNM (*n* = 107)	*P* value
Age (years)	63.65 ± 10.95	61.72 ± 10.66	0.214[1]
Gender			0.501[2]
Male	43 (70.5)	70 (65.4)	
Female	18 (29.5)	37 (34.6)	
Clinical symptoms			
Abdominal pain	45 (73.8)	69 (64.5)	0.215[2]
Abdominal bloating or diarrhea	12 (19.7)	19 (17.8)	0.758[2]
Yellow urine or icterus	18 (29.5)	30(28.0)	0.839[2]
Marasmus	9 (14.8)	14 (13.1)	0.762[2]
Asymptomatic	22 (36.1)	31 (29.0)	0.341[2]
Tumor markers			
CA125	22.80 (15.60-39.40)	20.50 (3.20-34.70)	0.325[3]
CA199	205.75 (43.90-954.8)	178.96 (39.98-832.67)	0.105[3]
CEA	4.59 (2.68-6.02)	3.99 (2.44-5.80)	0.432[3]
AFP	2.95 (2.11-4.54)	2.65 (1.85-4.04)	0.665[3]

[1]Calculated with a *t*-test.
[2]Calculated with a Fisher's exact test or an χ^2 test.
[3]Calculated with Mann-Whitney *U* test.
LNM: Lymph node metastasis; PC: Pancreatic cancer; CEA: Carcinoembryonic antigen; AFP: Alpha-fetoprotein.

Table 2 Diagnostic performance of Radscore model for prediction of lymph node metastasis in pancreatic cancer patients using receiver operating characteristic analysis

Group	Model	AUC (95%CI)	Accuracy	Sensitivity	Specificity	PPV	NPV
Training set	Radscore_A	0.92 (0.87-0.97)	86.7%	89.8%	84.9%	77.2%	93.6%
	Radscore_P	0.94 (0.90-0.98)	91.1%	85.7%	94.2%	89.4%	92.0%
Test set	Radscore_A	0.86 (0.73-1.00)	78.8%	91.7%	71.4%	64.7%	93.8%
	Radscore_P	0.93 (0.83-1.00)	87.9%	66.7%	100.0%	100.0%	84.0%

AUC: Area under the curve; PPV: Positive predictive value; NPV: Negative predictive value.

to preoperatively predict LNM in 186 PC patients. This model exhibited outstanding predictive performance in diagnosing LNM, achieving an AUC of 0.937, sensitivity of 87.10%, specificity of 87.18%, PPV of 84.38%, NPV of 89.47%, and an accuracy of 93.7% in the training set. In the test set, it maintained high performance with an AUC of 0.923, sensitivity of 80.77%, specificity of 90.00%, PPV of 91.30%, NPV of 78.24%, and an accuracy of 84.78%. Nonetheless, they proposed with 3 kernelled support tensor machine-based classifiers, which incorporates multiphase CE-CT imaging and clinical characteristics alongside experts' input, presents greater complexity and lacks adaptability in clinical practice. The decision curve analysis showed that the radiomics model provides a greater net benefit than either the treat-all or treat-none strategies across a wide range of threshold probabilities, indicating its potential to guide individualized treatment planning. For example, patients identified as high-risk for LNM based on the model could be considered for more extensive lymph node dissection or neoadjuvant therapy. Nonetheless, further clinical validation and integration with existing clinical workflows are needed to confirm its practical utility.

This study has several limitations. First, it was a retrospective, single-center study, which may introduce selection bias and limit generalizability. Future studies should adopt prospective, multicenter designs to improve robustness and external validity. Second, the model has not been externally validated using independent datasets. Validation with data from other institutions is necessary to confirm its applicability in broader clinical settings. Third, the test cohort size (n = 33) was relatively small, potentially affecting statistical power and model stability. Expanding the test cohort in future research is recommended. Forth, while multiple features were selected, their clinical relevance and biological in-

terpretation require further investigation to enhance model transparency and clinical utility. Finally, a direct comparison between the radiomics model and conventional clinical or radiological assessment methods was not performed, which limits the assessment of incremental value. Future research should include comparative analyses with established clinical models to better evaluate clinical relevance.

CONCLUSION

In conclusion, the radiomics model shows promising performance in identifying LNM in patients with PC. However, its clinical applicability remains limited by concerns about reproducibility and generalizability. Future research should focus on large-scale, multicenter studies with standardized imaging protocols. The use of federated learning may further support model validation and facilitate clinical implementation.

ACKNOWLEDGEMENTS

We thank all authors for their continuous and excellent support with patient data collection, imaging analysis, statistical analysis and valuable suggestions for the article.

FOOTNOTES

Author contributions: Ren S, Qin B, and Wang ZQ designed the research study; Ren S, Tian Y, and Zeng L performed the research; Ren S, Qin B, and Zeng L analyzed the data. Ren S wrote the manuscript; Daniels MJ and Wang ZQ revised the manuscript; all authors read and approved the final manuscript.

Supported by National Natural Science foundation of China, No. 82202135, No. 82371919, No. 82372017, and No. 82171925; China Postdoctoral Science Foundation, No. 2023M741808; Young Elite Scientists Sponsorship Program by China Association of Chinese Medicine, No. 2024-QNRC2-B16; Jiangsu Provincial Key Research and Development Program, No. BE2023789; Young Elite Scientists Sponsorship Program by Jiangsu Association for Science and Technology, No. JSTJ-2023-WJ027; Project funded by Nanjing Postdoctoral Science Foundation, Natural Science Foundation of Nanjing University of Chinese Medicine, No. XZR2023036; and Foundation of Excellent Young Doctor of Jiangsu Province Hospital of Chinese Medicine, No. 2023QB0112.

Institutional review board statement: The study was reviewed and approved by the Ethics Committee of Affiliated Hospital of Nanjing University of Chinese Medicine.

Informed consent statement: Informed consent statement was waived due to the retrospective nature of the study.

Conflict-of-interest statement: All the authors report having no relevant conflicts of interest for this article.

Data sharing statement: Patient imaging data contain sensitive patient information and cannot be released publicly due to the legal and ethical restrictions imposed by the institutional ethics committee. Data is available upon reasonable request from the following e-mail address: zhongqiuwang@njucm.edu.cn.

Country of origin: China

ORCID number: Shuai Ren 0000-0003-4902-6298; Bin Qin 0000-0002-5211-5630; Marcus J Daniels 0000-0003-1209-1918; Liang Zeng 0000-0001-9837-215X; Ying Tian 0000-0002-1525-0614; Zhong-Qiu Wang 0000-0001-6681-7345.

S-Editor: Liu H
L-Editor: A
P-Editor: Yu HG

REFERENCES

1 **Gyawali B**, Booth CM. Treatment of metastatic pancreatic cancer: 25 years of innovation with little progress for patients. *Lancet Oncol* 2024; **25**: 167-170 [*RCA*] [PMID: 38301687 DOI: 10.1016/S1470-2045(23)00516-8] [FullText]
2 **The Lancet Gastroenterology Hepatology**. Cause for concern: the rising incidence of early-onset pancreatic cancer. *Lancet Gastroenterol*

Hepatol 2023; **8**: 287 [*RCA*] [PMID: 36905932 DOI: 10.1016/S2468-1253(23)00039-0] [FullText]
3 **Cheng H**, Xu JH, Kang XH, Liu XM, Wang HF, Wang ZX, Pan HQ, Zhang QQ, Xu XL. Nomogram for predicting the preoperative lymph node metastasis in resectable pancreatic cancer. *J Cancer Res Clin Oncol* 2023; **149**: 12469-12477 [*RCA*] [PMID: 37442865 DOI: 10.1007/s00432-023-05048-8] [FullText] [Full Text(PDF)]
4 **Karamitopoulou E**. Emerging Prognostic and Predictive Factors in Pancreatic Cancer. *Mod Pathol* 2023; **36**: 100328 [*RCA*] [PMID: 37714333 DOI: 10.1016/j.modpat.2023.100328] [FullText]
5 **Yamada M**, Sugiura T, Okamura Y, Ito T, Yamamoto Y, Ashida R, Ohgi K, Aramaki T, Endo M, Uesaka K. Clinical Implication of Node-negative Resectable Pancreatic Cancer. *Ann Surg Oncol* 2021; **28**: 2257-2264 [*RCA*] [PMID: 33452602 DOI: 10.1245/s10434-020-09543-x] [FullText]
6 **Sugimoto M**, Takahashi N, Farnell MB, Smyrk TC, Truty MJ, Nagorney DM, Smoot RL, Chari ST, Carter RE, Kendrick ML. Survival benefit of neoadjuvant therapy in patients with non-metastatic pancreatic ductal adenocarcinoma: A propensity matching and intention-to-treat analysis. *J Surg Oncol* 2019; **120**: 976-984 [*RCA*] [PMID: 31452208 DOI: 10.1002/jso.25681] [FullText]
7 **Klaiber U**, Schnaidt ES, Hinz U, Gaida MM, Heger U, Hank T, Strobel O, Neoptolemos JP, Mihaljevic AL, Büchler MW, Hackert T. Prognostic Factors of Survival After Neoadjuvant Treatment and Resection for Initially Unresectable Pancreatic Cancer. *Ann Surg* 2021; **273**: 154-162 [*RCA*] [PMID: 30921051 DOI: 10.1097/SLA.0000000000003270] [FullText]
8 **Nagakawa Y**, Sahara Y, Hosokawa Y, Murakami Y, Yamaue H, Satoi S, Unno M, Isaji S, Endo I, Sho M, Fujii T, Takishita C, Hijikata Y, Suzuki S, Kawachi S, Katsumata K, Ohta T, Nagakawa T, Tsuchida A. Clinical Impact of Neoadjuvant Chemotherapy and Chemoradiotherapy in Borderline Resectable Pancreatic Cancer: Analysis of 884 Patients at Facilities Specializing in Pancreatic Surgery. *Ann Surg Oncol* 2019; **26**: 1629-1636 [*RCA*] [PMID: 30610555 DOI: 10.1245/s10434-018-07131-8] [FullText]
9 **Nishiwada S**, Sho M, Banwait JK, Yamamura K, Akahori T, Nakamura K, Baba H, Goel A. A MicroRNA Signature Identifies Pancreatic Ductal Adenocarcinoma Patients at Risk for Lymph Node Metastases. *Gastroenterology* 2020; **159**: 562-574 [*RCA*] [PMID: 32376411 DOI: 10.1053/j.gastro.2020.04.057] [FullText]
10 **Chen X**, Wang W, Jiang Y, Qian X. A dual-transformation with contrastive learning framework for lymph node metastasis prediction in pancreatic cancer. *Med Image Anal* 2023; **85**: 102753 [*RCA*] [PMID: 36682152 DOI: 10.1016/j.media.2023.102753] [FullText]
11 **Ren S**, Zhao R, Cui W, Qiu W, Guo K, Cao Y, Duan S, Wang Z, Chen R. Computed Tomography-Based Radiomics Signature for the Preoperative Differentiation of Pancreatic Adenosquamous Carcinoma From Pancreatic Ductal Adenocarcinoma. *Front Oncol* 2020; **10**: 1618 [*RCA*] [PMID: 32984030 DOI: 10.3389/fonc.2020.01618] [FullText] [Full Text(PDF)]
12 **Ren S**, Qian LC, Cao YY, Daniels MJ, Song LN, Tian Y, Wang ZQ. Computed tomography-based radiomics diagnostic approach for differential diagnosis between early- and late-stage pancreatic ductal adenocarcinoma. *World J Gastrointest Oncol* 2024; **16**: 1256-1267 [*RCA*] [PMID: 38660647 DOI: 10.4251/wjgo.v16.i4.1256] [FullText] [Full Text(PDF)]
13 **de la Pinta C**. Radiomics in pancreatic cancer for oncologist: Present and future. *Hepatobiliary Pancreat Dis Int* 2022; **21**: 356-361 [*RCA*] [PMID: 34961674 DOI: 10.1016/j.hbpd.2021.12.006] [FullText]
14 **Marti-Bonmati L**, Cerdá-Alberich L, Pérez-Girbés A, Díaz Beveridge R, Montalvá Orón E, Pérez Rojas J, Alberich-Bayarri A. Pancreatic cancer, radiomics and artificial intelligence. *Br J Radiol* 2022; **95**: 20220072 [*RCA*] [PMID: 35687700 DOI: 10.1259/bjr.20220072] [FullText]
15 **Shin DW**, Lee JC, Kim J, Woo SM, Lee WJ, Han SS, Park SJ, Choi KS, Cha HS, Yoon YS, Han HS, Hong EK, Hwang JH. Validation of the American Joint Committee on Cancer 8th edition staging system for the pancreatic ductal adenocarcinoma. *Eur J Surg Oncol* 2019; **45**: 2159-2165 [*RCA*] [PMID: 31202572 DOI: 10.1016/j.ejso.2019.06.002] [FullText]
16 **Fu N**, Fu W, Chen H, Chai W, Qian X, Wang W, Jiang Y, Shen B. A deep-learning radiomics-based lymph node metastasis predictive model for pancreatic cancer: a diagnostic study. *Int J Surg* 2023; **109**: 2196-2203 [*RCA*] [PMID: 37216230 DOI: 10.1097/JS9.0000000000000469] [FullText]
17 **Ren S**, Zhang J, Chen J, Cui W, Zhao R, Qiu W, Duan S, Chen R, Chen X, Wang Z. Evaluation of Texture Analysis for the Differential Diagnosis of Mass-Forming Pancreatitis From Pancreatic Ductal Adenocarcinoma on Contrast-Enhanced CT Images. *Front Oncol* 2019; **9**: 1171 [*RCA*] [PMID: 31750254 DOI: 10.3389/fonc.2019.01171] [FullText] [Full Text(PDF)]
18 **Barrak D**, Villano AM, Moslim MA, Hopkins SE, Lefton MD, Ruth K, Reddy SS. Total Neoadjuvant Treatment for Pancreatic Ductal Adenocarcinoma Is Associated With Limited Lymph Node Yield but Improved Ratio. *J Surg Res* 2022; **280**: 543-550 [*RCA*] [PMID: 36096019 DOI: 10.1016/j.jss.2022.08.002] [FullText]
19 **Roland CL**, Yang AD, Katz MH, Chatterjee D, Wang H, Lin H, Vauthey JN, Pisters PW, Varadhachary GR, Wolff RA, Crane CH, Lee JE, Fleming JB. Neoadjuvant therapy is associated with a reduced lymph node ratio in patients with potentially resectable pancreatic cancer. *Ann Surg Oncol* 2015; **22**: 1168-1175 [*RCA*] [PMID: 25352267 DOI: 10.1245/s10434-014-4192-6] [FullText]
20 **Bian Y**, Zheng Z, Fang X, Jiang H, Zhu M, Yu J, Zhao H, Zhang L, Yao J, Lu L, Lu J, Shao C. Artificial Intelligence to Predict Lymph Node Metastasis at CT in Pancreatic Ductal Adenocarcinoma. *Radiology* 2023; **306**: 160-169 [*RCA*] [PMID: 36066369 DOI: 10.1148/radiol.220329] [FullText]
21 **Tseng DS**, van Santvoort HC, Fegrachi S, Besselink MG, Zuithoff NP, Borel Rinkes IH, van Leeuwen MS, Molenaar IQ. Diagnostic accuracy of CT in assessing extra-regional lymphadenopathy in pancreatic and peri-ampullary cancer: a systematic review and meta-analysis. *Surg Oncol* 2014; **23**: 229-235 [*RCA*] [PMID: 25466853 DOI: 10.1016/j.suronc.2014.10.005] [FullText]
22 **Mayerhoefer ME**, Materka A, Langs G, Häggström I, Szczypiński P, Gibbs P, Cook G. Introduction to Radiomics. *J Nucl Med* 2020; **61**: 488-495 [*RCA*] [PMID: 32060219 DOI: 10.2967/jnumed.118.222893] [FullText]
23 **Miccichè F**, Rizzo G, Casà C, Leone M, Quero G, Boldrini L, Bulajic M, Corsi DC, Tondolo V. Role of radiomics in predicting lymph node metastasis in gastric cancer: a systematic review. *Front Med (Lausanne)* 2023; **10**: 1189740 [*RCA*] [PMID: 37663653 DOI: 10.3389/fmed.2023.1189740] [FullText]
24 **Ji GW**, Zhang YD, Zhang H, Zhu FP, Wang K, Xia YX, Zhang YD, Jiang WJ, Li XC, Wang XH. Biliary Tract Cancer at CT: A Radiomics-based Model to Predict Lymph Node Metastasis and Survival Outcomes. *Radiology* 2019; **290**: 90-98 [*RCA*] [PMID: 30325283 DOI: 10.1148/radiol.2018181408] [FullText]
25 **Yan B**, Jia Y, Li Z, Ding C, Lu J, Liu J, Zhang Y. Preoperative prediction of lymphovascular space invasion in endometrioid adenocarcinoma: an MRI-based radiomics nomogram with consideration of the peritumoral region. *Acta Radiol* 2023; **64**: 2636-2645 [*RCA*] [PMID: 37312525 DOI: 10.1177/02841851231181681] [FullText]
26 **Inchingolo R**, Maino C, Cannella R, Vernuccio F, Cortese F, Dezio M, Pisani AR, Giandola T, Gatti M, Giannini V, Ippolito D, Faletti R. Radiomics in colorectal cancer patients. *World J Gastroenterol* 2023; **29**: 2888-2904 [*RCA*] [PMID: 37274803 DOI:

10.3748/wjg.v29.i19.2888] [FullText] [Full Text(PDF)]

27 **Lu Q**, Zhou C, Zhang H, Liang L, Zhang Q, Chen X, Xu X, Zhao G, Ma J, Gao Y, Peng Q, Li S. A multimodal model fusing multiphase contrast-enhanced CT and clinical characteristics for predicting lymph node metastases of pancreatic cancer. *Phys Med Biol* 2022; **67** [*RCA*] [PMID: 35905729 DOI: 10.1088/1361-6560/ac858e] [FullText]

World Journal of Radiology

Submit a Manuscript: https://www.f6publishing.com

World J Radiol 2025 August 28; 17(8): 110307

DOI: 10.4329/wjr.v17.i8.110307

ISSN 1949-8470 (online)

ORIGINAL ARTICLE

Retrospective Study

Magnetic resonance imaging-based radiomics signature for predicting preoperative staging of esophageal cancer

Ri-Hui Yang, Zhi-Ping Lin, Ting Dong, Wei-Xiong Fan, Hao-Dong Qin, Gui-Hua Jiang, Hai-Yang Dai

Specialty type: Radiology, nuclear medicine and medical imaging

Provenance and peer review: Unsolicited article; Externally peer reviewed.

Peer-review model: Single blind

Peer-review report's classification

Scientific Quality: Grade B, Grade C

Novelty: Grade B, Grade C

Creativity or Innovation: Grade B, Grade D

Scientific Significance: Grade B, Grade B

P-Reviewer: Yang K

Received: June 4, 2025

Revised: June 24, 2025

Accepted: July 23, 2025

Published online: August 28, 2025

Processing time: 85 Days and 18.5 Hours

Ri-Hui Yang, Wei-Xiong Fan, Department of Magnetic Resonance, Meizhou People's Hospital, Meizhou 514031, Guangdong Province, China

Zhi-Ping Lin, GE Healthcare, Guangzhou 510623, Guangdong Province, China

Ting Dong, Gui-Hua Jiang, Department of Medical Imaging, Guangdong Second Province General Hospital, Guangzhou 510317, Guangdong Province, China

Hao-Dong Qin, Siemens Healthineers, Guangzhou 510317, Guangdong Province, China

Hai-Yang Dai, Department of Radiology, Huizhou Central People's Hospital, Huizhou 516001, Guangdong Province, China

Co-first authors: Ri-Hui Yang and Zhi-Ping Lin.

Co-corresponding authors: Gui-Hua Jiang and Hai-Yang Dai.

Corresponding author: Hai-Yang Dai, MD, Department of Radiology, Huizhou Central People's Hospital, No. 41 North Eling Road, Huizhou 516001, Guangdong Province, China.
d.ocean@163.com

Abstract

BACKGROUND

Esophageal cancer (EC) is one of the most prevalent malignant gastrointestinal tumors; accurate prediction of EC staging has high significance before treatment.

AIM

To explore a rational radiomic approach for predicting preoperative staging of EC based on magnetic resonance imaging (MRI).

METHODS

This retrospective study included 210 patients with pathologically confirmed EC, randomly divided into a primary cohort (n = 147) and a validation cohort (n = 63) in a ratio of 7:3. All patients underwent a preoperative MRI scan from the neck to the abdomen. High-throughput and quantitative radiomics features were extracted from T2-weighted imaging (T2WI) and gadolinium contrast-enhanced T1-weighted imaging (T1WI)-Gd images. Radiomics signatures were selected using minimal redundancy maximal relevance and the least absolute shrinkage and selection operator. Then a logistic regression model was built to predict the EC

stages. The diagnostic performance of the radiomics model for discriminating between stages I-II and III-IV was evaluated using the area under the curve (AUC), sensitivity (SEN), and specificity (SPE).

RESULTS

A total of 214 radiomics features were extracted. Following feature dimension reduction, the T1WI and T2WI sequences were retained, and 14 features from the T1WI sequence and 3 features from the T2WI sequence were selected to construct radiomics signatures. The radiomics signature combining T2WI with T1WI-Gd demonstrated superior discrimination of stages in the validation cohort (AUC: 0.851; SEN: 0.697; SPE: 0.793), which outperformed single-sequence models (AUC: 0.779, 0.844; SEN: 0.667, 0.636; SPE: 0.8, 0.8).

CONCLUSION

MRI-based radiomics signatures could identify EC stages before treatment, which could serve as a noninvasive and quantitative approach aiding personalized treatment planning.

Key Words: Esophageal cancer; Tumor staging; Magnetic resonance imaging; Radiomics; Logistic regression

Core Tip: This study developed a novel magnetic resonance imaging-based radiomics approach to noninvasively predict preoperative stage of esophageal cancer (EC). By integrating quantitative features from T2-weighted imaging and contrast-enhanced T1-weighted imaging sequences in 210 EC patients, a logistic regression model achieved high accuracy in distinguishing early-stage (I-II) from advanced-stage (III-IV) disease. This multimodal radiomics signature outperformed single-sequence models and offers a promising tool for guiding personalized treatment strategies.

Citation: Yang RH, Lin ZP, Dong T, Fan WX, Qin HD, Jiang GH, Dai HY. Magnetic resonance imaging-based radiomics signature for predicting preoperative staging of esophageal cancer. *World J Radiol* 2025; 17(8): 110307
URL: https://www.wjgnet.com/1949-8470/full/v17/i8/110307.htm
DOI: https://dx.doi.org/10.4329/wjr.v17.i8.110307

INTRODUCTION

Esophageal cancer (EC) poses a significant health burden in China, ranking sixth in incidence and fourth in cancer mortality, with a dismal 5-year survival of 19%[1,2]. Early-stage (I-II) disease typically undergoes endoscopic or surgical resection, whereas advanced (III-IV) EC requires neoadjuvant chemoradiation prior to surgery or definitive chemoradiation[3]. Lymph node (LN) metastasis correlates strongly with reduced survival[4], underscoring the imperative for accurate pretreatment staging. The accurate prediction of EC staging prior to treatment is clinically critical.

Radiomics is increasingly recognized as a critical tool in cancer research. High-throughput mining enables the extraction of quantitative image features from digitally encoded medical images. These robust image-based signatures could potentially enhance precision diagnosis and treatment strategies[5,6]. Recent radiomics research has demonstrated the possibility of using magnetic resonance imaging (MRI) to substantially improve the detection and prediction of LN metastases[7,8]. While computed tomography (CT), MRI, positron emission tomography-CT (PET-CT), and endoscopic ultrasonography (EUS) each exhibit variable sensitivity (SEN)/specificity (SPE) for EC staging and LN detection[9-11], contrast-enhanced CT remains the clinical mainstay despite controversial LN detection accuracy (SEN: 37.3%-67.2%; SPE: 63.9%-96.4%)[12]. Notably, the new Chinese EC guidelines has now recognized MRI's diagnostic parity with CT for LN assessment[13].

At present, radiomics research on EC based on MRI mainly focuses on predicting LN metastases and evaluating the efficacy of neoadjuvant therapy[14-16], However, there has been little research on predicting the early and local progression stages of EC based on MRI radiomics, which has significant clinical significance for personalized treatment of EC patients. Our study addresses this by extracting radiomic features from T2-weighted imaging (T2WI) and T1-weighted imaging (T1WI)-Gd sequences to build a predictive model for distinguishing early (I-II) from locally advanced (III-IV) EC, providing a reference for guiding clinical treatment decisions.

MATERIALS AND METHODS

Patients

The clinical and MRI data of EC patients who underwent LN dissection confirmed by surgery and pathology between March 2017 and November 2020 were retrospectively collected. The inclusion criteria were: (1) Pathologically confirmed EC; (2) Underwent radical resection and LN dissection, with clear postoperative pathological stage and clear pathological

LN results; (3) Preoperative MRI scan (T2WI and T1WI-Gd) within two weeks before surgery; (4) No anticancer treatment prior to MRI; and (5) No history of other malignant tumors. The exclusion criteria were: (1) Received preoperative anticancer therapy; (2) Concurred other malignant tumors; and (3) Non-diagnostic MRI image quality, precluding subsequent feature extraction.

This study was approved by the Ethics Committee on Clinical Researches and Novel Technologies of Meizhou People's Hospital (Grant No. 2023-C-45), and patient informed consent was waived for this retrospective study. All procedures were carried out in accordance with relevant guidelines and regulations. Ultimately, 210 patients with EC (165 males and 45 females, aged 40 to 86 years, mean age 63.1 ± 7.92 years) were included. Among them, there were 207 cases of squamous cell carcinoma, 2 cases of adenosquamous cell carcinoma, and 1 case of mixed neuroendocrine carcinoma. Based on tumor node metastasis staging, 101 patients had stages I-II (74 males, 27 females, mean age 63.2 ± 8.01 years), and 109 had stages III-IV EC (91 males and 18 females, mean age 62.9 ± 7.86 years). The clinicopathologic characteristics of the patients are presented in Table 1.

Image acquisition

Imaging was performed with a 3.0 T Siemens (Erlangen, Germany) Skyra MR scanner equipped with 18-channel phased array coil. The patient was placed supine and told to breathe as calmly as possible to reduce motion artifacts. The scanning range was from the level of the supraclavicular fossa to the gastric cardia. The scanning sequence and parameters were: (1) T2WI: Slice thickness 3 mm, TR 3000 ms, TE 91 ms, NEX = 1, matrix 256 × 256, field of view (FOV) 210 mm × 210 mm and scanning time 2 minutes; and (2) T1WI-Gd: Slice thickness 1.5 mm, TR 4.4 ms, TE 2.0 ms, NEX = 1, matrix 160 × 160, FOV 150 mm × 150 mm, and flip angle 12. During enhanced scanning, Gd-DTPA contrast agent was injected intravenously through the elbow using a high-pressure syringe at 0.1 mmol/kg. The scanning time was 3 minutes and 26 seconds.

Tumor segmentation

Manual segmentation of the EC was performed on each patient's MR images utilizing an Artificial Intelligent Kit (AK), a new application platform for the overall solution of artificial intelligence in medical imaging radiomics launched by GE Healthcare. Two experienced associate senior radiologists (readers 1 and 2) carefully delineated the tumor on all T2WI and T1WI-Gd images to generate two 3D segmentations of the entire tumor. These regions of interests were applied for subsequent feature extraction and further analysis.

Radiomic feature extraction

Patients were randomly divided into a primary cohort (n = 147) and a validation cohort (n = 63) at a 7:3 ratio, as according to previous reports[17,18], and the sample size was estimated by using the package of R software (version 4.3.1). Radiomic features were extracted based on the segmentation results from the primary cohort using a homemade program in the AK. Preprocessing included: (1) The image was first resampled using linear interpolation algorithm to a standard voxel spacing of 1 mm × 1 mm × 1 mm; and (2) Z-score for MRI intensity values were standardized. The Python PyRadiomics module was used to extract radiomic features through AK, where the bin width of the histogram was set to 5 to quantify the intensity distribution of the image. The distance parameter for texture features such as gray level co-occurrence matrix (GLCM) was uniformly set to 1. For each MRI sequence, the 214 extracted features covered the major feature pool in recent radiomic studies. The features were categorized into six primary types (Figure 1): (1) Histogram features; (2) Form factor features; (3) GLCM and Harilick features; (4) Gray level run length matrix features; (5) Grey level size zone matrix (GLSZM) features; and (6) Gray level dependence matrix (GLDM) features.

A rigorous feature selection pipeline was implemented to simplify the model development and avoid over-fitting. Minimal redundancy maximal relevance (mRMR) and least absolute shrinkage and selection operator (LASSO) method were used for feature dimensionality reduction. For tuning coefficients λ and α, the respective minimum standard deviation and maximum area under the curve (AUC) criteria were followed. Dimensionality reduction was performed using the variance method (excluding features with zero variance), the mRMR method selecting the top 50 features, and the LASSO method with lambda selection standard set to 'λ.min', and selecting the optimal λ through five fold cross validation on the training set. For accurate prediction of the EC stages, 16 features selected from the T2WI with T1WI-Gd images made the greatest contribution. Then, each patient's two radiomic signature sets were integrated into a multivariate logistic regression framework. Model training generated weighted linear combinations of selected features, which constituted the final radiomic signature scores for individual patients.

Statistical analysis

The statistical analysis was performed in R (version 3.5.1; http://www.Rproject.org). The Shapiro-Wilk test was used to test whether the quantitative data were normally distributed. The rank-sum test was used to compare the differences in age, between patients with EC stage I-II and stage III-IV. The χ^2 test or correction χ^2 test was used to compare the differences in sex, tumor location, and pathological type between patients with EC stage I-II and stage III-IV. In addition, the primary cohort was used to train the logistic regression model, and the validation cohort was used to test the model. Finally, the receiver operating characteristic (ROC) curve, SEN, and SPE were used to evaluate the performance of the prediction model. The DeLong test compared the AUC between the single-sequence and mixed-sequence models. A two-sided P value < 0.05 was considered statistically significant.

Table 1 Clinical and pathological characteristics of 210 esophageal cancer patients

Characteristics	Primary cohort		*P* value	Validation cohort		*P* value
	Stage I-II	Stage III-IV		Stage I-II	Stage III-IV	
Age (years)	62.0	61.0	0.548	62.5	64.0	0.842
Gender			0.073			0.613
Male	50	63		24	28	
Female	21	13		6	5	
Location			0.33			0.705
Upper	2	6		2	2	
Middle	47	51		17	22	
Lower	22	19		11	9	

RESULTS

Clinical data

Patient clinicopathological features are summarized in Table 1. No significant intergroup differences (stages I-II *vs* III-IV) existed in age, sex, or tumor location ($P > 0.05$).

Radiomic features

After feature selection and dimensionality reduction, 14 and 3 of the 214 radiomic features were retained for EC staging prediction (Table 2). Fourteen and three features distinguished stages I-II from stages III-IV in the T1WI and T2WI models, respectively.

Radiomics signature discrimination performance

The radiomics signature was constructed using the selected features from the previous section, forming a linear combination based on a logistic regression model. There were four first-order features, four shape features, four GLCM features, two GLSZM features, one GLDM feature, and two neighboring gray-tone difference matrix features. The formula for the combined model was as follows: Radscore = T1WI × 5.27600436 + T2WI × 3.21937331 - 4.36897257.

The discriminative power of the radiomic signature for tumor, node, metastasis staging was assessed using ROC curves in both the primary and validation cohorts (Figure 2). Subsequently, the ROC curves corresponding to different models were compared using the Delong test, and the AUC, SEN, and SPE were calculated (Tables 3 and 4). The radiomics signature combining T2WI with T1WI-Gd exhibited superior discrimination of the stages in the primary (AUC: 0.788, 0.859; SEN: 0.75, 0.829; SPE: 0.746, 0.789) and validation cohorts (AUC: 0.851; SEN: 0.697; SPE: 0.793), outperforming single-sequence models (AUC: 0.779, 0.844; SEN: 0.667, 0.636; SPE: 0.8, 0.8). Radiomic scores (Rad-scores) for EC patients in both the primary and validation cohorts were calculated using the elastic net model.

DISCUSSION

This study demonstrated that a quantitative approach utilizing multimodal MRI can effectively identify EC stages prior to treatment initiation. Leveraging significant differences in the Rad-score, the radiomics signature successfully distinguished between esophageal squamous cell carcinoma stages I-II and III-IV during the preoperative period. These findings were supported by MRI's superior soft-tissue contrast and multiparametric capabilities, which provide high-quality imaging foundation for precise tumor delineation and radiomics analysis.

Surgical resection remains the cornerstone of EC management, yet surgical intervention for advanced EC (stages III-IV) is associated with significant challenges and a high postoperative recurrence rate. LN status is a critical independent prognostic factor, and the approach for LN dissection plays a pivotal role in treatment strategies[4]. Several studies have suggested that systematic LN dissection should be performed in EC patients only when the tumor invades the submucosa, as extended LN resection may elevate the risk of postoperative complications[19,20]. In addition, accurate LN staging is essential for guiding the implementation of neoadjuvant therapy[21]. Although CT is widely used for preoperative EC staging, its accuracy remains limited. Radiomics addresses these limitations by decoding tumor heterogeneity through high-throughput feature extraction from medical images, thereby enhancing diagnostic and prognostic precision.

This study confirmed the feasibility of predicting EC stages using MR-based radiomic features. We extracted 214 quantitative features from tumors using T2WI and T1WI-Gd images. The seventeen features that contributed most to the differentiation of EC stages were selected for model construction. Radiomics features derived from T2WI are based on the signal intensity of water molecules, primarily reflecting the water content characteristics of the tumor.

Table 2 Selected radiomics features of esophageal cancer patients

Task	MRI	Feature name	Coefficient
Tumor node metastasis stage prediction	T2WI		
		Original_firstorder_Median	0.921642536
		Original_shape_Elongation	0.967002183
		Original_glcm_Correlation	0.246781324
	T1WI-Gd		
		Original_shape_LeastAxisLength	0.875999143
		Original_shape_Elongation	0.967002356
		Original_glcm_DifferenceAverage	0.109732763
		Original_firstorder_Kurtosis	0.605404872
		Original_firstorder_Median	0.921642536
		Original_glszm_LowGrayLevelZoneEmphasis	0.274812737
		Original_glcm_Imc1	0.638235237
		Original_gldm_LargeDependenceHighGrayLevelEmphasis	0.209360630
		Original_shape_MajorAxisLength	0.149464274
		Original_ngtdm_Strength	0.214134941
		Original_glcm_Idn	0.983044251
		Original_firstorder_10Percentile	0.303070619
		Original_glszm_SizeZoneNonUniformity	0.126542445
		Original_ngtdm_Complexity	0.524606933

MRI: Magnetic resonance imaging; T1WI: T1-weighted imaging; T2WI: T2-weighted imaging.

Table 3 Delong test results in the primary and validation cohort

Model	Primary cohort			Validation cohort		
	T2WI	T1WI	Combined	T2WI	T1WI	Combined
T2WI	0	0.081	0.0035	0	0.27	0.09
T1WI	-1.74	0	0.19	-1.09	0	0.80
Combined	-2.95	-1.30	0	-1.65	-0.25	0

T1WI: T1-weighted imaging; T2WI: T2-weighted imaging.

Table 4 Model performance for predicting tumor node metastasis stages in esophageal cancer patients

Model	Primary cohort			Validation cohorts		
	AUC (95%CI)	SEN (95%CI)	SPE (95%CI)	AUC (95%CI)	SEN (95%CI)	SPE (95%CI)
T2WI	0.788 (0.712, 0.858)	0.75 (0.642, 0.834)	0.746 (0.634, 0.833)	0.779 (0.651, 0.892)	0.667 (0.496, 0.803)	0.8 (0.627, 0.905)
T1WI	0.859 (0.799, 0.919)	0.829 (0.729, 0.897)	0.789 (0.681, 0.868)	0.844 (0.728, 0.941)	0.636 (0.466, 0.778)	0.8 (0.627, 0.905)
Combined	0.877 (0.819, 0.929)	0.842 (0.744, 0.907)	0.761 (0.65, 0.845)	0.851 (0.739, 0.948)	0.697 (0.527, 0.826)	0.8 (0.627, 0.905)

95%CI: 95% confidence interval; T1WI: T1-weighted imaging; T2WI: T2-weighted imaging; AUC: Area under the curve; SEN: Sensitivity; SPE: Specificity.

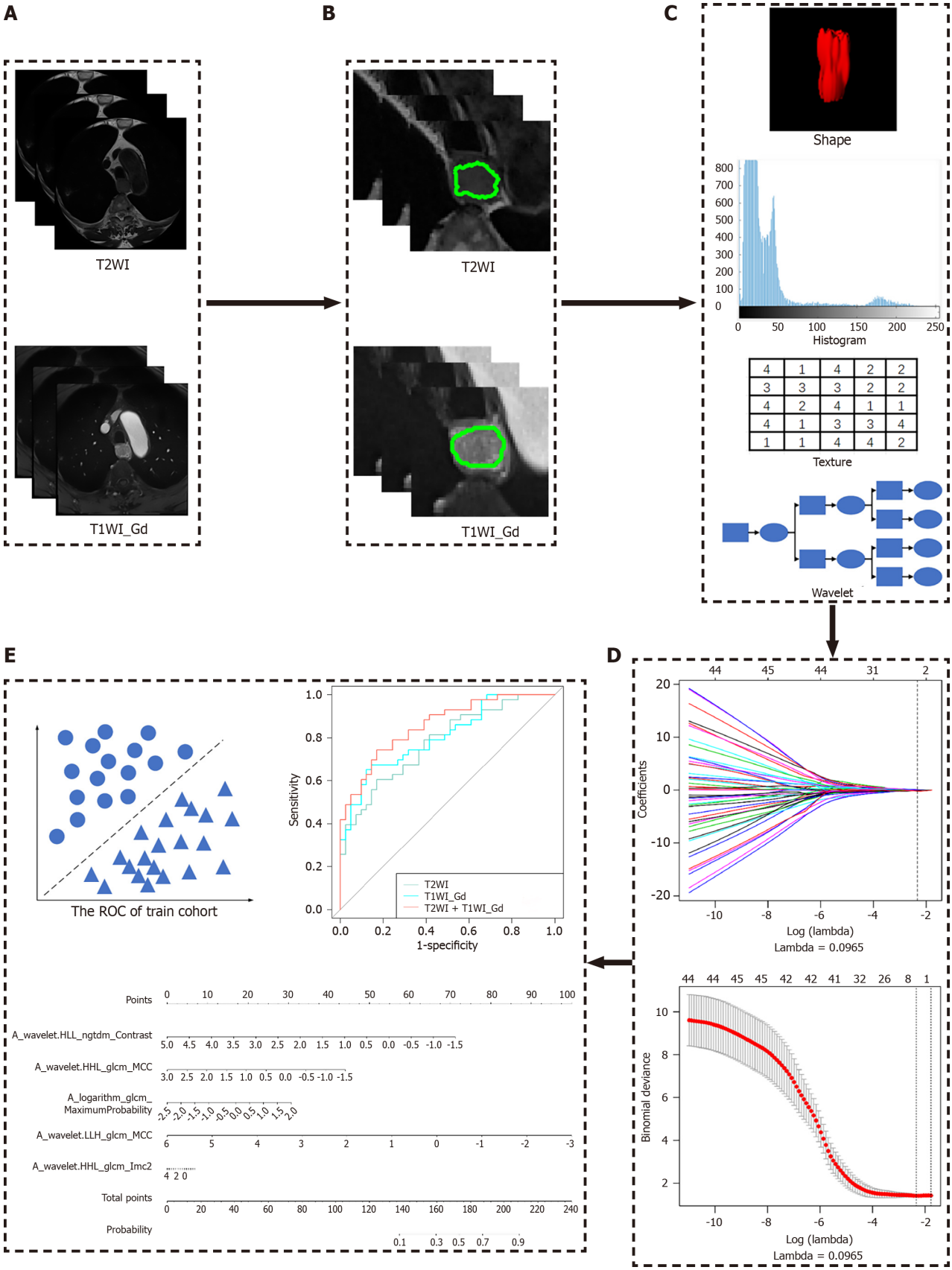

Figure 1 Flowchart of the study. A: Original magnetic resonance imaging images, including T2-weighted imaging (T2WI) and T1-weighted imaging (T1WI)-Gd; B: Segmentation of both T2WI and T1WI-Gd images delineated the tumor region; C: Radiomic features were extracted from the tumor region, including shape, first-order histogram, texture and wavelet group analysis; D: A series of features were selected to build the radiomics signature using the minimal redundancy maximal relevance and the least absolute shrinkage and selection operator method; E: The classification performance of the radiomic signature was evaluated using the receiver operating characteristic curves in both the primary and validation cohort. ROC: Receiver operating characteristic; T1WI: T1-weighted imaging; T2WI: T2-weighted imaging.

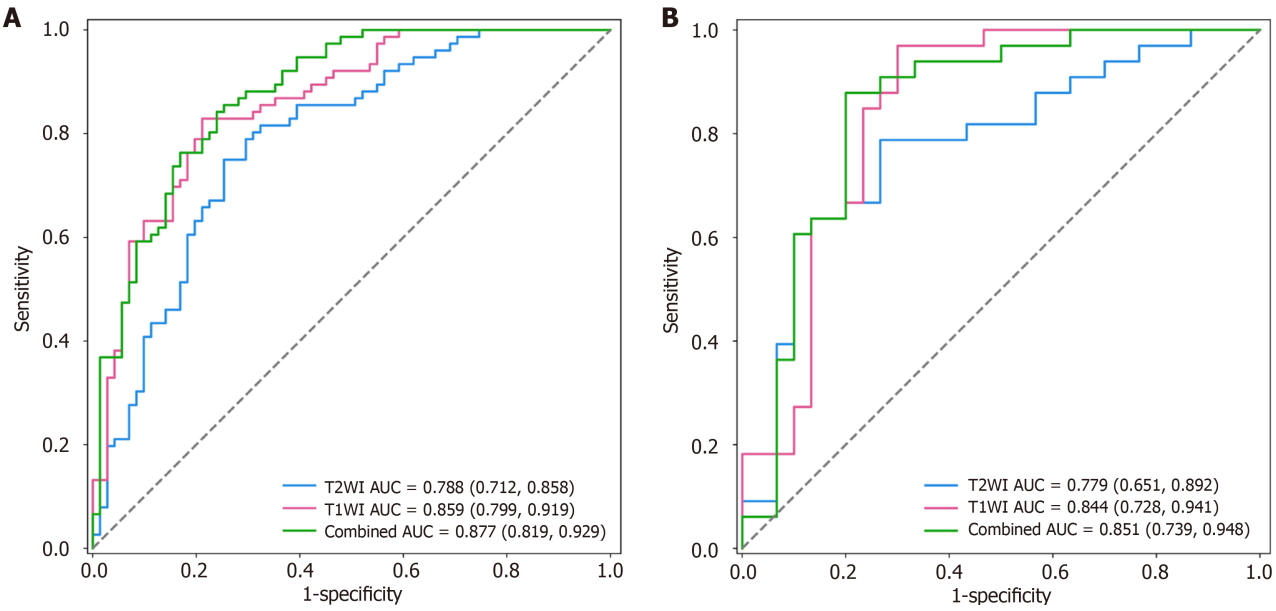

Figure 2 Receiver operating characteristic curves of the radiomics signature's discriminative performance in esophageal cancer staging in the primary and validation cohorts. A: Primary cohorts; B: Validation cohorts. The combined radiomics signature demonstrated superior area under the curve (AUC) in both the primary (AUC: 0.877) and validation cohorts (AUC: 0.851), outperforming single-sequence models. AUC: Area under the curve; T1WI: T1-weighted imaging; T2WI: T2-weighted imaging.

The high-order radiomics features comprised the GLCM, which reflects the gray level difference, including distribution uniformity and texture thickness. Greater heterogeneity of the tumor was associated with an uneven gray level and increased texture complexity. Histological features derived from T1WI-Gd images predominantly indicative of microvascular density and histologic grading[22]. Higher-order texture features, exemplified by GLCM metrics, quantified spatial complexity patterns correlating with biologically aggressive phenotypes[23].

Consistent with prior studies, our results showed that integrating radiomics features from dual-sequence MRI achieved strong discriminatory performance in differentiating stage I-II from stage III-IV EC in both the primary and validation cohorts[16,24,25]. Our MRI-based radiomics model outperformed CT and PET-CT radiomics methods for staging EC[26,27]. This advantage may originate from MRI's superior soft-tissue resolution coupled with synergistic information integration from multiparametric sequences. The improvement may also stem from the complementary information provided by multiparametric MRI, which enables a more comprehensive and objective assessment of tumor heterogeneity. In addition, our results demonstrated performance comparable with prior MRI radiomics studies predicting LN metastasis in EC[16]. This reinforces the potential of MRI-based radiomics for EC staging.

This study had several limitations. First, the single-center design and modest sample size necessitate validation through multicenter studies with larger cohorts. Second, although we focused on tumor staging, the prediction efficiency of LN metastasis, including its extent, in different regions remains unassessed. Future work will be dedicated to developing models focused on predicting LN metastasis. Last, the exclusive use of a single MRI scanner limits generalizability. Future work should evaluate the impact of varying equipment, field strength, and scanning parameters.

CONCLUSION

This study demonstrates that MRI-based radiomics can effectively differentiate between stage I–II and stage III-IV EC before treatment. We developed a multiparametric radiomics model incorporating features from multiple MRI sequences. MRI-based radiomics could serve as a valuable noninvasive adjunct tool for preoperative staging and personalized therapeutic strategy formulation in EC.

FOOTNOTES

Author contributions: Yang RH and Lin ZP participated in the conception and design of the study, and contributed equally to this work as co-first authors; Dong T was involved in the acquisition, analysis, or interpretation of data; Fan WX and Qin HD prepared the tables and figures; Yang RH wrote the first draft and subsequent versions; Jiang GH and Dai HY was responsible for project administration and supervision, and contributed equally to this work as co-corresponding authors; all authors critically reviewed and approved the final manuscript to be published.

Supported by Guangdong Medical Research Foundation, No. B2023272.

Institutional review board statement: This study was approved by the Ethics Committee on Clinical Researches and Novel Technologies of Meizhou People's Hospital (No. 2023-C-45).

Informed consent statement: Patient informed consent was waived for this retrospective study.

Conflict-of-interest statement: All the authors report no relevant conflicts of interest for this article.

Data sharing statement: The data that support the findings of this study are available from the corresponding author upon reasonable request at d.ocean@163.com.

Country of origin: China

ORCID number: Hai-Yang Dai 0000-0001-5875-2262.

S-Editor: Lin C
L-Editor: A
P-Editor: Yu HG

REFERENCES

1 **Siegel RL**, Miller KD, Wagle NS, Jemal A. Cancer statistics, 2023. *CA Cancer J Clin* 2023; **73**: 17-48 [*RCA*] [PMID: 36633525 DOI: 10.3322/caac.21763] [FullText]
2 **Sheikh M**, Roshandel G, McCormack V, Malekzadeh R. Current Status and Future Prospects for Esophageal Cancer. *Cancers (Basel)* 2023; **15**: 765 [*RCA*] [PMID: 36765722 DOI: 10.3390/cancers15030765] [FullText] [Full Text(PDF)]
3 **Liu S**, Zheng H, Pan X, Chen L, Shi M, Guan Y, Ge Y, He J, Zhou Z. Texture analysis of CT imaging for assessment of esophageal squamous cancer aggressiveness. *J Thorac Dis* 2017; **9**: 4724-4732 [*RCA*] [PMID: 29268543 DOI: 10.21037/jtd.2017.06.46] [FullText]
4 **Rice TW**, Ishwaran H, Hofstetter WL, Schipper PH, Kesler KA, Law S, Lerut EM, Denlinger CE, Salo JA, Scott WJ, Watson TJ, Allen MS, Chen LQ, Rusch VW, Cerfolio RJ, Luketich JD, Duranceau A, Darling GE, Pera M, Apperson-Hansen C, Blackstone EH. Esophageal Cancer: Associations With (pN+) Lymph Node Metastases. *Ann Surg* 2017; **265**: 122-129 [*RCA*] [PMID: 28009736 DOI: 10.1097/SLA.0000000000001594] [FullText]
5 **Coroller TP**, Agrawal V, Huynh E, Narayan V, Lee SW, Mak RH, Aerts HJWL. Radiomic-Based Pathological Response Prediction from Primary Tumors and Lymph Nodes in NSCLC. *J Thorac Oncol* 2017; **12**: 467-476 [*RCA*] [PMID: 27903462 DOI: 10.1016/j.jtho.2016.11.2226] [FullText]
6 **Shi L**, Wang X, Li C, Bai Y, Zhang Y, Li H. Radiomics applications in the modern management of esophageal squamous cell carcinoma. *Med Oncol* 2025; **42**: 221 [*RCA*] [PMID: 40425893 DOI: 10.1007/s12032-025-02775-5] [FullText]
7 **Ma D**, Zhou T, Chen J, Chen J. Radiomics diagnostic performance for predicting lymph node metastasis in esophageal cancer: a systematic review and meta-analysis. *BMC Med Imaging* 2024; **24**: 144 [*RCA*] [PMID: 38867143 DOI: 10.1186/s12880-024-01278-5] [FullText]
8 **Jannatdoust P**, Valizadeh P, Pahlevan-Fallahy MT, Hassankhani A, Amoukhteh M, Behrouzieh S, Ghadimi DJ, Bilgin C, Gholamrezanezhad A. Diagnostic accuracy of CT-based radiomics and deep learning for predicting lymph node metastasis in esophageal cancer. *Clin Imaging* 2024; **113**: 110225 [*RCA*] [PMID: 38905878 DOI: 10.1016/j.clinimag.2024.110225] [FullText]
9 **Li X**, Wang Y, Kong M, Lin J. Systematic review and meta-analysis of endoscopic ultrasonography in staging diagnosis of esophageal cancer after neoadjuvant radiotherapy and chemotherapy. *J Gastrointest Oncol* 2022; **13**: 1525-1540 [*RCA*] [PMID: 36092358 DOI: 10.21037/jgo-22-437] [FullText] [Full Text(PDF)]
10 **Goense L**, Heethuis SE, van Rossum PSN, Voncken FEM, Lagendijk JJW, Lam MGEH, Terhaard CH, van Hillegersberg R, Ruurda JP, Mook S, van Lier ALHMW, Lin SH, Meijer GJ. Correlation between functional imaging markers derived from diffusion-weighted MRI and 18F-FDG PET/CT in esophageal cancer. *Nucl Med Commun* 2018; **39**: 60-67 [*RCA*] [PMID: 29023336 DOI: 10.1097/MNM.0000000000000771] [FullText]
11 **Luo LN**, He LJ, Gao XY, Huang XX, Shan HB, Luo GY, Li Y, Lin SY, Wang GB, Zhang R, Xu GL, Li JJ. Evaluation of preoperative staging for esophageal squamous cell carcinoma. *World J Gastroenterol* 2016; **22**: 6683-6689 [*RCA*] [PMID: 27547011 DOI: 10.3748/wjg.v22.i29.6683] [FullText] [Full Text(PDF)]
12 **Liu J**, Wang Z, Shao H, Qu D, Liu J, Yao L. Improving CT detection sensitivity for nodal metastases in oesophageal cancer with combination of smaller size and lymph node axial ratio. *Eur Radiol* 2018; **28**: 188-195 [*RCA*] [PMID: 28677059 DOI: 10.1007/s00330-017-4935-4] [Full Text]
13 **Chinese National Cancer Center**; Chinese Association of Thoracic Surgeons; Chinese Society for Thoracic and Cardiovascular Surgery; Chinese Society for Diseases of the Esophagus. [Chinese Guidelines on Perioperative Management of Resectable Esophageal Cancer (2023 edition)]. *Zhonghua Yi Xue Za Zhi* 2023; **103**: 2552-2570 [*RCA*] [PMID: 37650202 DOI: 10.3760/cma.j.cn112137-20230604-00933] [Full Text]
14 **Guo H**, Tang HT, Hu WL, Wang JJ, Liu PZ, Yang JJ, Hou SL, Zuo YJ, Deng ZQ, Zheng XY, Yan HJ, Jiang KY, Huang H, Zhou HN, Tian D. The application of radiomics in esophageal cancer: Predicting the response after neoadjuvant therapy. *Front Oncol* 2023; **13**: 1082960 [*RCA*] [PMID: 37091180 DOI: 10.3389/fonc.2023.1082960] [FullText] [Full Text(PDF)]
15 **Lu S**, Wang C, Liu Y, Chu F, Jia Z, Zhang H, Wang Z, Lu Y, Wang S, Yang G, Qu J. The MRI radiomics signature can predict the pathologic

response to neoadjuvant chemotherapy in locally advanced esophageal squamous cell carcinoma. *Eur Radiol* 2024; **34**: 485-494 [*RCA*] [PMID: 37540319 DOI: 10.1007/s00330-023-10040-4] [FullText]

16 **Qu J**, Shen C, Qin J, Wang Z, Liu Z, Guo J, Zhang H, Gao P, Bei T, Wang Y, Liu H, Kamel IR, Tian J, Li H. The MR radiomic signature can predict preoperative lymph node metastasis in patients with esophageal cancer. *Eur Radiol* 2019; **29**: 906-914 [*RCA*] [PMID: 30039220 DOI: 10.1007/s00330-018-5583-z] [FullText]

17 **Luo T**, Wan J, Liu S, Wang X, Zhou P, Xue Q, Hou J, Wang P. Establishment of a scoring model for predicting clinical outcomes in patients with unilateral primary aldosteronism after superselective adrenal artery embolization. *Ir J Med Sci* 2024; **193**: 2269-2279 [*RCA*] [PMID: 38856963 DOI: 10.1007/s11845-024-03730-5] [FullText]

18 **Yan X**, Fu X, Gui Y, Chen X, Cheng Y, Dai M, Wang W, Xiao M, Tan L, Zhang J, Shao Y, Wang H, Chang X, Lv K. Development and validation of a nomogram model based on pretreatment ultrasound and contrast-enhanced ultrasound to predict the efficacy of neoadjuvant chemotherapy in patients with borderline resectable or locally advanced pancreatic cancer. *Cancer Imaging* 2024; **24**: 13 [*RCA*] [PMID: 38245789 DOI: 10.1186/s40644-024-00662-2] [FullText]

19 **Visser E**, van Rossum PSN, Ruurda JP, van Hillegersberg R. Impact of Lymph Node Yield on Overall Survival in Patients Treated With Neoadjuvant Chemoradiotherapy Followed by Esophagectomy for Cancer: A Population-based Cohort Study in the Netherlands. *Ann Surg* 2017; **266**: 863-869 [*RCA*] [PMID: 28742691 DOI: 10.1097/SLA.0000000000002389] [FullText]

20 **Booka E**, Takeuchi H, Nishi T, Matsuda S, Kaburagi T, Fukuda K, Nakamura R, Takahashi T, Wada N, Kawakubo H, Omori T, Kitagawa Y. The Impact of Postoperative Complications on Survivals After Esophagectomy for Esophageal Cancer. *Medicine (Baltimore)* 2015; **94**: e1369 [*RCA*] [PMID: 26287423 DOI: 10.1097/MD.0000000000001369] [FullText] [Full Text(PDF)]

21 **van Rossum PSN**, van Hillegersberg R, Lever FM, Lips IM, van Lier AL, Meijer GJ, van Leeuwen MS, van Vulpen M, Ruurda JP. Imaging strategies in the management of oesophageal cancer: what's the role of MRI? *Eur Radiol* 2013; **23**: 1753-1765 [*RCA*] [PMID: 23404138 DOI: 10.1007/s00330-013-2773-6] [FullText]

22 **Dong X**, Chunrong Y, Hongjun H, Xuexi Z. Differentiating the lymph node metastasis of breast cancer through dynamic contrast-enhanced magnetic resonance imaging. *BJR Open* 2019; **1**: 20180023 [*RCA*] [PMID: 33178917 DOI: 10.1259/bjro.20180023] [FullText] [Full Text (PDF)]

23 **Brown AM**, Nagala S, McLean MA, Lu Y, Scoffings D, Apte A, Gonen M, Stambuk HE, Shaha AR, Tuttle RM, Deasy JO, Priest AN, Jani P, Shukla-Dave A, Griffiths J. Multi-institutional validation of a novel textural analysis tool for preoperative stratification of suspected thyroid tumors on diffusion-weighted MRI. *Magn Reson Med* 2016; **75**: 1708-1716 [*RCA*] [PMID: 25995019 DOI: 10.1002/mrm.25743] [FullText] [Full Text(PDF)]

24 **Hou Z**, Li S, Ren W, Liu J, Yan J, Wan S. Radiomic analysis in T2W and SPAIR T2W MRI: predict treatment response to chemoradiotherapy in esophageal squamous cell carcinoma. *J Thorac Dis* 2018; **10**: 2256-2267 [*RCA*] [PMID: 29850130 DOI: 10.21037/jtd.2018.03.123] [Full Text]

25 **van Rossum PSN**, Xu C, Fried DV, Goense L, Court LE, Lin SH. The emerging field of radiomics in esophageal cancer: current evidence and future potential. *Transl Cancer Res* 2016; **5**: 410-423 [*RCA*] [PMID: 30687593 DOI: 10.21037/tcr.2016.06.19] [FullText]

26 **Wu L**, Wang C, Tan X, Cheng Z, Zhao K, Yan L, Liang Y, Liu Z, Liang C. Radiomics approach for preoperative identification of stages I-II and III-IV of esophageal cancer. *Chin J Cancer Res* 2018; **30**: 396-405 [*RCA*] [PMID: 30210219 DOI: 10.21147/j.issn.1000-9604.2018.04.02] [FullText] [Full Text(PDF)]

27 **Lei X**, Cao Z, Wu Y, Lin J, Zhang Z, Jin J, Ai Y, Zhang J, Du D, Tian Z, Xie C, Yin W, Jin X. Preoperative prediction of clinical and pathological stages for patients with esophageal cancer using PET/CT radiomics. *Insights Imaging* 2023; **14**: 174 [*RCA*] [PMID: 37840068 DOI: 10.1186/s13244-023-01528-0] [FullText]

World Journal of Radiology

Submit a Manuscript: https://www.f6publishing.com

World J Radiol 2025 August 28; 17(8): 110407

DOI: 10.4329/wjr.v17.i8.110407

ISSN 1949-8470 (online)

ORIGINAL ARTICLE

Prospective Study

Ultra-low dose computed tomography chest *vs* chest radiography in paediatric primary ciliary dyskinesia: A prospective study

Michael G Waldron, Patrick W O'Regan, Michael Lane, Sahil S Shet, Eid Kakish, Fiachra Moloney, Niamh Moore, Mary Jane Murphy, Louise Beagan, Barry J Plant, David Mullane, Muireann Ni Chroinin, David J Ryan, Kevin O'Regan, Stephen P Power, Michael M Maher

Specialty type: Radiology, nuclear medicine and medical imaging

Provenance and peer review: Invited article; Externally peer reviewed.

Peer-review model: Single blind

Peer-review report's classification

Scientific Quality: Grade B
Novelty: Grade B
Creativity or Innovation: Grade C
Scientific Significance: Grade B

P-Reviewer: Tabakoğlu NT

Received: June 7, 2025
Revised: June 23, 2025
Accepted: July 23, 2025
Published online: August 28, 2025
Processing time: 83 Days and 22 Hours

Michael G Waldron, Patrick W O'Regan, Fiachra Moloney, David J Ryan, Kevin O'Regan, Stephen P Power, Michael M Maher, Department of Radiology, Cork University Hospital, Cork T12 DC4A, Ireland

Michael Lane, David Mullane, Muireann Ni Chroinin, Department of Paediatrics, Cork University Hospital, Cork T12 DC4A, Ireland

Sahil S Shet, Eid Kakish, Niamh Moore, Department of Radiology, School of Medicine, University College Cork, Cork T12 AK54, Ireland

Mary Jane Murphy, Louise Beagan, Department of Radiography, Cork University Hospital, Cork T12 DC4A, Ireland

Barry J Plant, Department of Respiratory Medicine, Cork University Hospital, Cork T12 DC4A, Ireland

Corresponding author: Sahil S Shet, Lecturer, Research Fellow, Department of Radiology, School of Medicine, University College Cork, College Road, Cork T12 AK54, Ireland. sshet@ucc.ie

Abstract

BACKGROUND

Primary ciliary dyskinesia (PCD) is a rare condition characterised by dysmotile, immotile, or absent cilia. As a result of the impairment in respiratory mucociliary clearance, patients with PCD typically develop neonatal respiratory distress, nasal congestion, otitis media and recurrent respiratory infections leading to bronchiectasis and structural lung changes. These changes have been shown by chest computed tomography (CT) to develop in infancy and early childhood. Recent development and refinement of radiation-reducing CT techniques have allowed significant radiation dose reductions, with chest CT doses now in the range of chest radiography (CR).

AIM

To evaluate the efficacy of ultra-low dose CT (ULDCT) chest in identifying pulmonary changes within a PCD paediatric patient cohort.

METHODS
Paediatric patients with PCD who presented for routine clinical outpatient follow-up within the study period, were eligible for inclusion in the study. ULDCT and CR were performed on these patients and the results compared. Comparison metrics included radiation dose, subjective and objective image quality and disease severity.

RESULTS
Six paediatric patients (mean age 9 years) underwent clinically indicated ULDCT chest examinations and CR for surveillance of their PCD. The mean effective dose was 0.08 ± 0.02 mSv, a dose that approximates that of a frontal and lateral chest radiograph. The average Brody II score across the entire cohort was 12.92, with excellent inter-rater reliability and intra-class correlation coefficient (ICC) of 0.98. The average Chrispin-Norman score on CR was 1 with excellent inter-rater reliability and ICC of 0.92.

CONCLUSION
ULDCT demonstrates superior diagnostic capabilities, minimal radiation dose penalty, and high interobserver reliability in comparison to CR. Thus, we advocate for ULDCT to be the preferred modality for surveillance imaging in paediatric PCD.

Key Words: Primary ciliary dyskinesia; Ultra-low dose computed tomography; Chest radiography; Radiation dose; Image quality

Core Tip: Ultra-low dose computed tomography (ULDCT) is an exciting technique developed over the last decade that allows acquisition of diagnostic quality images at remarkably low radiation doses. This technique is especially important in patients requiring regular repeated imaging such as children with primary ciliary dyskinesia (PCD). Patients with PCD frequently suffer from recurrent respiratory tract infections and develop structural lung changes that require regular imaging to monitor. While chest radiography is traditionally used, subtle findings may be missed due to limitations of this modality. Our study offers an alternative; ULDCT which is superior in diagnostic capability with a minimal radiation dose penalty.

Citation: Waldron MG, O'Regan PW, Lane M, Shet SS, Kakish E, Moloney F, Moore N, Murphy MJ, Beagan L, Plant BJ, Mullane D, Ni Chroinin M, Ryan DJ, O'Regan K, Power SP, Maher MM. Ultra-low dose computed tomography chest *vs* chest radiography in paediatric primary ciliary dyskinesia: A prospective study. *World J Radiol* 2025; 17(8): 110407
URL: https://www.wjgnet.com/1949-8470/full/v17/i8/110407.htm
DOI: https://dx.doi.org/10.4329/wjr.v17.i8.110407

INTRODUCTION

Primary ciliary dyskinesia (PCD) is a rare, primarily autosomal recessive, inherited condition characterised by dysmotile, immotile, or absent cilia[1]. As a result of the impairment in respiratory mucociliary clearance, patients with PCD typically develop neonatal respiratory distress, nasal congestion, otitis media and recurrent respiratory infections leading to bronchiectasis[2]. A laterality defect, male infertility and congenital heart disease are also commonly associated with PCD[3].

Correct diagnosis of PCD can present challenges as its clinical manifestations mimic that of other diseases such as cystic fibrosis (CF), primary immunodeficiencies and asthma[4]. A knowledge of the disease manifestations and robust diagnostics are important to avoid delayed or incorrect diagnosis[5]. There is no specific single gold-standard test to diagnose PCD, and it requires multiple investigations such as genetic testing, mucosal biopsies, nasal nitric oxide levels and electron microscopy[6,7]. Management of PCD draws from the treatment strategies employed for CF and non-CF bronchiectasis and includes respiratory physiotherapy, comprehensive treatment of acute infections, lifestyle management and even lung transplant for end stage disease[8].

Structural lung changes such as mucus plugging, bronchial wall thickening, atelectasis, and bronchiectasis have been shown by chest computed tomography (CT) to develop in infancy and early childhood in patients with PCD[9-11]. Chest CT has increased sensitivity over pulmonary function tests in diagnosing early lung disease in PCD[12]. A cornerstone of PCD management is regular surveillance and prompt treatment of any pulmonary exacerbation to minimise or prevent the establishment of permanent lung damage. In an inherently young PCD patient cohort that will receive early and regular diagnostic and surveillance chest CTs, it is prudent to minimise exposure to ionising radiation[13]. There has been recent development and subsequent refinement of radiation-reducing CT techniques that have allowed significant radiation dose reductions, with chest CT doses in the range of chest radiography[14-16]. The continued assurance of diagnostic integrity of these reduced-dose protocols is clearly of paramount importance.

This study is designed to prospectively evaluate ultra-low dose CT (ULDCT) chest in identifying pulmonary changes within a paediatric PCD cohort in comparison to chest radiography.

MATERIALS AND METHODS

Study design and setting

This prospective study received approval from the local institutional review board (Clinical Research Ethics Committee Reference Number: ECM 4 (n) 12/11/2019 & ECM 3 (ll) 28/06/2022). Written informed consent was obtained from each patient or their guardian prior to participation.

Study population

Paediatric patients with PCD between the ages of 4 and 16 years, who presented for routine clinical outpatient follow-up between July 1, 2022 and July 1, 2023, were eligible for inclusion in the study. The patients were scheduled to undergo a clinically indicated surveillance ULDCT of the chest. Those who did not have a recent chest radiograph had one performed in addition to the CT chest.

Study protocol

ULDCT Chest was performed on a single Aquilion Prime SP CT Scanner (Canon Medical Systems, Otawara, Tochigi, Japan). Only one lateral scout performed at 80Kv and 10mA. The ultra-low dose helical CT scan was performed with the following acquisition parameters; 120 Kv, 10 mA, 0.35 second rotation time, small focus, standard pitch factor of 0.813, standard helical pitch of 65 and thickness of 0.5 × 80. Images were reconstructed in 2 mm and 1 mm soft tissue and lung windows.

All images were acquired on inspiration to include lung apex to diaphragm and no additional expiration views were obtained. No conscious sedation or general anaesthesia were utilised. Spirometry assisted CT was not performed. Patients received coaching from a respiratory physiotherapist with satisfactory outcome in breath holding.

CT image assessment

Disease severity: For the evaluation of PCD severity using chest CT, we utilized the Brody II CT scoring system[17]. The Brody II score comprises five components: Bronchiectasis, mucus plugging, peri-bronchial thickening, parenchymal abnormalities, and air trapping. Each component is evaluated based on the extent of involvement in central and peripheral lung areas and specific severity criteria. Bronchiectasis is scored from 1-12, considering the extent in both lung areas and bronchiectasis size, with multipliers ranging from 0.5 to 3. Mucus plugging is scored from 0-6, again based on the extent in both lung areas. Peribronchial thickening, scored from 0-9 and considers the extent and severity (mild, moderate, severe) in both lung areas. The parenchyma score, ranging from 0-9, is based on the extent of dense parenchymal opacity, ground glass opacity, and cysts or bullae. Lastly, air trapping is scored from 0-4.5, reflecting the extent of lung involvement and the size of affected areas. Our approach did not assess air trapping as to minimise radiation exposure, expiratory CT examinations were not acquired. This scoring system provides a detailed and standardized assessment of disease severity in PCD patients, enabling accurate comparisons within our study cohort.

Subjective image quality: Subjective image quality was assessed on a Picture Archiving and Communication System (Impax 6.5.3; Agfa Health- care, Mortsel, Belgium) on a monitor with a resolution of 3 megapixels.

Diagnostic acceptability on both soft tissue and lung windows, image noise on both soft tissue and lung windows, depiction of bronchovascular structures centrally and within 2 cm of the pleural surface and streak artefact were assessed by consensus by 2 radiologists utilising a previously validated subjective scoring system[14,15].

Briefly, images were graded on a scale of 1-5 with 1 = unacceptable, 2 = minimally acceptable, 3 = acceptable, 4 = highly acceptable and 5 = excellent. This assessment was carried out on six different levels of each CT scan; at the level of the apices, aortopulmonary window, carina, largest cardiac diameter, largest thoracic diameter, and upper abdomen (on soft tissue window assessment). Again, images were anonymised and randomly assessed to minimise bias.

Objective image quality: Objective image quality analysis was conducted on a dedicated workstation (Advantage Workstation VolumeShare 2, Version 4.4, GE Medical Systems) using previously validated quantitative signal to noise measurements by placing homogenous region of interests (ROIs) (diameter 10 mm) in predefined homogenous anatomic locations[14]. These ROIs were placed on the thoracic aorta and right paraspinal musculature at the level of the aortic arch, carina, and largest cardiac diameter. Each measurement was taken on three consecutive slices of the CT series and a mean value calculated to ensure accuracy. The mean attenuation value in Hounsfield units (HU) within the ROI and the standard deviation represented the signal and noise level, respectively. The signal-to-noise ratio (SNR) within each ROI was calculated by dividing mean HU by standard deviation.

A subgroup of 2 of the patients in this study had previously undergone modified low dose CT chest examinations prior to this study and these examinations [mean age 22 months and mean dose-length product (DLP) 10.5 mGycm] will serve as a baseline comparison/internal control group for image quality assessment.

Chest radiograph image assessment: The severity of pulmonary changes in chest radiographs was quantified with the Modified Chrispin-Norman score, with a possible range of 0 to 38[18,19]. Readers conducting the chest radiograph assessment were blinded to the ULDCT chest result. This scoring system evaluates five radiological parameters: Overin-

flation, bronchial line shadows, ring shadows, mottled shadows, and large soft shadows. Each parameter consists of specific elements that are assessed within different lung zones (right upper, left upper, right lower, and left lower). For overinflation, elements such as diaphragmatic depression, chest wall shape, and lung field appearance are scored. Each element within the parameters is rated on a scale from 0 to 2, where 0 signifies 'Not Present', 1 denotes 'Present, not marked', and 2 indicates 'Marked' presence of the feature.

Radiation dose assessment: The radiation dose delivered to the patient in each CT was calculated in terms of volumetric CT dose index ($CTDI_{vol}$), DLP, size-specific dose estimate (SSDE) as per American Association of Physicists in Medicine, and effective dose (ED) was calculated by multiplying the DLP by an age specific multiplier for CT chest[20,21].

Clinical assessment: Comprehensive clinical data were collected for each participant to facilitate a thorough analysis of disease characteristics and treatment outcomes. Demographic information included gender and date of birth. Pulmonary function was assessed using spirometry measurements: Forced expiratory volume in one second (FEV^1) and forced vital capacity (FVC), recorded both in litres (L) and as a percentage of the predicted values for the patient's age, gender, and height. The frequency of pulmonary exacerbations, particularly those necessitating intravenous antibiotic treatment, was recorded to evaluate disease severity and progression. Nutritional status was assessed using body mass index (BMI), Weight in kilograms, and weight centile, aligning with age-specific growth charts. Additionally, airway microbial composition was analysed to identify predominant bacterial colonisations or infections. This holistic approach to data collection aimed to capture a broad spectrum of clinical variables that influence the course and management of PCD.

Statistical analysis

Statistical analyses were carried out using statistical package for the social sciences (SPSS) version 29 (IBM SPSS Inc., Chicago, Il). Data were exported from Microsoft Office Excel (Microsoft Corporation, CA, United States) into SPSS for statistical analysis. For continuous variables, normality testing was first conducted using a Shapiro-Wilk test. Data are presented as mean ± SD unless otherwise specified.

Inter-rater agreement for ordinal-scaled Brody II ratings was estimated with Krippendorff alpha using the ordinal difference function, and calculated 95%CIs using percentile bootstrap intervals with 10000 bootstrap samples to account for clustering. Inter-rater agreement of the total Brody II scores was estimated using the intraclass correlation coefficient (ICC) with 95%CI. ICC values below 0.5 indicate poor reliability, between 0.5 and 0.75 moderate reliability, between 0.75 and 0.9 good reliability, and above 0.9 excellent reliability.

CT and radiograph image quality metrics were reported using descriptive statistics.

RESULTS

Study population

6 paediatric patients (67% male) underwent clinically indicated ULDCT chest examinations, with an additional CR if not already recently performed, for surveillance of their PCD. The patient ages were 4, 6, 6, 7, 11 and 16.

Clinical analysis

Mean FEV^1 was 98.6 ± 7.5% predicted and 2.1 ± 1.1 L. The mean FVC was 99 ± 2.9% predicted and 2.0 ± 0.6 L.

Patients experienced a mean 4 ± 3.8 pulmonary exacerbations requiring intravenous antibiotics per year. Mean BMI was 19.8 ± 4.6 kg/m^2 with a mean weight of 34.8 ± 14.8 kg and mean percentile for weight of 66 ± 34 percentile. The predominant airway microbial identified was pseudomonas aeruginosa (50%).

Radiation dose analysis

The mean ULDCT chest $CTDI_{vol}$ was 0.11 ± 0 mGy. The mean DLP was 2.11 ± 0.35 mGycm. The mean SSDE was 0.18 ± 0.02 mGy. The mean ED was 0.08 ± 0.02 mSv. In comparison, the mean ED from CR was 0.03 mSv ± 0.03 mSv.

Image analysis

CT disease severity: The average Brody II CT score across the entire cohort was 12.92, with excellent inter-rater reliability and ICC of 0.98 (95%CI: 0.87, 0.99). Inter-rater reliability of each component of the Brody II score in terms of Krippendorff alpha was good for mucus plugging (0.8) and parenchymal opacity (0.79) and poor for bronchiectasis (0.34) and peribronchial thickening (0.34) (Table 1).

Figure 1 demonstrates representative ULDCT chest images of a 7-year-old female patient with PCD and the protocol's ability to identify associated structural lung pathology. Figure 2 demonstrates comparative images of ULDCT chest and a modified low dose CT chest in the same patient obtained 7 years apart. The assessment of lung structure is acceptable in our ultra-low dose protocol with greater noise being evident in the mediastinum on soft tissue windows.

CT subjective image quality: The mean of both readers subjective quality scores was utilised for image quality assessment.

Subjective image quality was acceptable to highly acceptable on all categories. There were comparable quality scores in the small 2-patient subgroup who underwent prior modified low dose CT imaging (Table 2).

Table 1 Inter-rater reliability of Brody II score

Brody II criteria	Inter-rater reliability
Bronchiectasis	0.34 (-0.46–0.87)
Peribronchial thickening	0.34 (-0.33–0.92)
Mucus plugging	0.8 (0.52–0.99)
Parenchymal opacity	0.79 (0.67–0.91)
Air trapping	Not assessed

Inter-rater reliability calculated using the Krippendorff alpha with bootstrapping to account for clustering. 95%CIs in parentheses.

Table 2 Subjective image quality

Mean subjective image quality score	Image noise lung windows	Image noise soft tissue windows	Central bronchovascular structure depiction	Peripheral (within 2 cm of parietal pleura) bronchovascular structure depiction	Streak artifact	Overall diagnostic acceptability on lung windows	Overall diagnostic acceptability on soft tissue windows
Overall	4.1 ± 0.49	3.2 ± 0.06	3.9 ± 0.91	3.5 ± 1.12	3.3 ± 0.15	3.9 ± 1.07	3.3 ± 0.11
2-patient subgroup	3.5 ± 0.71	2.8 ± 0.05	3.9 ± 0.14	3.7 ± 0.21	3.4 ± 0.77	3.8 ± 0.28	3.0 ± 0.29

CT objective image quality: The mean SNR at the level of the arch, carina, and largest cardiac diameter for the ULDCT chest examinations were 1.38 ± 2.89, 1.82 ± 1.61 and 1.03 ± 1.7 respectively. For the 2-patient internal control subgroup that previously underwent modified low dose CT chest examinations prior to this study, the mean SNR at the level of the arch, carina, and largest cardiac diameter were 1.06 ± 0.19, 0.96 ± 0.36 and 1.05 ± 0.43 respectively (Figure 3).

Chest radiograph disease severity: The average Chrispin-Norman score on chest radiograph was 1 with excellent inter-rater reliability and ICC of 0.92 (95%CI: 0.41, 0.99).

DISCUSSION

This study illustrates the potential of ULDCT chest in paediatric patients with PCD to produce diagnostic-quality images capable of identifying key PCD-related pulmonary features, including bronchiectasis, peri-bronchial thickening, and airspace opacities, some of which are seen in Figures 1 and 2. These images facilitate relatively consistent and reproducible evaluations using the Brody II CT score that is superior to chest radiography, without a significant radiation penalty.

Our patient cohort demonstrated expected clinical characteristics of a PCD patient cohort including satisfactory PFTs, an expected average number of pulmonary exacerbations requiring hospital care annually and typical airway microbials. The spectrum of disease in PCD is like that of CF and utilising a CF specific scoring system to assess disease burden is a reasonable approach. Magnetic resonance imaging (MRI) based lung clearance index has been proposed as a possible reliable disease monitoring metric in PCD[22]. This, however, has the associated practical limitations of MRI in a paediatric population in terms of sedation, cost, expertise and limited access to appropriate MRI infrastructure.

It has been proposed that CF specific CT scoring systems do not capture the entirety of the PCD disease process[23]. Rademacher *et al*[24] were one of the first to describe a PCD specific CT scoring system (PCD-CT) in adults in 2021 and further work was carried out by Chowdhary *et al*[25] having proposed the Specific PCD Evaluation by CT (SPEC) score in a cohort of 30 patients that correlated well with PFTs. The PCD-CT scoring system was developed by evaluating several imaging markers of lung disease including mucus plugging, tree-in-bud pattern, atelectasis, peripheral and central consolidations, peripheral and central ground glass opacities, interlobular septal thickening, mosaic attenuation, cavities, emphysema and fibrosis. Using multivariate logistic regression, 5 variables: Absence of fibrosis and emphysema, predominance of bronchiectasis in the middle/Lower lobe and atelectasis, tree-in-bud pattern, and atelectasis or history of resection of a middle/Lower lobe were selected for the final scoring system. In contrast, the SPEC scoring system has several overlapping elements with the Brody II scoring system such as bronchiectasis severity and extent, extent of bronchial wall thickening, presence of atelectasis and presence of air trapping. In addition, each lobe is evaluated separately just like the Brody II scoring system. However, the SPEC system also assesses bronchoceles, the extent of tree-in-bud pattern of mucus plugging and the presence of interlobar septal thickening. The additional elements aim to cater

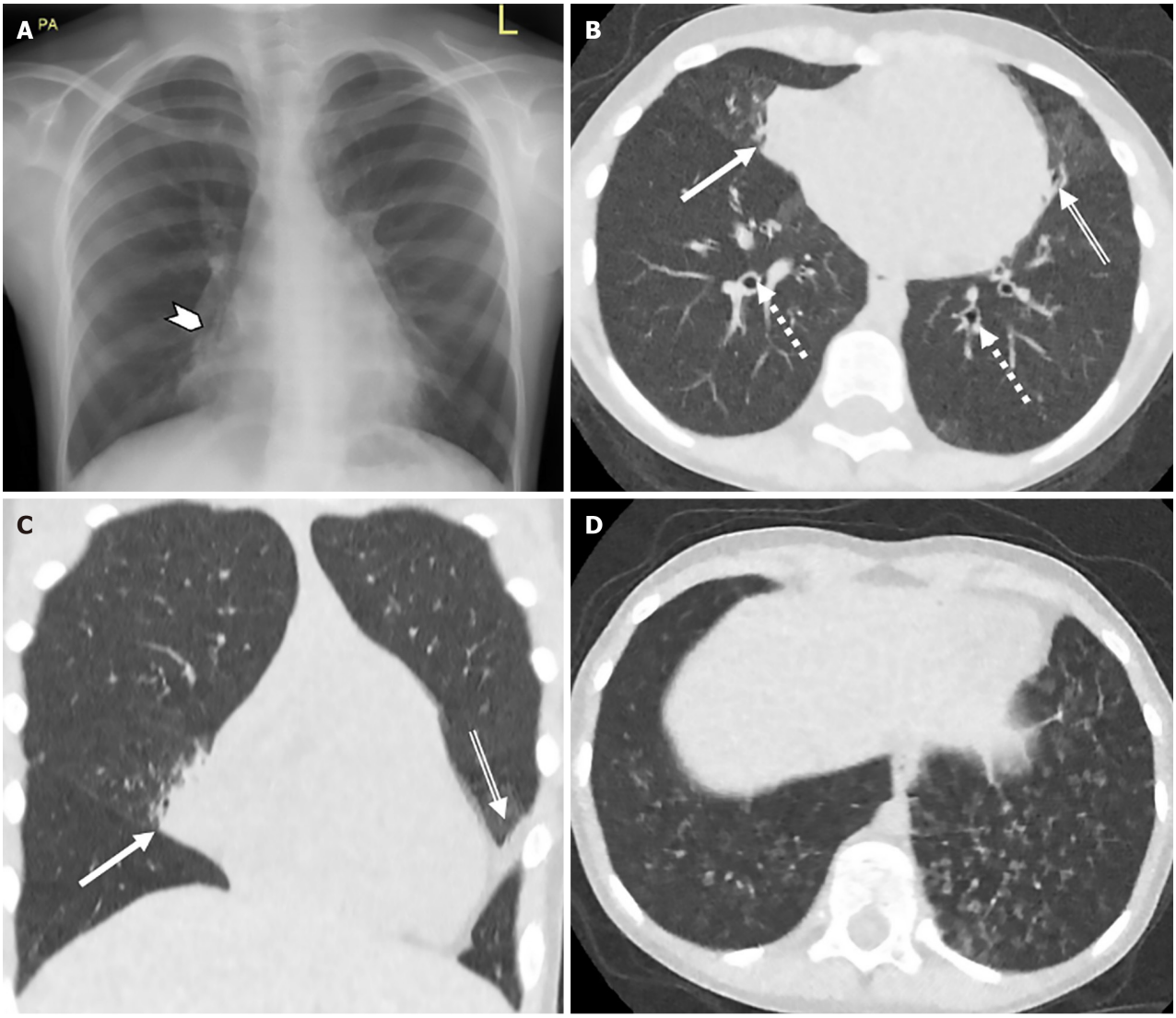

Figure 1 Chest radiography and ultra-low dose computed tomography chest assessment of structural lung pathology. A: Chest radiography; B: Axial ultra-low dose computed tomography (ULDCT); C: Coronal ULDCT; D: Axial ULDCT with lung windows of a 7-year-old female with dense medial middle lobe consolidation (solid arrow & arrowhead), bilateral bronchiectasis (dashed arrow), lingular atelectasis (double line arrow) and basal centrilobular ground-glass nodules (D). These representative images demonstrate the superiority of ULDCT in assessment of structural changes relating to primary ciliary dyskinesia in comparison to plain radiography.

specifically to the PCD pattern of disease. While the initial results for both scoring systems show promise with strong correlation to pulmonary function tests, they remain less well established than the Brody II score. Additionally, neither of these scoring systems have been compared directly with the Brody II score to evaluate any differences in performance[24,25]. Therefore, our study utilised the Brody II CF scoring system, which has previously been well established in PCD cohorts, to minimise unknown variables in the assessment of our novel ULDCT chest protocol[9,10].

As seen in Table 1, inter-rater reliability for both overall Brody II score on CT and Chrispin Norman score on CR was excellent. On more detailed analysis of the specific elements of the Brody II score, there was poor inter-rater reliability when assessing bronchiectasis and peri-bronchial thickening. A likely cause for this is the relatively mild disease burden of this young patient group and the inherent subjective nature of scoring systems.

Quantitative analysis of airway dilation and airway to artery ratios have been demonstrated in 13 paediatric patients with PCD in comparison with healthy controls, highlighting the potential benefit of novel software developments in the routine assessment of PCD patients[26]. Interestingly, in this study, airway thickening was not a predominant feature.

Objective and subjective image quality is grossly comparable to the small internal control group who underwent prior modified low dose CT chest examination prior to this study (Table 2, Figure 3). The ability to conduct CT examinations at such low radiation doses (mean ED 0.08 mSv), in combination with the added diagnostic value compared to CR, suggests substantial implications for PCD imaging guidelines.

This study highlights the potential significant radiation dose saving available with the application of relatively straightforward imaging protocol adjustments, without compromising diagnostic integrity. ULDCT chest will establish and maintain a central role in paediatric PCD diagnostics going forward. However, ULDCT may be further improved by a revolutionary new CT technology: The photon counting CT (PCCT). This technology makes use of photon counting

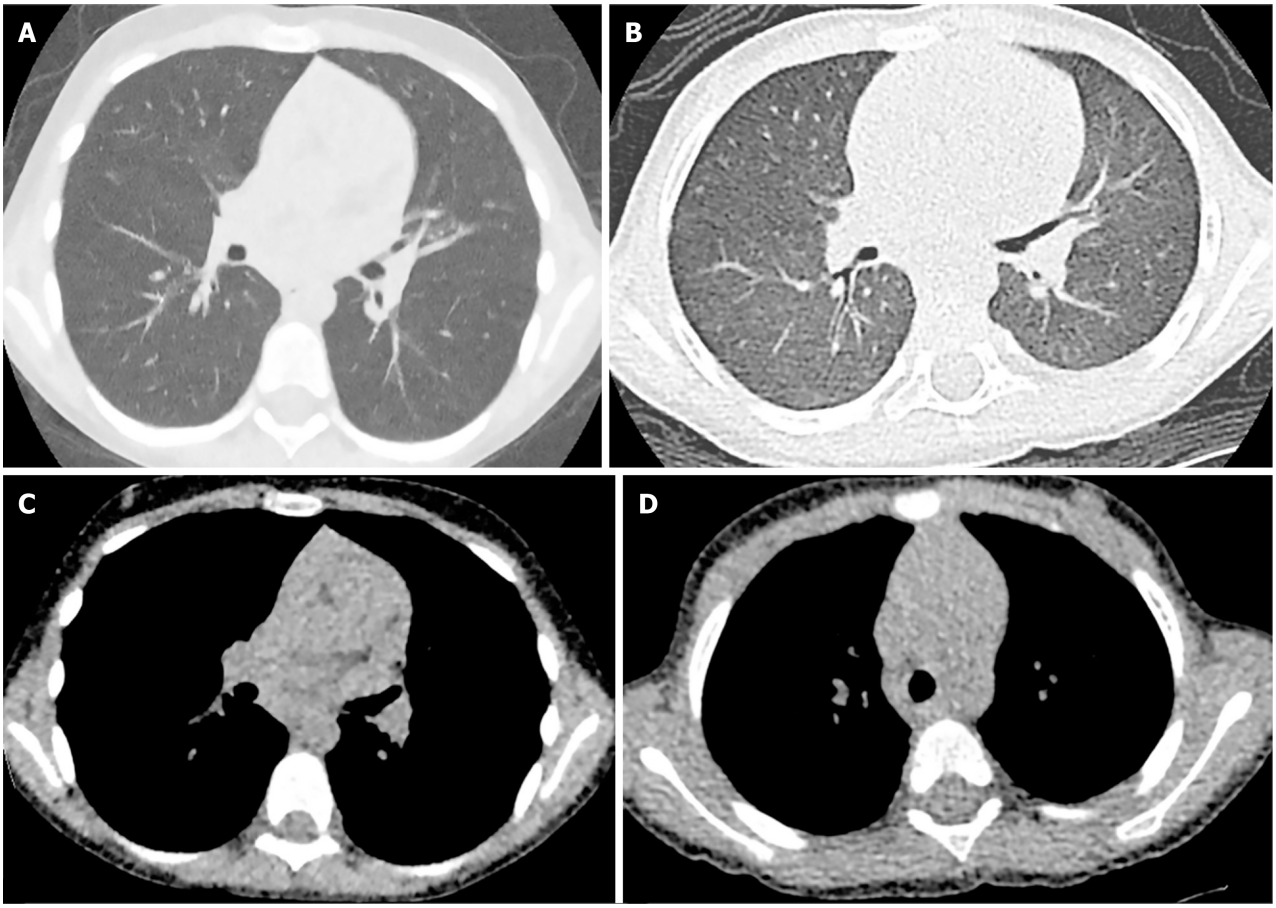

Figure 2 Comparison of ultra-low dose computed tomography chest and modified low dose computed tomography chest protocols. A-D: Comparison of axial ultra-low dose chest computed tomography (CT) in lung windows (A) and soft tissue windows (C) and modified low dose chest CT images in lung windows (B) and soft tissue windows (D) in the same paediatric patient acquired 7 years apart. These images demonstrate the acceptable assessment of lung structure in ULDCT chest imaging.

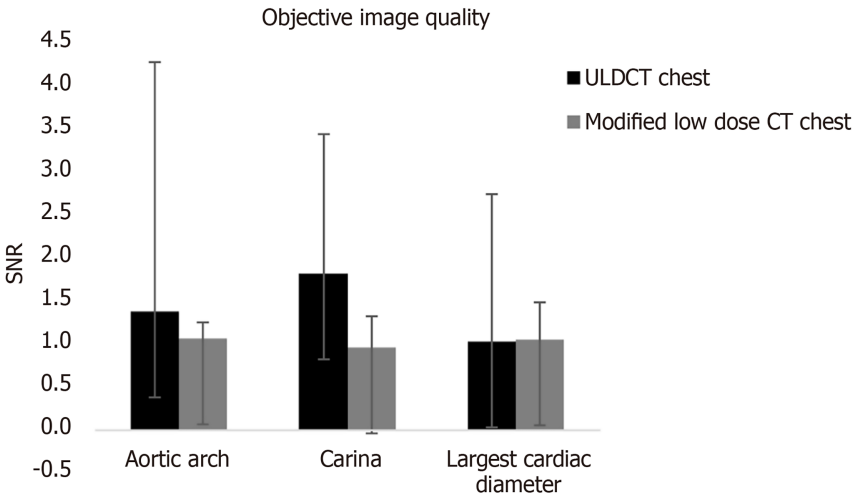

Figure 3 Objective image quality comparison. Chart depicting mean signal to noise ratio (SNR) for the ultra-low dose CT (ULDCT) Chest and modified low dose CT chest protocols at each of the three levels assessed. Data are plotted as mean and standard deviation as indicated by error bars. A comparable to improved SNR is evident in our novel ULDCT Chest protocol. SNR: Signal to noise ratio; ULDCT: Ultra-low dose computed tomography; CT: Computed tomography.

detectors in place of the standard energy integrating detectors and shows great improvement in image resolution while reducing radiation dose. Indeed, in the paediatric chest, PCCT offers improved visualisation of peripheral airways, the bronchial wall and the bronchial segments, all of which may be useful in monitoring progression of PCD[27,28]. Furthermore, application of low dose image acquisition protocols to CT scanners with photon counting detectors shows greater reductions in radiation dose levels with reduced image noise when compared with standard energy integrating

detectors[29]. However, although promising for future use in PCD diagnostics and follow-up, this technology is unfortunately limited by its scarce availability and high cost[30].

The strength of this study lies in its prospective design and the blinded image assessment of two consultant radiologists. This single centre study is limited with a small sample size, however, PCD remains a relatively rare condition.

CONCLUSION

ULDCT offers a viable alternative to conventional imaging for patients with PCD providing diagnostic quality images at a dose equivalent to a frontal and lateral CR. These low-dose images can be reliably assessed with the Brody II scoring system and offer superior diagnostic capability compared to CR. This study reinforces the limitations of CR and further supports the integration of ULDCT into routine care with potential for further enhancement through new technologies such as the photon counting CT. Although this study has limitations such as a small sample size and a single centre cohort, the prospective design and blinded scoring strengthen the findings. Future research may be directed towards validation of ULDCT in larger multicentre cohorts and assessment of newer technologies such as the photon counting CT in a PCD specific cohort.

FOOTNOTES

Author contributions: Waldron MG contributed to investigation; Waldron MG and O'Regan PW contributed to writing - original draft; O'Regan PW contributed to visualization; Lane M contributed to data collection; Shet SS, Kakish E, Mullane D, Ni Chroinin M, and O'Regan K contributed to writing - review and editing; Moloney F, Moore N, Beagan L, Plant BJ, Mullane D, and Ni Chroinin M contributed to resources; O'Regan PW and Murphy MJ contributed to data curation; Plant BJ and Ryan DJ contributed to supervision; Plant BJ, Power SP, and Maher MM contributed to validation; Ryan DJ and Power SP contributed to methodology; O'Regan K and Maher MM contributed to project administration; Power SP contributed to formal analysis; Maher MM contributed to conceptualization.

Institutional review board statement: This prospective study received approval from the local institutional review board (Clinical Research Ethics Committee Reference Number: ECM 4 (n) 12/11/2019 & ECM 3 (ll) 28/06/2022).

Informed consent statement: Written informed consent was obtained from each patient or their guardian prior to participation.

Conflict-of-interest statement: There is no conflict of interest associated with any of the authors who contributed their efforts in this manuscript.

Data sharing statement: The data that support the findings of this study are available on request from the corresponding author.

CONSORT 2010 statement: The authors have read the CONSORT 2010 Statement, and the manuscript was prepared and revised according to the CONSORT 2010 Statement.

Country of origin: Ireland

ORCID number: Sahil S Shet 0000-0003-3104-7234; Mary Jane Murphy 0000-0001-5467-309X; Michael M Maher 0000-0001-7423-7439.

S-Editor: Liu JH
L-Editor: A
P-Editor: Yu HG

REFERENCES

1 **Knowles MR**, Zariwala M, Leigh M. Primary Ciliary Dyskinesia. *Clin Chest Med* 2016; **37**: 449-461 [*RCA*] [PMID: 27514592 DOI: 10.1016/j.ccm.2016.04.008] [FullText]

2 **Leigh MW**, Ferkol TW, Davis SD, Lee HS, Rosenfeld M, Dell SD, Sagel SD, Milla C, Olivier KN, Sullivan KM, Zariwala MA, Pittman JE, Shapiro AJ, Carson JL, Krischer J, Hazucha MJ, Knowles MR. Clinical Features and Associated Likelihood of Primary Ciliary Dyskinesia in Children and Adolescents. *Ann Am Thorac Soc* 2016; **13**: 1305-1313 [*RCA*] [PMID: 27070726 DOI: 10.1513/AnnalsATS.201511-748OC] [FullText]

3 **Horani A**, Ferkol TW. Understanding Primary Ciliary Dyskinesia and Other Ciliopathies. *J Pediatr* 2021; **230**: 15-22.e1 [*RCA*] [PMID: 33242470 DOI: 10.1016/j.jpeds.2020.11.040] [FullText]

4 **Shapiro AJ**, Davis SD, Polineni D, Manion M, Rosenfeld M, Dell SD, Chilvers MA, Ferkol TW, Zariwala MA, Sagel SD, Josephson M, Morgan L, Yilmaz O, Olivier KN, Milla C, Pittman JE, Daniels MLA, Jones MH, Janahi IA, Ware SM, Daniel SJ, Cooper ML, Nogee LM,

Anton B, Eastvold T, Ehrne L, Guadagno E, Knowles MR, Leigh MW, Lavergne V; American Thoracic Society Assembly on Pediatrics. Diagnosis of Primary Ciliary Dyskinesia. An Official American Thoracic Society Clinical Practice Guideline. *Am J Respir Crit Care Med* 2018; **197**: e24-e39 [*RCA*] [PMID: 29905515 DOI: 10.1164/rccm.201805-0819ST] [FullText]

5 **Shapiro AJ**, Zariwala MA, Ferkol T, Davis SD, Sagel SD, Dell SD, Rosenfeld M, Olivier KN, Milla C, Daniel SJ, Kimple AJ, Manion M, Knowles MR, Leigh MW; Genetic Disorders of Mucociliary Clearance Consortium. Diagnosis, monitoring, and treatment of primary ciliary dyskinesia: PCD foundation consensus recommendations based on state of the art review. *Pediatr Pulmonol* 2016; **51**: 115-132 [*RCA*] [PMID: 26418604 DOI: 10.1002/ppul.23304] [FullText] [Full Text(PDF)]

6 **Lucas JS**, Alanin MC, Collins S, Harris A, Johansen HK, Nielsen KG, Papon JF, Robinson P, Walker WT. Clinical care of children with primary ciliary dyskinesia. *Expert Rev Respir Med* 2017; **11**: 779-790 [*RCA*] [PMID: 28745925 DOI: 10.1080/17476348.2017.1360770] [Full Text]

7 **Noone PG**, Leigh MW, Sannuti A, Minnix SL, Carson JL, Hazucha M, Zariwala MA, Knowles MR. Primary ciliary dyskinesia: diagnostic and phenotypic features. *Am J Respir Crit Care Med* 2004; **169**: 459-467 [*RCA*] [PMID: 14656747 DOI: 10.1164/rccm.200303-365OC] [FullText]

8 **Lucas JS**, Carroll M. Primary ciliary dyskinesia and cystic fibrosis: different diseases require different treatment. *Chest* 2014; **145**: 674-676 [*RCA*] [PMID: 24687702 DOI: 10.1378/chest.13-2590] [FullText]

9 **Santamaria F**, Montella S, Tiddens HAWM, Guidi G, Casotti V, Maglione M, de Jong PA. Structural and functional lung disease in primary ciliary dyskinesia. *Chest* 2008; **134**: 351-357 [*RCA*] [PMID: 18403663 DOI: 10.1378/chest.07-2812] [FullText]

10 **Jain K**, Padley SP, Goldstraw EJ, Kidd SJ, Hogg C, Biggart E, Bush A. Primary ciliary dyskinesia in the paediatric population: range and severity of radiological findings in a cohort of patients receiving tertiary care. *Clin Radiol* 2007; **62**: 986-993 [*RCA*] [PMID: 17765464 DOI: 10.1016/j.crad.2007.04.015] [FullText]

11 **Kennedy MP**, Noone PG, Leigh MW, Zariwala MA, Minnix SL, Knowles MR, Molina PL. High-resolution CT of patients with primary ciliary dyskinesia. *AJR Am J Roentgenol* 2007; **188**: 1232-1238 [*RCA*] [PMID: 17449765 DOI: 10.2214/AJR.06.0965] [FullText]

12 **Maglione M**, Bush A, Montella S, Mollica C, Manna A, Esposito A, Santamaria F. Progression of lung disease in primary ciliary dyskinesia: is spirometry less accurate than CT? *Pediatr Pulmonol* 2012; **47**: 498-504 [*RCA*] [PMID: 22006708 DOI: 10.1002/ppul.21569] [FullText]

13 **Joyce S**, Carey BW, Moore N, Mullane D, Moore M, McEntee MF, Plant BJ, Maher MM, O'Connor OJ. Computed tomography in cystic fibrosis lung disease: a focus on radiation exposure. *Pediatr Radiol* 2021; **51**: 544-553 [*RCA*] [PMID: 33743038 DOI: 10.1007/s00247-020-04706-0] [FullText]

14 **O'Connor OJ**, Vandeleur M, McGarrigle AM, Moore N, McWilliams SR, McSweeney SE, O'Neill M, Ni Chroinin M, Maher MM. Development of low-dose protocols for thin-section CT assessment of cystic fibrosis in pediatric patients. *Radiology* 2010; **257**: 820-829 [*RCA*] [PMID: 20876388 DOI: 10.1148/radiol.10100278] [FullText]

15 **Moloney F**, Kavanagh RG, Ronan NJ, Grey TM, Joyce S, Ryan DJ, Moore N, O'Connor OJ, Plant BJ, Maher MM. Ultra-low-dose thoracic CT with model-based iterative reconstruction (MBIR) in cystic fibrosis patients undergoing treatment with cystic fibrosis transmembrane conductance regulators (CFTR). *Clin Radiol* 2021; **76**: 393.e9-393.e17 [*RCA*] [PMID: 33468311 DOI: 10.1016/j.crad.2020.12.003] [FullText]

16 **Sheahan KP**, O'Mahony AT, Morrissy D, Ibrahim H, Crowley C, Waldron MG, Sokol-Randell D, McMahon A, Maher MM, O'Connor OJ, Plant BJ. Replacing Plain Radiograph with ultra-low dose CT thorax in cystic fibrosis (CF) in the era of CFTR modulation and its impact on cumulative effective dose. *J Cyst Fibros* 2023; **22**: 715-721 [*RCA*] [PMID: 37400300 DOI: 10.1016/j.jcf.2023.06.006] [FullText]

17 **Brody AS**, Klein JS, Molina PL, Quan J, Bean JA, Wilmott RW. High-resolution computed tomography in young patients with cystic fibrosis: distribution of abnormalities and correlation with pulmonary function tests. *J Pediatr* 2004; **145**: 32-38 [*RCA*] [PMID: 15238903 DOI: 10.1016/j.jpeds.2004.02.038] [FullText]

18 **Chrispin AR**, Norman AP. The systematic evaluation of the chest radiograph in cystic fibrosis. *Pediatr Radiol* 1974; **2**: 101-105 [*RCA*] [PMID: 15822331 DOI: 10.1007/BF01314939] [FullText]

19 **de Jong PA**, Achterberg JA, Kessels OA, van Ginneken B, Hogeweg L, Beek FJ, Terheggen-Lagro SW. Modified Chrispin-Norman chest radiography score for cystic fibrosis: observer agreement and correlation with lung function. *Eur Radiol* 2011; **21**: 722-729 [*RCA*] [PMID: 20924586 DOI: 10.1007/s00330-010-1972-7] [FullText] [Full Text(PDF)]

20 **Romanyukha A**, Folio L, Lamart S, Simon SL, Lee C. BODY SIZE-SPECIFIC EFFECTIVE DOSE CONVERSION COEFFICIENTS FOR CT SCANS. *Radiat Prot Dosimetry* 2016; **172**: 428-437 [*RCA*] [PMID: 26755767 DOI: 10.1093/rpd/ncv511] [FullText]

21 **Brady SL**, Kaufman RA. Investigation of American Association of Physicists in Medicine Report 204 size-specific dose estimates for pediatric CT implementation. *Radiology* 2012; **265**: 832-840 [*RCA*] [PMID: 23093679 DOI: 10.1148/radiol.12120131] [FullText]

22 **Boon M**, Vermeulen FL, Gysemans W, Proesmans M, Jorissen M, De Boeck K. Lung structure-function correlation in patients with primary ciliary dyskinesia. *Thorax* 2015; **70**: 339-345 [*RCA*] [PMID: 25673230 DOI: 10.1136/thoraxjnl-2014-206578] [FullText]

23 **Tadd K**, Morgan L, Rosenow T, Schultz A, Susanto C, Murray C, Robinson P. CF derived scoring systems do not fully describe the range of structural changes seen on CT scans in PCD. *Pediatr Pulmonol* 2019; **54**: 471-477 [*RCA*] [PMID: 30663844 DOI: 10.1002/ppul.24249] [Full Text]

24 **Rademacher J**, Dettmer S, Fuge J, Vogel-Claussen J, Shin HO, Shah A, Pedro PI, Wilson R, Welte T, Wacker F, Loebinger MR, Ringshausen FC. The Primary Ciliary Dyskinesia Computed Tomography Score in Adults with Bronchiectasis: A Derivation und Validation Study. *Respiration* 2021; **100**: 499-509 [*RCA*] [PMID: 33895745 DOI: 10.1159/000514927] [FullText]

25 **Chowdhary T**, Bracken J, Morgan L, Schultz A, Robinson P. The SPEC score-A quantifiable CT scoring system for primary ciliary dyskinesia. *Pediatr Pulmonol* 2024; **59**: 72-80 [*RCA*] [PMID: 37842974 DOI: 10.1002/ppul.26709] [FullText]

26 **Ferraro V**, Andrinopoulou ER, Sijbring AMM, Haarman EG, Tiddens HAWM, Pijnenburg MWH. Airway-artery quantitative assessment on chest computed tomography in paediatric primary ciliary dyskinesia. *ERJ Open Res* 2020; **6**: 00210-02019 [*RCA*] [PMID: 32964004 DOI: 10.1183/23120541.00210-2019] [FullText] [Full Text(PDF)]

27 **Siegel MJ**, Bugenhagen SM, Sanchez A, Kim S, Abadia A, Ramirez-Giraldo JC. Comparison of Radiation Dose and Image Quality of Pediatric High-Resolution Chest CT Between Photon-Counting Detector CT and Energy-Integrated Detector CT: A Matched Study. *AJR Am J Roentgenol* 2023; **221**: 363-371 [*RCA*] [PMID: 37095666 DOI: 10.2214/AJR.23.29077] [FullText]

28 **Aliukonyte I**, Caudri D, Booij R, van Straten M, Dijkshoorn ML, Budde RPJ, Oei EHG, Saba L, Tiddens HAWM, Ciet P. Unlocking the potential of photon counting detector CT for paediatric imaging: a pictorial essay. *BJR Open* 2024; **6**: tzae015 [*RCA*] [PMID: 39021509 DOI: 10.1093/bjro/tzae015] [FullText]

29 **Rajagopal JR**, Farhadi F, Solomon J, Sahbaee P, Saboury B, Pritchard WF, Jones EC, Samei E. Comparison of Low Dose Performance of Photon-Counting and Energy Integrating CT. *Acad Radiol* 2021; **28**: 1754-1760 [*RCA*] [PMID: 32855051 DOI: 10.1016/j.acra.2020.07.033] [FullText]

30 **Lachance CC**, Horton J. Photon-Counting CT: High Resolution, Less Radiation. *CADTH* 2024; **4** [DOI: 10.51731/cjht.2024.843] [FullText]

World Journal of Radiology

Submit a Manuscript: https://www.f6publishing.com

World J Radiol 2025 August 28; 17(8): 107732

DOI: 10.4329/wjr.v17.i8.107732

ISSN 1949-8470 (online)

SYSTEMATIC REVIEWS

Applications of photon-counting CT in oncologic imaging: A systematic review

Arosh S Perera Molligoda Arachchige, Anna Dashiell, Anton Shiraan Jesuraj, Antonia Immacolata D'Urso, Benedetta Fiore, Martina Cattaneo, Emilia Pierzynska, Sandra Szydelko, Francesca Romana Centini, Yash Verma

Specialty type: Radiology, nuclear medicine and medical imaging

Provenance and peer review: Invited article; Externally peer reviewed.

Peer-review model: Single blind

Peer-review report's classification

Scientific Quality: Grade C, Grade D

Novelty: Grade C, Grade D

Creativity or Innovation: Grade C, Grade D

Scientific Significance: Grade C, Grade D

P-Reviewer: Suda T

Received: March 28, 2025

Revised: May 4, 2025

Accepted: July 18, 2025

Published online: August 28, 2025

Processing time: 153 Days and 10.6 Hours

Arosh S Perera Molligoda Arachchige, Emergency Service, GHOL-Hopital de Nyon, Nyon 1260, Vaud, Switzerland

Anna Dashiell, Anton Shiraan Jesuraj, Antonia Immacolata D'Urso, Benedetta Fiore, Martina Cattaneo, Emilia Pierzynska, Sandra Szydelko, Francesca Romana Centini, Faculty of Medicine, Humanitas University, Pieve Emanuele 20072, Lombardy, Italy

Yash Verma, Department of Radiology, Mayo Clinic, Rochester, MN 55905, United States

Co-first authors: Arosh S Perera Molligoda Arachchige and Anna Dashiell.

Corresponding author: Arosh S Perera Molligoda Arachchige, MD, Emergency Service, GHOL-Hopital de Nyon, Chemin Monastier 10, Nyon 1260, Vaud, Switzerland.
aroshperera@outlook.it

Abstract

BACKGROUND

Photon-counting detector (PCD) CT represents a transformative advancement in radiological imaging, offering superior spatial resolution, enhanced contrast-to-noise ratio, and reduced radiation dose compared with the conventional energy-integrating detector CT.

AIM

To evaluate PCD CT in oncologic imaging, focusing on its role in tumor detection, staging, and treatment response assessment.

METHODS

We performed a systematic PubMed search from January 1, 2017 to December 31, 2024, using the keywords "photon-counting CT", "cancer", and "tumor" to identify studies on its use in oncologic imaging. We included experimental studies on humans or human phantoms and excluded reviews, commentaries, editorials, non-English, animal, and non-experimental studies. Study selection followed Preferred Reporting Items for Systematic Reviews and Meta-Analyses guidelines. Out of 175 initial studies, 39 met the inclusion criteria after screening and full-text review. Data extraction focused on study type, country of origin, and oncologic applications of photon-counting CT. No formal risk of bias assessment was performed, and the review was not registered in PROSPERO as it did not include

a meta-analysis.

RESULTS
Key findings highlighted the advantages of PCD CT in imaging renal masses, adrenal adenomas, ovarian cancer, breast cancer, prostate cancer, pancreatic tumors, hepatocellular carcinoma, metastases, multiple myeloma, and lung cancer. Additionally, PCD CT has demonstrated improved lesion characterization and enhanced diagnostic accuracy in oncology. Despite its promising capabilities challenges related to data processing, storage, and accessibility remain.

CONCLUSION
As PCD CT technology evolves, its integration into routine oncologic imaging has the potential to significantly enhance cancer diagnosis and patient management.

Key Words: Photon-counting detector CT; Oncologic imaging; Cancer detection; Tumor characterization; Spectral imaging; Radiology; Computed tomography; Photon-counting detector CT applications; Diagnostic imaging; Radiation dose reduction

Core Tip: Photon-counting detector (PCD) CT represents a paradigm shift in oncologic imaging, offering superior spatial resolution, reduced radiation dose, and enhanced material decomposition compared with conventional CT. This study highlighted the potential of PCD CT in tumor detection, characterization, and therapy response assessment, underscoring its role in advancing precision oncology. By leveraging energy-resolved photon detection, PCD CT enhances lesion conspicuity and quantification, paving the way for improved diagnostic accuracy and personalized treatment strategies.

Citation: Perera Molligoda Arachchige AS, Dashiell A, Jesuraj AS, D'Urso AI, Fiore B, Cattaneo M, Pierzynska E, Szydelko S, Centini FR, Verma Y. Applications of photon-counting CT in oncologic imaging: A systematic review. *World J Radiol* 2025; 17(8): 107732
URL: https://www.wjgnet.com/1949-8470/full/v17/i8/107732.htm
DOI: https://dx.doi.org/10.4329/wjr.v17.i8.107732

INTRODUCTION

Photon-counting detector (PCD) CT represents a groundbreaking advancement in radiological imaging, offering significant improvements over traditional CT modalities. Traditional CT uses energy-integrating detectors (EIDs), which sum the total energy deposited by X-ray photons. This process inherently reduces spectral information and limits spatial resolution and image quality, especially in patients with a high body mass index. Unlike traditional EIDs, PCD CT utilizes PCDs, which individually capture each X-ray photon and its energy, enabling enhanced spatial resolution, contrast-to-noise ratio, and spectral imaging capabilities while reducing radiation dose. Beyond the hardware innovation PCD CT integrates novel image reconstruction techniques such as virtual non-contrast (VNC) imaging, which allows reconstruction of unenhanced images from contrast-enhanced scans, eliminating the need for multiple phases, and quantum iterative reconstruction (QIR), which enhances image quality by reducing noise while preserving spatial detail. This technological evolution aims to address several inherent limitations of conventional CT, providing a more refined imaging tool for clinical practice[1].

The clinical potential of PCD CT has been under investigation for over a decade with early experimental systems demonstrating promising results. However, the technology initially faced challenges related to detector performance under high X-ray flux rates. A major milestone was achieved on September 29, 2021 when the Food and Drug Administration cleared the first PCD CT scanner developed by Siemens Healthineers for clinical use. This regulatory approval marked a turning point, providing real-world validation of the advantages of PCD CT[2]. This milestone marked the beginning of broader clinical adoption with over 50 installations worldwide and a sharp rise in scientific publications (over 500 in the last year) demonstrating increasing interest and application.

Among the various clinical domains where PCD CT is making strides, oncologic imaging is emerging as a key area of interest. The superior spectral resolution, improved lesion characterization, and reduced radiation dose of PCD CT offer distinct advantages in oncologic applications, particularly in tumor detection, staging, and treatment response assessment [3,4]. However, the literature is currently fragmented, spanning diverse tumor types and protocols. This systematic review aimed to consolidate these findings by evaluating trends, identifying strengths and limitations of PCD CT in oncologic imaging, and presenting visual comparisons to clarify its clinical value relative to conventional CT.

MATERIALS AND METHODS

A systematic search was conducted for the period of January 1, 2017 to December 31, 2024 using PubMed to identify relevant literature on the applications of PCD CT in oncologic imaging. The search strategy included the following keywords: ("photon-counting CT") AND ("cancer") and ("photon-counting CT") AND ("tumor"). Studies were considered eligible for inclusion if they were experimental studies involving human subjects or human phantom studies. Non-experimental reports such as scoping reviews, narrative reviews, systematic reviews, and meta-analyses along with editorials, letters, commentaries, non-English studies, and animal studies were excluded.

The study selection process followed the Preferred Reporting Items for Systematic Reviews and Meta-Analyses guidelines[5]. The Preferred Reporting Items for Systematic Reviews and Meta-Analyses flow diagram (Figure 1) outlines the screening process, including study identification, screening, eligibility assessment, and final inclusion. Initially, 175 studies were identified from PubMed. After the removal of 27 ineligible studies using automation tools, 148 studies remained for screening based on title and abstract. At this stage 73 studies were excluded, and the remaining 75 reports were sought for retrieval. Six reports could not be retrieved, leading to a full-text assessment of 69 studies. Following this assessment, 30 studies were excluded due to irrelevance, resulting in a final inclusion of 39 studies.

Data extraction focused on key study characteristics, including study type (comparison *vs* non-comparison), the first author's country of origin, and the application of PCD CT in oncologic imaging. A formal risk of bias assessment was not conducted as the review primarily included experimental studies without direct intervention comparisons, thereby minimizing the risk of systematic bias in study design. Data synthesis was performed using a qualitative approach to summarize trends in the literature and the various applications of PCD CT in oncologic imaging.

This systematic review was not registered in PROSPERO because it did not involve a meta-analysis or a formal risk-of-bias assessment, both of which are key requirements for PROSPERO registration (Figure 1).

RESULTS

The present systematic review included 39 studies with key trends illustrated in the form of charts. Figure 2 highlights concentrated research efforts in high-resource settings with the United States contributing the most published studies (n = 16), followed by Germany (n = 15) and France (n = 3). Lower contributions from countries like India (n = 1) and Iran (n = 1) underscored geographic disparities in PCD CT research accessibility. Figure 3 illustrates multiple myeloma as the most frequently investigated malignancy (n = 6), followed by pancreatic tumors (n = 5) and breast cancer (n = 4) as well as metastasis (n = 4), reflecting diverse oncologic applications being investigated.

Figure 4 illustrates study design trends from 2017-2024, and our analyses demonstrated a marked increase in comparison studies [*e.g.*, PCD CT *vs* conventional CT or magnetic resonance imaging (MRI)] beginning in 2017, coinciding with Food and Drug Administration approval of the first clinical PCD CT scanner correlating with the necessity of validating the diagnostic superiority of PCD CT. Starting in 2020, non-comparison studies have started to gradually expand, demonstrating the diagnostic superiority of PCD CT (Figures 2, 3, and 4).

DISCUSSION

This systematic review highlighted the evolving role of PCD CT in oncologic imaging, showcasing its advantages over conventional CT in terms of spatial resolution, spectral imaging, and radiation dose reduction. The increasing number of experimental studies in recent years reflects the growing interest in integrating PCD CT into oncologic workflows with applications spanning tumor detection, characterization, and treatment monitoring.

In the following sections we discussed the key applications of PCD CT in oncologic imaging, examining how this technology enhances diagnostic accuracy, improves lesion differentiation, and influences clinical decision-making. Furthermore, we explored current limitations and future directions that may shape the widespread adoption of PCD CT in oncology.

Renal masses

PCD CT is comparable in performance with MRI in detecting and characterizing renal cell carcinoma and other renal masses, particularly in terms of inter-reader reliability and sensitivity. This capability is especially beneficial in the detection of benign renal cysts *vs* renal neoplasms in which the ability of PCD CT to differentiate based on iodine concentration (IC) has proven effective. Specifically, studies have demonstrated that renal neoplasms exhibit higher IC values compared with benign cysts with maximum and mean IC values offering excellent discriminatory power (area under the curve = 0.983 and 0.992, respectively) for heterogeneous lesions[6]. Moreover, the single-phase imaging capability of PCD CT reduces scan complexity and radiation exposure, an important consideration in clinical practice. However, challenges remain with virtual monochromatic imaging (VMI) at low energy levels (*e.g.*, 40 keV), which may misclassify non-enhancing cysts as enhancing ones. Higher VMI levels (70 keV and above) appear optimal for minimizing such misclassification and ensuring accurate lesion characterization[7]. Furthermore, the use of VNC images derived from PCD CT has shown promise in reliable cyst detection, potentially replacing non-contrast imaging to reduce radiation dose[8].

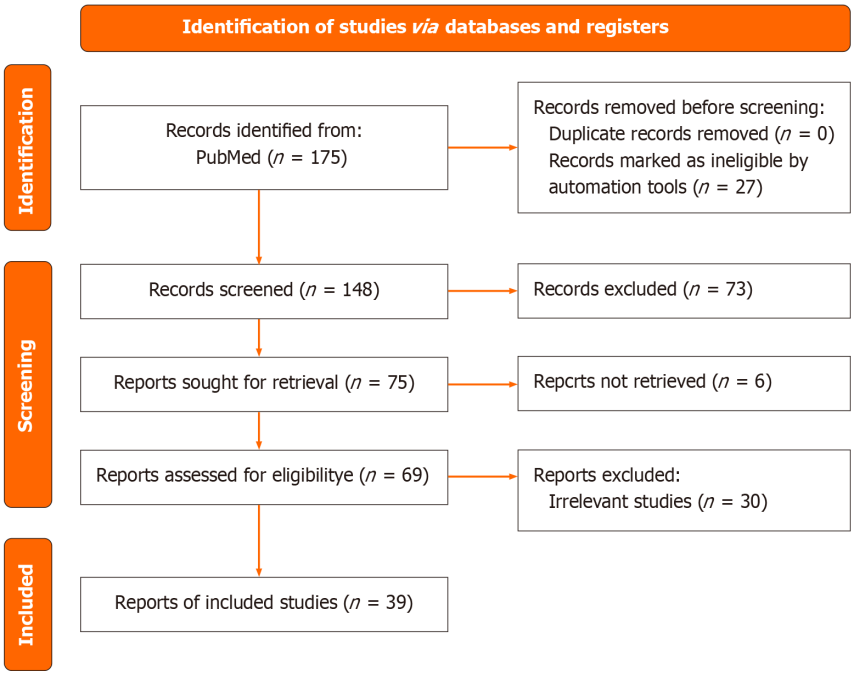

Figure 1 Preferred Reporting Items for Systematic Reviews and Meta-Analyses flow diagram outlining the study selection process for a systematic review of the applications of photon-counting detector CT in oncologic imaging.

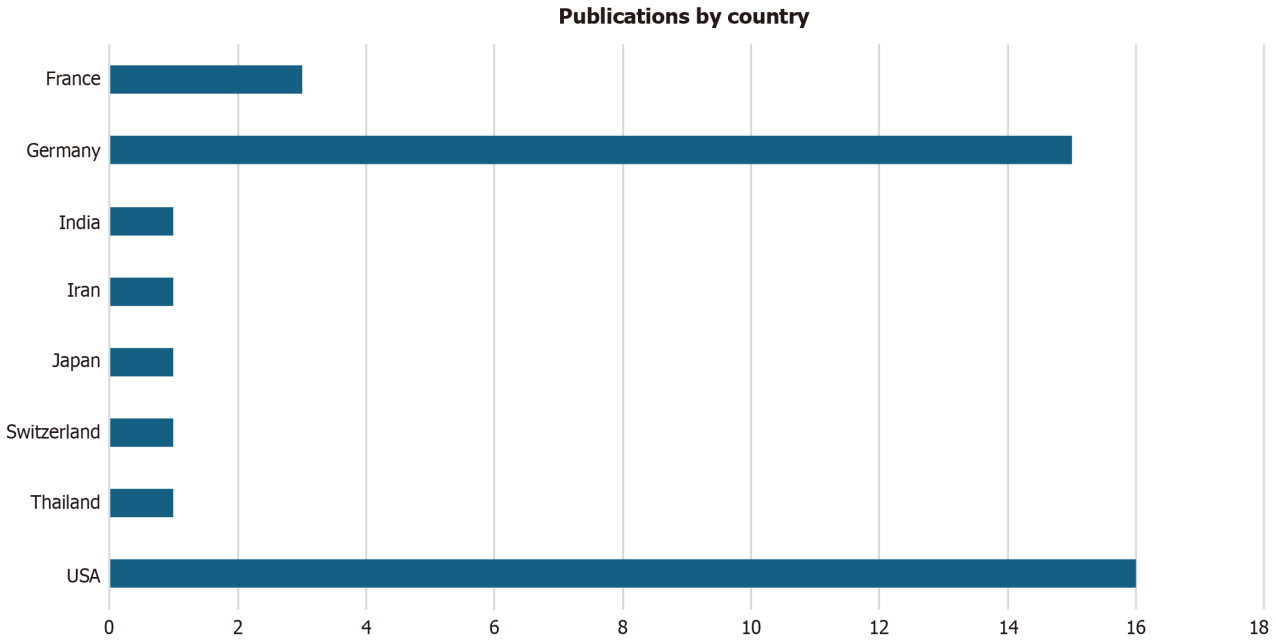

Figure 2 Number of publications by country. USA: United States of America.

Adrenal adenomas

The application of PCD CT in adrenal lesion characterization, particularly in differentiating adrenal adenomas from metastases, has been explored with promising results. VNC reconstructions, both conventional and new algorithms, show significant potential in distinguishing adrenal adenomas, which have lower CT values, from metastases, which typically present with higher CT values[9]. However, while VNC reconstruction offers a useful diagnostic tool, it tends to overestimate CT values compared with true non-contrast images, suggesting that adjusted threshold values may be necessary for optimal diagnostic accuracy. Studies have recommended thresholds of 26 Hounsfield unit (HU) instead of the traditional 10 HU for accurate lesion differentiation. Further research with larger cohorts is necessary to refine these thresholds and confirm the clinical utility of VNC reconstructions in routine practice[10].

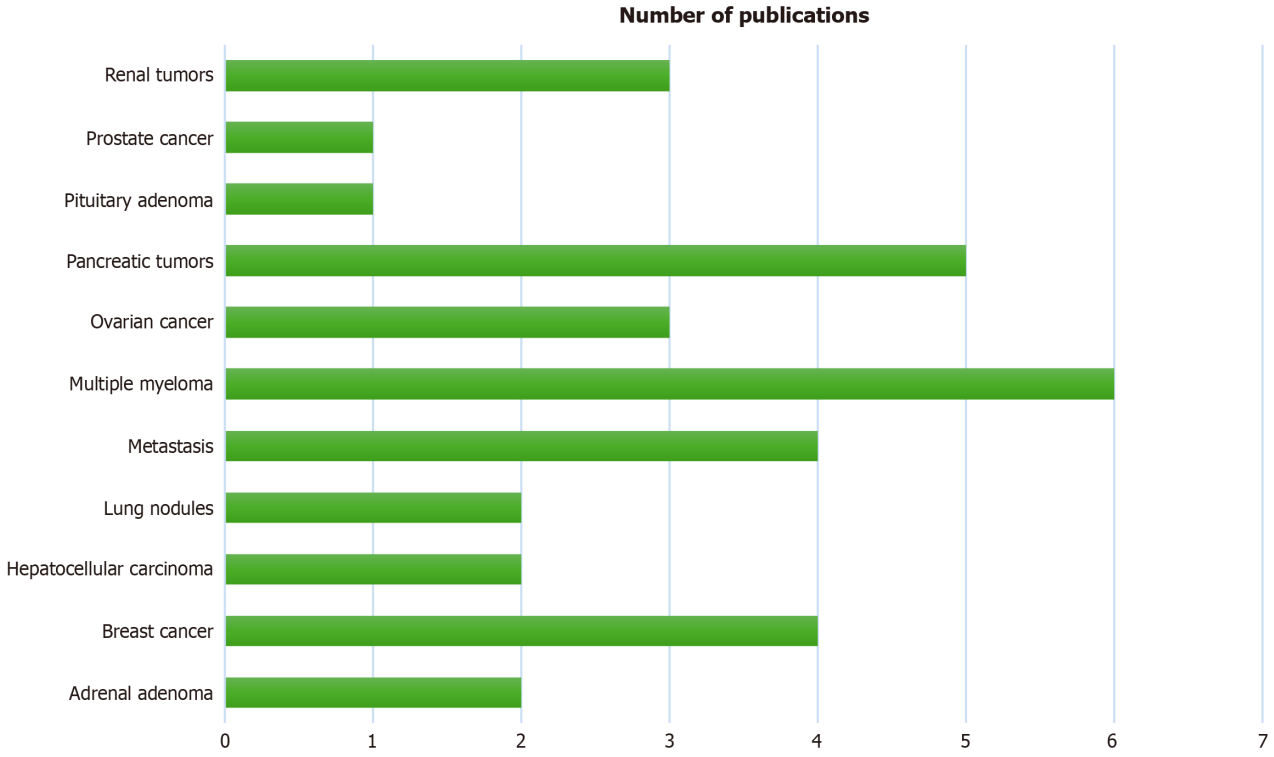

Figure 3 Types of tumors assessed by photon-counting detector CT and the relative number of publications.

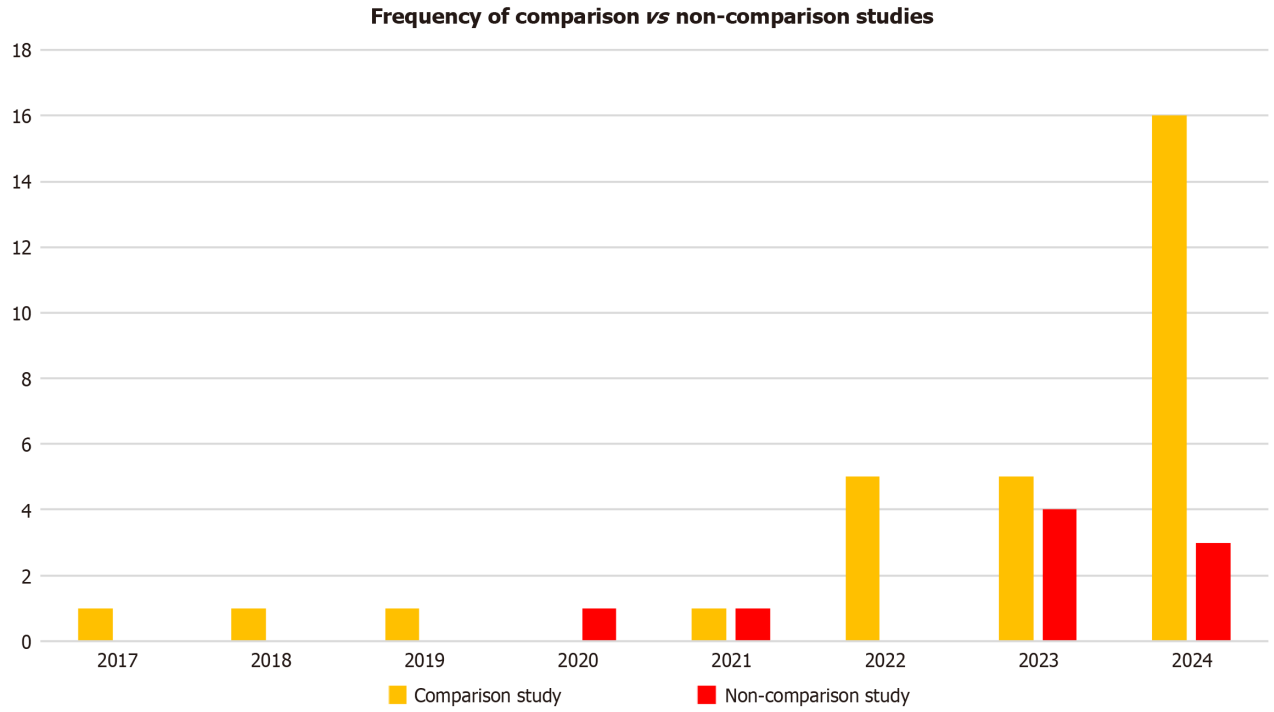

Figure 4 Frequency of comparison studies *vs* non-comparison studies in each year from 2017-2024.

Ovarian cancer

In the context of ovarian cancer, PCD CT has emerged as a novel tool for non-invasive real-time monitoring and diagnosis. The selective uptake of gold nanoparticles by ovarian cancer cells has shown potential for enhancing PCD CT imaging, offering both diagnostic and therapeutic applications[11]. The ability to characterize ovarian cancer with high sensitivity, aided by advanced nanoparticulate formulations, suggests that PCD CT could become an essential component in ovarian cancer detection and monitoring.

Breast cancer

PCD CT has demonstrated superior diagnostic performance in breast cancer staging compared with traditional mammography, particularly in terms of tumor conspicuity and classification of locoregional disease. Studies show that PCD CT outperforms traditional mammography, especially in dense breasts, providing higher sensitivity and specificity for detecting ductal carcinoma in situ and T classification of tumors[12]. Furthermore, the ability of PCD CT to detect metastatic lymph nodes and multifocal breast cancer suggests its potential as a complementary modality to breast MRI in certain clinical scenarios. In addition the higher diagnostic accuracy and inter-reader agreement observed with PCD CT could lead to more confident clinical decision-making and improved patient outcomes.

Prostate cancer

While traditional CT imaging is limited in prostate cancer management due to its reliance on size-based assessments, PCD CT offers a promising alternative by providing better tissue characterization through spectral imaging. This capability enables more accurate evaluation of prostate cancer and its metastases with the added benefit of reduced radiation exposure and improved radiotherapy treatment planning. However, despite these advantages technical challenges remain. Specifically, image quality can degrade in pelvic imaging due to motion artifacts from bowel peristalsis, beam hardening near the bladder and rectum, and high attenuation from surrounding bony structures. These issues can compromise lesion conspicuity and spectral accuracy, limiting the reliability of PCD CT in certain diagnostic and staging scenarios. As a result the clinical adoption of PCD CT in routine prostate cancer imaging remains cautious, pending further technical refinements and validation in large-scale studies[13].

Pituitary tumors

In the case of pituitary tumors, particularly in the context of Cushing's disease, dynamic contrast-enhanced PCD CT has shown potential in improving adenoma identification. The ability of PCD CT to provide high-resolution imaging of the pituitary gland, coupled with its ability to delineate the peripheral margins of adenomas, offers a distinct advantage in presurgical planning. This technique when combined with advanced image reconstruction protocols provides enhanced sensitivity in detecting hypoenhancing lesions, which are often difficult to visualize on conventional imaging modalities like MRI[14].

Pancreatic tumors

PCD CT offers significant improvements over conventional EID CT in detecting and staging pancreatic ductal adenocarcinoma. Low keV VMI derived from PCD CT enhance tumor conspicuity, especially in the portal venous phase, which aids earlier detection and diagnostic confidence[15]. Studies show that PCD CT improves tumor delineation and reduces radiation dose compared to EID CT with substantial inter-reader agreement for vascular involvement in pancreatic ductal adenocarcinoma, particularly in critical arteries and veins such as the celiac artery and superior mesenteric artery. These improvements in image quality and diagnostic accuracy are critical for surgical planning[16,17].

Additionally, PCD CT excels in detecting small pancreatic lesions, such as side-branch intraductal papillary mucinous neoplasms, which are challenging to detect on conventional CT. In a prevalence study PCD CT demonstrated higher cyst detection rates (4.9% *vs* 3.0%, $P = 0.017$) and detected previously overlooked cysts, further highlighting its potential in early tumor detection and surveillance[18]. An example of this high-precision visualization is shown in Figure 5[19], which demonstrates a superior depiction of a pancreatic insulinoma using PCD CT when compared with conventional CT and MRI.

Hepatocellular carcinoma

PCD CT combined with QIR provides superior image quality for diagnosing hepatocellular carcinoma in patients with cirrhosis. Higher QIR levels (*e.g.*, QIR-4) significantly reduce image noise, improving the contrast-to-noise ratio by up to 50%. Soft reconstruction kernels with a sharpness level of 36 offer the best balance between noise suppression and lesion visualization, making them ideal for spectral imaging applications in oncologic settings[20,21]. These advancements in PCD CT reconstruction parameters improve lesion conspicuity and may enhance diagnostic confidence in routine clinical practice (Figure 5).

Metastasis

PCD CT has demonstrated significant advantages in oncologic imaging, particularly in detecting bone metastases. It provides improved lesion characterization with reduced inter-reader variability, helping assess tumor size and structural integrity. PCD CT also offers substantial radiation dose reduction compared with dual-source (DS) CT while maintaining or improving image quality[22,23]. In peritoneal metastasis assessment spectral PCD CT has improved contrast resolution, especially with low-energy virtual monoenergetic images, aiding in better differentiation between malignant and benign lesions[23,24].

Multiple myeloma

Several studies have compared the diagnostic impact of PCD CT *vs* EID CT in the context of multiple myeloma. Baffour *et al*[25] showed that whole-body low-dose PCD CT in ultra-high-resolution mode with and without a deep learning noise reduction algorithm was superior in viewing multiple myeloma lesions compared with EID CT[25].

In a prospective study involving 7 patients with monoclonal gammopathy, it was demonstrated that PCD CT offered significant benefits for multiple myeloma imaging compared with EID CT with both imaging modalities performed

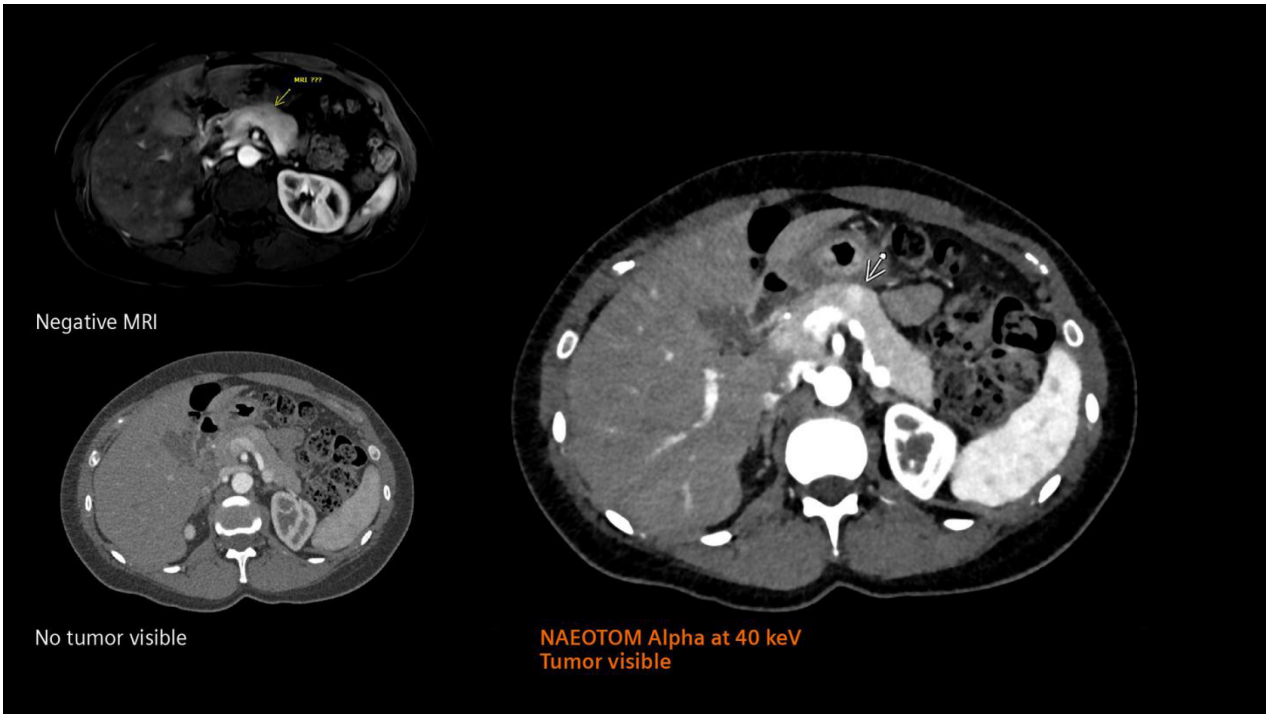

Figure 5 Combination of high resolution and spectral information obtained with photon-counting detector CT. NAEOTOM Alpha allows the high-precision visualization of a pancreatic insulinoma with high precision when compared with conventional CT and magnetic resonance imaging[19]. Citation: Siemens Healthineers. The NAEOTOM Alpha class. Available from: https://www.siemens-healthineers.com/computed-tomography/naeotom. Copyright ©Siemens Healthineers AG 2024. The authors have obtained the permission (Supplementary material). MRI: Magnetic resonance imaging.

under standardized protocols. Specifically, PCD CT delivered an 83% reduction in radiation dose compared with EID CT, and PCD CT identified 79% of osteolytic lesions compared with 64% detected with EID CT; moreover, PCD CT demonstrated more sensitivity for small (< 1 cm) lesions without statistically significant differences in larger axial regions [26].

Similarly, a study involving 9 patients with stage III myeloma who underwent imaging of the lower lumbar spine and pelvis showed that PCD CT identified 21% more osteolytic bone lesions than EID CT with improved sensitivity for smaller lesions[27].

Compared with EIDs, PCDs significantly increase the spatial resolution of bone microstructure in patients with multiple myeloma. Subjective and objective image quality comparison of bone microstructure and disease-related abnormalities in multiple myeloma patients using a first-generation DS-PCD CT and a second-generation DS-EID CT showed that overall quality as well as detectability and sharpness in the delineation of lytic bone lesions were superior for DS-PCD CT compared with DS-EID CT ($P < 0.0001$; Figure 6)[19]. The quantitative metric for bone microstructure in the femoral head showed significantly better visualization of trabeculae in DS-PCD CT compared with DS-EID CT ($P < 0.0001$). Quantitative analyses of edge sharpness of osteolysis showed significant steeper edges for DS-PCD CT ($P < 0.0001$)[28,29].

Lung cancer

Symons *et al*[28] evaluated the feasibility of using a whole-body PCD CT scanner for low dose lung cancer screening compared with a conventional EID CT system and showed that PCD CT provides better HU stability for lung, ground-glass, and emphysema equivalent forms at lower radiation dose settings with better reproducibility than EID CT. Additionally, PCD CT showed up to 10% less noise and 11% higher contrast-to-noise ratio at 0.75 mGy for both 100 and 80 kVp. Thus, PCD CT technology may help reduce radiation exposure in lung cancer screening while maintaining diagnostic quality[30,31].

Similarly, another study evaluated the potential of PCD CT for dose reduction in pulmonary nodule visualization for human readers as well as for computer-aided detection (CAD) studies. At the half radiation dose, sensitivity remained 100% for the human reader and CAD studies in PCD CT. At the quarter radiation dose, PCD CT achieved the same results as EID CT at the standard radiation dose setting (93%, $P = 1.00$) in human reading studies. Thus, CAD algorithms can be effective even at ultra-low doses[32].

Limitations

This systematic review had several limitations. First, trends in the literature may have changed in 2025, potentially influencing the relevance and applicability of our findings. As the field of PCD CT continues to evolve, newer studies published beyond our search period may provide additional insights into its oncologic applications. Second, our study was limited to PubMed as the sole database for literature retrieval. While this decision was made to ensure that included studies met the rigorous indexing criteria of PubMed, particularly given the clinical nature of our review, it may have led

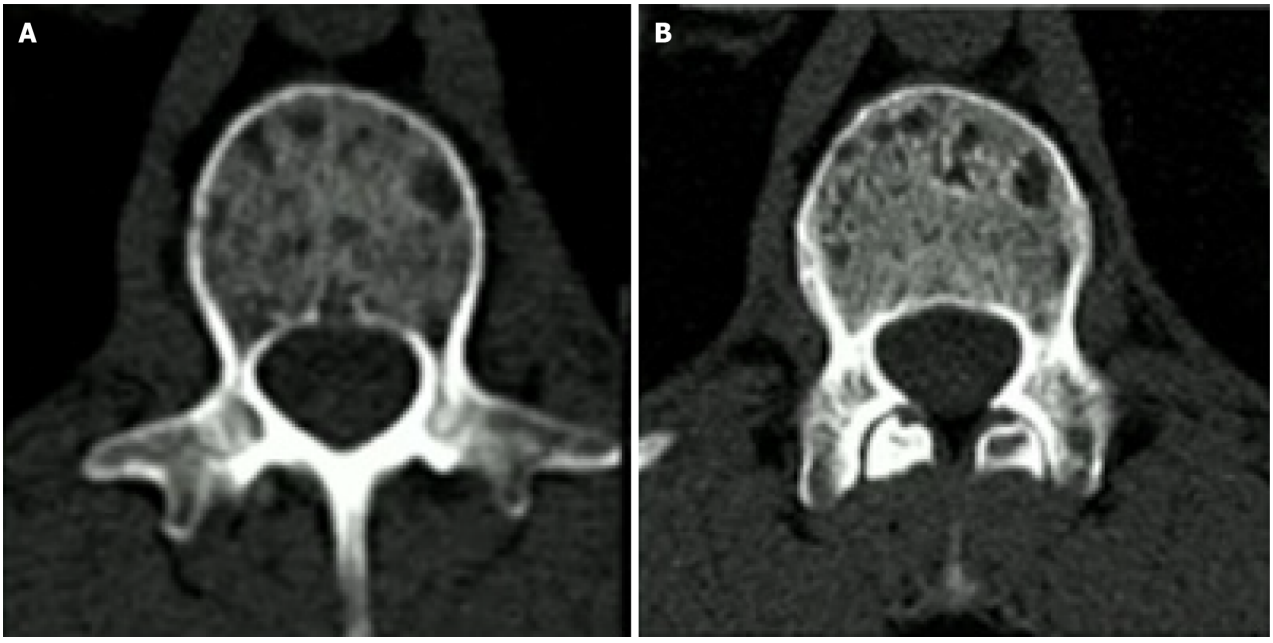

Figure 6 Comparison between second generation dual energy CT and photon-counting detector CT. The images were obtained from the vertebra of a 56-year-old patient with multiple myeloma[19]. Note the improvement in spatial resolution in the photon-counting detector CT image with a better depiction of trabeculae and osteolysis. A: Second generation dual energy CT; B: Photon-counting detector CT. Citation: Siemens Healthineers. The NAEOTOM Alpha class. Available from: https://www.siemens-healthineers.com/computed-tomography/naeotom. Copyright ©Siemens Healthineers AG 2024. The authors have obtained the permission (Supplementary material).

to the omission of relevant studies from other databases such as Web of Science, Google Scholar, EMBASE, and Scopus. As a result some valuable contributions from non-PubMed-indexed journals may not have been considered in our analysis. Future systematic reviews incorporating multiple databases may provide a more comprehensive overview of the expanding role of PCD CT in oncologic imaging.

CONCLUSION

Despite all the benefits arising from the ultra-high resolution, some limitations need to be addressed mainly linked to the large amount of data extracted, amounting to approximately 16-fold of that of standard CT and giving rise to problems of storage and extreme data volumes to be processed[32]. PCD CT is poised to significantly enhance oncologic imaging by providing unprecedented image quality, reducing radiation doses, and improving diagnostic accuracy. As the technology continues to evolve and become more widely adopted, it is likely to play a central role in pushing the borders of cancer imaging, ultimately leading to better patient outcomes.

FOOTNOTES

Author contributions: Arachchige ASPM contributed to the conceptualization, methodology, investigation, writing the original draft, and supervision; Dashiell A contributed to methodology, data curation, reviewing, and editing; Jesuraj AS, D'Urso AI, Fiore B, Cattaneo M, Szydelko S, Centini FR, and Verma Y contributed to reviewing and editing; Pierzynska E contributed to the investigation and validation; All authors read and agreed to the published version of the manuscript.

Conflict-of-interest statement: The authors have no conflicts of interest to declare.

PRISMA 2009 Checklist statement: The authors have read the PRISMA 2009 Checklist, and the manuscript was prepared and revised according to the PRISMA 2009 Checklist.

Country of origin: Switzerland

ORCID number: Arosh S Perera Molligoda Arachchige 0000-0002-3875-0267.

S-Editor: Liu H
L-Editor: Filipodia
P-Editor: Lei YY

REFERENCES

1 **Hsieh SS**, Leng S, Rajendran K, Tao S, McCollough CH. Photon Counting CT: Clinical Applications and Future Developments. *IEEE Trans Radiat Plasma Med Sci* 2021; **5**: 441-452 [*RCA*] [PMID: 34485784 DOI: 10.1109/trpms.2020.3020212] [FullText]
2 **United States Food and Drug Administration**. FDA Clears First Major Imaging Device Advancement for Computed Tomography in Nearly a Decade. [cited 3 July 2025]. Available from: https://www.fda.gov/news-events/press-announcements/fda-clears-first-major-imaging-device-advancement-computed-tomography-nearly-decade
3 **Perera Molligoda Arachchige AS**, Catapano F, Lisi C, El Choueiri J, Pellicanò F, Figliozzi S, Politi LS, Francone M. Trends in Clinical Cardiac Photon-Counting Detector CT Research: A Comprehensive Bibliometric Analysis. *Diagnostics (Basel)* 2025; **15**: 504 [*RCA*] [PMID: 40002654 DOI: 10.3390/diagnostics15040504] [FullText]
4 **Perera Molligoda Arachchige AS**, Verma Y. Role of photon-counting computed tomography in pediatric cardiovascular imaging. *World J Clin Pediatr* 2025; **14**: 99288 [*RCA*] [PMID: 40059896 DOI: 10.5409/wjcp.v14.i1.99288] [FullText] [Full Text(PDF)]
5 **Page MJ**, McKenzie JE, Bossuyt PM, Boutron I, Hoffmann TC, Mulrow CD, Shamseer L, Tetzlaff JM, Akl EA, Brennan SE, Chou R, Glanville J, Grimshaw JM, Hróbjartsson A, Lalu MM, Li T, Loder EW, Mayo-Wilson E, McDonald S, McGuinness LA, Stewart LA, Thomas J, Tricco AC, Welch VA, Whiting P, Moher D. The PRISMA 2020 statement: an updated guideline for reporting systematic reviews. *BMJ* 2021; **372**: n71 [*RCA*] [PMID: 33782057 DOI: 10.1136/bmj.n71] [FullText] [Full Text(PDF)]
6 **Tóth A**, Chamberlin JH, Mendez S, Varga-Szemes A, Hardie AD. Iodine quantification of renal lesions: Preliminary results using spectral-based material extraction on photon-counting CT. *J Clin Imaging Sci* 2024; **14**: 7 [*RCA*] [PMID: 38628606 DOI: 10.25259/JCIS_1_2024] [Full Text] [Full Text(PDF)]
7 **Schade KA**, Mergen V, Sartoretti T, Alkadhi H, Euler A. Pseudoenhancement in Cystic Renal Lesions - Impact of Virtual Monoenergetic Images of Photon-Counting Detector CT on Lesion Classification. *Acad Radiol* 2023; **30** Suppl 1: S305-S313 [*RCA*] [PMID: 37150736 DOI: 10.1016/j.acra.2023.04.005] [FullText]
8 **Rau S**, Rau A, Stein T, Hagar MT, Faby S, Bamberg F, Weiss J. Value of virtual non-contrast images to identify uncomplicated cystic renal lesions: photon-counting detector CT vs. dual-energy integrating detector CT. *Radiol Med* 2024; **129**: 669-676 [*RCA*] [PMID: 38512614 DOI: 10.1007/s11547-024-01801-2] [FullText] [Full Text(PDF)]
9 **Bette S**, Risch F, Canalini L, Becker J, Leithner EV, Huber A, Haerting M, Jehs B, Wollny C, Schwarz F, Tehlan K, Scheurig-Muenkler C, Wendler T, Kroencke T, Decker JA. Diagnostic performance of photon-counting detector CT for differentiation between adrenal adenomas and metastases. *Eur Radiol* 2024; **34**: 5944-5953 [*RCA*] [PMID: 38480567 DOI: 10.1007/s00330-024-10675-x] [FullText]
10 **Lennartz S**, Schoenbeck D, Kröger JR, Borggrefe J, Henning Niehoff J. Photon-counting CT Material Decomposition: Initial Experience in Assessing Adrenal Adenoma. *Radiology* 2023; **306**: 202-204 [*RCA*] [PMID: 35997606 DOI: 10.1148/radiol.220919] [FullText]
11 **Kumar D**, Moghiseh M, Chitcholtan K, Mutreja I, Lowe C, Kaushik A, Butler A, Sykes P, Anderson N, Raja A. LHRH conjugated gold nanoparticles assisted efficient ovarian cancer targeting evaluated *via* spectral photon-counting CT imaging: a proof-of-concept research. *J Mater Chem B* 2023; **11**: 1916-1928 [*RCA*] [PMID: 36744575 DOI: 10.1039/d2tb02416k] [FullText]
12 **Neubauer J**, Wilpert C, Gebler O, Taran FA, Pichotka M, Stein T, Molina-Fuentes MF, Weiss J, Juhasz-Böss I, Bamberg F, Windfuhr-Blum M, Neubauer C. Diagnostic Accuracy of Contrast-Enhanced Thoracic Photon-Counting Computed Tomography for Opportunistic Locoregional Staging of Breast Cancer Compared With Digital Mammography: A Prospective Trial. *Invest Radiol* 2024; **59**: 489-494 [*RCA*] [PMID: 38038693 DOI: 10.1097/RLI.0000000000001051] [FullText]
13 **O'Connell J**, Schwartz F, Morris T, and Dunning C, Harris TC, Ferguson D, Myronakis M, Sodickson A, Berbeco RI. Initial Examination of Commercial Photon Counting CT for Prostate Planning. *Int J Radiat Oncol Biol Phys* 2024; **120**: e172 [DOI: 10.1016/j.ijrobp.2024.07.387] [FullText]
14 **Mark IT**, Van Gompel J, Bancos I, Nagelschneider AA, Johnson DR, Bathla G, Madhavan AA, Weber NM, Yu L. Back to the Future: Dynamic Contrast-Enhanced Photon-Counting Detector CT for the Detection of Pituitary Adenoma in Cushing Disease. *AJNR Am J Neuroradiol* 2024; **45**: 743-746 [*RCA*] [PMID: 38290737 DOI: 10.3174/ajnr.A8171] [FullText]
15 **Woeltjen MM**, Niehoff JH, Roggel R, Michael AE, Gerdes B, Surov A, Borggrefe J, Kroeger JR. Pancreatic cancer in photon-counting CT: Low keV virtual monoenergetic images improve tumor conspicuity. *Eur J Radiol* 2024; **173**: 111374 [*RCA*] [PMID: 38422607 DOI: 10.1016/j.ejrad.2024.111374] [FullText]
16 **Decker JA**, Becker J, Härting M, Jehs B, Risch F, Canalini L, Wollny C, Scheurig-Muenkler C, Kroencke T, Schwarz F, Bette S. Optimal conspicuity of pancreatic ductal adenocarcinoma in virtual monochromatic imaging reconstructions on a photon-counting detector CT: comparison to conventional MDCT. *Abdom Radiol (NY)* 2024; **49**: 103-116 [*RCA*] [PMID: 37796327 DOI: 10.1007/s00261-023-04042-5] [FullText]
17 **Kim J**, Mabud T, Huang C, Lloret Del Hoyo J, Petrocelli R, Vij A, Dane B. Inter-reader agreement of pancreatic adenocarcinoma resectability assessment with photon counting versus energy integrating detector CT. *Abdom Radiol (NY)* 2024; **49**: 3149-3157 [*RCA*] [PMID: 38630314 DOI: 10.1007/s00261-024-04298-5] [FullText]
18 **Khanungwanitkul K**, Schwartz FR. Photon-Counting CT Shows Side-Branch Intraductal Papillary Mucinous Neoplasm-Pancreatic Duct Connection. *Radiology* 2024; **312**: e240611 [*RCA*] [PMID: 39105646 DOI: 10.1148/radiol.240611] [FullText]
19 **Siemens Healthineers**. The NAEOTOM Alpha class. [cited 7 July 2025]. Available from: https://www.siemens-healthineers.com/computed-tomography/naeotom
20 **Graafen D**, Stoehr F, Halfmann MC, Emrich T, Foerster F, Yang Y, Düber C, Müller L, Kloeckner R. Quantum iterative reconstruction on a photon-counting detector CT improves the quality of hepatocellular carcinoma imaging. *Cancer Imaging* 2023; **23**: 69 [*RCA*] [PMID: 37480062 DOI: 10.1186/s40644-023-00592-5] [FullText]
21 **Graafen D**, Müller L, Halfmann MC, Stoehr F, Foerster F, Düber C, Yang Y, Emrich T, Kloeckner R. Soft Reconstruction Kernels Improve

HCC Imaging on a Photon-Counting Detector CT. *Acad Radiol* 2023; **30** Suppl 1: S143-S154 [*RCA*] [PMID: 37095047 DOI: 10.1016/j.acra.2023.03.026] [FullText]

22 **Wehrse E**, Sawall S, Klein L, Glemser P, Delorme S, Schlemmer HP, Kachelrieß M, Uhrig M, Ziener CH, Rotkopf LT. Potential of ultra-high-resolution photon-counting CT of bone metastases: initial experiences in breast cancer patients. *NPJ Breast Cancer* 2021; **7**: 3 [*RCA*] [PMID: 33398008 DOI: 10.1038/s41523-020-00207-3] [FullText] [Full Text(PDF)]

23 **Hagen F**, Walder L, Fritz J, Gutjahr R, Schmidt B, Faby S, Bamberg F, Schoenberg S, Nikolaou K, Horger M. Image Quality and Radiation Dose of Contrast-Enhanced Chest-CT Acquired on a Clinical Photon-Counting Detector CT vs. Second-Generation Dual-Source CT in an Oncologic Cohort: Preliminary Results. *Tomography* 2022; **8**: 1466-1476 [*RCA*] [PMID: 35736867 DOI: 10.3390/tomography8030119] [Full Text] [Full Text(PDF)]

24 **Grange R**, Si-Mohamed S, Kepenekian V, Boccalini S, Glehen O, Rousset P. Spectral photon-counting CT: Hype or hope for colorectal peritoneal metastases imaging? *Diagn Interv Imaging* 2024; **105**: 118-120 [*RCA*] [PMID: 38262873 DOI: 10.1016/j.diii.2024.01.002] [Full Text]

25 **Baffour FI**, Huber NR, Ferrero A, Rajendran K, Glazebrook KN, Larson NB, Kumar S, Cook JM, Leng S, Shanblatt ER, McCollough CH, Fletcher JG. Photon-counting Detector CT with Deep Learning Noise Reduction to Detect Multiple Myeloma. *Radiology* 2023; **306**: 229-236 [*RCA*] [PMID: 36066364 DOI: 10.1148/radiol.220311] [FullText]

26 **Schwartz FR**, Vinson EN, Spritzer CE, Colglazier R, Samei E, French RJ, Said N, Waldman L, McCrum E. Prospective Multireader Evaluation of Photon-counting CT for Multiple Myeloma Screening. *Radiol Imaging Cancer* 2022; **4**: e220073 [*RCA*] [PMID: 36399038 DOI: 10.1148/rycan.220073] [FullText]

27 **Grözinger M**, Wennmann M, Sawall S, Wehrse E, Sedaghat S, Neelsen C, Bauer F, Goldschmidt H, Weru V, Ziener CH, Kopp-Schneider A, Schlemmer HP, Rotkopf LT. Detection of myeloma-associated osteolytic bone lesions with energy-integrating and photon-counting detector CT. *Radiologie (Heidelb)* 2024; **64**: 24-31 [*RCA*] [PMID: 39020050 DOI: 10.1007/s00117-024-01344-7] [FullText]

28 **Winkelmann MT**, Hagen F, Le-Yannou L, Weiss J, Riffel P, Gutjahr R, Faby S, Nikolaou K, Horger M. Myeloma bone disease imaging on a 1st-generation clinical photon-counting detector CT vs. 2nd-generation dual-source dual-energy CT. *Eur Radiol* 2023; **33**: 2415-2425 [*RCA*] [PMID: 36350390 DOI: 10.1007/s00330-022-09225-0] [FullText]

29 **Symons R**, Cork TE, Sahbaee P, Fuld MK, Kappler S, Folio LR, Bluemke DA, Pourmorteza A. Low-dose lung cancer screening with photon-counting CT: a feasibility study. *Phys Med Biol* 2017; **62**: 202-213 [*RCA*] [PMID: 27991453 DOI: 10.1088/1361-6560/62/1/202] [FullText]

30 **Jungblut L**, Euler A, Landsmann A, Englmaier V, Mergen V, Sefirovic M, Frauenfelder T. Pulmonary nodule visualization and evaluation of AI-based detection at various ultra-low-dose levels using photon-counting detector CT. *Acta Radiol* 2024; **65**: 1238-1245 [*RCA*] [PMID: 39279297 DOI: 10.1177/02841851241275289] [FullText]

31 **Perera Molligoda Arachchige AS**. MRI versus CT in Detecting Pulmonary Nodules. *Radiology* 2022; **304**: E51 [*RCA*] [PMID: 35727153 DOI: 10.1148/radiol.213078] [FullText]

32 **Flohr T**, Petersilka M, Henning A, Ulzheimer S, Ferda J, Schmidt B. Photon-counting CT review. *Phys Med* 2020; **79**: 126-136 [*RCA*] [PMID: 33249223 DOI: 10.1016/j.ejmp.2020.10.030] [FullText]

World Journal of Radiology

Submit a Manuscript: https://www.f6publishing.com

World J Radiol 2025 August 28; 17(8): 109146

DOI: 10.4329/wjr.v17.i8.109146

ISSN 1949-8470 (online)

CASE REPORT

Does ultrasound detect joint and intestinal changes in psoriatic arthritis and ulcerative colitis after immunobiological treatment: A case report

José Alexandre Mendonça, José Luís Braga de Aquino

Specialty type: Radiology, nuclear medicine and medical imaging

Provenance and peer review: Unsolicited article; Externally peer reviewed.

Peer-review model: Single blind

Peer-review report's classification
Scientific Quality: Grade C
Novelty: Grade D
Creativity or Innovation: Grade D
Scientific Significance: Grade D

P-Reviewer: Xie D

Received: April 30, 2025
Revised: May 25, 2025
Accepted: July 24, 2025
Published online: August 28, 2025
Processing time: 120 Days and 10.9 Hours

José Alexandre Mendonça, Stricto Sensu Postgraduate Program in Health Sciences/Ultrasonography/Rheumatology Service, Pontifical Catholic University of Campinas (PUC-Campinas) School of Life Sciences, Sumare 13175665, São Paulo, Brazil

José Luís Braga de Aquino, Stricto Sensu Postgraduate Program in Health Sciences/Surgery Service, Pontifical Catholic University of Campinas (PUC-Campinas) School of Life Sciences, Campinas 13060-604, São Paulo, Brazil

Co-corresponding authors: José Alexandre Mendonça and José Luís Braga de Aquino.

Corresponding author: José Alexandre Mendonça, PhD, Professor, Stricto Sensu Postgraduate Program in Health Sciences/Ultrasonography/Rheumatology Service, Pontifical Catholic University of Campinas (PUC-Campinas) School of Life Sciences, Avenue John Boyd Dunlop, Jardim Ipaussurama, Campinas, Sumare 13175665, São Paulo, Brazil.
alexandre@josealexandre.com

Abstract

BACKGROUND

Ultrasound (US) can be a valuable tool for assessing arthritis associated with inflammatory bowel disease (IBD), especially in cases of psoriatic disease. The clinical case reviewed in this article addresses an exploratory finding that evaluates the effects of immunobiological treatments on dactylitis and IBD with the use of US techniques.

CASE SUMMARY

A 40-year-old Caucasian woman with psoriatic arthritis (PsA) and ulcerative colitis (UC) reported experiencing finger pain, knee arthritis, and bloody diarrhea. She showed a high Disease Activity index for PsA score and a severe Mayo score. She began treatment with adalimumab. Over the course of six months, the 18 MHz US procedure was performed on her joints and a 3.5 MHz US on her intestines. The joint US indicated dactylitis and swelling in her finger joints, while the intestinal US revealed 6.6 mm swelling in the sigmoid colon, increased abdominal fat, and high Doppler signal. Her fecal calprotectin level was 5984 mg/kg, and a colonoscopy showed that UC extended to the hepatic flexure, along with mild narrowing of the transverse colon. After six months treatment, all parameters showed improvement, including a remission of the Mayo score, better

colonoscopy results, and Limberg score of 0.

CONCLUSION
More research is needed to find out the importance of using US in patients with PsA and UC as this could improve treatment strategies.

Key Words: Ultrasonography; Psoriatic arthritis; Ulcerative colitis; Tumor necrosis factor; Case report

Core Tip: This case study highlights a promising ultrasound (US) use in the simultaneous assessment of joint and intestinal inflammation in a patient diagnosed with psoriatic arthritis (PsA) and ulcerative colitis (UC). By employing high-frequency US (18 MHz) to evaluate dactylitis as well as abdominal US (3.5 MHz) to detect colonic inflammation, the findings underscore the versatility of this imaging technique. Following a six-month treatment regimen with adalimumab, significant improvements were observed in various clinical, laboratory, endoscopic, and sonographic parameters. These results suggest that US may represent a valuable tool for the integrated monitoring of PsA and UC and can potentially guide and enhance therapeutic strategies.

Citation: Mendonça JA, de Aquino JLB. Does ultrasound detect joint and intestinal changes in psoriatic arthritis and ulcerative colitis after immunobiological treatment: A case report. *World J Radiol* 2025; 17(8): 109146
URL: https://www.wjgnet.com/1949-8470/full/v17/i8/109146.htm
DOI: https://dx.doi.org/10.4329/wjr.v17.i8.109146

INTRODUCTION

Psoriasis (PsO) is associated with several manifestations, including joint involvement and systemic conditions such as uveitis and inflammatory bowel disease (IBD). Patients with PsO, psoriatic arthritis (PsA), and spondyloarthritis have a 1-4 times higher risk and a 1-6 times higher risk of developing IBD compared to the general population. IBD includes primarily two main forms: (1) Crohn's disease (CD); and (2) Ulcerative colitis (UC). Both CD and UC are chronic disorders characterized by intermittent remission phases and periods of active inflammation, with symptoms such as abdominal pain, diarrhea, and rectal bleeding. The risk of developing PsO, PsA, ankylosing spondylitis (AS), and IBD is polygenic and often these disorders overlap, which may explain the clustering of immune-mediated chronic inflammatory diseases with various phenotypes across generations[1]. IBD encompasses two conditions: (1) CD, which can affect any part of the gastrointestinal tract in a discontinuous manner and impact the intestinal wall transmurally; and (2) UC, which affects the mucosa continuum and concentrates primarily in the rectum[1-3]. Notably, the prevalence of IBD does not reflect the significant rates of subclinical intestinal involvement detected by endoscopic examinations or biopsies; actually, this condition rate can be as high as 65%-70%. A connection between joint manifestations and IBD may also be observed.

The pathophysiology underlying the hypothesis of "arthritogenic bowel" involves genetic factors. A significant cause is the high prevalence of the human leukocyte antigen (HLA)-B27 antigen, found in approximately 25% of individuals with spondyloarthritis and 78% of those with IBD. Other genetic factors, such as HLA-DRB1 and HLA-B44, have also been identified, along with non-histocompatibility factors like variations in the *CARD15* gene, which increases the risk of sacroiliitis in CD[4,5]. These conditions are supported by transcriptomic analysis, which identifies CD 64+ myeloid cells as a source of interleukin (IL)-23 stimulation in the intestine. The situation is exacerbated by epigenetic alterations thought to occur due to microbial dysbiosis, triggering the transcription of several interleukins, including IL-17 and tumor necrosis factor (TNF). This process leads to the differentiation of Th17 Lymphocytes, mediated by autoreactive T and B lymphocytes. Consequently, locally recruited macrophages and lymphocytes that express intestinal markers, along with cytokines IL-17 and IL-23, can migrate through the intestinal vasculature. This movement is facilitated by increased vascular permeability associated with inflammation, allowing those cells to reach the synovial vessels. While substantial evidence supports such hypothesis, further research is necessary for its validation.[5,6].

Regarding AS, few reports detailing this disorder association with IBD are available. However, one study indicates a significant reduction in microbiota among AS patients, demonstrating dysbiosis similar to that seen in IBD patients, with a comparable bacterial profile. Nevertheless, stronger evidence is needed to provide more evidence for this association[7].

In recent years, high-resolution ultrasound (US), particularly Doppler technology in US, has proven beneficial in diagnosing and monitoring rheumatological diseases helping to evaluate synovitis and enthesopathies, especially in cases of subclinical disease activity. Advances in understanding intestinal imaging using US techniques have also allowed for the demonstration of pathological changes associated with IBD[8,9]. US can help characterize intestinal inflammation by highlighting hypoechogenicity and thickening of the inflamed intestinal wall, while Doppler assesses vascular changes due to intense neovascularization, inflammatory infiltration, small artery thrombosis, and dilation of arteries and veins that are manifestations of IBD[9,10].

CASE PRESENTATION

Chief complaints

This clinical case emphasizes the importance of US for assessing joint ill manifestations as well as detecting intestinal inflammation and helping monitoring treatments.

History of present illness

Two patients, 51 ± 11 years of age, were diagnosed with PsA and UC through colonoscopy. The intestinal US examinations performed revealed signs of inflammation while remaining blinded to their clinical conditions. One patient was female and the other was male. The female patient, a businesswoman, completed US treatment and follow-up, allowing her to be included in the study. In contrast, the male patient was excluded due to lack of follow-up on his intestinal US procedure.

History of past illness

The female patient had been diagnosed with PsO on her scalp and elbows eight years before.

Personal and family history

After experiencing skin lesions for four years, she began to develop inflammatory joint pain while opening and closing her fingers, along with arthritis in her left knee. Three years after these joint complaints started, she experienced over 20 episodes of bloody diarrhea and was subsequently diagnosed with UC. Her father had been diagnosed with PsA 20 years earlier.

Physical examination

Before starting the adalimumab treatment, the patient's exams indicated she had: (1) Mild PsO according to the Psoriasis Area and Severity Index (PASI); (2) High score on the Disease Activity Index for PsA (DAPSA); and (3) Severe Mayo score (Table 1). The clinical evaluation was conducted using the PASI, which measures the severity of PsO based on four criteria: (1) Crythema; (2) Induration; (3) Scaling; and (4) The extent of the affected area. The severity of skin involvement is categorized based on the surface area affected (BSA) as follows: (1) No PsO (0 BSA); (2) Mild (< 10 BSA); (3) Moderate (10-20 BSA); and (4) Severe (> 20 BSA)[11].

To assess arthritis, the DAPSA score was used. This score includes the number of painful and swollen joints (28 in total), the patient's visual analogue pain scale (ranging from 0 to 10), the physician's assessment, and the inflammatory marker C-reactive protein. Disease activity is classified into four categories: (1) High (≥ 28); (2) Moderate (15-28); (3) Low (5-14); and (4) In remission (≤ 4)[12-14].

Laboratory examinations

The patient's laboratory exams showed a negative rheumatoid factor, a fecal calprotectin level of 5984 mg/kg[15], serology testing for hepatitis B, C, human immunodeficiency virus, and syphilis, a negative Mantoux test, and no anomalies on the chest X-ray.

Imaging examinations

The patient gave her consent by signing the Informed Consent Form for the US evaluation and other procedures conducted at the Rheumatology Clinic. This evaluation was performed by a single rheumatologist with 17 years' experience in general and articular US examinations, specifically for rheumatology and immune-mediated diseases, as part of the University's postgraduate program and the Hospital's US service. The assessment followed established protocols, using all appropriate equipment configurations for monitoring the treatment, and all images were recorded on an external hard drive. For the evaluation, the MyLab Gold 25 US system (Esaote SpA, São Paulo, Brazil) was used. It was equipped with an 18 MHz high-frequency linear probe for use in the joint assessment and a 3.5 MHz convex probe for intestinal examination. The Doppler specifications were standardized, featuring a frequency range of 2.5-8.0 MHz and pulse repetition frequencies of 0.7-1.0 kHz. The joints US assessment covered all the fingers, evaluating both dorsal and palmar recesses[9,16]. The intestinal US evaluation was conducted with the patient fasting and positioned supine to preserve the intestines' physiological state, minimizing interference from luminal contents and vascular changes. A comprehensive assessment of both the small intestine and colon was performed, scanning all segments in both the long and short axes, paying particular attention to any abnormal areas. The intestinal loops in the sigmoid colon region, including assessments of mesenteric fat thickening were specifically measured. Doppler signal evaluations were carried out to monitor the treatment parameters. Importantly, oral contrast was not used, as US allows dynamic, real-time observation of intestinal movements and caliber while the patient is at rest. The evaluation focused on the five concentric, compressible layers with varying echogenicities, assessing increased wall thickness greater than 3 mm, depending on the specific location. Additionally, the mesenteric fat and Doppler signal were graded from 0 to 3 to semi-quantify the severity of the inflammatory process[9,17].

MULTIDISCIPLINARY EXPERT CONSULTATION

When there is a link between arthritis and IBD, the concept of an arthritogenic bowel becomes particularly important.

Table 1 Clinical, ultrasound, laboratory, and colonoscopy parameters before and after treatment

	Before	After
Psoriasis Area and Severity Index	8.3	2.0
Disease Activity Index for Psoriatic Arthritis	29.16	0
Mayo score	12	0
Paratenonitis	Present	Absent
Fecal calprotectin	5984 mg/kg	600 mg/kg
Colonoscopy	Intense inflammation	Remission
Intestinal wall thickness	6.6 mm	2.8 mm
Degree of thickening of perienteric fat	2	0
Doppler degree in the intestinal wall	3	0

This connection emphasizes the need for a multidisciplinary approach, which is associated with better clinical outcomes. These outcomes include higher rates of sustained remission, reduced hospitalizations stay and reduced surgical procedures, as well as an overall improved quality of life as reported by patients. Additionally, a multidisciplinary approach encourages collaborative clinical decision-making, humanizes patient care, and enhances the integration of support, education, and research within specialized centers. Therefore, it is crucial to promote and incorporate multidisciplinary consultations as a standard practice for managing patients with UC, especially in complex clinical situations within tertiary care centers and IBD referral units[18,19].

FINAL DIAGNOSIS

The fingers' joints examination revealed findings consistent with dactylitis, which was attributed to significant paratenonitis in the second and third proximal interphalangeal joints of the right hand, characterized by effusion. A bowel US showed 6.6 mm edema in the sigmoid colon wall and indicated grade 2 mesenteric fat and grade 3 Doppler signal on the Limberg scale. Additionally, a colonoscopy revealed severe UC extending to the hepatic flexure and mild stenosis of the transverse colon, with a Mayo score 3 and 7 UC Disease Activity Index Score.

TREATMENT

The treatment consisted of 100 mg adalimumab and azathioprine during six months.

OUTCOME AND FOLLOW-UP

All clinical, US, laboratory, and colonoscopy parameters showed improvement, indicating preserved mucosa with a distinct vascular pattern, with no edema, erosions, or ulcerations, and no signs of inflammatory activity (Table 1, Figures 1, 2 and 3).

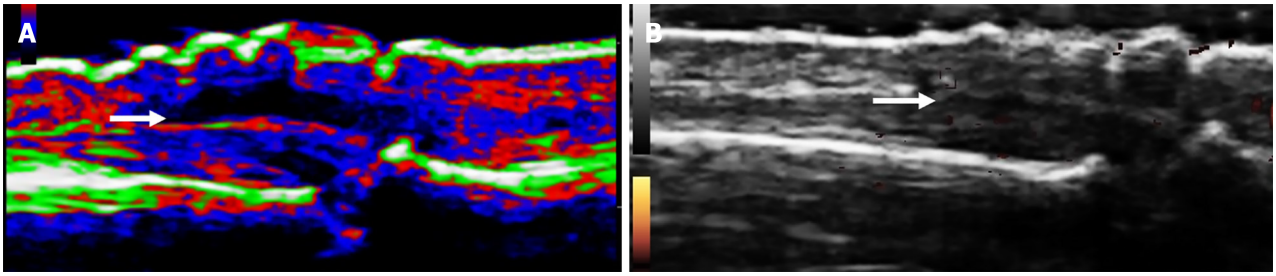

Figure 1 Follow-up treatment after the use of adalimumab. A: It shows the presence of effusion as indicated by the color map in B-mode; B: It shows the absence of effusion (arrows). They illustrate the longitudinal dorsal recess of the second proximal interphalangeal joint with peritendinitis.

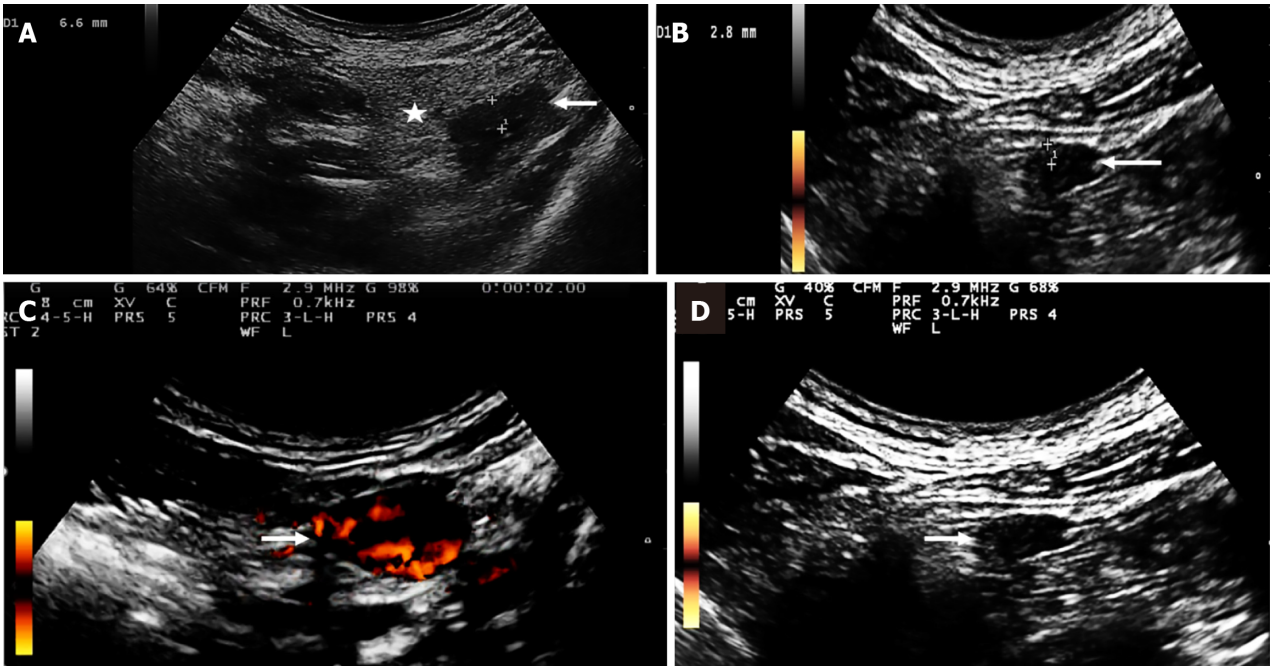

Figure 2 Monitoring intestinal inflammatory activity: Improvement after adalimumab treatment. A and B: Reduced intestinal wall thickening (arrows) and perienteric fat (star) (short axis images of the sigmoid colon); C and D: Decreased Doppler signal per the Limberg scale (arrows).

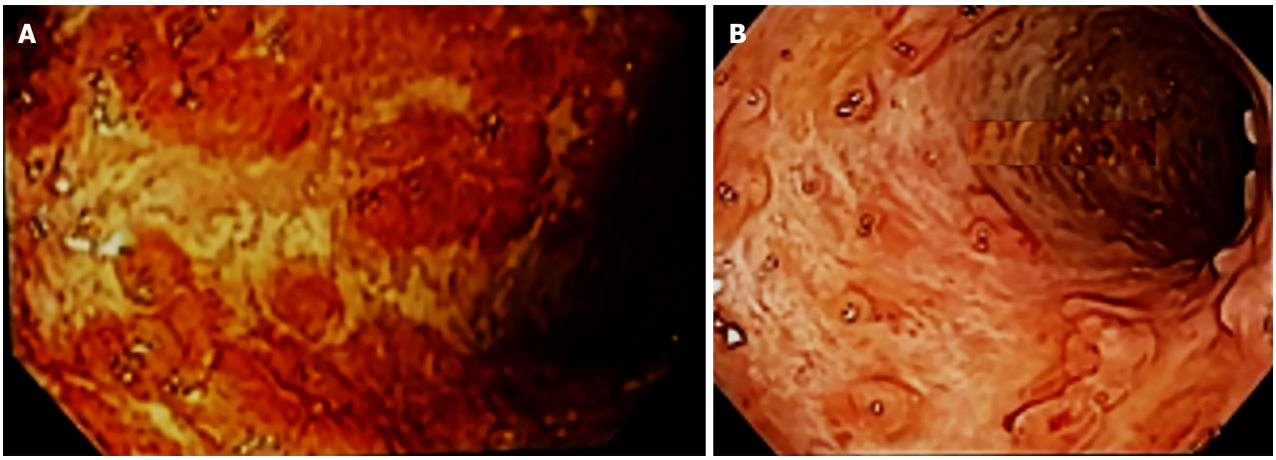

Figure 3 Treatment follow-up after adalimumab use. A: Colonoscopy show intense proctocolitis; B: Remission, respectively.

DISCUSSION

High-resolution B-mode and Doppler ultrasonography effectively translate clinical and often subclinical dactylitis into observable conditions such as synovitis, tenosynovitis, enthesitis, and inflammation of both the subcutaneous tissue and the periextensor tendon. Recently, a dactylitis score scale has been developed for patients with PsA, as this condition can be challenging to detect during clinical examinations. Patients frequently exhibit US abnormalities without accompanying inflammatory signs. The clinical significance of dactylitis is highlighted by its role as a marker of disease aggressiveness and poor prognosis in affected patients. An US study found that 35.7% of PsO patients exhibited subclinical dactylitis compared to a control group, along with a 30% occurrence of moderate peritendinitis of the fingers' extensor tendon[18,20,21].

The use of US in UC has proven beneficial as it helps to identify structural damage to the large intestine a damage which is an indication of an active inflammatory process in the bowel. Accuracy of US in assessing the bowel inflammation extent and severity, as well as in monitoring therapeutic responses has been evidenced[19].

The TNF plays a crucial role in the pathogenesis of immune-mediated inflammatory diseases; hence, inhibiting TNF is vital for managing severe and progressive inflammatory conditions. This intervention can lead to rapid and sustained clinical remission, enhance quality of life, and prevent damage to other target organs. Adalimumab, the first fully human monoclonal antibody targeting TNF, has demonstrated efficacy and tolerability in patients with various extensive inflammatory diseases, including PsA, plaque PsO, and IBD such as CD and UC. Accurate mapping of intestinal manifestations in patients with PsA is crucial, as it allows for more precise treatment approaches. Adjustments in the therapeutic classes

and the potential increase of the anti-TNF drug dosage may be necessary for effectively managing intestinal inflammation, since differences in dosing requirements compared to arthritis treatment exist. Research indicates that a higher dosage of adalimumab achieves sustained efficacy in inducing remission of intestinal inflammation, reporting a 25% success rate in moderate to severe cases over four years[22,23].

However, the limitations of US in UC affect its effectiveness in the assessments, as inflammation primarily affects the mucosa. The technique is better suited for identifying changes in deeper bowel layers, as seen in CD. Visualizing the rectum can be challenging, and mild or microscopic inflammation may not be detected, the tissues often appearing normal. In cases of remission, the bowel wall thickness typically returns to normal, further decreasing US sensitivity. Factors such as flatulence, obesity, and operator's skill can also impact image quality. Therefore, while US may have some use, it cannot replace colonoscopy for confirming remission or for monitoring[19].

CONCLUSION

Our study emphasizes the importance of joint and intestinal mapping when treating patients with a humanized monoclonal anti-TNF agent. Further research is needed to determine the necessity of US monitoring in patients with PsA and IBD. This could improve the selection of safer and more appropriate treatment options for these patients.

ACKNOWLEDGEMENTS

We are grateful to the patients for their participation in this exploratory and innovative investigation of joint and bowel imaging.

FOOTNOTES

Author contributions: Mendonça JA did the ultrasound exams; Mendonça JA and de Aquino JLB contributed equally, with the writing and the method description of this article as the co-corresponding authors; all authors read and approved the final manuscript.

Informed consent statement: Informed consent for publication was obtained for this case report.

Conflict-of-interest statement: The authors declare that they have no conflict of interest.

CARE Checklist (2016) statement: The authors have read the CARE Checklist (2016), and the manuscript was prepared and revised according to the CARE Checklist (2016).

Country of origin: Brazil

ORCID number: José Alexandre Mendonça 0000-0003-1689-6705; José Luís Braga de Aquino 0000-0002-0604-9054.

S-Editor: Luo ML
L-Editor: A
P-Editor: Yu HG

REFERENCES

1 **Bolt JW**, van Ansenwoude CMJ, Hammoura I, van de Sande MG, van Baarsen LGM. Translational Research Studies Unraveling the Origins of Psoriatic Arthritis: Moving Beyond Skin and Joints. *Front Med (Lausanne)* 2021; **8**: 711823 [*RCA*] [PMID: 34485340 DOI: 10.3389/fmed.2021.711823] [FullText] [Full Text(PDF)]

2 **Ono K**, Kishimoto M, Deshpande GA, Fukui S, Kawaai S, Sawada H, Matsuura M, Rodriguez VR, Proft F, Tada K, Tamura N, Taniguchi Y, Hirata A, Kameda H, Tsuji S, Kaneko Y, Dobashi H, Okano T, Haji Y, Morita A, Okada M, Komagata Y, Medina CL, Molto A, Dougados M, Hisamatsu T, Tomita T, Kaname S. Clinical characteristics of patients with spondyloarthritis and inflammatory bowel disease versus inflammatory bowel disease-related arthritis. *Rheumatol Int* 2022; **42**: 1751-1766 [*RCA*] [PMID: 35532790 DOI: 10.1007/s00296-022-05117-0] [FullText]

3 **Schreiber S**, Colombel JF, Feagan BG, Reich K, Deodhar AA, McInnes IB, Porter B, Das Gupta A, Pricop L, Fox T. Incidence rates of inflammatory bowel disease in patients with psoriasis, psoriatic arthritis and ankylosing spondylitis treated with secukinumab: a retrospective analysis of pooled data from 21 clinical trials. *Ann Rheum Dis* 2019; **78**: 473-479 [*RCA*] [PMID: 30674475 DOI: 10.1136/annrheumdis-2018-214273] [FullText] [Full Text(PDF)]

4 **Danve A**. Thoracic Manifestations of Ankylosing Spondylitis, Inflammatory Bowel Disease, and Relapsing Polychondritis. *Clin Chest Med* 2019; **40**: 599-608 [*RCA*] [PMID: 31376894 DOI: 10.1016/j.ccm.2019.05.006] [FullText]

5 **Atreya R**, Abreu MT, Krueger JG, Eyerich K, Greving C, Hammaker D, Stoveken B, Hartman J, Leppard K, Sarabia I, Wertheimer J, Deming J, Kohler K, Li H, Freeman T, Hart A, Keyes B, Ritchlin C, Mcinnes IB, Allez M, Fourie A, Sachen K. P165 Guselkumab binding to CD64+ IL-23–producing myeloid cells enhances potency for neutralizing IL-23 signaling. *J Crohns Colitis* 2024; **18**: i465-i465 [DOI: 10.1093/ecco-jcc/jjad212.0295] [FullText]

6 **Bourgonje AR**, Ungaro RC, Mehandru S, Colombel JF. Targeting the Interleukin 23 Pathway in Inflammatory Bowel Disease. *Gastroenterology* 2025; **168**: 29-52.e3 [*RCA*] [PMID: 38945499 DOI: 10.1053/j.gastro.2024.05.036] [FullText]

7 **Breban M**. Gut microbiota and inflammatory joint diseases. *Joint Bone Spine* 2016; **83**: 645-649 [*RCA*] [PMID: 27238190 DOI: 10.1016/j.jbspin.2016.04.005] [FullText]

8 **Balint PV**, Terslev L, Aegerter P, Bruyn GAW, Chary-Valckenaere I, Gandjbakhch F, Iagnocco A, Jousse-Joulin S, Möller I, Naredo E, Schmidt WA, Wakefield RJ, D'Agostino MA; OMERACT Ultrasound Task Force members. Reliability of a consensus-based ultrasound definition and scoring for enthesitis in spondyloarthritis and psoriatic arthritis: an OMERACT US initiative. *Ann Rheum Dis* 2018; **77**: 1730-1735 [*RCA*] [PMID: 30076154 DOI: 10.1136/annrheumdis-2018-213609] [FullText]

9 **Nassef MA**, Botros SM, Adel Ghaffar MK. The update of ultrasound techniques in diagnosis of inflammatory bowel disease. *Egypt J Radiol Nucl Med* 2014; **45**: 289-294 [*RCA*] [DOI: 10.1016/j.ejrnm.2014.02.002] [FullText]

10 **Huber MK**, Valim V, Serrano ÉV, Mendonça JA, Lourenço RB, Espírito Santo TMR, Nordal H, de Fátima Bissoli M, de Oliveira Gavi MBR. Prevalence of spondyloarthritis in inflammatory bowel disease according ASAS and ultrassonography and its correlation with plasma calprotectin. *Adv Rheumatol* 2024; **64**: 27 [*RCA*] [PMID: 38622711 DOI: 10.1186/s42358-023-00348-6] [FullText]

11 **Mattei PL**, Corey KC, Kimball AB. Psoriasis Area Severity Index (PASI) and the Dermatology Life Quality Index (DLQI): the correlation between disease severity and psychological burden in patients treated with biological therapies. *J Eur Acad Dermatol Venereol* 2014; **28**: 333-337 [*RCA*] [PMID: 23425140 DOI: 10.1111/jdv.12106] [FullText]

12 **Schoels MM**, Aletaha D, Alasti F, Smolen JS. Disease activity in psoriatic arthritis (PsA): defining remission and treatment success using the DAPSA score. *Ann Rheum Dis* 2016; **75**: 811-818 [*RCA*] [PMID: 26269398 DOI: 10.1136/annrheumdis-2015-207507] [FullText]

13 **Hackett S**, Coates LC. Outcome measures in psoriatic arthritis: Where next? *Musculoskeletal Care* 2022; **20** Suppl 1: S22-S31 [*RCA*] [PMID: 36356107 DOI: 10.1002/msc.1692] [FullText]

14 **Lewis JD**, Chuai S, Nessel L, Lichtenstein GR, Aberra FN, Ellenberg JH. Use of the noninvasive components of the Mayo score to assess clinical response in ulcerative colitis. *Inflamm Bowel Dis* 2008; **14**: 1660-1666 [*RCA*] [PMID: 18623174 DOI: 10.1002/ibd.20520] [FullText] [Full Text(PDF)]

15 **Mahdipour M**, Shafaghi A, Mansour-ghanaei F, Hojati A, Joukar F, Mavaddati S. Fecal calprotectin role in diagnosis of ulcerative colitis and treatment follow-up. *J Coloproctol* 2019; **39**: 115-120 [DOI: 10.1016/j.jcol.2018.10.012] [FullText]

16 **Bruyn GA**, Iagnocco A, Naredo E, Balint PV, Gutierrez M, Hammer HB, Collado P, Filippou G, Schmidt WA, Jousse-Joulin S, Mandl P, Conaghan PG, Wakefield RJ, Keen HI, Terslev L, D'Agostino MA; OMERACT Ultrasound Working Group. OMERACT Definitions for Ultrasonographic Pathologies and Elementary Lesions of Rheumatic Disorders 15 Years On. *J Rheumatol* 2019; **46**: 1388-1393 [*RCA*] [PMID: 30709946 DOI: 10.3899/jrheum.181095] [FullText]

17 **Frias-Gomes C**, Torres J, Palmela C. Intestinal Ultrasound in Inflammatory Bowel Disease: A Valuable and Increasingly Important Tool. *GE Port J Gastroenterol* 2022; **29**: 223-239 [*RCA*] [PMID: 35979252 DOI: 10.1159/000520212] [FullText] [Full Text(PDF)]

18 **Mendonca J**, Heloísa Ferreira W, Gutierrez M. AB0481 Subclinical Dactylitis in Patients with Psoriasis: Role of Ultrasound. *Ann Rheum Dis* 2024; **83**: 1507-1508 [DOI: 10.1136/annrheumdis-2024-eular.2985] [FullText]

19 **Nagarajan KV**, Bhat N. Intestinal ultrasound in inflammatory bowel disease: New kid on the block. *Indian J Gastroenterol* 2024; **43**: 160-171 [*RCA*] [PMID: 37996771 DOI: 10.1007/s12664-023-01468-z] [FullText]

20 **Naredo E**, D'Agostino MA, Terslev L, Pineda C, Miguel MI, Blasi J, Bruyn GA, Kortekaas MC, Mandl P, Nestorova R, Szkudlarek M, Todorov P, Vlad V, Wong P, Bakewell C, Filippucci E, Zabotti A, Micu M, Vreju F, Mortada M, Mendonça JA, Guillen-Astete CA, Olivas-Vergara O, Iagnocco A, Hanova P, Tinazzi I, Balint PV, Aydin SZ, Kane D, Keen H, Kaeley GS, Möller I. Validation and incorporation of digital entheses into a preliminary GLobal OMERACT Ultrasound DActylitis Score (GLOUDAS) in psoriatic arthritis. *Ann Rheum Dis* 2024; **83**: 1060-1071 [*RCA*] [PMID: 38531611 DOI: 10.1136/ard-2023-225278] [FullText]

21 **Felbo SK**, Østergaard M, Sørensen IJ, Terslev L. Which ultrasound lesions contribute to dactylitis in psoriatic arthritis and their reliability in a clinical setting. *Clin Rheumatol* 2021; **40**: 1061-1067 [*RCA*] [PMID: 33155158 DOI: 10.1007/s10067-020-05483-9] [FullText]

22 **Korman NJ**. Management of psoriasis as a systemic disease: what is the evidence? *Br J Dermatol* 2020; **182**: 840-848 [*RCA*] [PMID: 31225638 DOI: 10.1111/bjd.18245] [FullText] [Full Text(PDF)]

23 **Calvo Moya M**, González Lama Y, Ruíz Antorán B, Omella Usieto I, El Hajra Martinez I, Santos Pérez E, Menchén Viso B, Matallana Royo V, González Partida I, de Lucas Tellez de Meneses R, Bella Castillo P, González Rodriguez M, Vera Mendoza MI. Treatment With Adalimumab 80 mg Every Other Week in Inflammatory Bowel Disease: Results of Treatment Intensification in Clinical Practice. *Crohns Colitis 360* 2023; **5**: otac051 [*RCA*] [PMID: 36785555 DOI: 10.1093/crocol/otac051] [FullText]

World Journal of Radiology

Submit a Manuscript: https://www.f6publishing.com

World J Radiol 2025 August 28; 17(8): 110868

DOI: 10.4329/wjr.v17.i8.110868

ISSN 1949-8470 (online)

CASE REPORT

Imaging features of appendiceal signet ring cell carcinoma with uterine implantation: A case report

Jia-Mi Liu, Zhi Li, Ling-Hong Qi, Bo-Liang Chu, Zai-Xing Deng, Feng-Yun Tang

Specialty type: Radiology, nuclear medicine and medical imaging

Provenance and peer review: Unsolicited article; Externally peer reviewed.

Peer-review model: Single blind

Peer-review report's classification

Scientific Quality: Grade A, Grade B, Grade B, Grade C

Novelty: Grade A, Grade B, Grade B, Grade D

Creativity or Innovation: Grade A, Grade B, Grade B, Grade C

Scientific Significance: Grade A, Grade A, Grade A, Grade C

P-Reviewer: Corbaci K, MD, Türkiye; Ma RQ, Assistant Professor, Vice Director, China; Turan B, MD, Assistant Professor, Researcher, Türkiye

Received: June 18, 2025

Revised: July 16, 2025

Accepted: August 8, 2025

Published online: August 28, 2025

Processing time: 72 Days and 6.2 Hours

Jia-Mi Liu, Zhi Li, Ling-Hong Qi, Department of Radiology, Huzhou Maternity & Child Health Care Hospital, Huzhou 313000, Zhejiang Province, China

Bo-Liang Chu, Department of Gynaecology, Huzhou Maternity & Child Health Care Hospital, Huzhou 313002, Zhejiang Province, China

Zai-Xing Deng, Department of Pathology, Huzhou Maternity & Child Health Care Hospital, Huzhou 313000, Zhejiang Province, China

Feng-Yun Tang, Department of General Practice, Baiyang Community Health Service Center, Hangzhou 310000, Zhejiang Province, China

Co-first authors: Jia-Mi Liu and Zhi Li.

Corresponding author: Feng-Yun Tang, Deputy Director, Department of General Practice, Baiyang Community Health Service Center, Baiyang Street, Qiantang District, Hangzhou 310000, Zhejiang Province, China. bbyxy804@126.com

Abstract

BACKGROUND

Signet ring cell carcinoma originating from the appendix is extremely rare, and the lack of specific clinical symptoms and imaging features makes preoperative diagnosis particularly challenging.

CASE SUMMARY

We report a case of a 49-year-old woman who presented with irregular vaginal bleeding lasting more than five months. Computed tomography (CT) and magnetic resonance imaging (MRI) revealed an enlarged appendix with a thickened wall and progressive enhancement after contrast administration. The uterine myometrium and cervix were markedly thickened, with heterogeneous density and signal intensity, along with progressive enhancement. The uterine serosal surface remained intact. Preoperative MRI suggested diffuse uterine adenomyosis; however, postoperative histopathology confirmed Signet ring cell carcinoma originating from the appendix with implantation involving the entire uterus.

CONCLUSION

Imaging showed appendiceal wall thickening and marked thickening of the uterine myometrium, with lesions demonstrating progressive enhancement after contrast administration. These findings should raise suspicion for the implan-

tation of Signet ring cell carcinoma originating from the appendix and involving the uterus. Signet ring cell carcinoma originating from the appendix is relatively rare, and its imaging features are seldom reported, making preoperative diagnosis extremely challenging. This study retrospectively analyzes a case of Signet ring cell carcinoma originating from the appendix with implantation involving the entire uterus. The imaging characteristics of the appendix and the uterus were evaluated using CT and MRI to enhance awareness of this disease.

Key Words: Signet ring cell carcinoma; Appendix; Magnetic resonance imaging; Malignant tumor; Case report

Core Tip: Signet ring cell carcinoma originating from the appendix is relatively rare, and its imaging features are seldom reported, making preoperative diagnosis extremely challenging. This study retrospectively analyzes a case of Signet ring cell carcinoma originating from the appendix and implantation to the entire uterus. The imaging characteristics of both the appendix and the uterus were analyzed using computed tomography and magnetic resonance imaging, with the aim of enhancing awareness of this disease.

Citation: Liu JM, Li Z, Qi LH, Chu BL, Deng ZX, Tang FY. Imaging features of appendiceal signet ring cell carcinoma with uterine implantation: A case report. *World J Radiol* 2025; 17(8): 110868
URL: https://www.wjgnet.com/1949-8470/full/v17/i8/110868.htm
DOI: https://dx.doi.org/10.4329/wjr.v17.i8.110868

INTRODUCTION

Signet ring cell carcinoma is a distinct clinical and pathological subtype of colorectal cancer, characterized by aggressive behavior and a low incidence of approximately 0.6%-2.3%[1–6]. Signet ring cell carcinoma originating from the appendix is even rarer, accounting for about 16% of all Signet ring cell carcinoma cases[6]. Approximately 93% of appendiceal signet ring cell carcinomas have metastasized to adjacent organs, lymph nodes, or the peritoneal cavity at diagnosis[6]. Early detection and intervention are therefore essential for improving patient outcomes[7]. Accurate preoperative diagnosis remains challenging because of nonspecific clinical symptoms and a lack of characteristic imaging findings. This report presents a rare case of appendiceal Signet ring cell carcinoma with implantation to the entire uterus, emphasizing its computed tomography (CT) and magnetic resonance imaging (MRI) characteristics to improve disease recognition.

CASE PRESENTATION

Chief complaints

A 49-year-old woman presented with more than 5 months of irregular vaginal bleeding.

History of present illness

Her last menstrual period occurred on April 15, 2023, and was initially accompanied by heavy bleeding. She sought care at a local hospital and received unspecified medical therapy that reduced the bleeding; intermittent spotting persisted. She denied significant abdominal pain, dizziness, headache, palpitations, or anal fullness.

History of past illness

No notable past medical history.

Personal and family history

There was no significant personal and family history.

Physical examination

Vital signs were as follows: Temperature, 36.8 °C; heart rate, 75 beats per minute; respiratory rate, 19 breaths per min; and blood pressure, 150/82 mmHg. She was alert and appeared well, with no jaundice of the skin or sclera. Cardiopulmonary auscultation was unremarkable. The liver and spleen were not palpable below the costal margins, and there was no edema of the lower extremities.

Laboratory examinations

Laboratory results were as follows: Hemoglobin 94 g/L (reference range: 115–150 g/L); carcinoembryonic antigen

6.2 ng/mL (≤ 5 ng/mL); cancer antigen 125 60.2 U/mL (≤ 35 U/mL); cancer antigen 19-9 3.2 U/mL (≤ 37 U/mL); human epididymis protein 4 50.1 pmol/L (≤ 70 pmol/L for premenopausal women); and risk of ovarian malignancy algorithm index 8.11% (reference range for premenopausal women, 0%–7.4%.

Imaging examinations

Enhancement rate measurement method: A round region-of-interest (20-40 mm^2) was set in the solid component of lesion. Plain scan CT value, arterial phase CT value, venous phase CT value and lag phase CT value were measured on the same level, and each CT value was measured three times. The means were recorded as the final results. CT enhancement rate of arterial phase: (Arterial phase CT value-plain scan CT value)/plain scan CT value. Enhancement rate of venous phase: (Venous phase CT value-plain scan CT value)/plain scan CT value. Enhancement rate of lag phase: (Lag phase CT value-plain scan CT value)/plain scan CT value[8]. The enhancement rate of lesion in MR referred to the CT measurement method. The MR enhancement rate of arterial phase: (Arterial phase MR value-plain scan MR value)/plain scan MR value. Enhancement rate of venous phase: (Venous phase MR value-plain scan MR value)/plain scan MR value. Enhancement rate of lag phase: (Lag phase MR value-plain scan MR value)/plain scan MR value.

CT findings: The appendix was enlarged with concentric wall thickening and lacked significant intraluminal gas or fecalith-like density. Following contrast administration, the appendiceal wall demonstrated gradual and progressive enhancement, with enhancement rates of 17.8% in the arterial phase, 21.4% in the venous phase, and 46.4% in the delayed phase (Figure 1A). The lesion exhibited a clear boundary from the surrounding tissues, with no evidence of exudative changes.

The uterus appeared uniformly enlarged with an uneven myometrial texture and a smooth perimetrium. It also showed continuous progressive enhancement after contrast administration (Figure 1B), with enhancement rates of 25.0% in the arterial phase, 36.8% in the venous phase, and 55.3% in the delayed phase. The uterine lesion maintained a well-defined border from adjacent structures. No obvious pelvic lymphadenopathy was observed.

MRI findings: The appendix appeared enlarged, demonstrating isointensity on T1-weighted imaging (T1WI) and slight hyperintensity on T2-weighted imaging (T2WI) (Figure 2A). Diffusion-weighted imaging (DWI) showed mildly hyperintense signals, with no significant reduction in the apparent diffusion coefficient value. After contrast administration, the lesion exhibited gradual and progressive enhancement, with enhancement rates of 35.4% in the arterial phase, 60.6% in the venous phase, and 71.6% in the delayed phase. The lesion was well demarcated from adjacent tissues.

The uterine junctional zone was indistinct, with significant thickening of the myometrium and cervix. The lesion showed isointensity on T1WI and iso- to hyperintense signals on T2WI (Figure 2B). DWI revealed mild hyperintensity (Figure 2C), and the ADC value showed no obvious reduction. Post-contrast images demonstrated gradual and progressive enhancement of the uterus and cervix (Figure 2D), with enhancement rates of 35.8% in the arterial phase, 76.6% in the venous phase, and 97.5% in the delayed phase.

Both ovaries were clearly visualized, showing no abnormal signal on DWI and no significant enhancement post-contrast. A small amount of free fluid was noted in the pelvic cavity.

CT diagnosis: Enlarged appendix noted; differential diagnosis requires further evaluation. Significant uterine enlargement with heterogeneous myometrial enhancement was observed.

MRI diagnosis: Thickened appendix; specialist consultation recommended for comprehensive assessment. Marked heterogeneous thickening of the myometrium and cervix, suggestive of diffuse adenomyosis; additional evaluation warranted. Small volume of free pelvic fluid.

Preliminary clinical diagnosis: Abnormal uterine bleeding; mild anemia; uterine adenomyosis; appendiceal tumor?

Postoperative pathological diagnosis: Appendiceal Signet ring cell carcinoma involved the entire appendix and serosa, extending into the cecal muscular layer and serosa. Signet ring cell carcinoma was identified in the endometrium, myometrium, and serosa. Signet ring cell carcinoma also involved the cervical stroma.

FINAL DIAGNOSIS

Appendiceal Signet ring cell carcinoma involved the entire appendix and serosa (Figure 3), extending into the cecal muscle layer, serosa. Signet ring cell carcinoma was identified in the endometrium, myometrium, and serosa (Figure 4). Signet ring cell carcinoma also involved the cervical stroma.

TREATMENT

The patient received adjuvant chemotherapy after surgery.

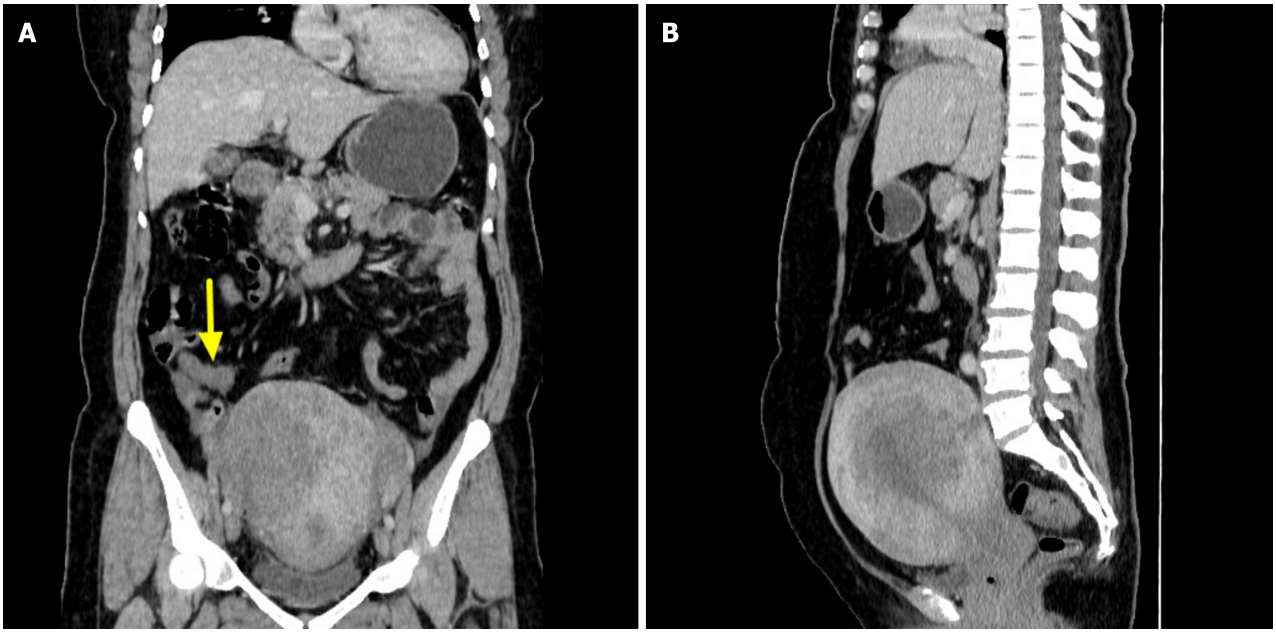

Figure 1 Computed tomography features of the appendix and uterus. A: Computed tomography (CT) enhanced coronal view: Coarsening appendix (arrowhead), strengthening after enhancement, clear boundary between focus and surrounding tissues; B: CT enhanced sagittal view: Obvious uterus enlargement, obvious muscular.

OUTCOME AND FOLLOW-UP

Has been followed for two years. Regular monitoring with tumor markers and imaging has revealed no evidence of recurrence, and follow-up is ongoing.

DISCUSSION

Appendiceal Signet ring cell carcinoma often presents with nonspecific clinical manifestations and may be asymptomatic or mimic acute appendicitis[7,9]. The tumor commonly causes obstruction of the appendiceal lumen, leading to increased intraluminal pressure or compression of the appendiceal mesentery. This results in ischemia, congestion, and potentially secondary bacterial infection. These pathological changes manifest as appendicitis, influenced by the appendix's anatomical characteristics, making preoperative diagnosis extremely challenging. Therefore, histopathological evaluation after surgery is essential for accurate diagnosis[10]. Signet ring cell carcinoma is considered the histopathological subtype of gastrointestinal cancers with the poorest prognosis[11], characterized by high invasiveness and aggressive clinical behavior[12]. Alarmingly, the 5-year survival rate is only 7%[6]. Turaga *et al*[13] reported a median survival time of 24 months for patients with appendiceal. Signet ring cell carcinoma. The patient received adjuvant chemotherapy after surgery and has been followed for two years. Regular monitoring with tumor markers and imaging has revealed no evidence of recurrence, and follow-up is ongoing[14-17].

In this case, the appendix was enlarged and exhibited concentric wall thickening, consistent with the findings reported by Cho *et al*[14]. Both CT and MRI demonstrated gradual progressive enhancement following contrast administration, resembling the enhancement pattern described by Wang *et al*[16]. The uterus and cervix, affected by tumor implantation, showed diffuse thickening with an indistinct junctional zone. The uterine serosal layer remained intact, and the uterine lesions exhibited gradual progressive enhancement similar to the primary appendiceal lesion.

Based on this case and a review of the literature, several insights can be summarized: (1) Following implantation of Signet ring cell carcinoma to the uterus, diffuse thickening of the uterine myometrium may occur, often involving the cervix; (2) MRI characteristics of both primary and implantation lesions typically include iso-intensity on T1WI, iso- to hyperintensity on T2WI, slightly increased signal on DWI, with both CT and MRI showing gradual progressive enhancement after contrast administration; and (3) A small amount of ascitic fluid may be present in the pelvic cavity.

Preoperative accurate diagnosis is critical, as it may necessitate modifications in the surgical approach and the extent of resection[18]. Patients with appendiceal malignancy often present with symptoms and signs that mimic acute appendicitis[7]. In this case, the appendix appeared enlarged with concentric wall thickening, without signs of exudation, and was clearly demarcated from surrounding tissues; therefore, acute appendicitis was not considered. However, both preoperative CT and MRI failed to establish an accurate diagnosis. The uterine lesion was preoperatively misdiagnosed by MRI and clinically as adenomyosis.

Retrospective analysis revealed that the Signet ring cell carcinoma had metastasized to the uterus, and several features distinguished it from uterine adenomyosis: (1) Adenomyosis commonly presents with dysmenorrhea[19], whereas this patient had no history of abdominal pain; (2) Adenomyosis typically involves the uterine myometrium and rarely affects

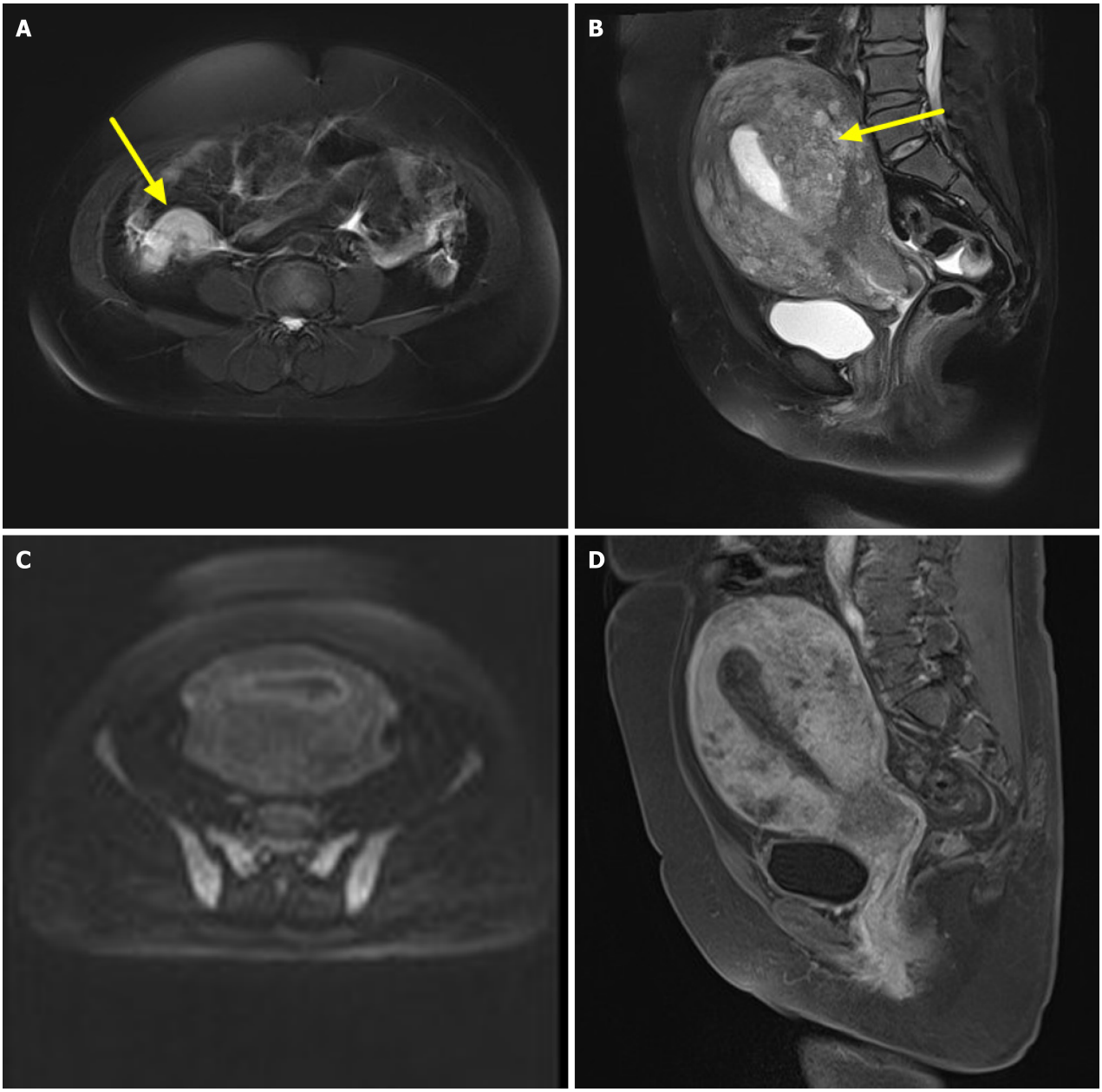

Figure 2 Magnetic resonance imaging features of appendix and uterus. A: T2-weighted imaging (T2WI) transverse view: Coarsening appendix (arrowhead), T2WI high signal, and signals are relatively uniform; B: T2WI sagittal view, obvious thickening mesometrium (arrowhead), and ambiguous display of bonding zone; C: Diffusion-weighted imaging, the enlarged uterus presents slightly high signals; D: T1-weighted imaging enhanced sagittal view, strengthening mesometrium and relatively complete serosa.

the cervix, while in this case, both the uterus and cervix were involved; and (3) Typical MRI findings of adenomyosis include high signal intensity in the myometrium on T2WI and focal high signal on T1WI in cases of hemorrhage[20]. In contrast, this case demonstrated significant myometrial thickening with an indistinct junctional zone and lacked focal high signal on both T1WI and T2WI.

The differential diagnosis of appendiceal signet ring cell carcinoma should include endometrial carcinoma, cervical cancer, and Krukenberg tumors. Endometrial carcinoma is one of the most common gynecologic malignancies[21], with lesions typically confined to the endometrial cavity. While it may invade the myometrium, the extent is usually limited. On DWI, endometrial carcinoma generally exhibits high signal intensity. In contrast, uterine implantation from SRCC tend to involve the uterus diffusely, with DWI signals that are less intense than those of endometrial carcinoma. Cervical cancer is the second most common malignancy in women[22], often originating in the cervix and potentially spreading upward to the uterus or downward to the vagina. It usually presents as a high-intensity signal on DWI. However, signet ring cell carcinoma implantation to the uterus show diffuse thickening of both the uterus and cervix, with lower DWI signal intensity than cervical cancer. Krukenberg tumors—metastatic ovarian tumors commonly originating from the gastrointestinal tract—affect both ovaries in approximately 80% of cases[23]. MRI findings typically include well-defined margins, predominantly solid components, and marked heterogeneous enhancement following contrast administration. Ascites is frequently present[24]. In comparison, signet ring cell carcinoma implantation to the uterus demonstrate lower

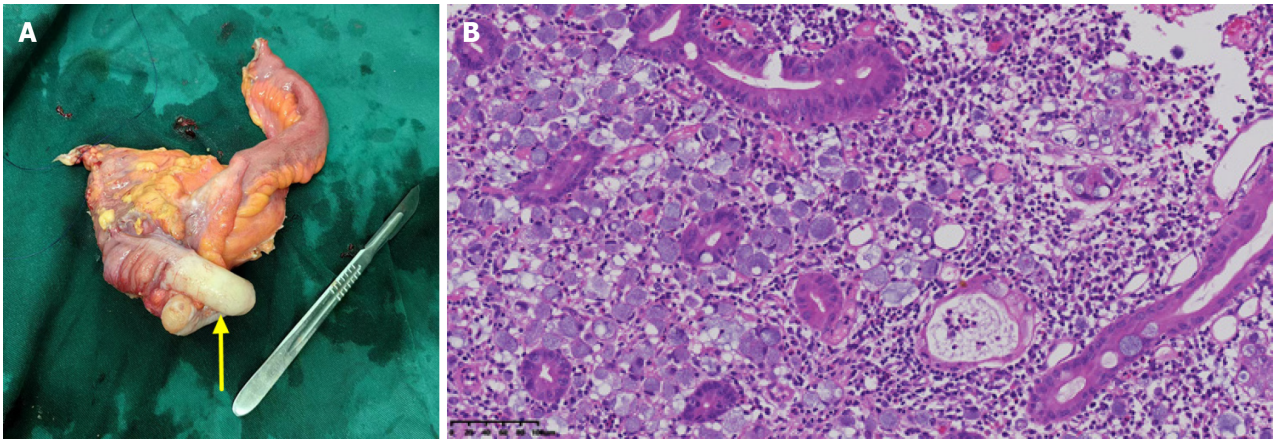

Figure 3 Intraoperative specimens and pathological images of appendix surgery. A: Intraoperative enlargement of the appendix; B: Pathological images (original magnification, × 200).

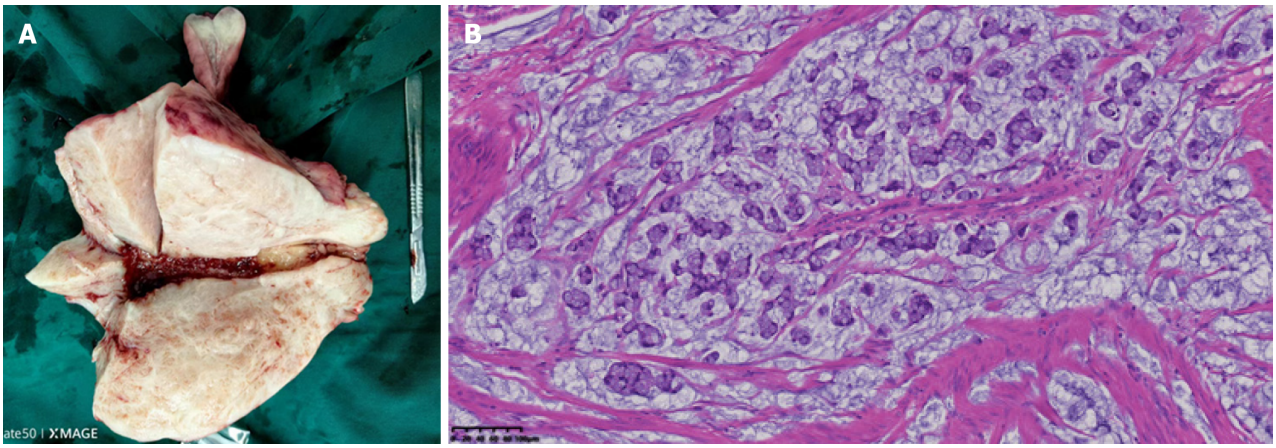

Figure 4 Intraoperative specimens and pathological images of uterine surgery. A: Intraoperative enlarged uterus; B: Pathological images (original magnification, × 400).

degrees of enhancement and ascites is rarely observed.

CONCLUSION

Appendiceal Signet ring cell carcinoma is relatively rare, and preoperative diagnosis remains challenging. However, when imaging reveals thickening of the appendiceal wall alongside marked thickening of the uterine myometrium, with lesions demonstrating progressive enhancement after contrast administration, implantation appendiceal signet ring cell carcinoma involving the uterus should be considered.

FOOTNOTES

Author contributions: Liu JM and Li Z have the equal contribution to the manuscript; Liu JM and Li Z contributed to drafting of manuscript; Qi LH and Liu JM contributed to assessment of imaging examination; Chu BL and Deng ZX contributed to the acquisition of data; Tang FY was responsible for conceptualization and design of the study, guiding the writing of the paper and quality control; all the authors solely contributed to this paper.

Informed consent statement: Written informed consent was obtained from the patient to publish this paper.

Conflict-of-interest statement: We have no financial relationships to disclose.

CARE Checklist (2016) statement: The authors have read the CARE Checklist (2016), and the manuscript was prepared and revised according to the CARE Checklist (2016).

Country of origin: China

ORCID number: Zhi Li 0000-0002-9416-5927; Feng-Yun Tang 0000-0001-7439-2287.

S-Editor: Liu H
L-Editor: A
P-Editor: Lei YY

REFERENCES

1 **Hugen N**, Verhoeven RH, Lemmens VE, van Aart CJ, Elferink MA, Radema SA, Nagtegaal ID, de Wilt JH. Colorectal signet-ring cell carcinoma: benefit from adjuvant chemotherapy but a poor prognostic factor. *Int J Cancer* 2015; **136**: 333-339 [*RCA*] [PMID: 24841868 DOI: 10.1002/ijc.28981] [FullText]
2 **Nitsche U**, Friess H, Agha A, Angele M, Eckel R, Heitland W, Jauch KW, Krenz D, Nüssler NC, Rau HG, Ruppert R, Schubert-Fritschle G, Wilhelm D, Werner J, Engel J. Prognosis of mucinous and signet-ring cell colorectal cancer in a population-based cohort. *J Cancer Res Clin Oncol* 2016; **142**: 2357-2366 [*RCA*] [PMID: 27573386 DOI: 10.1007/s00432-016-2224-2] [FullText] [Full Text(PDF)]
3 **Benesch MGK**, Mathieson A. Epidemiology of Signet Ring Cell Adenocarcinomas. *Cancers (Basel)* 2020; **12**: 1544 [*RCA*] [PMID: 32545410 DOI: 10.3390/cancers12061544] [FullText] [Full Text(PDF)]
4 **Thota R**, Fang X, Subbiah S. Clinicopathological features and survival outcomes of primary signet ring cell and mucinous adenocarcinoma of colon: retrospective analysis of VACCR database. *J Gastrointest Oncol* 2014; **5**: 18-24 [*RCA*] [PMID: 24490039 DOI: 10.3978/j.issn.2078-6891.2013.051] [FullText]
5 **Wu X**, Lin H, Li S. Prognoses of different pathological subtypes of colorectal cancer at different stages: A population-based retrospective cohort study. *BMC Gastroenterol* 2019; **19**: 164 [*RCA*] [PMID: 31601167 DOI: 10.1186/s12876-019-1083-0] [FullText] [Full Text(PDF)]
6 **Enblad M**, Egerszegi PP, Birgisson H, Sjöblom T, Glimelius B, Folkesson J. Signet Ring Cell Colorectal and Appendiceal Cancer: A Small Signet Ring Cell Component Is Also Associated with Poor Outcome. *Cancers (Basel)* 2023; **15**: 2497 [*RCA*] [PMID: 37173961 DOI: 10.3390/cancers15092497] [FullText] [Full Text(PDF)]
7 **Andjelkovic B**, Stojanovic B, Stojanovic MD, Milosevic B, Cvetkovic A, Spasic M, Jakovljevic S, Cvetkovic D, Stojanovic BS, Milosev D, Mitrovic M, Stankovic V. Appendiceal Signet Ring Cell Carcinoma: An Atypical Cause of Acute Appendicitis-A Case Study and Review of Current Knowledge. *Diagnostics (Basel)* 2023; **13**: 2359 [*RCA*] [PMID: 37510102 DOI: 10.3390/diagnostics13142359] [FullText] [Full Text (PDF)]
8 **An YY**, Yang GZ, Lin B, Zhang N, Hou HT, Zhu FM, Tian FJ, Wang J. Differentiation of lipid-poor adenoma from pheochromocytoma on biphasic contrast-enhanced CT. *Abdom Radiol (NY)* 2021; **46**: 4353-4361 [*RCA*] [PMID: 34036424 DOI: 10.1007/s00261-021-03121-9] [Full Text]
9 **Caesar-Peterson S**, Tulla K, Southall C, Lin Y, Genelus-Dominique E. A rare case of signet ring cell carcinoma of the appendix. *J Surg Case Rep* 2020; **2020**: rjaa139 [*RCA*] [PMID: 32699593 DOI: 10.1093/jscr/rjaa139] [FullText] [Full Text(PDF)]
10 **Kulkarni RV**, Ingle SB, Siddiqui S. Primary signet ring cell carcinoma of the appendix: A rare case report. *World J Clin Cases* 2015; **3**: 538-541 [*RCA*] [PMID: 26090376 DOI: 10.12998/wjcc.v3.i6.538] [FullText] [Full Text(PDF)]
11 **Hyngstrom JR**, Hu CY, Xing Y, You YN, Feig BW, Skibber JM, Rodriguez-Bigas MA, Cormier JN, Chang GJ. Clinicopathology and outcomes for mucinous and signet ring colorectal adenocarcinoma: analysis from the National Cancer Data Base. *Ann Surg Oncol* 2012; **19**: 2814-2821 [*RCA*] [PMID: 22476818 DOI: 10.1245/s10434-012-2321-7] [FullText]
12 **Vukovic J**, Vrebalov Cindro P, Tomic S, Tonkic A. Signet Ring Carcinoma of the Appendix Presenting as Crohn's Disease in a Young Male. *Case Rep Gastroenterol* 2018; **12**: 277-285 [*RCA*] [PMID: 30022916 DOI: 10.1159/000489298] [FullText] [Full Text(PDF)]
13 **Turaga KK**, Pappas SG, Gamblin T. Importance of histologic subtype in the staging of appendiceal tumors. *Ann Surg Oncol* 2012; **19**: 1379-1385 [*RCA*] [PMID: 22302267 DOI: 10.1245/s10434-012-2238-1] [FullText]
14 **Cho YJ**, Kim HJ, Jang SK, Yeon JW, Kim KH, Paik SY. Signet-ring cell carcinoma of the appendix: a case report with an emphasis on sonographic findings. *Ultrasonography* 2016; **35**: 164-167 [*RCA*] [PMID: 26753605 DOI: 10.14366/usg.15063] [FullText] [Full Text(PDF)]
15 **Ina EA**, Sobczak A, Drzymalski K, Biglione A. Appendiceal Signet Ring Cell Carcinoma Presenting As Acute Appendicitis: A Case Report. *Cureus* 2024; **16**: e59137 [*RCA*] [PMID: 38803764 DOI: 10.7759/cureus.59137] [FullText]
16 **Wang F**, Tao Y, Liu Y, Tang G. Primary signet ring cell carcinoma of the appendix: An interesting case. *Am J Med Sci* 2022; **364**: e10-e11 [*RCA*] [PMID: 35595079 DOI: 10.1016/j.amjms.2022.05.011] [FullText]
17 **Okumura K**, Oura S. A Metastatic Breast Tumor of an Appendiceal Signet Ring Cell Carcinoma. *Case Rep Oncol* 2023; **16**: 267-272 [*RCA*] [PMID: 37123607 DOI: 10.1159/000529672] [FullText] [Full Text(PDF)]
18 **Kwag KS**, Kim HJ, Jang SK, Yeon JW, Paik S, Jeon BG, Kim KH, Park JH, Shin E. Sonographic Findings of Malignant Appendix Tumors in Seven Cases. *J Med Ultrasound* 2018; **26**: 52-55 [*RCA*] [PMID: 30065515 DOI: 10.4103/JMU.JMU_16_17] [FullText] [Full Text(PDF)]
19 **Habiba M**, Benagiano G. Classifying Adenomyosis: Progress and Challenges. *Int J Environ Res Public Health* 2021; **18**: 12386 [*RCA*] [PMID: 34886111 DOI: 10.3390/ijerph182312386] [FullText] [Full Text(PDF)]
20 **Harmsen MJ**, Trommelen LM, de Leeuw RA, Tellum T, Juffermans LJM, Griffioen AW, Thomassin-Naggara I, Van den Bosch T, Huirne JAF. Uterine junctional zone and adenomyosis: comparison of MRI, transvaginal ultrasound and histology. *Ultrasound Obstet Gynecol* 2023; **62**: 42-60 [*RCA*] [PMID: 36370446 DOI: 10.1002/uog.26117] [FullText]
21 **Ferlay J**, Soerjomataram I, Dikshit R, Eser S, Mathers C, Rebelo M, Parkin DM, Forman D, Bray F. Cancer incidence and mortality

worldwide: sources, methods and major patterns in GLOBOCAN 2012. *Int J Cancer* 2015; **136**: E359-E386 [*RCA*] [PMID: 25220842 DOI: 10.1002/ijc.29210] [FullText]

22 **Torre LA**, Bray F, Siegel RL, Ferlay J, Lortet-Tieulent J, Jemal A. Global cancer statistics, 2012. *CA Cancer J Clin* 2015; **65**: 87-108 [*RCA*] [PMID: 25651787 DOI: 10.3322/caac.21262] [FullText]

23 **Xie H**, Erickson BJ, Sheedy SP, Yin J, Hubbard JM. The diagnosis and outcome of Krukenberg tumors. *J Gastrointest Oncol* 2021; **12**: 226-236 [*RCA*] [PMID: 34012621 DOI: 10.21037/jgo-20-364] [FullText]

24 **Kakushima N**, Kamoshida T, Hirai S, Hotta S, Hirayama T, Yamada J, Ueda K, Sato M, Okumura M, Shimokama T, Oka Y. Early gastric cancer with Krukenberg tumor and review of cases of intramucosal gastric cancers with Krukenberg tumor. *J Gastroenterol* 2003; **38**: 1176-1180 [*RCA*] [PMID: 14714257 DOI: 10.1007/s00535-003-1227-3] [FullText]

Published by **Baishideng Publishing Group Inc**
7041 Koll Center Parkway, Suite 160, Pleasanton, CA 94566, USA
Telephone: +1-925-3991568
E-mail: office@baishideng.com
Help Desk: https://www.f6publishing.com/helpdesk
https://www.wjgnet.com